Prediction of creep deformation and rupture behavior of 304HCu austenitic stainless steel under uniaxial and multiaxial state of stress at different temperatures

By

KANHU CHARAN SAHOO

(Enrolment No: ENGG02201405008)

INDIRA GANDHI CENTRE FOR ATOMIC RESEARCH, KALPAKKAM

A thesis submitted to the

Board of Studies in Engineering Sciences

In partial fulfillment of requirements
for the Degree of

DOCTOR OF PHILOSOPHY

of

HOMI BHABHA NATIONAL INSTITUTE

August, 2020

Homi Bhabha National Institute

Recommendations of the Viva Voce Committee

As members of the Viva Voce Committee, we certify that we have read the dissertation prepared by **Kanhu Charan Sahoo** entitled **"Prediction of creep deformation and rupture behavior of 304HCu austenitic stainless steel under uniaxial and multiaxial state of stress at different temperatures"** and recommend that it may be accepted as fulfilling the thesis requirement for the award of Degree of Doctor of Philosophy.

Chairman – **Dr. Shaju K Albert**		**Date:** 12/2/21
Guide / Convener – **Dr. P. Parameswaran**		**Date:** 12/2/21
Examiner - **Prof. Rahul Mitra**	Rahul Mitra	**Date:** 12.02.2021
Member 1- **Dr. R. Divakar**		**Date:** 12/02/2021
Member 2- **Prof. M. Kamaraj (IIT-M)**	M. Kamaraj	**Date:** 12/02/2021
Member 3- **Dr. G. V. Prasad Reddy**	Reddy	**Date:** 12/2/2021

Final approval and acceptance of this thesis is contingent upon the candidate's submission of the final copies of the thesis to HBNI.

I/We hereby certify that I/we have read this thesis prepared under my/our direction and recommend that it may be accepted as fulfilling the thesis requirement.

Date: 12/2/21

Place: Kalpakkam

Signature
Co-guide (if any)

Signature
Guide
12/2/21
P. PARAMESWARAN

STATEMENT BY AUTHOR

This dissertation has been submitted in partial fulfillment of requirements for an advanced degree at Homi Bhabha National Institute (HBNI) and is deposited in the Library to be made available to borrowers under rules of the HBNI.

Brief quotations from this dissertation are allowable without special permission, provided that accurate acknowledgement of source is made. Requests for permission for extended quotation from or reproduction of this manuscript in whole or in part may be granted by the Competent Authority of HBNI when in his or her judgment the proposed use of the material is in the interests of scholarship. In all other instances, however, permission must be obtained from the author.

Kanhu Charan Sahoo

(Kanhu Charan Sahoo)

DECLARATION

I, hereby declare that the investigation presented in the thesis has been carried out by me. The work is original and has not been submitted earlier as a whole or in part for a degree / diploma at this or any other Institution / University.

Kanhu Charan Sahoo

(Kanhu Charan Sahoo)

<u>List of Publications arising from the thesis</u>

Journal

1. *"Creep Rupture Behavior and Microscopic Analysis of 304HCu Austenitic Stainless Steel Under Multiaxial State of Stresses at 973 K"*, **Kanhu Charan Sahoo,** S. Ravi, Sunil Goyal, P. Parameswaran, K. Laha, Transactions of the Indian Institute of Metals (2016), vol. 69, pp. 451–455.
2. "*Assessment of creep deformation, damage, and rupture life of 304HCu austenitic stainless steel under multiaxial state of stress",* **Kanhu Charan Sahoo,** S. Goyal, P. Parameswaran, S. Ravi and K. Laha, Metallurgical and Materials Transactions A (2018), vol. 49, pp. 881-898.
3. "*Analysis of creep deformation and damage behaviour of 304HCu austenitic stainless steel* ", **Kanhu Charan Sahoo,** S. Goyal, V. Ganesan, J. Vanaja, G. V. Prasad Reddy, P. Parameswaran & K. Laha, Materials at High Temperature (2019), vol. 36, pp. 388-403.
4. "*Influence of notch geometry and temperature on creep behaviour of 304HCu SS",* **Kanhu Charan Sahoo,** V. D. Vijayanand, Sunil Goyal, P. Parameswaran and K. Laha, to Materials Science and Technology (2019), vol. 35, pp. 2181-2199.
5. *"Assessment of creep deformation and rupture behaviour of 304HCu austenitic stainless steel"*, **Kanhu Charan Sahoo,** Sunil Goyal, K. Laha, Proceedia structural integrity (2019), vol. 14, pp. 60-67.
6. *"Effect of notch depth on creep rupture behaviour of 304HCu austenitic stainless steel",* **Kanhu Charan Sahoo,** Sunil Goyal, V. Thomas Paul, K. Laha, Materials at High Temperature (2020), vol. 37, pp. 295-304.

Chapters in books and lectures notes

1. "*Structural integrity mechanics and creep life prediction of 304HCu austenitic stainless steel under multiaxial state of stress",* **Kanhu Charan Sahoo,** Sunil Goyal, P. Parameswaran, S. Ravi, K. Laha, Advance in Structural Integrity Proceedings of SICE-2016, pp. 353-367.

Conferences

1. "*Effect of multiaxial state of stress on creep behavior of 304HCu austenitic stainless steel",* **Kanhu Charan Sahoo,** S. Ravi, Sunil Goyal, P. Parameswaran, K. Laha, 4th National Convention on Hydrogen Energy and Advanced Materials (HEAM Scientist & Scholar 2015) November 28-29, 2015 Bhopal, India.
2. "*Creep Rupture Behavior and Microscopic Analysis of 304HCu Austenitic Stainless Steel Under Multiaxial State of Stresses at 973 K",* **Kanhu Charan Sahoo,** S. Ravi, Sunil Goyal, P. Parameswaran, K. Laha, Creep, Fatigue and Creep-fatigue interaction, January 19-22, 2016, IGCAR, Kalpakkam.
3. *"Structural integrity mechanics and creep life prediction of 304HCu austenitic stainless steel under multiaxial state of stress",* **Kanhu Charan Sahoo,** Sunil Goyal, P. Parameswaran, S. Ravi, K. Laha, First Structural Integrity and Conference and Exhibition (SICE-2016), Bangalore, July 4-6, 2016.
4. *"Mechanistic approach of Creep deformation and damage behaviour of 304HCu SS with the effect of temperature",* **Kanhu Charan Sahoo,** Sunil Goyal, P. Parameswaran, K. Laha, Indian Institute of Metals, NMD-ATM 71st Annual Technical Meeting November 11-14, 2017.
5. *"Effect of temperature and multiaxial state of stress on creep deformation and rupture life of 304HCu Austenitic stainless steel"* **Kanhu Charan Sahoo,** Sunil Goyal, K. Laha, Research Scholars Meet on Materials Science and Engineering of Nuclear Materials-HBNI, May 7 to 9, 2018, IGCAR, Kalpakkam, Tamilnadu.
6. *"Assessment of creep deformation and rupture behaviour of 304HCu austenitic stainless steel",* **Kanhu Charan Sahoo,** Sunil Goyal, K. Laha, Second Structural Integrity and Conference and Exhibition (SICE-2018), Hyderabad, July 25-27, 2018.
7. *"Effect of U-notch depth on creep deformation behaviour and rupture life of 304HCu SS",* **Kanhu Charan Sahoo,** Sunil Goyal, P. Parameswaran, K. Laha, International Conference on Structural integrity (ICONS 2018), 14-17 December, 2018, IIT-Madras, Chennai, India

Others

1. Attended Pre-conference workshop held at DMRL, Hyderabad, 23-24 July 2018.
2. Attended Training on ABAQUS 2017 unified FEA by M/s Dassault Systems, Computer centre, IGCAR Kalpakkam, 23-30 Jan 2017.

Kanhu Charan Sahoo

(Kanhu Charan Sahoo)

Dedicated to…

My beloved parents and brothers

ACKNOWLEDGEMENTS

First I would like to express my sincere and deepest gratitude to my former guide Dr. K. Laha, currently working as a Raja Raman Fellow at AUSC Mission Directorate, Noida, New Delhi, for his valuable guidance, inspiration, supervision and constant encouragement throughout my research work. I have worked four years with him, during which he helped me in several occasions, right from making specimens to the analyzing results, correcting the manuscripts, critically reviewing thesis and important technical discussion to put me in the right path. He had extended his good office still submission of the thesis.

I thank to my current guide Dr. P. Parameswaran, Head, XRDSES, Physical Metallurgy Division, Metallurgy & Materials Group, IGCAR, Kalpakkam for his timely help, insightful comments and constant inspiration for successfully completion of my thesis work.

I am deeply obliged to my eminent members of PhD Doctoral Committee, Dr. Shaju K. Albert, Chairman, Doctoral Committee and members of the committee, Dr. R. Divakar, Prof. M. Kamaraj, IIT Madras and Dr. G. V. Prasad Reddy for their valuable comments and fruitful suggestions during the reviews of my PhD work.

I thank to Dr. A.K. Bhaduri, Director, IGCAR, Kalpakkam and Dr. G. Amarendra, Director, MMG, IGCAR, Kalpakkam for providing support during the course of the research work.

I am sincerely thankful to Dr. Sunil Goyal for sharing his knowledge and useful discussion during analyzing the results and correcting the manuscripts. I also thank to Dr. S. Ravi and Dr. V. D. Vijayanand for their help in specimen fabrication and carrying out creep experiment. I would like to acknowledge Dr. C. R. Das and Dr.

Vani Shankar for his support and assistance during SEM and EBSD investigations. I am grateful to Shri. Utpal Borah and Dr. H. C. Dey for providing material for my research work.

I would like to express my sincere regards to Creep Studies Section colleagues, Shri T. Shaktivel, Shri J. Christopher, Dr. J. Ganesh Kumar, Smt. J. Vanaja for their help, support and valuable suggestions during the research tenure. I acknowledge the help received from Shri. K. Mariappan and Shri. V. Ganesan during EBSD characterization. I would like to acknowledge Smt. S. Vidya and Smt. Paneer Selvi for their help during SEM and tensile testing, respectively. I thank to Shri. Sameer Kumar Paul, Shri. M. Srinivasa Rao, Shri. Yogesh Kumar, Shri Abinash kumar for their help during preparation of the chemicals and samples for optical micrograph, SEM and EBSD investigations.

I wish to acknowledge my JRF and SRF friends especially, Shri. C. Praveen, Shri. V. Shiva, Shri. T. Suresh, Shri. M. Raghavendran, Shri. Chiranjit Poddar, Smt. Teena Mouni for their informal encouragement, support, making several funs which always made me happy in my day to day life.

My Special thanks to DAE Hospital, Kalpakkam for taking care of my health which strengthen me in the research work.

I am expressing my sincere gratitude and love to my father Shri. Sahadev Sahoo and mother Smt. Drowpadi Sahoo for their sacrifices and blessings without which it could have not possible for completion of thesis. Last but not in the list, I thank to my brothers Shri. Jagannath Sahoo, Shri. Balaram Sahoo, Shri. Manoranjan Sahoo and Shri. Naresh Sahoo for providing moral support with care during difficult situations.

Contents

Chapter-6: CREEEP LIFE PREDICTION UNDER MULTIAXIAL STATE OF STRESS & CONSTRUCTION OF MASTER PLOT

Chapter-7 EFFECT OF U-NOTCH DEPTH ON CREEP BEHAVIOUR AND RUPTURE LIFE

LIST OF FIGURES

Chapter-2

Chapter 3

Chapter-4

Chapter-5

Chapter-6

Chapter-7

List of tables

List of Symbols and Abbreviations

σ	Applied stress
σ_{eff}	Effective stress
σ_R	Resisting stress
σ_T	Transition stress
σ_t	True stress
σ_{vm}	von-Mises stress
σ_{rep}	Representative stress
σ_{net}	Net applied stress
σ_1	Maximum principal stress
σ_2	Intermediate principal stress
σ_3	Minimum principal stresses
ε_c	Total creep strain
ε_0	Instantaneous creep strain on loading
ε_p	Primary creep strain
ε_s	Secondary creep strain
ε_t	Tertiary creep strain
ε_f	Fracture strain
$\dot{\varepsilon}$	Strain rate
$\dot{\varepsilon}_{ss}$	Steady state creep rate
ε_T	Transient creep strain

$\dot{\varepsilon}_i$	Initial creep rate
τ_1, τ_2, τ_3	Principal shear stresses
$\gamma_1, \gamma_2, \gamma_3$	Principal shear strains
$\dot{\gamma}_1, \dot{\gamma}_2, \dot{\gamma}_3$	Principal shear strain rates
t_{os}	Time to onset secondary stage of creep deformation
t_{ot}	Time to onset tertiary stage
t_r	Rupture life
ω	Creep Damage
ω_{cr}	Critical Creep Damage
$\dot{\omega}$	Creep Damage rate
A and n	Coefficients of Norton's creep law (relating stress with steady state creep rate)
φ *and* B	Coefficients of damage rate equation
α and C	Monkman-Grant relation coefficients
M *and* m (*or* φ)	Coefficients of relation between stress and rupture life
K	Strength coefficient
n'	Strain hardening exponent
K'	Proportionality constants relating initial creep rate with steady state creep rate.
D	Shoulder diameter of the notch
d	Notch throat plane diameter
R	Notch root radius
A'	Pre-exponential complex constant

r'	Rate of exhaustion of transient creep
τ	Relaxation time
μ	Shear modulus
λ	Creep damage tolerance factor
β	Proportionality constant relating rate of exhaustion with steady state creep rate
P	Internal pressure
t	Thickness of pipe
r	Radius of the pipe
Q_c	Activation energy for creep deformation
D_o	Frequency factor
G	Shear modulus
d'	Grain size
b	Burger vector
k	Boltzman's constant
T	The absolute temperature (Kelvin)
R'	Universal gas constant
p	Inverse of grain size exponent
$2c$	Particle diameter
2d	Interparticle spacing
τ	Cavity nucleation stress
γ_b	Grain boundary energy

ν	Poisson's ratio
a	Cavity radius
γ_c	Surface energy
$2h$	Cavity height
$2l$	Distance between the cavities
Λ	Diffusion length
D_{gb}	Diffusion coefficient
Ω	Atomic volume
δ	Grain boundary width

Abbreviations

AUSC	Advanced Ultra Super Critical
2D	Two dimensional
FE	Finite element
CDM	Continum Damage Mechanics
FE-CDM	Finite Element coupled with Continum Damage Mechanics
NAR	Notch acuity ratio
NDR	Notch depth ratio
NSR	Normalised stress ratio
NH	Nabaro Herring
LT	Low temperature
HT	High temperature

GBS	Grain boundary sliding
DCCG	Diffusion controlled cavity growth
TF	Triaxiality factor
CEEQ	Creep equivalent strain
SNCF	Strain concentration factor
K-R	Kachanov Rabotnov
SANS	Small angle neutron scattering
SEM	Scanning electron microscopy
TEM	Transmission electron microscopy
EBSD	Electron backscattered diffraction
OIM	Orientation imaging microscopy
KAM	Kernel average misorientation
HV	Vickers hardness

Chapter: 8

SUMMARY AND SCOPE FOR FUTURE WORK

The studies pertaining to wide range of creep test of different notched specimen to assess the multiaxiality and smooth specimen on 304HCu SS at 923, 973 and 1023 K have been summarized and further work have been reported.

8.1 Summary

The rupture life of the material was found to increase in the presence of notch, exhibiting notch strengthening for the same net applied stress at all the temperature under study. The rupture life of the material was found to increase with increase in notch sharpness and tended towards saturation with higher notch acuity ratio. However, material exhibits tendency to decrease in rupture life at relatively lower stresses for sharper notch (notch acuity ratio 20). The rupture ductility was found to decrease with increase in notch sharpness and tended towards saturation and the test temperature had less effect on multiaxial ductility. The extent of strengthening depends on the testing temperature appreciably.

The fracture mode was found to change from predominantly ductile dimple to predominantly intergranular creep cavitation with decrease in stress, increase in temperature and notch sharpness. For a given temperature, fracture appearance depends on the notch acuity ratio and applied stress. The fractographic studies revealed the mixed mode of failure consisting of transgranular dimples and intergranular creep cavitation for shallow notches, whereas the failure was predominantly intergranular creep cavitation for relatively sharper notches. Intergranular creep cavitation with microcracks was predominantly seen at the notch root for maximum notch acuities at 973 and 1023 K while in centre the proportion of transgranular dimple decreases with increase in notch sharpness (higher notch acuity). At 923 K, transgranular dimples with isolated cavities was predominantly observed at the notch root for maximum notch acuities while centre shows transgranular dimple to mixed mode failure with increase in notch sharpness. On creep exposure, hardness near the notch root was much higher than the hardness value before creep testing and gradually decreased towards central region. With increase in test temperature, the overall hardness decreased across the notch throat plane and remained above the hardness value before creep testing for the steel tested at 923 K and 973 K. However, at 1023 K the hardness values reduced than the hardness value before creep testing. Extensive dislocation cell formation as well as precipitation of Cu-particles pinning the dislocation movement were observed from TEM observation near to the notch root. This is due to higher degree of triaxiality (relatively sharper notch) that results increase in strain induced precipitation and their complex interaction with dislocations results well defined dislocation structures/cells and tangles, increases hardness at the notch root. The above result needs a systematic study invoking finite element analysis of multiaxial state of stress and strain.

The FE-analysis reported that stress distribution in the notch throat plane remained same irrespective of the plastic strain in the notch region. The role of plastic deformation in the stress distribution across the notch throat plane under creep condition was almost negligible. Hence, further analysis of stress distribution across the notch root throat plane has been carried out considering the elastic-creep behavior of the material only. The stress distribution with creep exposure was found to be dependent on the notch root radius significantly. For relatively sharper notch with creep exposure, the von-Mises stress increased at the notch central region and decreased at the notch root region leading to stationary state having high stress at the notch root region and lower stress at the notch central region. The maximum principal stress distribution possessed peak at close to notch root with value more the net applied stress for relatively sharper notch. The stationary von-Mises stress was less than the net applied stress for both the shallow and sharp notches; where the stationary maximum principal stress was more than the net applied stress at central region for relatively shallow notches and at close to notch root region for relatively sharper notches. The von-Mises stress decreased with notch sharpness and for relatively sharper notches exhibited higher values at notch root which causes enhanced cavity nucleation at the notch root but much lower than the net applied stress which results notch strengthening and extent of strengthening decreases with decrease in notch sharpness. The maximum principal stress exhibited peak value at intermediate location between the center and notch root, which became more for relatively sharper notches and was higher than the net applied stress. The variation of hydrostatic stress with notch sharpness was similar to that of the principal stress with peak value close to the notch root. Presence of high maximum principal and hydrostatic stress results uniform growth of the nucleated cavities that causes predominance transgranular dimple failure at the centre of the smooth notch specimen and decreases with increase in notch sharpness as seen experimentally. Further, higher normalized von-Mises, maximum principle and hydrostatic stresses for higher test temperature results enhanced cavitation.

OIM investigation showed that increase in strain with increase in notch sharpness and KAM value which is a signature of enhanced localized strain accumulation resulted in considerable nucleation of cavities and micro-cracks. However, in case of the steel tested at lower temperature and high stress the activation of twinning resulted in lowering the localized strain accumulation which resulted in lower incidence of isolated cavities.

Multiaxial creep rupture life prediction was carried out at different temperatures based on the relationship of representative stress on different components of stresses at the skeletal point, proposed by Hayhurst, Cane, and Nix et al. The relative contribution of von-Mises stress and maximum principal stress in governing creep rupture life at 923, 973 and 1023 K has been assessed. The maximum principal stress plays important role in assigning creep rupture life of the 304HCu stainless steel compared to ferritic steel. Further, with increase in temperature importance of maximum principle stress decreases and von-Mises stress increases which indicate creep cavitations tendency increases with increase in temperature for this precipitation hardened material. From all the models, Cane's model was found suitable for predicting the multiaxial creep rupture life along with the smooth specimen data of 304HCu SS at different temperatures. On the other hand a unique master plot which considers the independence of smooth, notch and creep tested temperature has been constructed based on Cane's model within a 12% standard error for the application of the steel in power plant. Creep rupture ductility under multiaxial state of stress has been assessed by using the models proposed by Cocks and Ashby, Rice and Tracey and Manjoine at the skeletal point triaxiality. Finally, a unique model has been proposed which is the cumulative model of all the above three model and can be used for the multiaxial creep ductility prediction at any temperatures and may be for other ferrous material also. An attempt has been made to understand the multiaxial creep behaviour by varying notch depth for a constant notch root radius at 973 K. It was found that the multiaxial creep rupture life of the material under notch depth variation was found to control by both equivalent stress and strain distribution.

8.2 Scope for future work

- Multiaxial creep test can be carried out by varying notch angle and notch depth for a wide range of stresses and their life prediction.
- The improvement in prediction of the creep deformation behaviour and rupture life is possible if change in dislocation density, phase change, grain boundary sliding, precipitation

coarsening etc. will be considered in the Continuum Damage Mechanics model which is associated with strain induced damage, thermal induced damage and environmental damage.

- Long term creep test can be carried out to assess the materials behaviour towards notch strengthening/weakening and predicting the creep life of the material in more realistic manner.
- Further, other mode of testing like biaxial testing of tube under internal pressure, tension-torsion test of thin-walled pipes could give a real deformation and rupture behaviour under multiaxial state of stress.
- Effect of ageing on microstructural characterization at different creep exposure time.
- Studies can also be performed under dynamic loading condition to assess creep-fatigue interaction under multiaxial state of stress.

ABSTRACT

The boiler tubes made of 304HCu austenitic stainless steel (304HCu SS) are subjected to multiaxial state of stress due to internal pressure, bends, changes in section thickness, presence of weld joints and having inhomogeneous structures. Hence, it is important to study the response of the material under multiaxial state of stress. In order to study the influence of multiaxial creep deformation and rupture behaviour on 304HCuSS, creep test has been carried out on both smooth and notched specimens of the given steel at 923 K, 973 K and 1023 K over the stress range of 100 to 260 MPa.

For smooth specimen, creep deformation of the material exhibited very short primary creep regime followed by limited secondary stage and significant tertiary stage. Variation of steady state creep rate ($\dot{\varepsilon}_s$) with applied stress (σ_a) at all the tested temperature obeys power law. The transient creep is analyzed using Garofalo equation and from steady-state creep regime, back stress was calculated using Lagneborg and Bergman graphical method at different temperatures. 304HCu SS has spent about 60, 64 and 72% of their creep rupture life in the tertiary stage of creep deformation based on the good linear fitting of 't_{ot}' with 't_r' at 923 K, 973 K and 1023 K respectively. Based on CDM approach an indication of damage process indicating tertiary creep is provided by the creep damage tolerance factor (λ) which is defined as the ratio of strain to failure (ε_f)to the steady state creep rate ($\dot{\varepsilon}_s$) and rupture life (t_r). The value of 'λ' was found to decrease with increase in rupture life. Creep strain and rupture life of the 304HCu SS were well predicted using the FE-analysis coupled with continum damage mechnics equations proposed by Kachanov model.

In the presence of notch, creep rupture strength was found to increase with increase in notch sharpness with associated decrease in ductility, however at relatively lower stress material possesses tendency towards notch weakening for relatively sharper notches. Fractographic studies revealed that proportion of transgranular ductile dimple to intergranular creep cavitation increases at and around notch location for relatively shallow notches and at lower temperature and with increase in notch sharpness and temperature percentage of intergranular creep cavitation becomes more pronounced. FE-analysis of the stationary stress distributions across the notch throat plane shows the reduction in von-Mises stress which is more pronounced for sharper notches, results notch strengthening in the material. The fracture behaviour of the material in the presence of notch based on the cavity nucleation and growth was elucidated through the contribution received from the von-Mises, maximum principal, and hydrostatic stresses. EBSD analysis at the notch root shows higher amount of strain accumulation with increase in temperature and notch sharpness. The higher degree of triaxiality (relatively sharper notch) results increase in strain induced precipitation and their complex interaction with dislocations results dislocation structures/cells and tangles, increases hardness at the notch root. Subsequently, the creep rupture life has been predicted at different temperatures using skeletal point method of representative stress through Hayhurst, Cane and Nix model. Further, a temperature independent unique master plot for multiaxial rupture life as a function of stress has been established. A modified model has been proposed for the prediction of multiaxial ductility at any temperature and other austenitic stainless steel based on the good fitting of experimental data. Multiaxial creep rupture life has also been studied by varying the notch depth for a constant root radius with detailed FE-analysis of stationary state distribution and correlated with fractographic observation and EBSD studies for strain mapping.

Keywords: 304HCu SS, Multiaxial creep, Finite element analysis, Transient creep analysis, Dorn’s equation, Kachanov-Rabotnov model, Skeletal point, Temperature independent Multiaxial model, Proposed ductility model, Effect of notch depth

Chapter: 1

Introduction and Literature review

1.1 Introduction

Pulverized coal power plants are divided into four categories depending on the operating temperature, pressure and efficiency (Table.1).

Table-1.1 Shows the different category of power plant depending upon the temperature, pressure and efficiency.

Category	**Temperature**	**Pressure**	**Efficiency**
Subcritical	$<540^0C$	170-220 bar	<38%
Supercritical	615^0C	250 bar	42%
Ultra-supercritical	$>620^0C$	330 bar	42-46%
Advanced ultra-supercritical (AUSC)	700^0C	>350 bar	>50%

Modern industry requires the decrease of carbon dioxide emission as well as reduction in cost of fuel on increasing the efficiency of power generation. It is reported that the UK's emission of CO2 has declined by around 38% since 1990, which is faster than any other major developed country [1]. Therefore, India has embarked on a mission project to design and develop an 800MWe Advanced Ultra Super Critical (AUSC) power plant with steam parameters of 710^oC / 720^oC /310 bar, as has been persuaded by other countries across the globe [2]. This is expected in 20% reduction in CO_2 emission at source combined with 20% saving in coal consumption compared to those in subcritical power plant. Currently, the supercritical power plants are operating at around 630^oC. Efficiency increase will be significant if the steam temperature would have increased above 700^oC which in turn calls for the use of high temperature creep resistant materials. The 304HCu austenitic stainless steel (SS) (Super 304H) is one of the candidate materials for AUSC, which has adequate elevated temperature creep strength. In this steel, creep resistance is mainly achieved by addition of 3 wt. % of copper which gives precipitation hardening during service. Additionally, the increase in carbon, niobium and nitrogen content in the steel are effective in retarding the dislocation motion compared to the conventional grades of austenitic stainless steel. Generally, the creep life of the components is designed based on the uniaxial state of stress. However, the components face multiaxial state of stress in presence of weld joints, notches or holes, tubes under internal pressure and the mode of loading during service etc. Under multiaxial state of stress, creep damage which results due to the formation and linkage of cavities and coarsening of precipitates and formation of dislocation substructure will be more as compared to uniaxial state of stress.

This chapter includes the creep deformation behaviour under different stress and temperature regimes, damage mechanics, change in microstructure on creep exposure, the factors influencing creep damage. The different modes of multiaxial state of stress have been reviewed [3]. Effect of notch sharpness (notch acuity ratio) on different materials has been discussed. The stress distribution by Finite element analysis across the notch plane investigated by different authors has been assessed. The multiaxial creep rupture life prediction of the material proposed by different authors has been reviewed. Also introduction of the 304HCu steel with general physical and mechanical properties has been made.

1.2 Creep deformation

Creep is defined as time dependent plastic deformation of material under the influence of constant stress/load at elevated temperature. The temperature for engineering consequence of creep will be more than $0.4T_m$, where T_m is the melting point of the material in Kelvin. Creep deformation will be severe if the operated temperature tends towards the melting point. A typical creep curve is shown in Fig. 1.1, indicating the different stages of creep deformation.

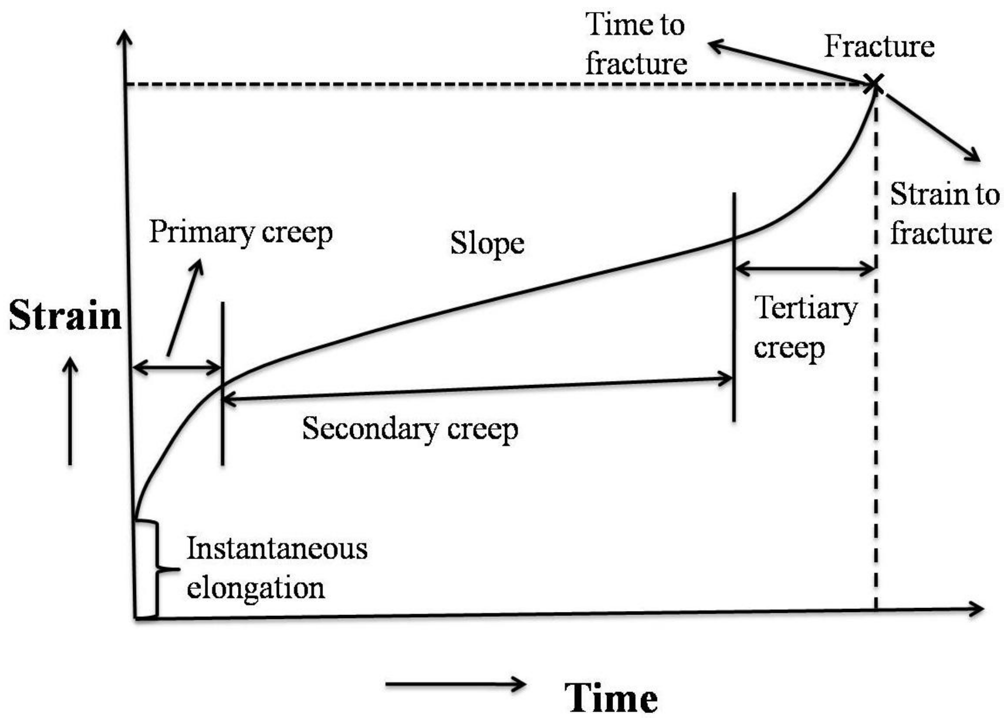

Fig. 1.1 Typical creep curve of Metals

The creep curve has been divided into three different stages apart from the instantaneous strain on loading. They are (i) Primary stage, (ii) Secondary stage and (iii) Tertiary stage of creep deformation. The total creep strain is $\varepsilon_c = \varepsilon_o + \varepsilon_p + \varepsilon_s + \varepsilon_t$, where ε_o is instantaneous strain on loading (elastic, anelastic and plastic), ε_p is primary or transient creep strain, ε_s is strain during steady-state creep deformation and ε_t is strain accumulation during the tertiary stage of creep deformation. The primary stage of creep deformation is associated with decrease in creep rate with increase in time. In primary stage, the rate of strain hardening is predominant than the rate of recovery of dislocation substructure. The secondary stage of creep deformation is associated with accumulation of creep deformation at constant rate. During secondary creep deformation, the rate of strain hardening and the rate of recovery are almost equal. Some materials, like tempered martensite ferritic steels, precipitate hardened superalloys etc., do not exhibit steady state creep deformation and hence minimum creep rate has been defined for such materials. Both the minimum creep rate and steady state creep rate are useful for designers for te purpose of component design. In tertiary stage of creep deformation, creep rate increases leading to the creep failure / rupture. In this stage, creep damage in the form of cavities or microcracks is predominant. The tertiary stage of creep deformation is associated with coarsening of particles, recrystallization and change of microstructure or formation of new phases, necking instability, increase in stress on deformation, oxidation/corrosion along with intergranular creep cavitation. The initiation of the damage process either externally or internally marks the onset of tertiary stage. All of these phenomena associated with different stages of creep deformation will determine the shape of creep curve. Neubauer et al. [4] reported that creep cavitation in the material has been characterized into four different stages as: 1 - isolated cavities, 2 - oriented cavities, 3 - linked cavities (microcracks) and 4 - macrocracks, as shown in Fig. 1.2

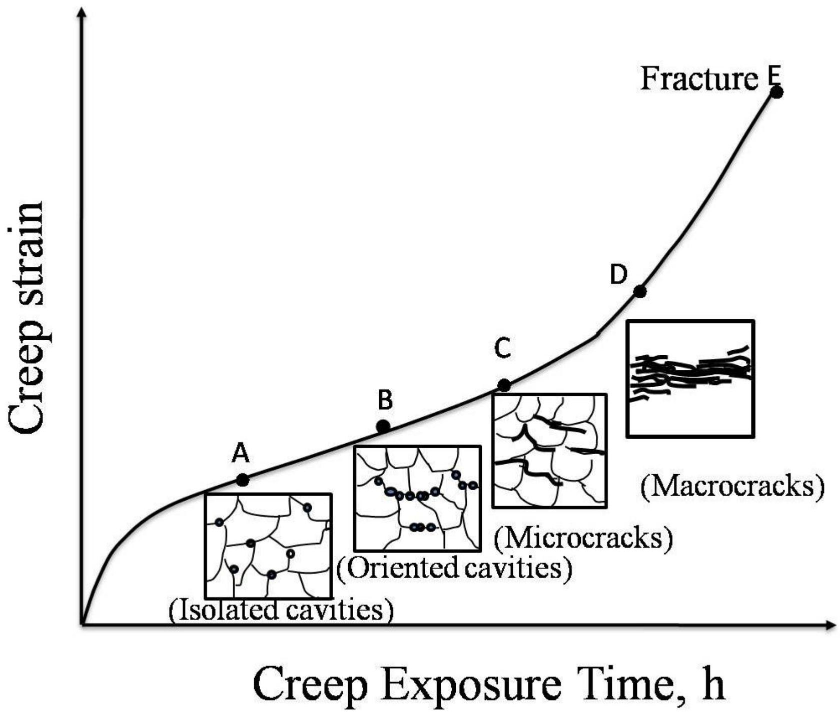

Fig.1.2 Schematics of several stages of creep cavity nucleation and its growth as a function of creep exposure [4].

1.2.1 Effect of Stress and Temperature

Creep tests are generally carried out for long durations. For this reason, short-term creep rupture test is similar to creep test but is carried out at high stresses and or at high temperatures up to the failure of the material for shorter durations. Several data points are obtained from the short-term creep tests. The log-log plot of stress with rupture life yields a straight line, indicating a power law relationship between stress and rupture life. In laboratory scale, this information is used to extrapolate the data for longer creep rupture life. Figure 1.3 (a) shows the dependence of creep curve at fixed stress with varying temperature; whereas Fig. 1.3 (b) shows the dependence of creep curve at fixed temperature with varying stress. At fixed temperature with increase in stress or at fixed stress with increase in temperature will result more creep strain rate and will shift the creep curve upward and left side.

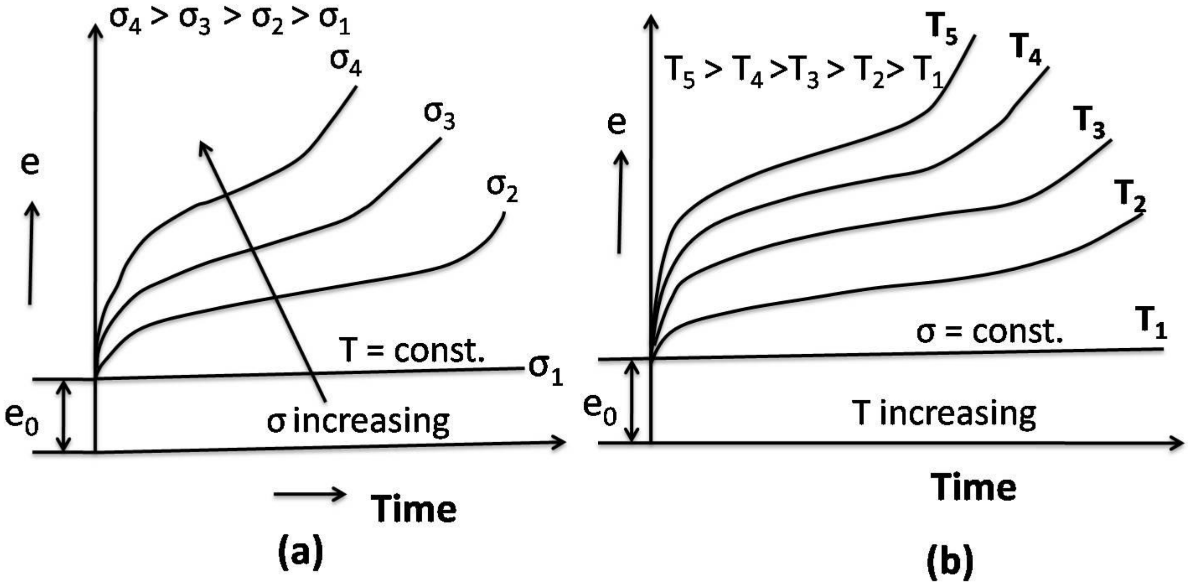

Fig.1.3 Schematic of creep curve with (a) different stress at fixed temperature and (b) different temperature at fixed stress.

1.3 Creep deformation mechanism

Creep deformation basically occurs either by movement of dislocations or by diffusion of atoms under stress gradient. The schematic view of different mechanisms associated with creep deformation is shown in Fig.1.4. It shows that creep deformation can be either dislocation creep or diffusion creep depending on temperature and stress. The dislocation creep can be either thermally controlled glide or climb (assisted by diffusion) controlled glide. Further, climb controlled glide can be bulk diffusion or pipe diffusion. On the other hand, diffusional creep is due to the diffusion of atom/vacancy which has been categorized into Nabaro-heering creep or Coble creep. Nabaro-heering creep is due to the bulk diffusion assisted process while Coble creep is due to the grain boundary diffusion. The details of each deformation mechanism have been described in the following sections.

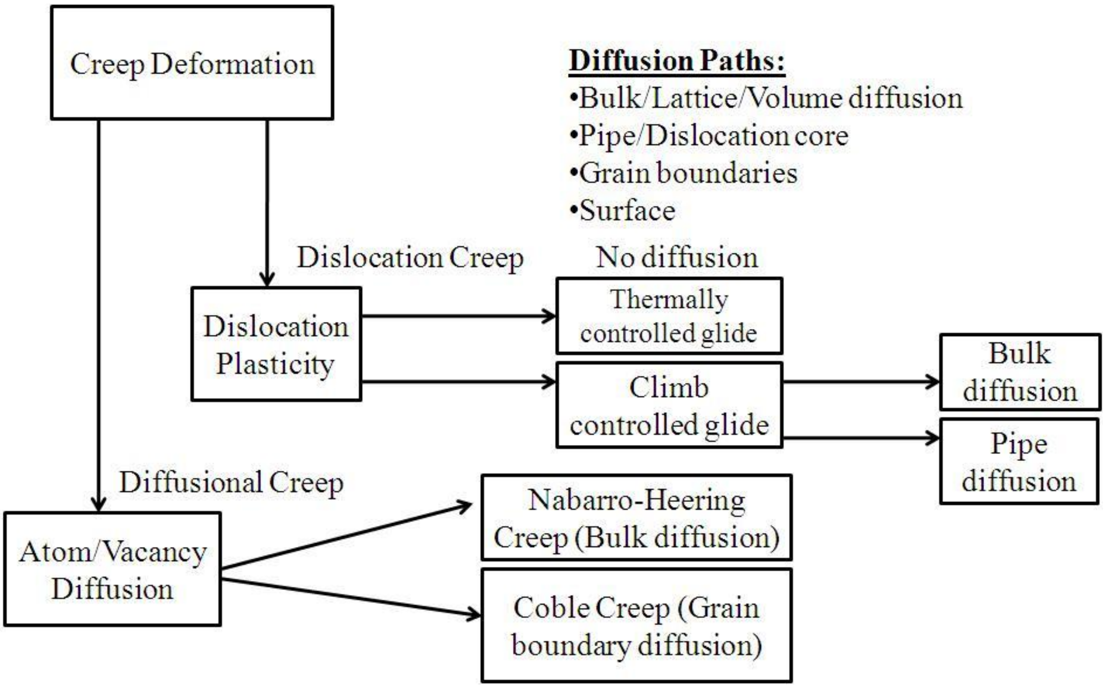

Fig. 1.4 Schematic representation of different mechanisms of creep deformation.

1.3.1 Dislocation glide

The movement of dislocations on glide plane overcomes short range barriers (lattice friction stress, solute atoms and fine particles) by combination of stress and thermal activation. This mechanism typically occurs at higher stress ($\frac{\sigma}{G} > 10^{-2}$) and needs no diffusion [Fig. 1.5]. Creep rate depends upon the ease at which dislocations are able to overcome the obstacles.

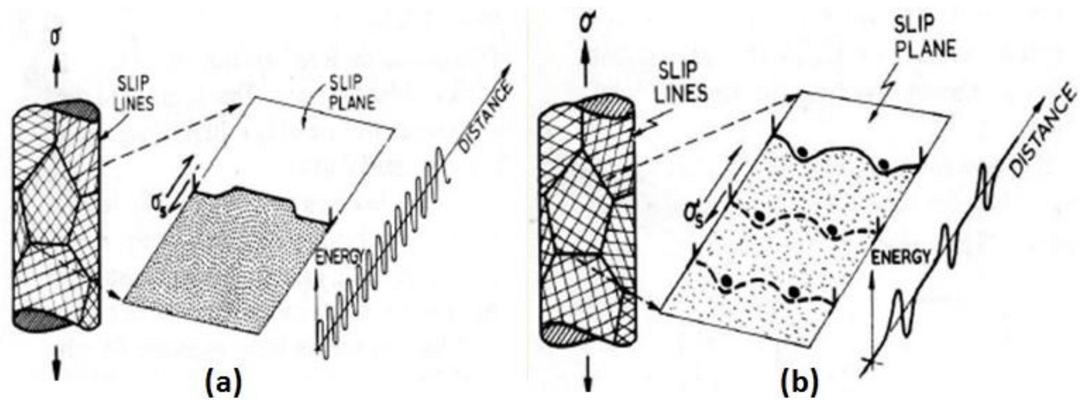

Fig. 1.5 Schematic representation of dislocation glide on a slip plane by overcoming the obstacles (a) lattice friction stress, and (b) solute atoms/fine particle.

1.3.2 Dislocation creep

The gliding of the dislocations is along the preferred slip plane and overcome the barriers by climb which is assisted by diffusion of vacancies or interstitials. It typically occurs at intermediate stresses $\left(10^{-4} < \frac{\sigma}{G} < 10^{-2}\right)$. Both glide and climb control the creep process. At elevated temperature, if glide process is obstructed by any barriers such as dislocation, fine particles or precipitates then a small amount of climb may permit to surmount the obstacle and allow it to glide to the next obstacle where the process is repeated [Fig.1.6 (a)]. This is typically seen in low stacking fault energy materials like copper, brass and stainless steel etc. For high stacking fault energy materials like aluminum and nickel, dislocations mainly move by climb and facilitates the formation of sub-grains/cell-type structure due to lattice and core diffusions [Fig.1.6 (b)]. Almost all the strain has been produced by glide and climb controls the velocity. In a sequential process slower step is the rate controlling process. Since climb is the diffusion controlled and is a slow process, climb controls the creep rate.

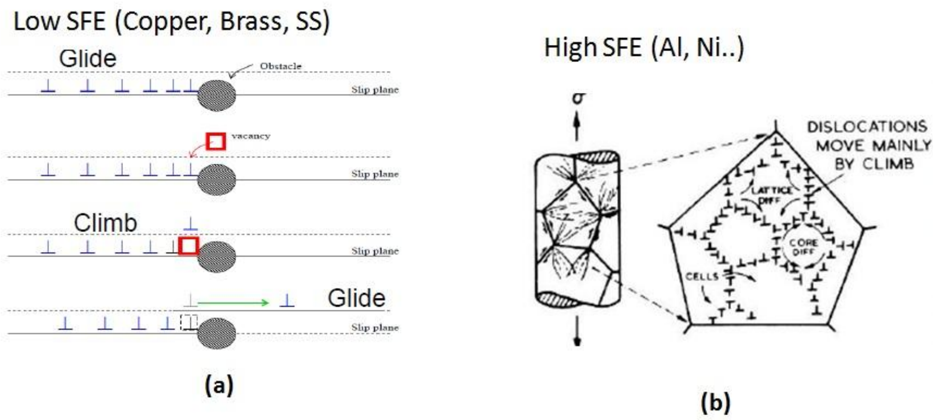

Fig. 1.6 Represents the schematic view of dislocation movement in (a) low SFE metals and (b) high SFE metals.

1.3.3 Diffusional creep

Diffusional creep mechanism dominates at very low stresses $\left(\frac{\sigma}{G} < 10^{-4}\right)$ and high temperatures. The stress directed flow of vacancies is due to the greater chemical potential difference at boundaries near to the tensile stress region than at boundaries near to the compressive stress region. Simultaneously, there is a corresponding flow of atoms from compressive region which leads to elongation of grains as shown in Fig. 1.7. At high temperature, Nabarro-Herring creep mechanism operates where lattice diffusion is more predominant. At relatively lower temperature, Coble creep diffusion operates where grain boundary diffusion occurs more predominantly.

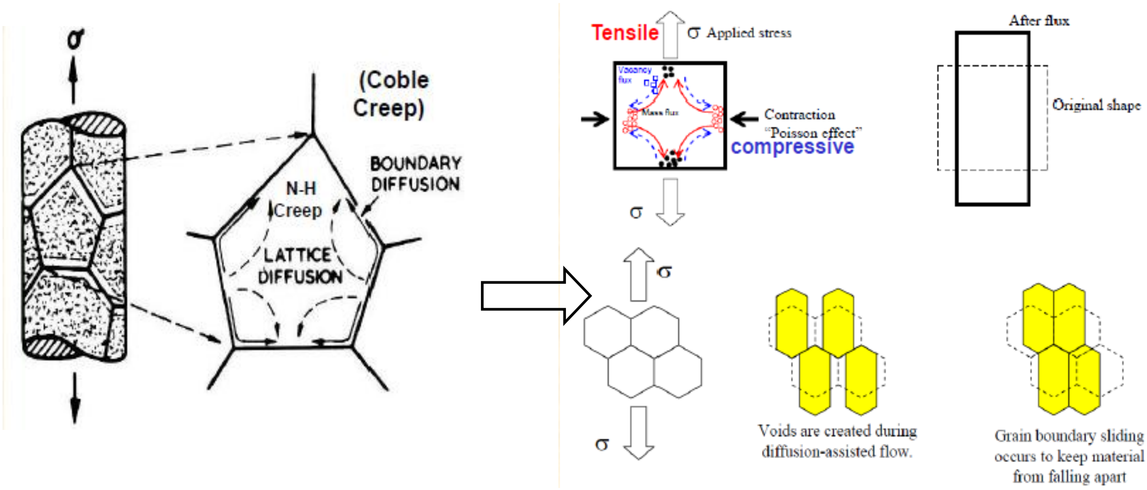

Fig. 1.7 Schematic representation of diffusion creep mechanism [5].

1.3.4 Grain boundary sliding

The sliding of the grains against each other leads to grain boundary sliding [Fig.1.8]. The intergranular creep fracture is mainly due to the grain boundary sliding. Its contribution to the overall creep deformation increases with decrease in stress and increase in temperature. Its presence maintains the grain continuity during diffusional flow mechanism. Grain boundary sliding is responsible for superplasticity with no net change in grain size and shape.

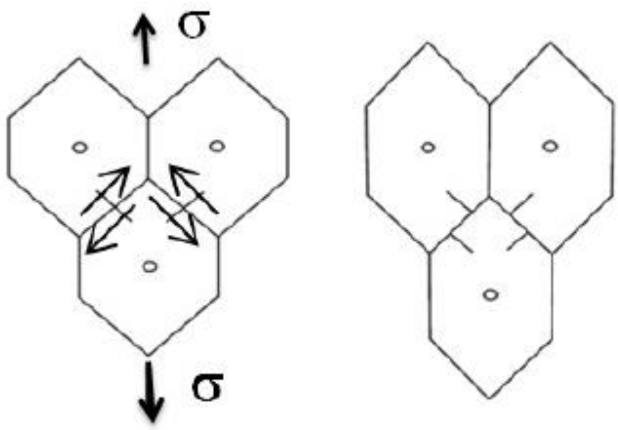

Fig. 1.8 Schematic representation of grain boundary sliding.

1.4 General form of creep equation

$$\dot{\varepsilon}_{ss} = \frac{ADGb}{kT}\left(\frac{\sigma}{G}\right)^{n}\left(\frac{b}{d'}\right)^{p}, where\ D = D_0 \exp\left({}^{Q}/_{R'T}\right) \qquad (1.1)$$

Where D = Diffusion coefficient

d' = Grain size

b = Burgers vector

k = Boltzmann's constant

T = The absolute temperature (Kelvin)

G = Shear modulus

σ = Applied stress

n = Stress exponent

p = Inverse grain size exponent A= a dimensionless constant

This form of the Dorn's equation applies for all the creep mechanism. The stress exponent (n) indicates the possible creep mechanism. The slope of plot of steady state creep rate ($\dot{\varepsilon}_{ss}$) versus stress (σ) in log-log scale gives the value of 'n'. The steady state creep rate is related to the activation energy during creep which can be expressed by an Arrhenius-type of rate equation.

$$\dot{\varepsilon}_{ss} = A' e^{\frac{-Q}{R'T}} \qquad (1.2)$$

Where Q = Activation energy for creep deformation

A' = Pre-exponential complex constant

T = Absolute temperature

R'= Universal gas constant

Experimentally the 'Q' value can be found from the slope of the plot between $ln(\dot{\varepsilon}_{ss})$ and ${}^{1}/_{T}$ at fixed stress (σ) at different temperatures such that the creep mechanism shouldn't change. The Q value depends on the operating mechanism and it is given by $Q_{surr} < Q_{GB} \sim Q_{pipe} < Q_{latticeorvol}$.

Table-1.2 Representative values of the parameters n and p and approximate values of the constant A for $\dot{\varepsilon}_{ss}$:

Mechanism	**Favoured by**	**Description**	**A**	**n**	**p**
Nabarro-Herring (NH) creep	High temperature, low stress, large grain size	Vacancy diffusion through crystal lattice	10-15	1	2
Coble creep	Low stress, fine grain size and temperature less than that in NH creep	Vacancy diffusion along the grain boundaries	30-50	1	3
Grain boundary sliding	Same range as in NH and coble creep	Sliding accommodated by vacancy diffusion through the crystal lattice (p=2) or along the grain boundaries(p=3)		2	2 or 3
Dislocation creep	High stress and lower temperature in comparison to Coble creep and larger grain size	At relatively high stress, controlled by thermal activated motion of dislocation and at relatively low stress, climb controlled motion of dislocation		3-7	0

1.5 Deformation mechanism map

The deformation mechanism of the materials are described by number of macroscopic variables namely stress (σ), temperature (T) and strain rate ($\dot{\varepsilon}$). Ashby and his co-workers developed a deformation mechanism map which gives a clear understanding of the dominance of deformation mechanics where normalized stress σ/G (where G is the shear modulus) is plotted against homologous temperature T/T_m (where T_m is the melting point in Kelvin) [Fig.1.9]. The upper limit of the diagram is known as ideal shear strength of material above which the deformation is completely elastic and catastrophic in nature. Just below the ideal shear strength, plastic flow occurs due to dislocation glide [Fig.1.5]. Then creep deformation which is time dependent, has been categorized in to two parts (i) dislocation creep [section 1.4.2] (ii) diffusion creep [section 1.7] [5]. Further, dislocation creep has been divided into high temperature creep and low temperature creep. On the other hand, diffusion creep is divided into Nabarro Herring creep and Coble creep [5].

The deformation mechanism map of 304 SS is shown in Fig. 1.10 The deformation mechanism map gives a clear understanding of the creep deformation in several ways. Firstly, it identifies the mechanism by which components or structure deforms; secondly, it identifies which constitutive law should be suitable for design; thirdly, it can be useful to estimate the total strain or strain rate of a component during service; and fourthly, it can be useful in alloy design and selection of material for a particular service condition.

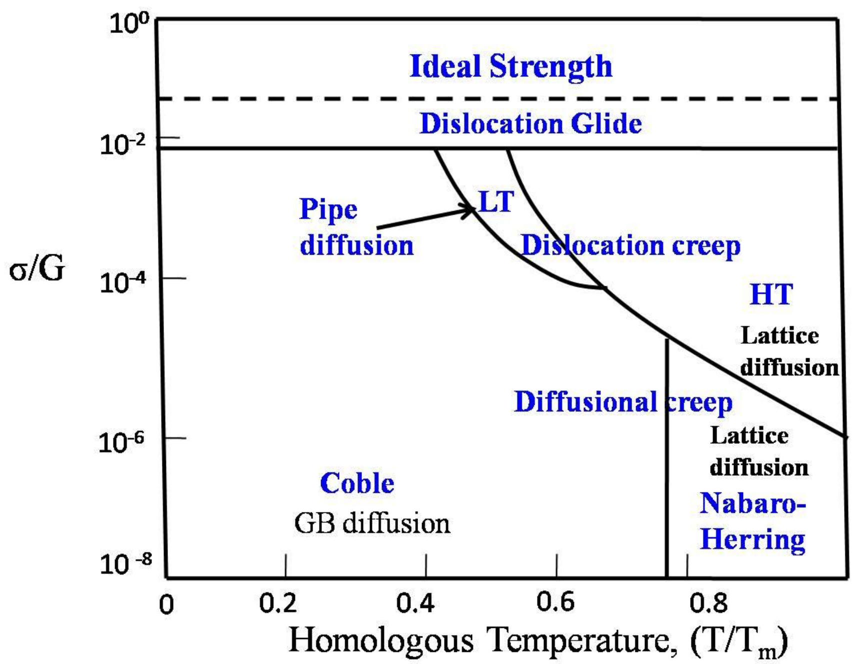

Fig. 1.9 Typical creep deformation mechanism map of metals [5].

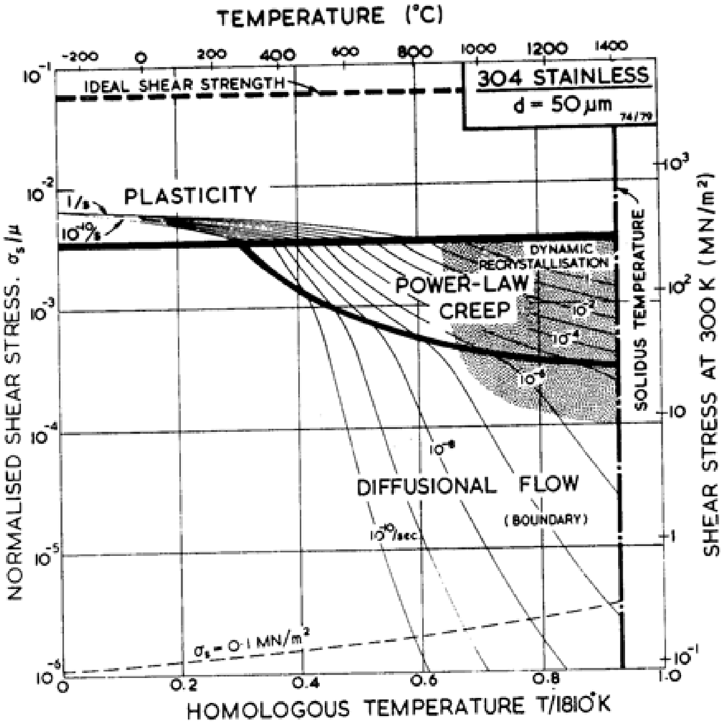

Fig. 1.10 Deformation mechanism maps of 304 SS after Frost and Ashby [5].

1.6 Fracture mechanics:

The creep fracture mode of cylinderical specimen under static tensile load at low and high temperatures has been categoriged in several ways [Fig 1.11]. At low temperatures, the fracture mode is either brittle intergranular/cleavage or ductile. At high temperature, the fracture mode changes to creep fracture; either transgranular at higher stressess or intergranular at lower stresses. Fracture mechanics maps are constructed by keeping homologous temperature T/T_m, where T_m is the melting point in Kelvin, in X-axis and normalised stress σ/G, where G is the shear modulus, in Y-axis [Fig 1.12]. If the stress applied in the specimen overcomes the inter-atomic forces in a perfect crystal, it causes the specimen to separate on a plane normal to the stress axis, and defines its upper limiting strength [Fig 1.12].

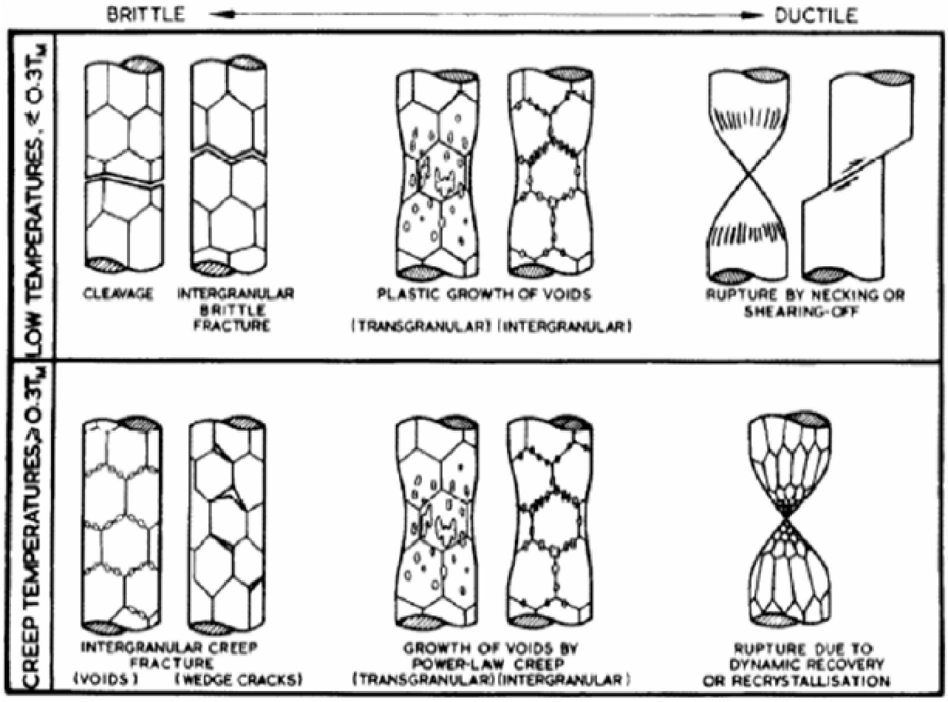

Fig. 1.11 A schematic diagram showing classification of fracture mechanisms at low temperature and high temperature.

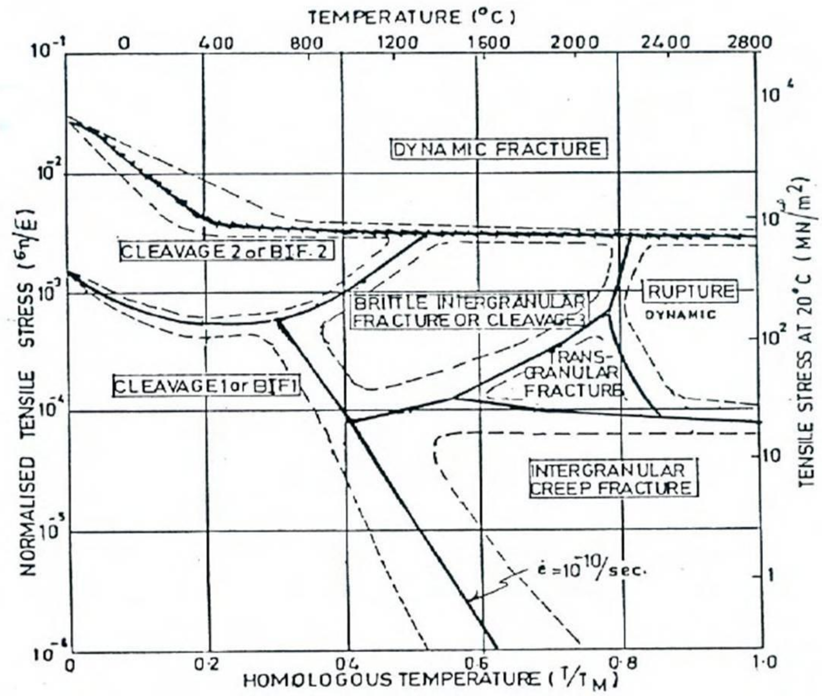

Fig.1.12 A schematic representation fracture mechanism, showing the dominance of different fracture mechanism stress-temperature regime.

At very low temperature, the fracture mode is mostly cleavage or intragranular brittle failure for all types crystalline material [6], except certain FCC metals and alloys. This type of failure is due to the existence of pre-crack or crack generated due to slip or twinning or grain boundary sliding, which can propagate catastrophically.

If the stress required for the crack propagation is lower than the stress required for slip or twinning to occur, then this kind of fracture occurs in the absence of gross plastic deformation and is known as *cleavage-1*. If the preexisting cracks are very small or absent then stress could reach level that required for initiation of slip/twinning. Slip occurs on a limited number of slip systems (less than 5) or twinning may have resulted in internal stress which is the cause of crack nucleation; known as slip or twin dominated cracking, *cleavage-2* type. This type of brittle fracture involves both crack nucleation and propagation stage and has limited ductility (less than 1%). Further, increase in temperature decreases the flow stress of the material and this kind of fracture is known as *cleavage-3.* This type of fracture may have significant ductility around 10 % due to sufficient plastic deformation which is large enough to blunt the pre-existing crack.

On the other hand, ductile transgranular fracture involves the nucleation and growth of voids. The presence of hard inclusions in the matrix interrupts both the elastic and plastic field in the deforming medium. This causes building of local stresses at the inclusion/matrix interface. If this stress attains critical value, it will either fracture the inclusions or tears open its interface with its matrix, causes void nucleation [7]. A spherical void concentrates the stress and because of this it elongates longitudinally and takes the shape of ellipse. At some critical strain void coalescence/fracture occurs due to localization of plastic strain. [Fig. 1.13]

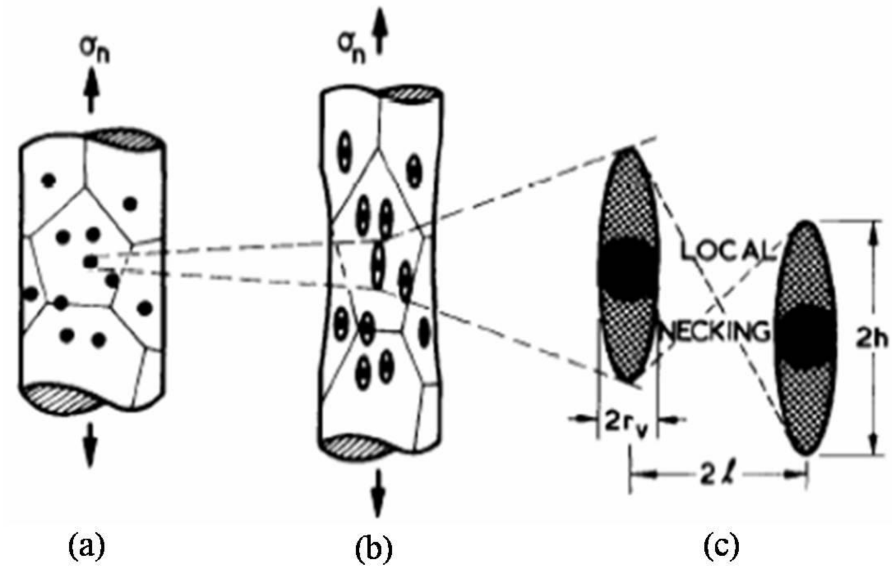

Fig.1.13 Schematic representation of ductile transgranular creep failure (a) preexisting holes/nucleated at the stress concentration sites, (b) elongation of holes due to deformation of the specimen (c) their linkage causing fracture.

1.7 Cavity nucleation and growth mechanisms

The present investigation is pertaining to the creep rupture behaviour of austenite stainless steel 304HCu under multiaxial state of stress. Austenitic stainless steels are a class of alloys with face-centered-cubic (FCC) lattice structure over the whole temperature range from room temperature (and below) to the melting point. Most of the austenitic stainless steels fail due to intergranular creep cavitation damage at elevated temperatures. The 304HCu SS is a new grade of austenitic stainless steel which has higher creep rupture strength at elevated temperatures among the austenitic stainless steels. The steel is more susceptible creep cavitation failure. Therefore, detailed understanding of cavity nucleation and their growth in the austenitic stainless steel is necessary. Further, the qualitative and quantitative study of creep cavitation based on different models is necessary.

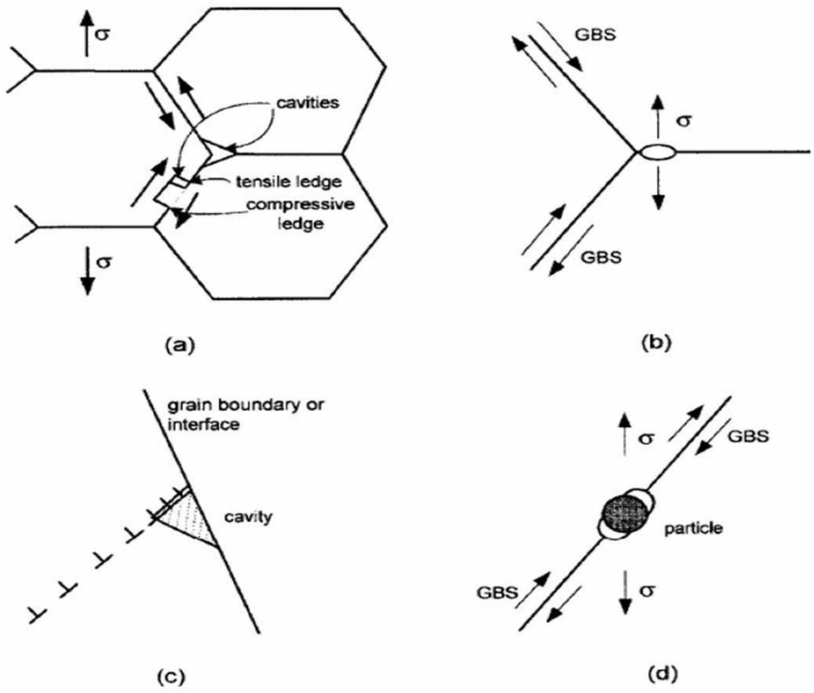

Fig. 1.14 Different modes of cavity nucleation mechanisms (a) sliding leading to cavitation from ledges (b) condensation of vacancies (c) Zener- Stroh mechanism (d) formation of cavity at matrix particle interface.

1.7.1 Cavity nucleation

Mechanism of cavity nucleation is not yet firmly established but still it is generally observed that creep cavity nucleates on the grain boundaries perpendicular to the tensile axis. Two main mechanisms are proposed for intergranular creep cavity nucleation. They are (i) thermally-activated vacancy clustering and (ii) interface fracture. Both mechanisms require high local stress concentration. Stress concentrations can occur by grain boundary sliding, dislocation pile-up and intergranular particle [Fig.1.14].

1.7.1.1 Grain boundary sliding (GBS)

Grain boundary sliding (GBS) can result in stress concentration at grain boundary triple points and hard particles on the GB. When the stress concentration developed at the grain boundaries is not relaxed by cooperative processes such as elastic flow, diffusion or creep then there is a possibility of either r-type cavity at grain boundary particles or w-type cavity on the grain boundary triple points. Another mode of cavity nucleation is due to tensile ledges where tensile stresses generated by GBS are sufficient to nucleate cavity. Most importantly, the transverse boundaries (the boundaries perpendicular to tensile axis) are found more susceptible to cavity nucleation [8].

1.7.1.2 Creep cavity nucleation by vacancy accumulation at grain boundaries

This mechanism assumes that the cavities nucleate by condensation of vacancies under the effect of normal local stress acting on the grain boundaries. From the thermodynamic point of view, Raj and Ashby [9] proposed an energy barrier based on the variation of Gibbs free energy, ΔG as

$$\Delta G = -\sigma_n V + \gamma_{free} S_{free} - \gamma_{interface} S_{interface} \qquad (1.3)$$

Three terms contribute to the energy variation:

1. The work induced by the application of a remote tensile stress on an elastic medium containing a cavity of volume V,
2. The energy to be supplied for creation of cavity free surface, S_{free},
3. The loss of grain boundary energy due to the reduction in its surface area as consumed by the cavity growth, $S_{interface}$.

Evans [10] suggests that the cavity nucleation is a function of stress and the cavity nucleation by vacancy accumulation requires large applied stress (e.g. 10^4 MPa order of magnitude), which is far greater than the stresses at which nucleation is usually observed to take place (below 10 MPa in pure metals and 100 MPa in engineering alloys), even taking into account the maximum estimated stress concentration ($\approx$20 times) at grain boundary irregularities by grain boundary sliding. This indicates that the cavities are unlikely to be nucleated by a vacancy condensation mechanism.

1.7.1.3 Cavity nucleation by particle-matrix interface fracture

Generally, the grain boundary triple points and second phase particles on grain boundary are the most common sites for cavity nucleation. If the stress concentrations, produced when grain boundary sliding is held up by a finite amount of material, are not relaxed, then cavities nucleate at the irregularities on the grain boundary like precipitate, ledge, grain boundary triple point etc. by athermal rupturing of atomic bonds. Smith and Barnby [11] showed that for grain boundary particles of 2c in diameter and distance 2d apart, the cavity nucleation stress τ, for rupturing the atomic bonds is given by:

$$\tau = \left(\frac{\pi}{2}\right)\left(\frac{c}{d}\right)^{1/2}\left(\frac{4\gamma_b G}{(1-\nu)d}\right)^{1/2} for\ c \ll \qquad (1.4)$$

Where γ_b is the grain boundary energy, G is the shear modulus and ν is Poisson's ratio. Nucleation of creep cavity by this mechanism is expected in materials having low particle/matrix interfacial energy and with high stress concentration at interface. The segregation of solutes like S, P etc. on grain boundaries may accelerate the grain boundary cavity nucleation on decreasing the interface energy [12]; whereas boron segregation is reported to suppress the creep cavity nucleation on increasing the interface energy [13].

Several mechanisms leading to stress concentration at grain boundary triple point, precipitate, ledge etc. have been proposed in literature. Grain boundary sliding and pile-up effects are described in the following.

1.7.2 Cavity growth

Once nucleated creep cavity growth may occur by different mechanisms. Most well-known cavity growth mechanisms are:

1. Diffusion-controlled cavity growth model proposed by Hull-Rimmer [14]. The constrained diffusion growth initially proposed by Dyson [15] and subsequently developed by Needleman and Rice [16].
2. Plasticity-controlled growth model is proposed by Riedel [17] and Nix [18].
3. Coupled model between diffusion and viscoplasticity proposed by Chen and Argon [19, 20].

1.7.2.1 Diffusion controlled growth

The intergranular creep cavity growth occurs by absorption of vacancies by cavity surface that has been controlled by different mode of diffusion mechanism namely (i) Only diffusion (ii) by coupled diffusion and plastic flow (iii) Only plastic flow.

Through diffusion controlled mechanism, the vacancy generated at the grain boundary transport to the cavity surfaces through grain boundaries, simultaneously atoms from the cavity surfaces deposited on the grain boundaries.

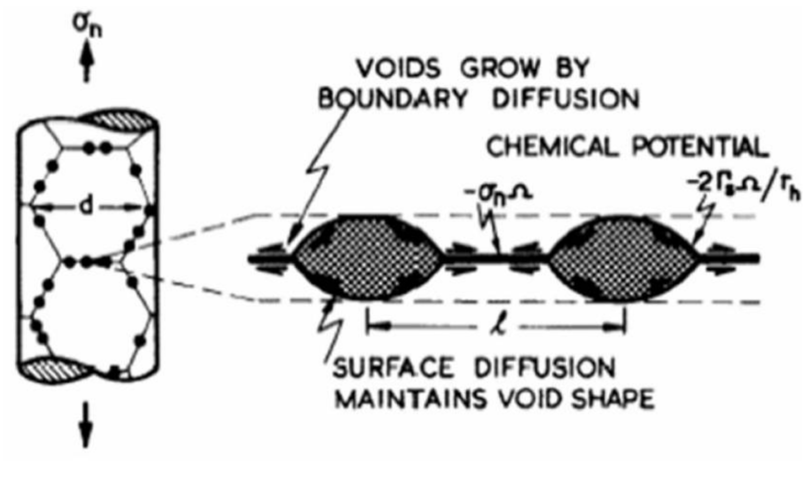

(a) (b)

Fig. 1.15 Schematic representation of (a) void growth and (b) voids lie on boundaries which carry a tensile stress and can grow by diffusional transport of matter from the periphery of the voids to the boundary plane by grain boundary diffusion [7].

The diffusion of vacancy primarily depends upon the chemical potential difference between the vacancy presented at boundary acted by tensile stress and vacancy presented at the cavity surface. The first detailed analysis done by Hull and Rimmer [14] explained the mechanism of diffusion cavity growth by considering different assumptions e.z.

(i) Grains have considered to behave as rigid blocks

(ii) The grains movement in a direction normal to the boundary is not constrained by external factors.

(iii) The grain boundaries are considered to be a perfect source of vacancies which maintain equilibrium between vacancy concentration and normal stresses.

For non-rigid grains the normal stress profile implicit in the classical diffusional growth model may be relaxed by dislocation creep. According to Beere and Speight [21], under coupled diffusion and plastic flow circumstances, the resulting growth can be obtained by adding the normal stress controlled and shear deformation controlled components. Under high strain rate the deformation controlled component may dominate and growth of cavity becomes analogous to plastic or continuum cavity growth [22].

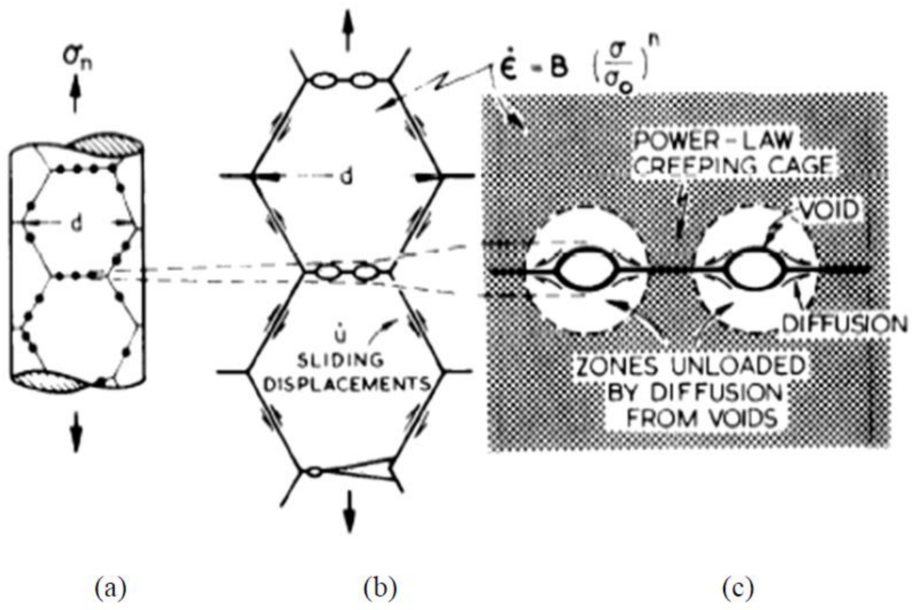

Fig.1.16 The schematic view of Intergranular creep controlled fracture. Simulation of grain boundary sliding (a) Grain (b) Boundary voids and (c) their growth by diffusion [6].

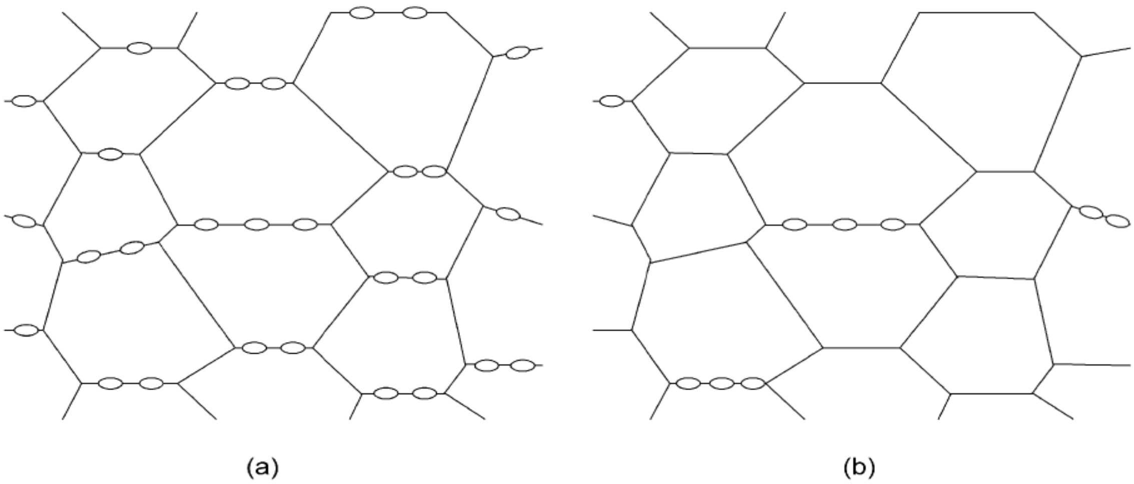

Fig. 1.17 Schematic view of cavities growing on isolated grain boundary facets (constrained cavity growth) (a) Pronounced cavitation (b) Slightly cavitated polycrystal [15].

Further, growth of the cavities can be classified into constrained or unconstrained. For unconstrained growth, the cavities are present on all of the grain boundaries in solid and are free to grow to the point of complete fracture [assumption (ii)] while for constrained cavity growth the cavities are present only on the isolated boundaries and here the growth of cavities on the cavitated grain displacements associated with the cavitation has to be accommodated by corresponding displacement in the matrix. As a consequence, the cavity growth may be limited entirely through the creep flow of matrix, however cavitation is still controlled by diffusion.

Further, efforts made by Dyson [15] reported that, in a perfect grain boundary vacancies are generated by grain boundaries dislocation moving in this type of boundaries [assumption (iii)]. However, in engineering alloys grain boundaries containing different second phase particles are not perfect source of vacancies. Under these circumstances, basically two possible mechanisms arises.

a) The growth of vacancies is typically controlled by the movement of intrinsic and extrinsic grain boundary dislocations.

b) The climbing of dislocations in grain boundaries originate entirely from the matrix and grain boundary dislocation sources created during dislocation creep. As a consequence, the growth of the cavities is limited by the availability of the dislocation sources and we have surface controlled vacancy growth [23]

The cavity growth has been enhanced based on the interaction between diffusive transfer of atoms from the cavity surface and the plasticity of matrix [24]. The main effect is that creep deformability of the grains permits the diffusion of matter from the surface of cavity which is accommodated by local separation of the adjoining grains in the center of the cavity. This process makes diffusion length paths shorter and results increase in cavity growth rate than would be the case if either diffusional or plasticity controlled flow of matter occur in isolation.

1.7.2.2 Plasticity controlled growth

The mechanism of cavity growth due to plasticity controlled growth is closely related to the cavity growth during low temperature ductile failure of the material [6] that involves creep deformation of the matrix surrounding the grain boundary cavities in the absence of vacancy flux [22, 25]. The strain concentration developed at the cavity surface results in its growth along the direction of maximum principal stress. According to this model cavity growth rate is given by:

$$\frac{da}{dt} = a\varepsilon - \frac{\gamma_c}{2G} \qquad (1.5)$$

Where a is the cavity radius, γ_c is the surface energy and G is the shear modulus. When the plastic deformation becomes localized at some critical strain, coalescence of cavities occurs followed by fracture. This mechanism is mostly prevalent under high strain rate condition, where significant strain is observed. A critical distance approach has been used by Thomason [26, 27] and [28] for the growth of cavities as a criterion for coalescence. Although both models have significant difference, both of them assumed to use a local slip line field which has been developed between the adjacent cavities. The following condition should be satisfied as per their models,

$$2h = \alpha(2l - 2a) \qquad (1.6)$$

Where $2h$ is the cavity height, α is a constant, $2l$ is the distance between the cavities as shown in Fig 1.13.

1.7.2.3 Coupled diffusion and plastic growth

Several authors suggested that [19-21, 24, 29-32] the growth of the creep cavity may be due to a coupling action between diffusional cavity growth and creep plasticity of the surrounding material. It is suggested that deposition of the material from the cavity surface on the grain boundary through surface and grain boundary diffusion would result in increase of the length of the specimen due to prolonged deposition of the atoms over the diffusion length. This deposition distance can be increased significantly if there is creep plasticity in the area ahead of the diffusion zone. A schematic of this coupled growth is shown in Fig. 1.18.

According to Needleman and Rice [24] the diffusion length has been described by the following expression.

$$\Lambda = \left(\frac{D_{gb}\Omega\delta\sigma}{kT\dot{\varepsilon}_s}\right)^{1/3} \qquad (1.7)$$

D_{gb} is the diffusion coefficient at the grain boundary, Ω is the atomic volume, δ is the grain boundary width, σ is the externally applied stress, $\dot{\varepsilon}_s$ is the steady state creep rate.

The coupling relation has been described by Chen and Argon [19, 20] which has been illustrated in Fig. 1.19

$$\frac{dV}{dt} = \dot{\varepsilon}_s 2\pi\Lambda^3 / \left[\ln\left(\frac{a+\Lambda}{a}\right) + \left(\frac{a}{a+\Lambda}\right)^2 \times \left(1 - \frac{1}{4}\left(\frac{a}{a+\Lambda}\right)^2\right) - \frac{3}{4}\right] \qquad (1.8)$$

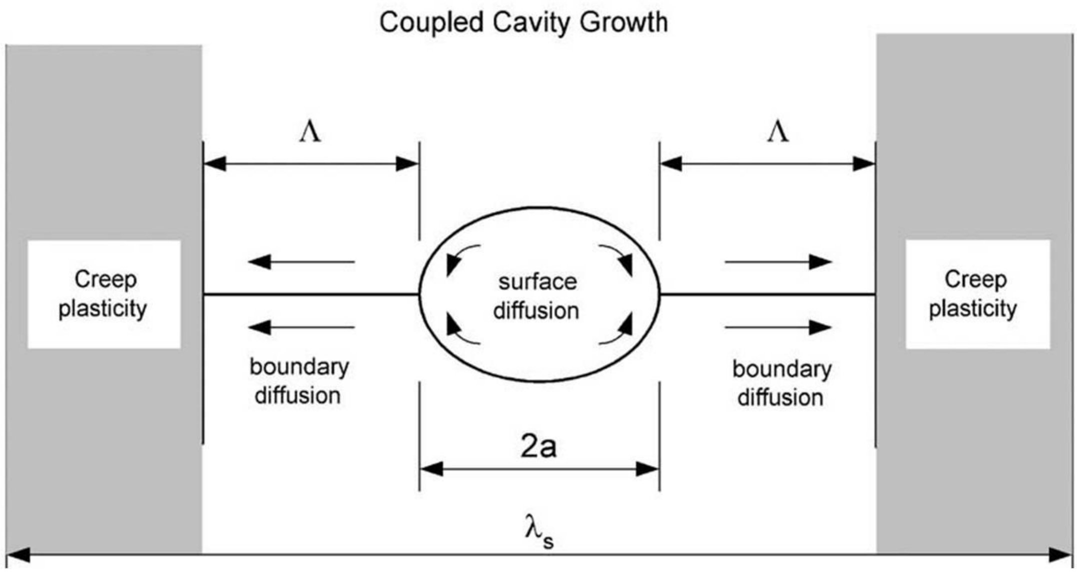

Fig. 1.18 Schematic of coupled diffusive cavity growth with creep plasticity. The diffusion length is suggested to be reduced by plasticity ahead of the cavity [30].

Similar analysis has been performed by other investigators [33, 34]. It has been shown that when $\Lambda << a$ and λ, there is no existence of diffusion controlled growth. Under extreme conditions this occurs at low temperatures. Creep flow becomes significant as $\frac{a}{\Lambda}$ increases. On the other hand, under slow creep rate and high temperature Λ approaches $\lambda_s/2$, $\frac{a}{\Lambda}$ is relatively small and rate of growth can be controlled by diffusion- controlled cavity growth (DCCG). The coupling action results significant increase in cavity growth over the individual operating mechanism that occurs at intermediate values of $\frac{a}{\Lambda}$ as shown in fig.1.19.

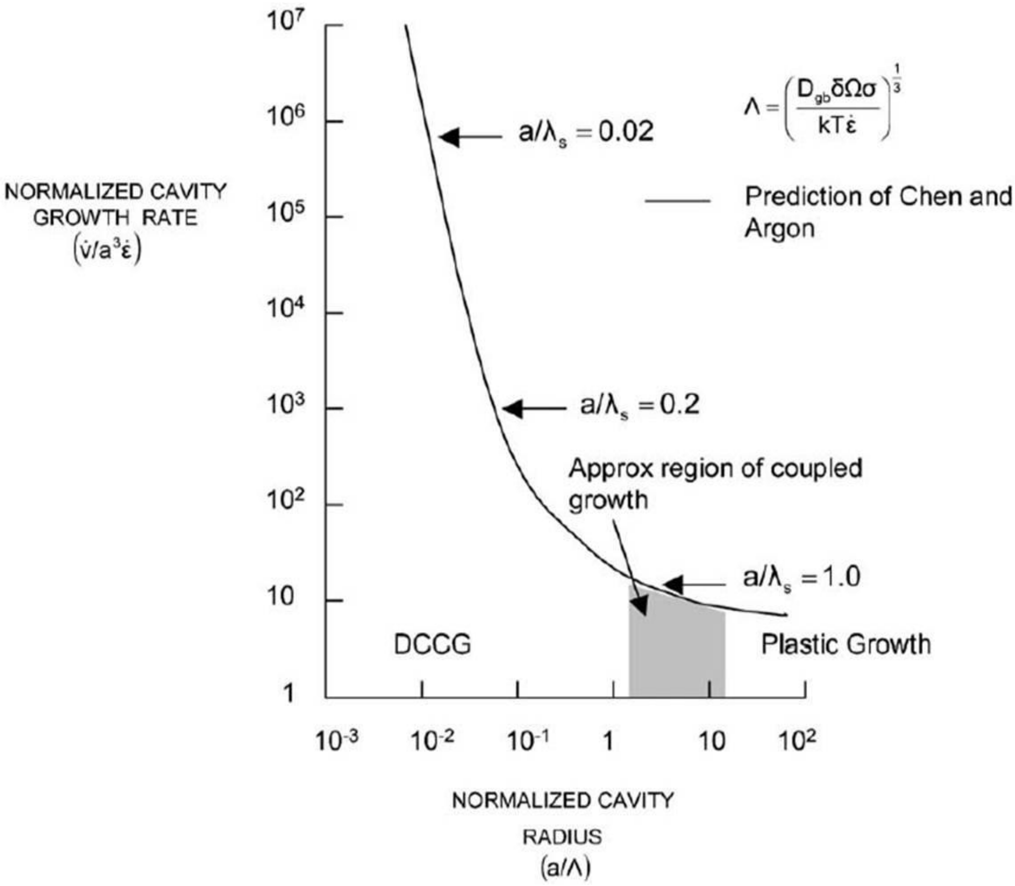

Fig. 1.19 Prediction of growth rate for different ratios of cavity spacing λ and diffusion zone sizes.

1.8 Creep damage

The initiation of tertiary creep is progressive damage process that includes loss of external cross section (constant load creep state), internal loss section (cavitation/cracking), precipitation coarsening, strain softening and environmental attack. The nucleation and growth of cavities reduces the material’s load bearing capability. Further, as the linkage of cavities constitutes microcracks and/ macrocracks, further linkage at some stage would constitute the final failure. Accordingly, the damage modes have been categorized into different stages as follows:

- Linear softening
- Exponential softening (loss of external cross section/ internal loss of section due to cavitation

- Time softening

Continuum damage mechanics proposed by Kachanov [35] has been widely used in characterizing the damage evolution in the material during tertiary creep.

1.8.1 Creep damage evaluation

1.8.1.1 Kachanov-Rabotnov model

L.M. Kachanov [35] and Rabotnov [36] consist of an internal scalar damage variable to characterize the internal creep damage of the material. If the initial cross section of the area is A_0 and the area covered by the cavities is A, then according to Kachanov, the damage (ω) is defined by:

$$\omega = \frac{A}{A_0}; 0 < \omega < 1 \qquad (1.9)$$

$$\psi = 1 - \omega = \frac{A_0 - A}{A} \qquad (1.10)$$

where ψ is a positive continuous function which tends to decrease continuously.

Therefore, $\psi = 1(\omega = 0)$ denotes virgin material while $\psi = 0(\omega = 1)$denotes fully fractured cross section.

Rabotnov [36] has taken assumption that creep rate is a function of stress and damage

$$\dot{\varepsilon}_c = \dot{\varepsilon}_c(\sigma, \omega)$$

On other words, the damage process can be reflected in evolution form

$$\dot{\omega} = \dot{\omega}(\sigma, \omega)$$

$$\dot{\varepsilon}_c = \frac{A\sigma^n}{(1-\omega)^{\varphi}} \qquad (1.11)$$

$$\dot{\omega} = \frac{B\sigma^{\chi}}{(1-\omega)^{\varphi}} \qquad (1.12)$$

when ω = 0 (virgin material), the creep rate equation becomes Norton's power law.

$$\dot{\varepsilon}_s = A\sigma^n \qquad (1.13)$$

Again, by setting $\chi = n$, the equation can be written as

$$\dot{\varepsilon}_c = A\sigma_{eff}^n \qquad (1.14)$$

Where $\sigma_{eff} = \frac{\sigma}{1-\omega}$ is called net stress or effective stress, which represents the Norton-Bailey secondary creep law to describe the tertiary stages of creep deformation.

Lemaitre and Chaboche [37] proposed the effective stress concept that developed constitutive equations for damaged materials based on the available constitutive equation of 'virgin material'.

At constant stress, the damage evolution (equation $\dot{\omega}$) can be integrated as follows

$$\int_0^{\omega_{cr}} (1-\omega)^{\varphi} d\omega = \int_0^{t_r} B\sigma^{\chi} dt \qquad (1.15)$$

where t_r is the rupture life and ω_{cr} is the is the critical damage (=1). On integration it leads to the following equation $t_r = \frac{1}{B(1+\varphi)\sigma^{\chi}}$ (1.16)

The above equation relates the rupture life (t_r) with stress (σ) which can be expressed by the following equation

$$t_r = M\sigma^{-m} \qquad (1.17)$$

Where m is the slope the uniaxial creep rupture life vs stress and $M = \frac{1}{B(1+\varphi)}$

The creep damage as a function of time can be expressed as

$$\omega = 1 - \left(1 - \frac{t}{t_r}\right)^{1/(1+\phi)} \qquad (1.18)$$

On incorporating the above equation in the strain rate equation and further integration leads to the following equation

$$\varepsilon_c = \frac{A\sigma^{n-\chi}}{B(n-\phi-1)} \left\{ \left[1 - \frac{t}{t_r}\right]^{\frac{\phi+1-n}{\phi+1}} - 1 \right\} \qquad (1.19)$$

At t = t_r, the creep strain before fracture $(\mathrm{i.e.}\, \varepsilon_c^r = \varepsilon_c^r(t_r))$can be written as

$$\varepsilon_c^r = \frac{A\sigma^{(n-\chi)}}{B(\phi+1-n)} \qquad (1.20)$$

On solving the above equations 1.17, 1.21, 1.24 it gives the following expression

$$\varepsilon_c^r = \frac{\dot{\varepsilon}_s t_r}{1-\frac{n}{\phi+1}} \qquad (1.21)$$

$$\dot{\varepsilon}_s \cdot \; t_r = \frac{A}{B(1+\phi)} \sigma^{n-\chi} \quad (1.22)$$

Under special condition, if n = χ, then

$$\dot{\varepsilon}_s t_r = \frac{A}{B(1+\varphi)} \quad (1.23)$$

The above equation is similar to Monkman-Grant relationship which states that the product of time of rupture and steady state creep rate is a constant for a given material. On the other hand, it can be observed that Monkman-Grant relationship follows from the Kachanov-Rabotnov model if the slopes of the steady state creep rate vs. stress and the stress Vs. time to fracture dependencies coincide in the double logarithmic scale.

P.J. Bouchard et al. [38] firstly quantified the creep cavities/damage around a crack in austenitic pressure vessel piping by Small Angle Neutron Scattering (SANS). The distribution and evolution of the cavities is discussed in terms of existing models of creep cavitation failure based on a ductility exhaustion model in which the corresponding multi-axial creep ductility, expressed as the von-Mises strain at failure, is a function of the strain rate and stress state. The detailed study of cavity size, their distribution, morphology, hardness distribution around a crack has been mapped through both metallographic assessment and SANS analysis [38].

1.8.1.2 Physically based continuum damage mechanics model

Physically based continuum damage mechanics model has generated from single-state variable description of tertiary creep introduced by Kachanov [35] and Rabotnov [36]. However, it differs significantly from the original empirical concept of Kachanov and Rabotnov (which considers the tertiary stage). In addition to tertiary stage, it considers the primary creep, secondary creep and microstructural induced damage for predicting creep deformation and rupture life.

Ashby [39], Dyson [40] and Dyson et al. [41] categorized four different modes of creep damage which are (a) loss of external cross section, (b) loss of internal cross section, (c) microstructural degradation and (d) gaseous environmental attack.

Each of the categories has been found to be associated with different micromechanism.

Strain induced damage

Cavitation at grain boundary, dynamic subgrain coarsening and multiplication of mobile dislocation fall under this category. Here cavity nucleation is assumed to be rapid compared to growth and fixed density of cavities is allowed to grow until their coalescence occurs followed by rupture. Most commonly cavity nucleation occurs throughout the creep process which is quite difficult problem to quantify but still in some cases it is easier to analyze and also have importance.

Thermally induced damage

The occurrence of thermally induced damage in some materials gives the signature of coarsening of constant volume of particles/ dissolution of precipitates especially carbides. The creep strength of the material increases through the dissolution of the precipitates while coarsening of the precipitates increases creep rate of the material and cause more damage.

Environmentally induced damage

This kind of damage mainly results from the oxidation or corrosive environment. The consequence of this type of damage results cracking of the material and exposure of new material for further damage and hence reduced the creep life.

1.9 Microstructural features in austenitic stainless steel

Austenitic stainless steels are generally alloy of Fe-Cr-Ni. Since 'Cr' is a ferrite stabilizer, it makes Fe-Cr steel to have a ferritic structure. It can be martensite depending upon the heat treatment. 'Ni' is added as basic substitutional element to stabilize austenite at room temperature. The stability of the phase depends upon the proportion of Fe, Cr and Ni, which can be well understood from the isothermal section of the ternary diagram calculated using MDATA [42] [Fig. 1.20]. Except these alloying elements, interstitial element such as carbon, nitrogen and substitutional element such as Mo, Mn, Ti, Nb, V, W, Cu, Al etc are used to obtain the physical and mechanical properties. These elements also can be classified as ferrite stabilizer or austenite stabilizer depending upon their equivalence effect with Cr and Ni as calculated by the formula given by equation 1.24 and 1.25.).

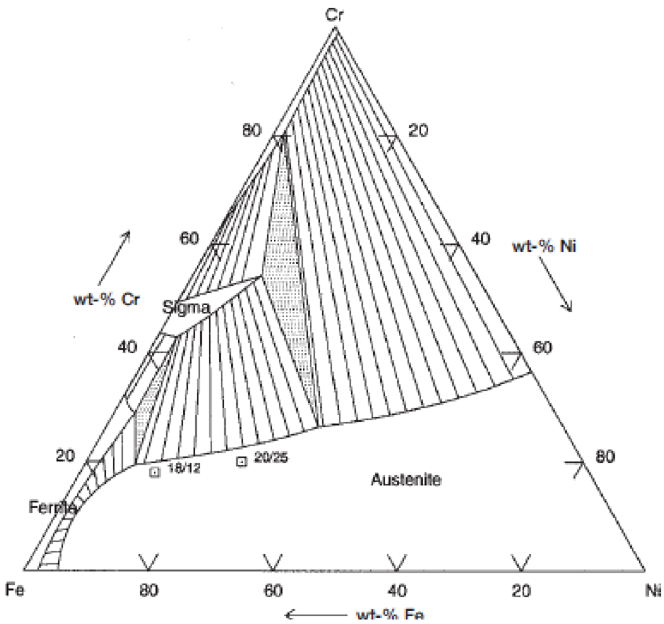

Fig. 1.20 Isothermal section of Fe-Cr-Ni diagram at 750^0C typical 18Cr-12Ni (wt%) steel in austenitic field calculated using MTDATA and SGTE.

Ni_{eq} = [Ni]+[Co]+0.5[Mn]+30[C]+0.3[Cu]+25[N] (1.24)

Cr_{eq}=[Cr]+2.5[Si]+1.5[Mo]+5.5[Al]+1.75[Nb]+1.5[Ti]+0.75[W] (1.25)

where composition is in wt. %.

1.9.1 Different precipitates in austenitic stainless steel

A brief description of the precipitates that arer commonly observed in AISI 300 family of austenitic stainless steels are presented below:

$M_{23}C_6$: This one is a more general form of $Cr_{23}C_6$. It is the most stabilized and common precipitates found in austenitic stainless steel. It is having FCC structure with lattice parameter varying between 1.057 and 1.068 nm. This is about three times the size of austenite. $M_{23}C_6$ carbides are mainly found precipitated on the grain boundaries, incoherent and coherent twin boundaries and intragranular sites. In general, $M_{23}C_6$ shows only {111} and {110} interface planes (best atomic correspondence with austenite) as explained by Beckitt and Clarck. [43]

MX: MX precipitates are formed due to the strong carbide and nitride formers viz. Ti, Nb, V, Zr, Ta etc. MX precipitates form on dislocations within matrix on stacking faults and on twin and grain boundaries. It is having a NaCl face centred cubic (fcc) crystal structure with lattice parameter around 0.44 nm. They have a characteristics cuboidal shape after long term thermal ageing. It stabilizes the alloy against intergranular corrosion and increases creep resistance.

M_6C: It is commonly known as η carbide. The structure of M_6C phase is diamond type FCC carbide with lattice parameter varying between 1.095 and 1.128 nm. This phase has variable composition and formed after long ageing time. Its composition can be molybdenum rich [$(FeCr)_{21}Mo_3C_6$] or niobium rich [Fe_3Nb_3C]. Silicon has been found to dissolve this phase to form M_5SiC but found rarely in matrix. Nitrogen has strong influence for its formation.

Z-phase: The Z-phase is a complex carbonitride which forms in a niobium stabilized austenitic stainless steels containing high level nitrogen. The structure of Z phase is tetragonal unit cell as described by Jack and Jack [44]. Its morphology is cuboidal or rodlike [45]. It will form very rapidly on grain boundaries. Further, its presence also observed on twin boundaries and inside the matrix where it is associated with the dislocations. Its formation reveals the fine dispersion of particles [45] which is a good phase when good creep properties were desired. However, Z-phase formation is still not yet fully understood. Nevertheless, it is having importance in both ferritic and austenitic power plants to assess the ternary system of Cr-Nb-N and to furnish the thermodynamic parameters required for any prediction.

σ phase: It is a well known intermetallic phase which forms in Fe-Cr system with composition Fe-Cr. Its structure has a tetragonal unit cell. Its formation is detrimental to creep properties if it forms intergranularly (on grain boundaries) and have little effect if it precipitates intragranularly. This phase precipitate first on triple points then on grain faces. Further, its formation also found on incoherent twin boundaries and intragranular inclusions [46].

Laves phase: It is found very little in austenitic stainless steel. It precipitates intragranularly in the form of equiaxed particles and occasionally on the grain boundaries. Its formation is detrimental to creep properties when it forms intergranularly or intragranularly. Laves phase is not found in 304 austenitic stainless steel because of the absence of Mo, Nb or Ti. In 316 SS it is found after long ageing time [47].

χ phase: Like laves phase, it is mainly found in 316SS above 1023 K but not in 304SS. It has BCC (body centred cubic) crystal structure. A typical composition is $Fe_{36}Cr_{12}Mo_{10}$ and the phase has high probability of metal interchanges. It nucleates on grain boundaries, incoherent twin boundaries and intragranularly on dislocations [46].

G-phase: The G-phases are silicides which form in austenitic stainless steel stabilized with niobium or titanium. Generally, it is found under irradiation for 300 series and 20-25 steels. It has a general form of $A_{16}D_6C_7$ where A & D are transition elements C is a group IV element, A is usually nickel while D is usually niobium [48]. The G-phase has a FCC structure with lattice parameter of 1.12 nm. It found predominantly on grain boundaries. Further, its presence is also seen in 20-25 niobium stabilized steel (500-850^{0}C) and its extent depends on the silicon content.

Other precipitates: The precipitates described above are most often studied and reported in creep resistant austenitic stainless steel. However, presence of other precipitates is also reported sometimes by different investigators depending on the alloy content. Some of the examples are listed below:

Cr_2N: This forms in non-stabilized austenite stainless steel with high levels of nitrogen content (0.2wt-% at 900^0C with 20wt-% Ni). It has a HCP structure with lattice parameter a=0.478nm and c=0.444 nm. The details of this precipitate can be found in [49].

π Nitride: This is reported by Jargelius-Petterson [50] to form in non-stabilized 20-25 steel with 0.21wt.%N. It has a cubic structure with lattice parameter of a=0.63nm [50].

Copper precipitates: The literature pertaining to effects of Cu in increasing the creep resistance of austenitic stainless steel is little available. Tohyama and Minami [51] used 3wt-% of Cu in Tempaloy-A1 steel (similar to 347/304 HCu SS) with the addition of small amount of Titanium, observed that precipitation of Cu-rich phases, independently from other phases. This results increase in creep strength significantly in comparison with original composition.

Titanium Carbosulphide: The Titanium Carbosulphide $Ti_4C_2S_2$ is specifically found in AISI321 grade stainless steels when the stainless steel is aged at 600^0C for time period between 16000 and 53000h as reported by Lai and Minami [46, 52].

1.10 Stress temperature dependence of steady state creep rate:

At high temperatures for pure metals and solid solutions, the dependence of the applied stress with steady state creep rate is quiet often described by the power law relationship of the type

$$\dot{\varepsilon}_s = {}^{AD\mu b}\!/_{kT}\ \left({}^{\sigma_a}\!/_{\mu}\right)^n \qquad (1.26)$$

with D = $D_o\exp(-Q_c/RT)$, where D is the self-diffusion coefficient, D_o is the frequency factor, Q_c is the activation energy for creep deformation, R is gas constant (8.314 J mol^{-1} K^{-1}), T is temperature in Kelvin, μ is the shear modulus, b is the Burgers vector, k is Boltzmann's constant, n is the stress exponent and A is a dimensionless constant. Precipitation hardened materials typically have higher values of stress-sensitivity 'n' in stress/creep rate relationship at high stresses than that of pure metal and solid solution alloy where the value of stress exponent 'n' was found to be in between 4-5. For precipitation hardened alloys like $\gamma^{'}$ hardened Ni-base alloys [53-55], Cu-Co alloys [56,57], Fe-Ni-Ti-Al alloys [58], carbide-strengthened austenitic stainless steels [59, 60] the 'n' value varies between 5-15 and dispersion-hardened alloys, like sintered aluminum powder [61] thoriated nickel, and nickel-chromium [62] reach even higher exponents more than 40 [62]. In general, the flow stress during plastic deformation consists of an effective and an internal stress component. In a precipitation-hardened alloy, the presence of dislocation structure and the dispersion of precipitates will contribute to internal stress. Further, the internal stress phenomenon is due to the dislocation structure which is related to the dislocation density. On the other hand, the activation energy was found to be higher at high stresses associated with high stress sensitivity. Based on this, the creep behaviour has been rationalized by fitting the large body of data in the modified form of eq (1.26) using the concept of resisting stress/back stress (σ_R) [58, 63, 64].

$$\dot{\varepsilon}_s = (\frac{A_0 D\mu b}{kT})((\sigma_a - \sigma_R)/\mu))^p \qquad (1.27)$$

with 'p' having a constant value of around 4 over the entire stress and temperature regime where dislocation creep is the rate controlling creep deformation mechanism.

1.10.1 Evaluation of resisting stress

The back stress or resisting stress (σ_R) opposing the climb/ glide phenomena is proportional to the applied stress (σ_a) which is given by,

$$\sigma_R = K_p \cdot \sigma_a \qquad (1.28)$$

The value of proportionality constant K_p is equal to 0.75 and independent of particle dispersion parameters, the interparticle spacing and particle diameter within a broad range [65]. Efforts made by Evans and Knowles [66] gave explanation about the energy advantage of cooperative climb around the group of particles rather than profiling each individual particle. On the other hand, Mc Lean [67] pointed out that co-operative climb could occur over group of particles which creates new dislocation length lesser than the threading mode of the general climb process.

The evaluation of resisting stress at high stress levels is not well established. The techniques, which are frequently used are stress drop and stress relaxation tests. However, these methods have difficulty in determine resisting stress in situ without changing the variables such as stress, temperature and strain rate. Further, the value of σ_R evaluated through stress drop technique depends critically on the accuracy of strain measurements [68]. Also, both the methods require experiments of long time [69]. Stevens and Flewitt viewed the experimental determination of σ_R for large number of creep data for different precipitation hardened materials. The resisting stress increases with increase in applied stress at the low stress region while it remains almost constant/weakly dependent on the applied stress at the high stress region.

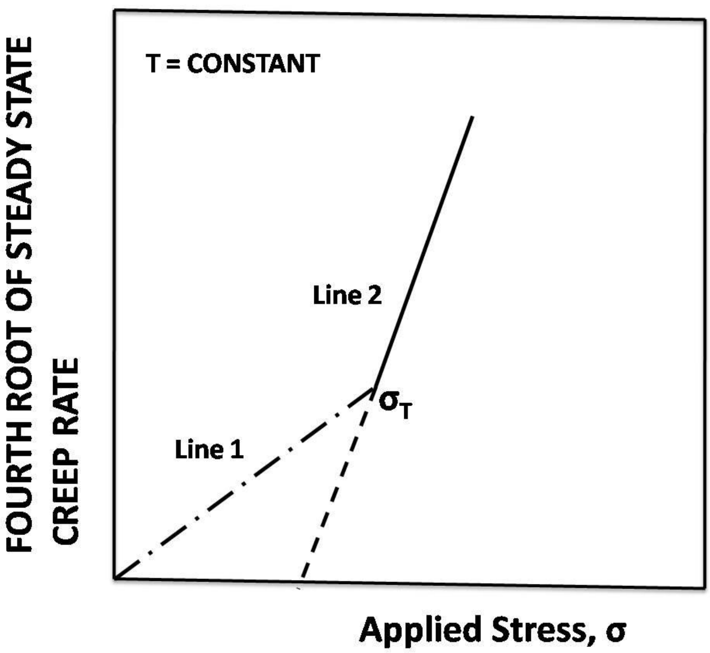

Fig. 1.21 Schematic representation for the determination of threshold stress from creep data for a given material and temperature.

Besides above two methods, the other mode of determining σ_R from the creep data is the graphical method proposed by Lagneborg and Bergman [65] as shown in Fig.1.21. In this method, fourth root of steady state creep rate ($\dot{\varepsilon}_s$) is plotted against applied stress (σ_a) in both the low and high stress regime. Equation 1.27 indicates that such type of plot would generate straight lines at both low (line 1) and high (line 2) stress regimes. On extrapolating the line 2 to $\dot{\varepsilon}_s = 0$ i.e. to intersect at σ_a axis, gives the threshold value of stress(σ_H). This technique involves the assumption that as the σ_a increases, the creep deformation mechanism undergoes a transition from climb controlled to Orwan bowing and/ or particle shearing at σ_a>σ_T,where σ_T is the transition stress in log-log plot of $\dot{\varepsilon}_s\ vs\ \sigma_a$ data as shown in Fig. 1.22(a). σ_R exhibits maximum constant or threshold value at high stresses Fig. 1.22(b). The ratio σ_H/σ_T is equal to K_p and σ_R vary as Kp.σ_a following eq.(1.28) in the low stress regime as shown in Fig. 1.22(b). This type of method has been successfully used to evaluate σ_R by Choudhary et al. [70] in ferritic steels, Vanaja et al in INRAFM steel [71], Reppich et al. [64] in Ni-base alloys, Ecob and Evans [72] for carbide dispersion hardened austenitic stainless steel and Singh and Banerjee [73] in Cr-Mo-V steel.

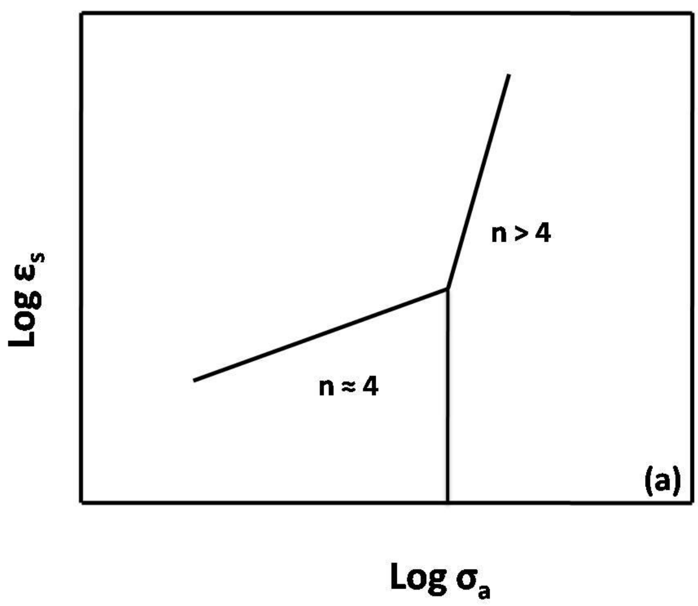

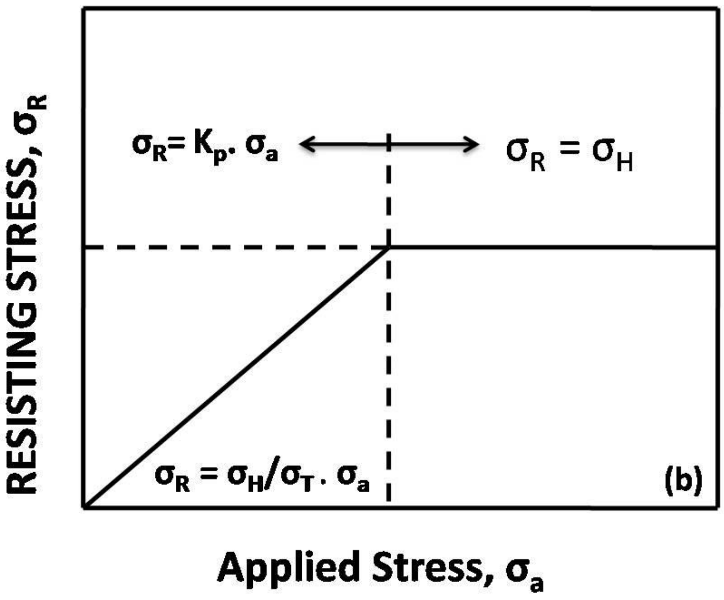

Fig. 1.22 Schematic representation of applied stress (σ_a) dependence of (a) steady state creep rate and (b) resisting stress due to particle.

1.11 Strain and time dependence relation

In this section, the β-envelope method given by Radhakrishnan [74-76] and Garofalo [77] has been described.

1.11.1 β-envelope method

Andrade [78] was the first to suggest a relationship between strain (ε) and time (t) as given below:

$$\varepsilon - \varepsilon_0 = \dot{\varepsilon}_s t + Bt^{1/3} \qquad (1.29)$$

Where ε_0 is the initial strain rate at time t = 0 and B is a constant. However, Andrade equation predicts an infinite value for initial creep rate and got major objection for this reason.In the β-envelope method the strain is quite often related to different powers of time; $\varepsilon_1 = \beta_1 t^{1/3}$, $\varepsilon_2 = \beta_2 t^1$, $\varepsilon_3 = \beta_3 t^3$ in the transient, secondary and the tertiary creep rates respectively where $\beta_1, \beta_2, \beta_3$ are the respective coefficients.

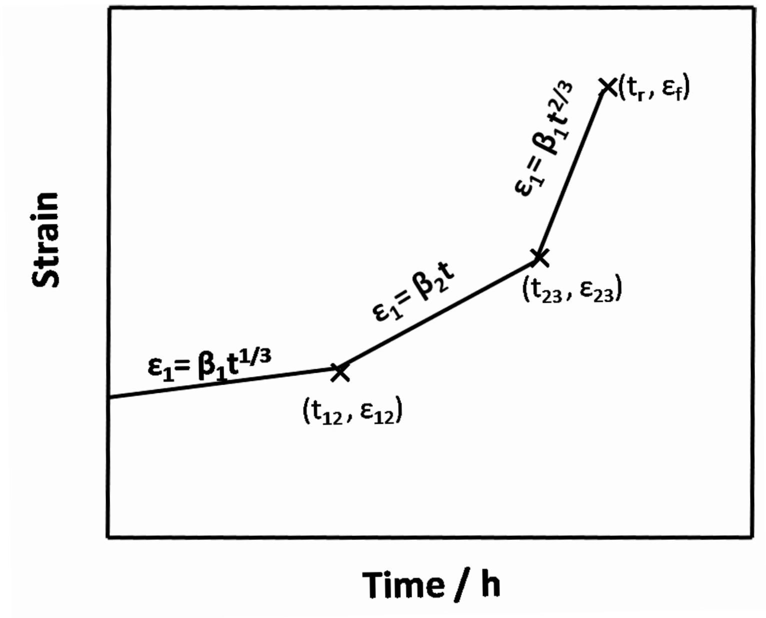

Fig. 1.23 Schematic representation of log(strain) vs log(time) plot illustrating the β-envelope method.

The log-log plot of strain and time develops straight lines with slopes of 1/3, 1 and 3 corresponding to the different stages of creep rates. The transition time and strain at the different stages of creep rates have indicated in the Fig. 1.22. On rearrangement, a relationship will develop between minimum creep rate and creep rupture life according to β envelope method

1.11.2 Garofalo equation: The numerical equation most commonly used to describe the transient and steady state creep behaviour under high temperature is

$$\varepsilon = \varepsilon_0 + \varepsilon_T[1 - exp(-r'.t)] + \dot{\varepsilon_s}.t \qquad (1.30)$$

where ε_o is the instantaneous strain on loading, ε_T the transient creep strain, r′ a parameter relating to the rate of exhaustion of transient creep, $\dot{\varepsilon_s}$is the steady state creep rate, ε_T is a constant equal to the smallest strain deviation from the steady state at the onset of tertiary stage of creep deformation. This equation originally formulated by McVetty [79] and extensively used by Garofalo for describing the high temperature creep data and known as

Garofalo equation. Further, this equation predicts a finite value of initial creep rate. The equation describes most adequately the high temperature creep data for austenitic stainless steel.

1.11.3 θ-projection technique

The other strain time relation is the θ-projection technique [80] and according to this method the strain and time are related as

$$\varepsilon - \varepsilon_0 = \theta_1[(1 - \exp(-\theta_2 t) + \theta_3[\exp(\theta_4 t) - 1] \qquad (1.31)$$

Where θ_1 and θ_2 corresponds to primary creep, and $\theta_3$and $\theta_4$corresponds to the tertiary creep.

1.12 Creep and first order kinetic

Under static tensile loading, creep rate decreases in the transient stage and reaches steady state value and finally accelerates in tertiary creep. The major structural changes that occur during transient creep are the rearrangement of dislocations which occurs due to diffusion controlled climb process. Both the transient and steady state creep process are controlled by the rate of dislocation climb process. Hence, the rearrangement of dislocations due to dislocation climb process for transient and steady state creep process governs first order reaction kinetics. According to Webster, Cox and Dorn [81], the decreasing and saturation value of creep rate at transient and steady state region can be expressed by the following expression

$$\frac{d\dot{\varepsilon}}{dt} = \frac{-(\dot{\varepsilon} - \dot{\varepsilon}_s)}{\tau} \qquad (1.32)$$

Where τ is the relaxation time for rearrangement of dislocation into a stable configuration, and the $\frac{1}{\tau} = r'$ has the same dependence on stress and temperature as in $\dot{\varepsilon}_s(\frac{1}{\tau} = r' = K'.\dot{\varepsilon}_s, K' = \text{constant})$. Integration twice of the above first-order rate equation for creep deformation has led to the Garofalo Equation (Eq. 1.30). Further, another condition which must apply is that the initial strain (ε_0) on loading is a thermal and depends on metal or alloy condition received and the value of σ/G. The initial creep rate which is proportional to the steady state creep rate, (i.e.$\dot{\varepsilon}_i = \beta\dot{\varepsilon}_s$, where β is a constant) governs the same kinetic process from transient to steady state creep rate. The differentiation of Garofalo equation and at time t = 0, one can obtain the relation between initial creep rate ($\dot{\varepsilon}_i$) and steady state creep rate which follows, $\dot{\varepsilon}_i = \dot{\varepsilon}_s + r\varepsilon_T$. Further, since $\dot{\varepsilon}_i = \beta\dot{\varepsilon}_s$ and $r = K'\dot{\varepsilon}_s$, the transient creep strain becomes as follow $\varepsilon_T = {\beta - 1}/{K'}$. The significant implication obtained from above analysis is that both $\dot{\varepsilon}_i$ and $\dot{\varepsilon}_s$ are functions of stress. On the other hand ε_T is a constant and like β and K' is independent of both stress and temperature. These lead to the development of uniaxial creep curve describing the transient creep deformation.

$$\varepsilon - \varepsilon_0 = \frac{\beta - 1}{K'}[1 - \exp(-K' \cdot \dot{\varepsilon}_s \cdot t)] + \dot{\varepsilon}_s.t \qquad (1.33)$$

Where $\varepsilon_T = \frac{\beta-1}{K'}$ as both β and K' are constants. The several creep parameters used in the transient analysis are shown in Fig. 1.24.

The materials which have constant ε_T at all the combination of stress and temperature, a single master curve is expected between $\varepsilon - \varepsilon_0$ and $\dot{\varepsilon}_s.t$ for conditions obeying first order reaction rate theory. This approach of creep describing the first order reaction theory is unique, in the sense the Garofalo equation has been provided with a physical interpretation.

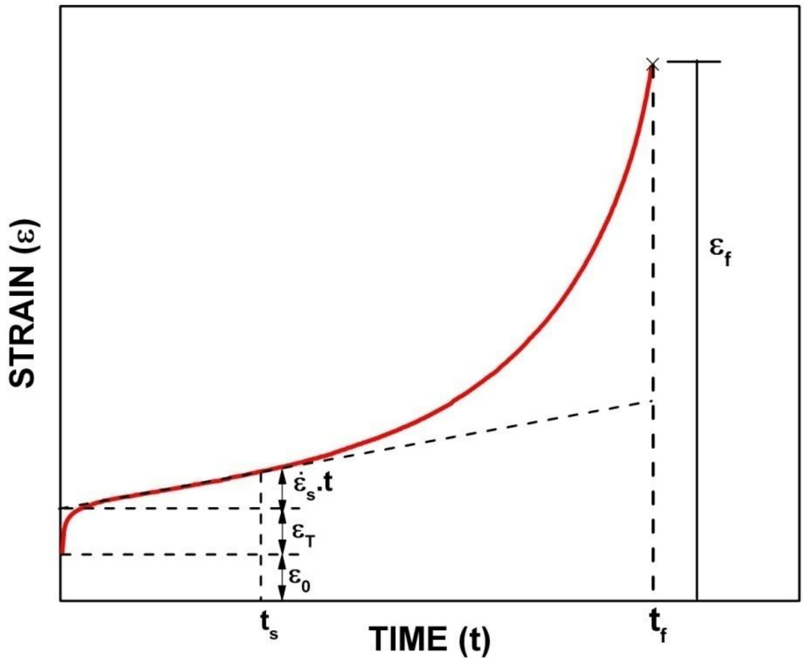

Fig. 1.24 Schematic illustration of analysis of transient creep behaviour of steel.

1.13 Multiaxial state of stress

In real life, **c**reep rupture life prediction under uniaxial state of stress condition couldn't give the accurate result. Because, the role of multiaxial state of stress arises due to the presence of heterogeneity in the material, the weld joints and the mode of testing [82]. Therefore, in order to access the life of such components effective stress criteria has employed and interpreted with uniaxial data.

There are some assumptions which must be taken into account for predicting the creep life under multiaxial state of stress [83].

1. Volume is made constant during creep test

$$\dot{\varepsilon}_1 + \dot{\varepsilon}_2 + \dot{\varepsilon}_3 = 0 \qquad (1.34)$$

2. The principal shear strain rates are proportional to the principal shear stresses

$$\frac{\dot{\gamma}_1}{\tau_1} = \frac{\dot{\gamma}_2}{\tau_2} = \frac{\dot{\gamma}_3}{\tau_3} = 2\psi \qquad (1.35)$$

where ψ is a constant and $\dot{\gamma_1}, \dot{\gamma_2}, \dot{\gamma_3}$ are shear strain rates and τ_1, τ_2, τ_3 are respective principal shear stresses and are defined as

$$\tau_1 = \frac{1}{2}(\sigma_2 - \sigma_3), \tau_2 = \frac{1}{2}(\sigma_3 - \sigma_1), \tau_3 = \frac{1}{2}(\sigma_1 - \sigma_2)$$

$$\gamma_1 = \varepsilon_2 - \varepsilon_3, \gamma_2 = \varepsilon_3 - \varepsilon_1, \gamma_3 = \varepsilon_1 - \varepsilon_2$$

Combining these two results leads to the relations

$$\dot{\varepsilon_{iJ}} = \psi(\sigma_{ij} - \sigma_m)$$

where $\psi = \frac{3\bar{\dot{\varepsilon}}}{2\sigma_{vm}}$ and $\sigma_m = \frac{1}{3}(\sigma_1 + \sigma_2 + \sigma_3)$

The effective strain rate is related to the effective stress in the same way as in the uniaxial loading, e.g.$\bar{\dot{\varepsilon}} = f_1(t) f_2(\sigma_{vm})$, where $\sigma_{vm}$is the von-Mises stress and is defined as

$$\sigma_{vm} = \frac{1}{\sqrt{2}} \sqrt{((\sigma_1 - \sigma_2)^2 + (\sigma_2 - \sigma_3)^2 + (\sigma_3 - \sigma_1)^2)}$$

Under stationary state conditions, the constitutive equations under multiaxial state of stress can be defined as

$$\dot{\varepsilon}_{ij} = {}^3/_2 \frac{f_2(\sigma_{vm})}{\sigma_{vm}} \sigma'_{ij} \qquad (1.36)$$

where σ'_{ij} denotes the deviatoric stress components $\left[\sigma'_{ij} = (\sigma_{ij} - \sigma_m)\right]$

Therefore,

$$\dot{\varepsilon}_{ij} = {}^3/_2 f_1(t) \frac{f_2(\sigma_{vm})}{\sigma_{vm}} \left(\sigma_{ij} - \sigma_m\right) \qquad (1.37)$$

The creep strain rate $(\dot{\varepsilon})$including one damage variable (ω) can be defined in the following mathematical form

$$\dot{\varepsilon}_c = {}^3/_2 A \left(\frac{\sigma_{vm}}{1 - \omega}\right)^{n-1} \frac{\sigma_{ij}}{(1 - \omega)} \qquad (1.38)$$

and the damage rate can be expressed in terms of the representative stress

$$\dot{\omega} = \frac{B\sigma_{rep}}{(1-\omega)} \tag{1.39}$$

1.14 Mode of multiaxial testing

The techniques which are used to test the multiaxial state of stress are tube under internal pressure, thin wall pipes subjected to axial force or torque, three-dimensional cruciform specimens subjected to axial forces, circumferential notch specimen subjected to axial geometry etc.

1.14.1Tubes under internal pressure

The tubes under internal pressure experiences multiaxial state of stress that transient with time from elastic state to a stationary state distribution and subsequently redistribution takes place during tertiary creep. The internal pressure is due to the steam or inert gas like argon. However, in some cases liquid sodium provides the pressure whereas in others some corrosive process gases are used. In the case of maximum principal stress governing behaviour, the simple thin wall elastic calculation should be made $\left(P = \frac{\sigma t}{r}\right)$ where P is the pressure, r is the radius, t is the thickness of pipe and σ is the stress even for thick walled specimen if n value is unknown. For known value of 'n' the maximum equivalent stress after redistribution should be used to determine the internal pressure. On the other hand if it is controlled by von-Mises stress, the thin wall elastic solution ($P = 2\sigma t/\sqrt{3}r$) should be used for calculation of internal pressure (for known values of 'n'). Maximum equivalent stress after redistribution should be used for calculation of internal pressure (for unknown values of 'n'). The benefit of using multiaxial test under internal pressure is that pipes of same dimension can be used for multiaxial creep rupture criteria, improved design and remnant life assessment can be made. However, limitation is that experimental set up required is larger in size and safety due to higher internal pressure.

1.14.2 Tension torsion of thin tubular specimens

Biaxial testing on thin walled pipes is carried out by applying torsional load along with axial load [84]. Axial load is applied through the lever arm while torque is applied to the test piece through the torque disc. Following precautions should be taken for this type of testing

I. The ratio of surface area to the volume of the specimen should be kept as small as possible to avoid the surface effect.

II. The thickness of the specimen should be low to avoid the gradient of stress through thickness.

III. Appropriate ratio of thickness to external diameter should be made to avoid premature buckling.

1.14.3 Cruciform specimen

The main problems associated with tube testing are rotation of principal stress plane due to shear deformation and buckling. These can be overcome by the use of cruciform specimen [85]. The design of such specimen includes series of limbs extending from each edge of a thinned central square section. The purpose of limbs is to prevent lateral constraint on the central location. Further, this type of specimen can be used in testing of tension-tension quadrant and tension-compression quadrant of two dimensional state of stresses.

1.14.4 Notched specimen

The most commonly and convenient method of doing multiaxial test is by introducing circumferential notch in the specimen and applying tensile load [86-90]. The constraint by the shank introduces a state of multiaxial stress in the notch region. The degree of constraints depends basically upon the notch geometry and condition of creep test (temperature and stress) [91].

1.15 Influence of notch on creep behaviour

1.15.1 Stress distribution

The stress around the notch redistributes during creep test and approaches to a stationary state [91]. The distribution of stress at the notch throat plane for both U-notch and V- has been extensively studied by Hayhurst et. al. The stationary state distribution was found to have relatively smooth gradient for U-type notch while V-type notch exhibits non-uniform stress distribution and a peak was developed adjacent to the notch root where plain strain condition prevailed. Further, the time required to attain the stationary state distribution for V-type notch was much higher than that U-type notch. In general, both U-type and V-type notches are used to study the degree of constraints on creep deformation behaviour [91]. In laboratory experiments U-notches which carries larger volume of material that facillates creep cavitation (post metallography study) are preferred over V-notches to study the creep deformation behaviour under multiaxial state of stress [92, 93]. On the other hand, Webster et al. [91, 94] observed that for each notch geometry there is a existence of skeletal point where the stresses are almost constant irrespective of the values of applied stress, temperature and material. The skeletal point is constant for particular notch geometry. The stresses at the skeletal point play a great role in characterizing the creep deformation and rupture behaviour of the material under multiaxial state of stress.

1.15.2 Notch strengthening or weakening

Presence of notch in the material can exhibit strengthening or weakening depending upon the notch shape, sharpness, loading condition and material ductility [83-86]. Notch strengthening is due to the quick redistribution of high axial stress below the applied stress across the notch plane while notch weakening is due to the very slow redistribution of high axial stress across the notch plane and locally accumulated strain exceed the critically strain which is required for fracture. Notch strengthening is typically observed in ductile metals while notch weakening is commonly seen in brittle metals.

Ng et al. studied the effect of notch on 0.5Cr-0.5Mo-0.25V which shows notch strengthening for shallow notch and notch weakening for sharper notch [87]. The studies of Webster et al [86] on notched specimens of beta processed titanium alloy Ti5331s and observations of Kwon et al. [88] on notched specimen of 2.25Cr-1Mo and Durehete 1055 steels showed notch strengthening. The CMSX-4 superalloy single crystals of orientations <001>, <011>and <111>exhibits notch strengthening effect in the presence of circumferential U-notches on the creep rupture life for the same net-section stress as that of smooth specimens [89]. Studies carried out by Ni et al. [90] showed notch strengthening in the P92 steel whereas creep studies on notched specimens of 2.25Cr-1Mo steel exhibited tendency towards notch weakening [95, 96]. The studies carried out on alloy X-750 by Pandey et al. [97] reported notch strengthening under the testing conditions.

1.16 Creep life prediction under multiaxial state of stress

The creep rupture life under uniaxial loading can be expressed as $t_r = M\sigma^{-m}$ where the constants M and m are used to characterize the damage evolution due to different creep mechanisims. However, in case of notched specimen the creep rupture life can't be predicted based on the smooth specimen data. Creep rupture life relation was modified to $t_r = M\sigma_{rep}^{-m}$ to account the creep rupture life prediction for different notched specimen with different root radius. The representative stress, σ_{rep}, is defined as the stress applied to the uniaxial plain bar specimen which has the same creep rupture life as the notched bar specimen. A notched specimen is said to be notch strengthening if $\sigma_{rep}<\sigma_{net}$ and notch weakening if $\sigma_{rep}>\sigma_{net}$.

The prediction of rupture life has been done by different investigators. Johnson et al. [98-99] who conducted biaxial creep tests on aluminum alloy and pure copper, showed the existence of good co-relation of creep rupture life with octahedral shear stress and maximum principal stress criteria. Hayhurst [100] suggested that the creep rupture behaviour of copper and alluminum alloys can be considered as representing the two extreme stress sensitive rupture where the deformation behaviour of other creep resistant alloys falls. Further, Hayhurst [100] suggested that isochronous rupture surface can be described in terms of combination of von-Mises stress, Maximum principal stress and Hydrostatic stress.

$$t_r = M(\alpha\sigma_1 + \beta\sigma_{vm} + \gamma\sigma_m) \quad (1.40)$$

Where α, β, and γ are constants. The loci of constant time to rupture in stress space can be represented as shown in Fig.1.25

Typical values of α for Aluminum, Copper and 316 SS were found to be 0.0, 0.7 and 0.75 respectively [101].

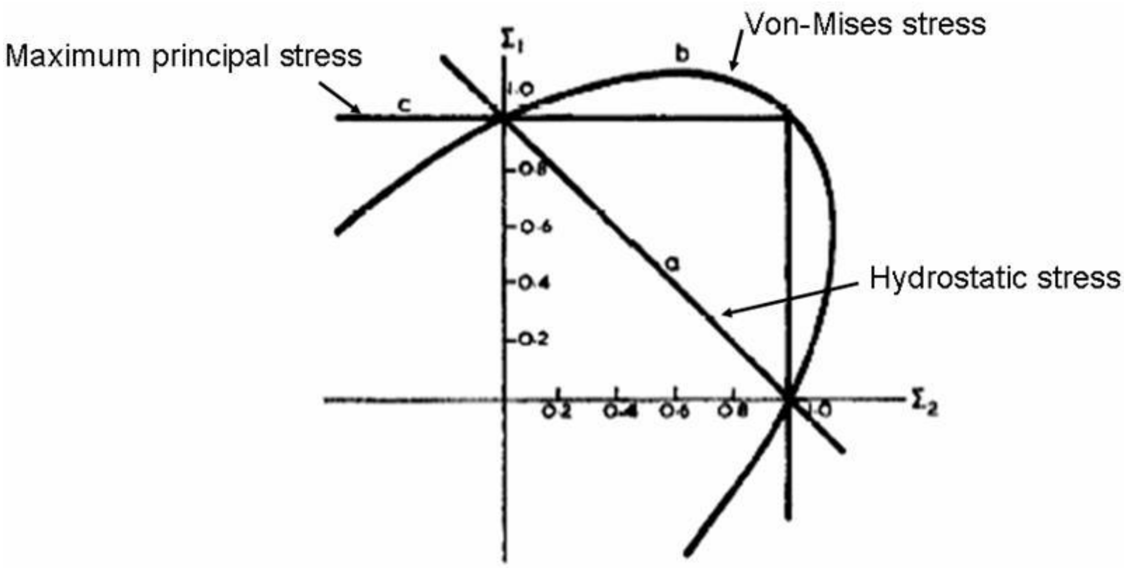

Fig. 1.25 Loci of constant rupture life considering different failure criteria

The value of β was found to be negligible as compared to other coefficient. Hence, the equation was further modified [102]

$$t_r = M(\alpha\sigma_1 + (1-\alpha)\sigma_{vm})^{-\chi} \quad (1.41)$$

Another multiaxial creep rupture life prediction was proposed by Cane [103] where creep rupture life has been co-related with the relative contribution of von-Mises stress and maximum principal stress, given by the following expression.

$$t_r = M\sigma_1^{-\gamma}\sigma_{vm}^{\gamma-m} \qquad (1.42)$$

The value of γ was found to vary in the range of 1.5-3.0 for generally used low alloy steel.

According to Nix et al. [104] creep rupture life under multiaxial state of stress can be predicted from uniaxial data by using the principal facet stress as a creep rupture parameter as shown below.

$$\sigma_{rep} = 2.24\sigma_1 - 0.62(\sigma_2 + \sigma_3) \qquad (1.43)$$

Where, σ_1 is the maximum principal stress and σ_2 and σ_3 are intermediate and minimum principal stresses, respectively. The parameter exhibits good co-relation for relatively creep cavitations prone material viz.316 stainless steels, Nimonic 80, 2.25Cr-1Mo steel and copper. However, the above expression can't predict the rupture behaviour of aluminum alloys where the failure is controlled mainly by von-Mises stress.

1.17 FE-analysis coupled with Continuum damage mechanics

Finite element analysis coupled with CDM has been extensively used for predicting the mechanical deformation and damage evolution under multiaxial state of stress [104-108]. Further, CDM uses an internal damage variable in the constitutive relation to describe the void growth in the material. Dhar et al. [109] observed that the critical value of damage is a geometry independent material parameter which can be used for predicting the initiation of micro-cracks by combining Lemaitre's CDM model [110] and Thomason's void coalescence condition [111]. Hyde etal. predicted the creep rupture life of both plain and notch specimen of Ti and Ni-base super alloys considering Kachanov model of single damage variable [112]. The damage was more pronounced at the notch centre for Ni-base super alloy while it was at the notch root in case of Ti-base alloys. Othman et al. carried out FE-CDM analysis on both single and double notch U- specimen and found that rupture life of double notch U-type specimen follows a very narrow scatter band (5%) with single U-notch specimen [113]. The creep rupture life of ferritic steel weldments (microstructural inhomogeneity 'metallurgical notch') has been well predicted through FE-CDM analysis by Hall and Hayhurst. [114]. Further, Goyal et al. predicted the creep rupture life of both smooth and double U-notch specimen of 2.25Cr-1Mo ferritic steel, 9Cr-1Mo ferritic steel and Modf.9Cr-1Mo ferritic steel through FE-CDM analysis considering Rabotov-Kachanov model [95, 96] .

1.18 Effect of notch geometry on creep damage behaviour

Circumferential (C-type), U-type and V-type notched specimens were chosen to study the influence of notch geometry on creep life [Fig. 1.26]. FE-analysis coupled with CDM was used to study systematically developed creep damage for different notched specimens (circumferential, U-type and V-type) under constant loading by Jiang et al. [115].

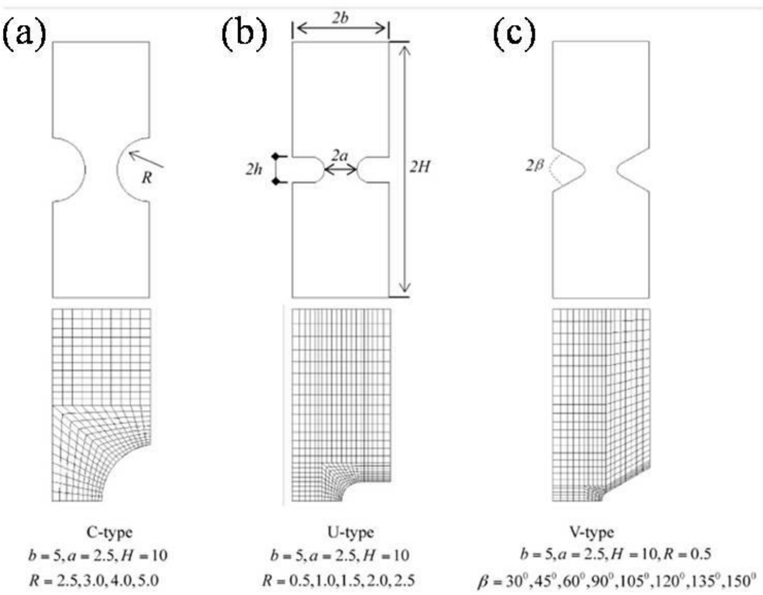

Fig. 1.26 Geometry of (a) C-type, (b) U-type and (c) V-type notch specimen and their corresponding FE-mesh.

For C-type notched specimen, the maximum creep damage lies at the point inside from the notch tip; for U-type notched specimen, the maximum damage is located at the point away from the notch root in the notch surface; for the V-type notched specimen, the maximum damage always happens at the notch root [fig.1.27].

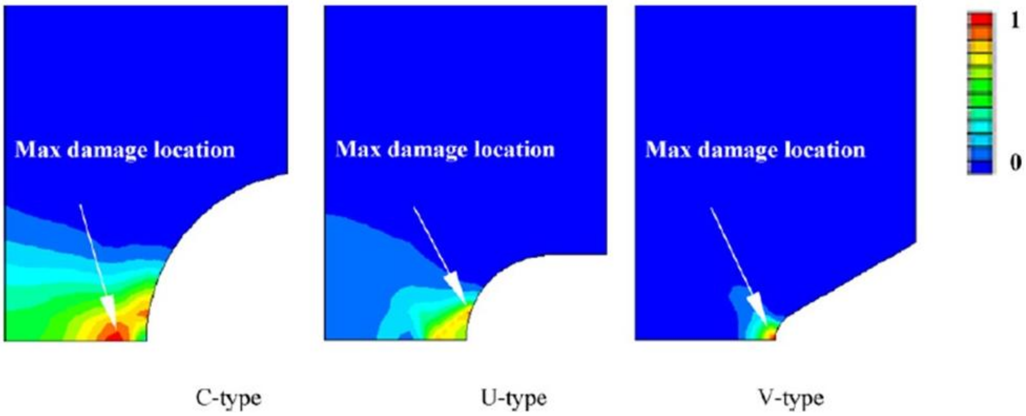

Fig. 1.27 Shows the contour of damage distribution of C-type, U-type and V-type notch specimen.

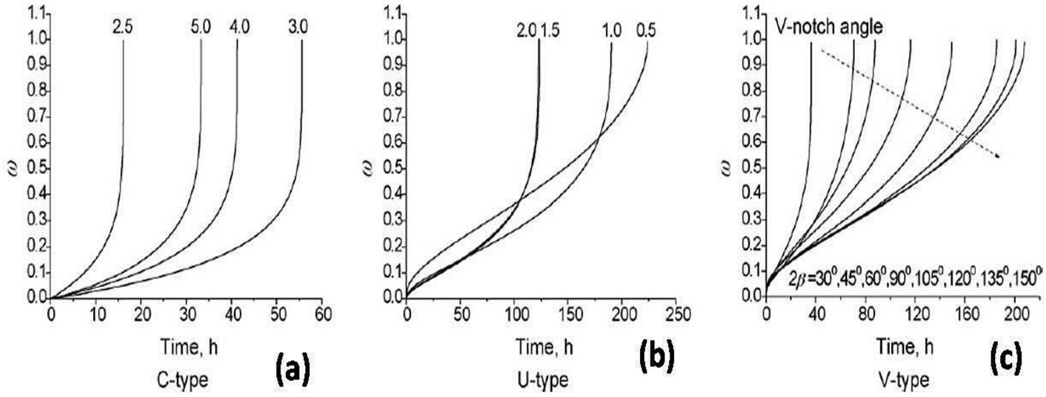

Fig.1.28 Dependence of the max damage on creep time for different notched specimens.

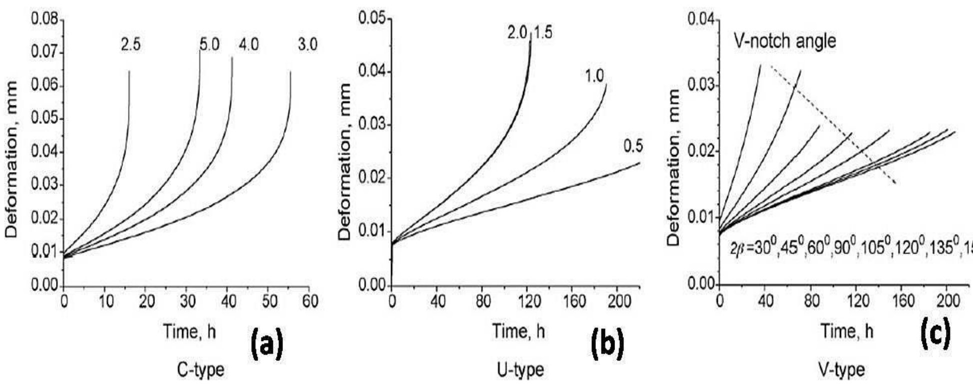

Fig. 1.29 Dependence of creep deformation on creep time for different notched specimens under stress of 275MPa.

The distance between the point of maximum creep damage and notch tip increases with increasing notch radius in the case of C-type and U-type notched specimens. However, for V-type notched specimen, the maximum creep damage occurs always exactly at the notch root [fig. 1.27]. Fig. 1.28, 1.29 show that the creep damage and deformation increase smoothly in the initial stage of the creep, and then increase rapidly until the final rupture during a short time in the final stage of the creep respectively. For C-type notched specimen, creep life increases with increasing notch root radius. But when notch radius reaches a critical value, at R = 3.0 mm, creep life decreases with increasing notch radius [Fig. 1.28(a) and 1.29(a)]. Further, for C-type notch with R = 2.5 mm, the maximum damage level happens at two points: notch plane and notch surface. Creep life increases with notch radius for the U-type notched specimen and with increasing notch angle for the V-type notched specimen [Fig. 1.28(b, c) and 1.29(b, c)]. Therefore, the creep life of the C-type notched specimen shows the complicated dependence on notch radius.

1.19 Multiaxial creep ductility prediction

The creep failure under multiaxial state of stress is linked with creep cavity nucleation and their growth. The phenomenon depends upon the stress distribution at the notch throat plane. Apparent reduction in ductility has been observed with increase in hydrostatic state of stress. Several models have been proposed to relate the multiaxial ductility with hydrostatic state of stress. All those models established their relation with multiaxial ductility and the ratio of hydrostatic stress to von-Mises stress, commonly known as triaxiality.

McClintock [25], Rice and Tracey [116] indicated the exponential amplification of the growth rate of microvoids with stress triaxiality in elastic-perfectly-plastic material.

Further, efforts made by Cocks and Ashby [117] who carried out approximate calculations with the effect of temperature of the grain boundary cavity growth rates of creeping material under multiaxial state of stress and its consequence on ductility. The mathematical expression which relates ratio of multiaxial ductility to uniaxial ductility with skeletal point triaxiality is given by.

$$\frac{\varepsilon_f^*}{\varepsilon_f} = \sinh\left[\frac{2}{3}\left(\frac{n-\frac{1}{2}}{n+\frac{1}{2}}\right)\right] \Big/ \sinh\left[2\left(\frac{n-\frac{1}{2}}{n+\frac{1}{2}}\right)\frac{\sigma_m}{\sigma_{vm}}\right] \qquad (1.46)$$

where $\frac{\varepsilon_f^*}{\varepsilon_f}$ is the ratio of multiaxial to uniaxial creep ductility (normalized ductility), $\frac{\sigma_m}{\sigma_{vm}}$ is the ratio of hydrostatic state of stress to von-Mises stress at the skeletal point and 'n' is the creep stress exponent in the variation of steady state creep rate with applied stress.

Rice and Tracey [116] model is based on the concept of hole growth by rigid plastic deformation of the surrounding matrix and doesn't account to consider the effect of temperature given by

$$\frac{\varepsilon_f^*}{\varepsilon_f} = exp\left(\frac{1}{2} - \frac{3\sigma_m}{2\sigma_{vm}}\right) \qquad (1.47)$$

Manjoine [117] proposed empirical relationship based on creep tests on different materials and expressed normalized ductility with power function of skeletal point triaxility. The expression is given by,

$$\frac{\varepsilon_f^*}{\varepsilon_f} = 2^{\left(1-3(\sigma_m/\sigma_{vm})\right)} \qquad (1.48)$$

1.20 Development of 304 HCu austenitic stainless steel for AUSC

The ever increasing global energy demand and the stringent policies towards mitigation of CO_2 emissions call for efficient energy generation technologies. One of such technologies is the Advanced Ultra Super Critical (AUSC) coal-fired power plant that requires improved material properties with good creep resistance, corrosion/oxidation resistance along with better fabricability, for e.g. for boiler components [119].The proposed materials for different working zones of boiler in the order of increasing temperature are ferritic steels (grade 91, grade 92, grade 122 etc.), austenitic stainless steels (super 304H, HR3C, HR35, HR6W etc.) and nickel based alloys (IN617, HR230, IN740, HAYNES 282, Alloy 263 etc.) [120].The copper and niobium containing 304HCu SS (Super 304 H) is one of the candidate materials for AUSC boiler piping and it has around 3 wt.% of copper, high carbon content and certain amounts of niobium and around 0.1% of nitrogen along with boron as compared to conventional 18Cr-8Ni austenitic stainless steel [120, 121, 122]. Copper has low solubility in the austenitic matrix and hence precipitates out as nano-size particles [123, 124] and is reported to increase the creep strength by precipitation hardening. Further, the precipitation of niobium carbonitride also contributes to the creep strength [13, 124]. The steel has been micro-alloyed with boron as the addition of boron in high-temperature alloys has been reported to improve creep rupture strength by strengthening the grain boundaries. The grain boundary strengthening in most instances is considered to be caused by the segregation of boron to grain boundaries wherein it enters the precipitates and alters the character of the grain boundary or matrix/particle interface in such a way that it retards the creep cavitation, and thus increase the creep rupture strength by minimizing the grain boundary sliding [125].

1.21 Scope of the work

In the above discussion, the different categories of power plants as per their efficiencies were listed and the need to go for AUSC plants for which use of 304HCu SS has been stressed or emphasized. Further, basic mechanism of creep, fracture behaviour, different modes of cavity nucleation and growth and their qualitative and quantitative description has been discussed. The literatures pertaining to transient creep behaviour and stress-temperature dependence of steady state creep rate of material has been discussed. Further, different ways of conducting of multiaxial testing has been emphasized. Here, more emphasis has given in the study of multiaxial sate of stress by introducing circumferential U-notch. Further, distribution of stress, multiaxial life prediction, and damage behaviour and ductility prediction based on different models has been discussed.

In this investigation, the effect of multiaxial state of stress, incorporated with the insertion of U-notches of different notch sharpness in smooth creep specimens, on creep rupture behaviour of 304HCu SS at different temperatures has been studied along with the behaviour of uniaxial creep deformation, transient creep behaviour and stress-temperature dependence of steady state creep rate. Extensive finite element analysis to estimate stress distribution across the notch plane along with detailed metallography including SEM, TEM and EBSD has been carried out to illustrate the creep damage under multiaxial state of stress. A unique master plot independence of notch, smooth and test temperature has been established for the prediction of creep rupture life of components in power plant. On the other hand, a model has been proposed for prediction of multiaxial ductility within 10% scatter band.

Work Plan

❖ Materials for investigation: 304HCu SS

❖ Temperature: 923 K, 973 K and 1023 K, Stress range: 100-260 MPa

❖ Analytical studies on different stages of uniaxial creep deformation at different temperatures over the wide stress range based on different mathematical equations.

❖ Prediction of uniaxial creep deformation and rupture life on creep exposure using CDM and FE-CDM analysis.

❖ Method of incorporating multiaxial sate of stress: Circumferential U-notch specimen with various root radius from 0.25 mm to 5 mm and also of different notch depth

❖ Finite element analysis of stress distribution across the notch on incorporating materials properties as elastic, plastic and creep

❖ Multiaxial creep life and ductility predictions of notch specimen based on the concept of representative stress though skeletal point.

❖ Effect of notch depth on creep life and their stress distribution at the notch plane through FE-analysis.

❖ Characterization using: Optical microscopy, Scanning Electron Microscopy (SEM), Transmission Electron Microscopy (TEM), Electron backscattered diffraction (EBSD).

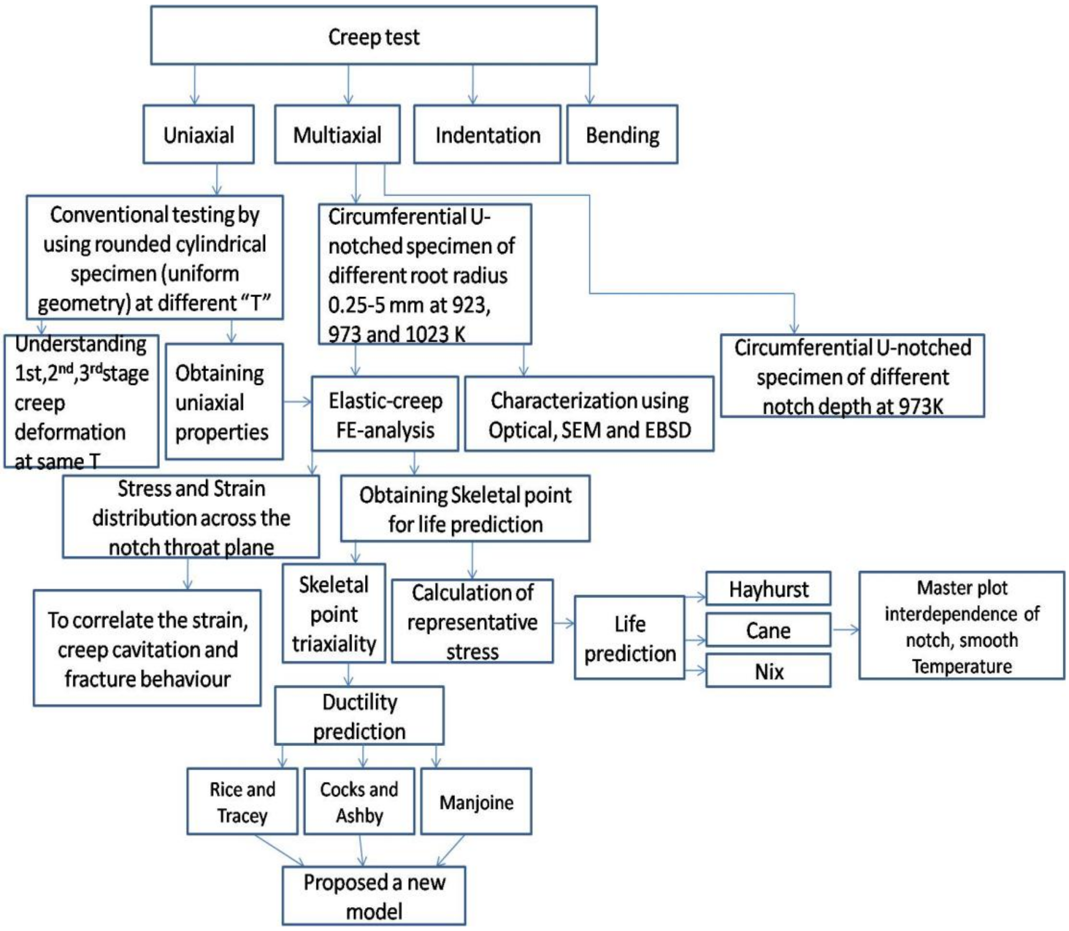

Chapter: 2

Experimental Procedures

2.1 Introduction

This chapter brings out the details related extensive experimental studies carried out in this thesis. In particular, details related to uniaxial creep and multiaxial creep along with the methodology of fractogrphy and electron micrography studies are described in this chapter. Creep tests are carried out at 923, 973 and 1023 K over the stress range of 100-260 MPa on 304HCu SS. Creep tests were carried out on the circumferential U-notch where the notch root radius is varied from 0.25 mm to 5 mm to induce different multiaxiality and also the notch depth is varied. Three notches are machined on the specimen to keep the distance adequate between the notches and unfailed notch can give significant information about the history of failure. FE-analysis has been carried out to assess the stress distribution across the notch throat plane. Tensile test has been done at 923, 973, 1023 K to incorporate the plastic properties in the FE-analysis. FE-analysis coupled with CDM has been used to predict the creep deformation and rupture life of the material. SEM fractography and microscopy investigation has been carried out to know the nature of fracture surface in terms of various features and micro features at the notch plane. EBSD analysis has been carried out at the notch throat plane for mapping the total strain by using HKL software. Transmission Electron Microscopy has been carried out on as-received material, post tested failed regions to know the nature of precipitates, sub grain formation, dislocation cell formation.

2.2 Materials

The material used in the present investigation is 304HCu SS, commonly known as Super 304H steel, which is a candidate material for Advanced Ultra Super Critical (AUSC) power plant. The 304HCu SS ingots were hot forged at 1473 K followed by solution annealing at 1443 K for 90 min. Hot extrusion was carried at 1430–1148 K. Then it was subjected to additional solution annealing at 1543 K for 2 h before multipass cold pilgering with intermediate annealing at 1373 K for 30 min. The 304HCu steel tube of 52 mm OD and 9.5

mm wall thickness was received in solution annealed condition at 1373 K for 30 minutes. Small tubes of 130 mm length were extracted in the intention to fabricate smooth and notch creep specimens from the periphery of the tube. Rods of 10 mm diameter were machined from the tube to give machining tolerance while fabricating the specimen from the rod [Fig.2.1]. Smooth as well as notched creep specimens were machined from the rods. The chemical composition of the steel is given in Table 2.1.

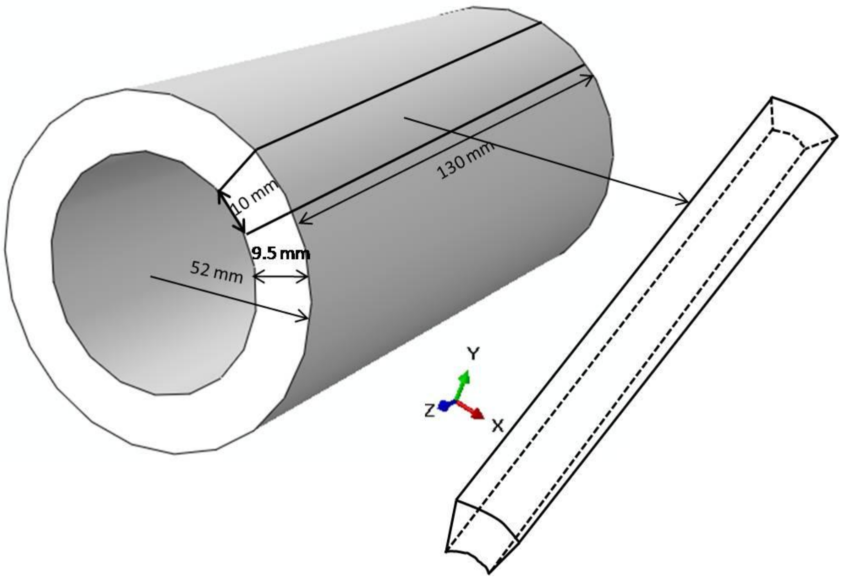

Fig. 2.1 The rod and tube details before fabrication of the smooth and notched creep specimen from the 304HCu SS tube.

Table-2.1 Chemical composition (wt. %) of 304HCu SS

Element	Al	B	C	Cr	Cu	Mn	Ni	Nb	N	P	Si	S	Fe
Wt%	0.002	0.003	0.096	17.7	2.88	0.88	9.94	0.55	0.1	0.02	0.19	0.004	Bal.

2.3 Tensile tests

Tensile tests were carried out for smooth specimen at 923, 973 and 1023 K. The geometry of the tensile specimen is given in Fig. 2.2. The tensile tests were carried out in air at 923, 973 and 1023 K employing a strain rate of 3×10^{-4} s^{-1} using Hung Ta 2402 model screw driven system. The tensile test temperature was carefully controlled within ±1 K during the test. The load-displacement data was recorded and logged in a data logger during the test.

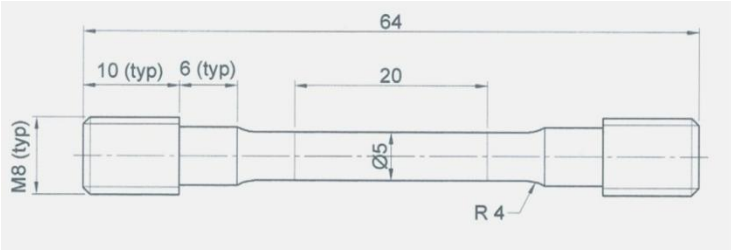

Fig. 2.2 Specimen details for tensile testing (all dimension in mm).

2.4 Creep tests

Creep experiments were carried out on both the smooth and notched specimens at 923, 973, 1023 K over the stress range of 100 – 220 MPa. Dimensions of the smooth specimens are shown in Fig. 2.3. The temperature was maintained within ±2 K across the creep specimen during the creep tests. The elongation was monitored by extensometer, digital dial indicator and data logger arrangement. All tests were continued till fracture. The pictorial image of machines used for creep testing is shown in Fig. 2.4.

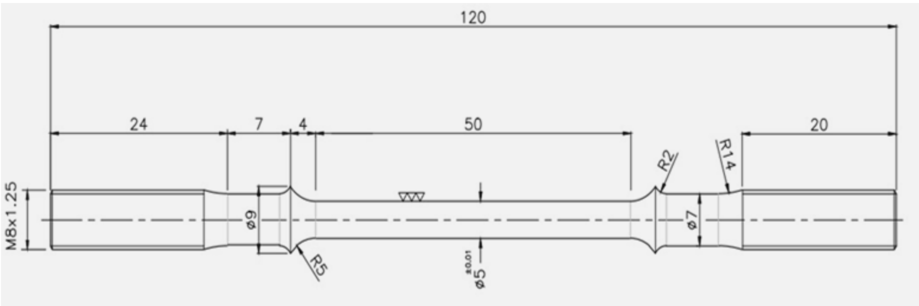

Fig. 2.3 Specimen details for uniaxial creep testing (all dimension in mm).

2.5 Notched specimen

Creep tests were also carried out on notch specimen of the 304HCu steel at net applied stresses (σ_{net}, stress applied to the minimum cross section in notch) ranging from 100 - 260 MPa and at 923, 973, 1023K. Dimensions of the notched specimens along with photographs are shown in Fig. 2.5. Three notches of same root radius were incorporated in the specimen with the intension of post creep metallographic study on the un-failed notches.

Fig. 2.4 Photograph of the machines used for both smooth and notch specimen creep test.

The notches were kept sufficiently apart so that the presence of one notch will not affect creep behaviour of the other. The inner diameter of the notched specimen was kept the same as that of smooth specimen. The ratio of notch outer diameter (D) to inner diameter (d) was kept fixed at 1.67 [131, 132]. The notch acuity ratio (d/R) was varied from 1 to 20, where R is the notch root radius of the specimen, which was varied as shown in Table 2.2

Table-2.2 Variation of notch acuity ratio with root radius

d	**R**	**Notch acuity**
5	5	1
5	2.5	2
5	1.25	4
5	0.5	10
5	0.25	20

The variation of notch acuity ratio from 1 to 20 resulted in an elastic stress concentration factor ranging from 1 to 3.37. Creep tests on notched specimens were carried out in such a way that net applied stress acting in the notch throat plane was equal to the nominal stress on plain specimen. Creep rupture results for different notch acuities have been shown in Table-2.3(a), 2.3(b), 2.3(c) at 923, 973 and 1023 K respectively.

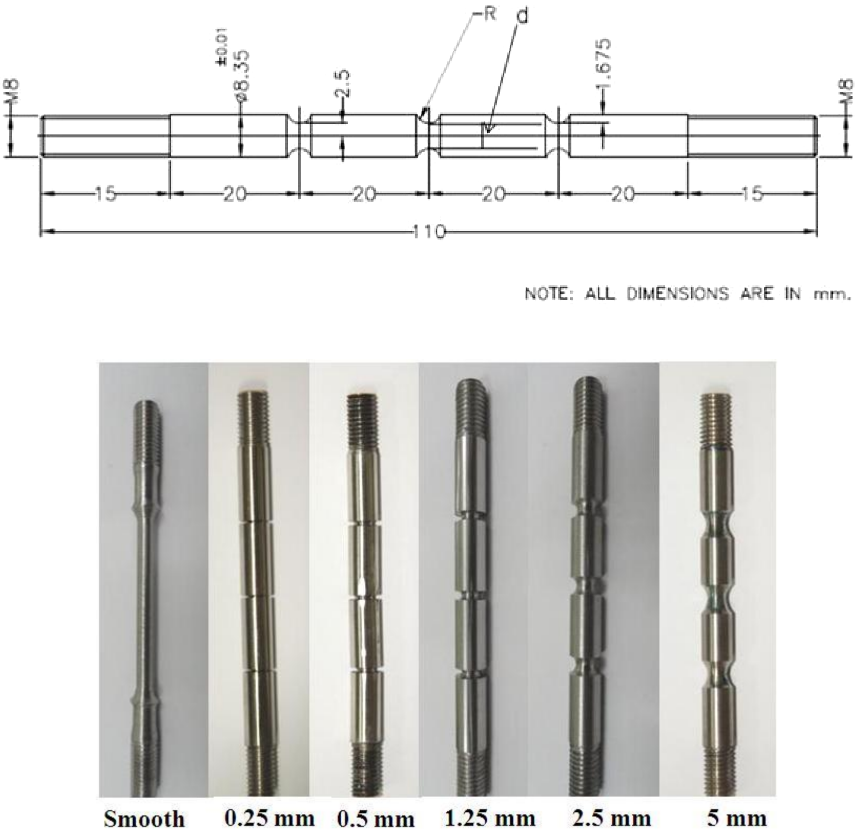

Fig. 2.5 Notched creep test specimen details (all dimensions are in mm) along with photograph of the specimens including smooth.

Table-2.3(a) Creep rupture properties of 304HCu SS at 923 K

Notch acuity ratio	**Net applied stress, MPa**	**Rupture life, h**	**Creep ductility, % RA**
0 (Plain specimen)	180	4740.17	28.5
	190	2680.25	29.6
	200	2220.32	30
	220	636	32.3
	240	320	34.2

1	200	2415.4	15.36
	220	1248.5	18.28
	240	595.1	20.1
	260	414.4	21.85
2	200	2619.23	12.56
	220	1622.2	16.1
	240	875.9	17.36
	260	472.5	19.7
4	180	4083	8.64
	200	2944.6	9.75
	220	1777.3	11.34
	240	1000.8	12.86
	260	695.3	14.62
20	200	2664.5	3.96
	220	2470	4.85
	240	1655.3	5.23
	260	675.3	7.02

Table-2.3(b) Creep rupture properties of 304HCu SS at 973 K

Notch acuity ratio	**Net applied stress, MPa**	**Rupture life, h**	**Creep ductility, % RA**
0 (Plain specimen)	125	4089	14.86
	140	877	16.06
	160	502	17.8
	180	202	22.56
	200	79.9	27.75
	220	40.3	29.44
1	160	1086.8	9.02
	180	468.9	10.5
	200	184.3	14.3

	220	96.1	18.25
2	160	1263.1	7.5
	180	512.3	8.18
	200	189	12.25
	220	114.14	16.24
4	160	1540.4	4.9
	180	1223.5	6.3
	200	283.7	10.09
	220	256	11.65
10	160	1477.4	3.1
	180	793.13	4.23
	200	498	7.09
	220	211.14	9.01
20	160	1610.66	1.05
	180	882.4	1.2
	200	544.3	1.78
	220	367	2.76

Table-2.3 (c) Creep rupture properties of 304HCu SS at 1023 K

Notch acuity ratio	**Net applied stress, MPa**	**Rupture life, h**	**Creep ductility, % RA**
0 (Plain specimen)	100	1053	9.25
	120	329	10.1
	140	140.2	11.07
	160	51	16.48
	180	15.1	22.59
1	120	586.0	12.4
	140	308.9	13.5
	160	112.6	16
	180	64	17.02
	200	16.4	20.79

2	120	608.8	5.5
	140	411.6	6.3
	160	179.9	7.8
	180	154.27	9.3
	200	55.12	11.64
4	120	812.5	3.2
	140	445.2	5.52
	160	240	7.07
	180	155.7	8.6
	200	60.2	10.13
10	120	1026.3	2.1
	140	511.3	3.17
	160	233.1	4.4
	180	213.9	6.68
	200	119.03	7.5
	220	93.03	8.6
20	120	1550.6	0.8
	140	454	1.4
	160	266.1	2.6
	180	168.9	3.17
	200	150.11	3.96

Further, the notch depth of the 1.25 mm root radius specimen has been varied to 2, 2.5 and 3 mm to study the effect of notch depth on creep rupture life [Fig. 2.6]. The creep test has been carried out at only 973 K and 200 MPa for all notch depth specimens. The R/d ratio has been varied to 0.25, 0.287, 0.373 and 0.532 where R is the root radius of the notch and d is the notch throat diameter (Table 2.4). Table 2.5 shows the creep rupture properties of different notch depth specimen of fixed root radius of 1.25 mm at 973 K, 200 MPa.

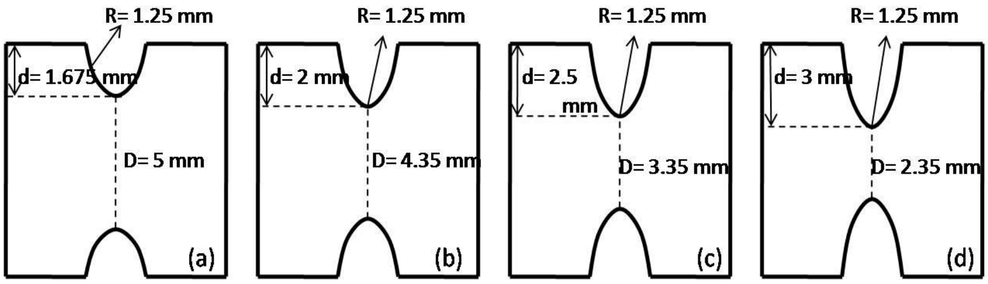

Fig. 2.6 Schematic of the notch details and notch diameter with the variation in notch depth (a) 1.675 mm (b) 2 mm (c) 2.5 mm (d) 3 mm in the specimen used for multiaxial creep study.

Table-2.4 Variation of notch throat diameter with notch depth ratio (R/d).

R	d	R/d
1.25	5	0.25
1.25	4.35	0.287
1.25	3.35	0.373
1.25	2.35	0.532

Table-2.5 Creep rupture properties of 304HCu SS for different notch depth at 973 K, 200 MPa.

Notch depth (mm)	Rupture life (hr)	Ductility
1.675	283.7, 220.5	10.09, 10.6
2	449	7.22
2.5	1252.7, 1596.7	7.04, 7.1
3	30.4, 42.2	6.7, 5.8

2.6 Finite element analysis

Finite element analysis of stress distribution across the notch throat plane during creep exposure was employed out to study the creep rupture behaviour of the notched specimens of different root radii. To understand the creep behaviour of the steel under multiaxial state of stress, 2D-axisymmetric FE analysis was carried to estimate the stress distribution across the notch throat plane. Due to axisymmetric circular geometry, 2D simulation was quite adequate to assess the stress distribution [94]. Due to axisymmetric circular geometry of the specimen, 1/16th part of the specimen was used for FE analysis along with appropriate boundary conditions as shown in Fig. 2.7(a). The 2D axisymmetric analysis was carried out using 4 nodded quadrilateral elements with ABAQUS 6.16 FE solver [Fig. 2.7(b)]. The element size was reduced at and close to the notch root, and elastic analysis was used to ensure that the mesh configuration was sufficiently refined near the notch root to predict the theoretical elastic stress concentration factor at the notch root [Fig. 2.7(c)]. Further, the effect of element type (4-noded and 8-noded) on the results shows not much difference in the axial stress distribution at the notch throat plane [Fig. 2.7(d)]. Again, different number of elements has been used near the notched region to compare the result with elastic-plastic stress distribution at notch throat plane [Fig. 2.7(e)]. The result shows not much difference in the axial stress distribution at the notch throat plane. Hence further analysis has been carried out using 4-nodded 2D-axisymmetric analysis.

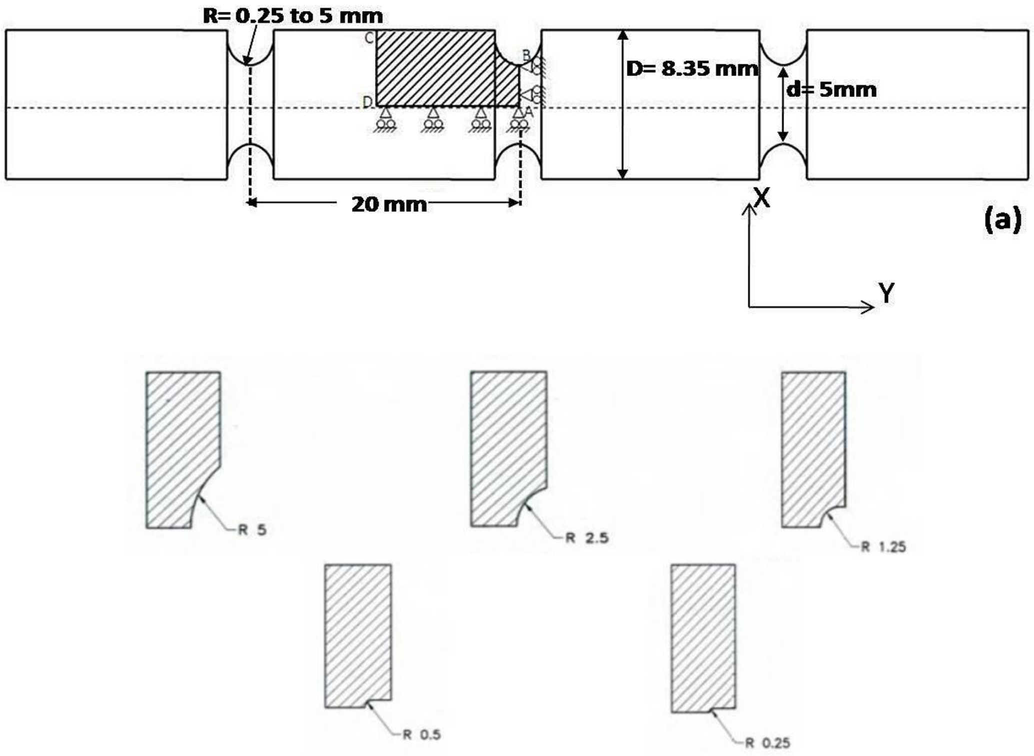

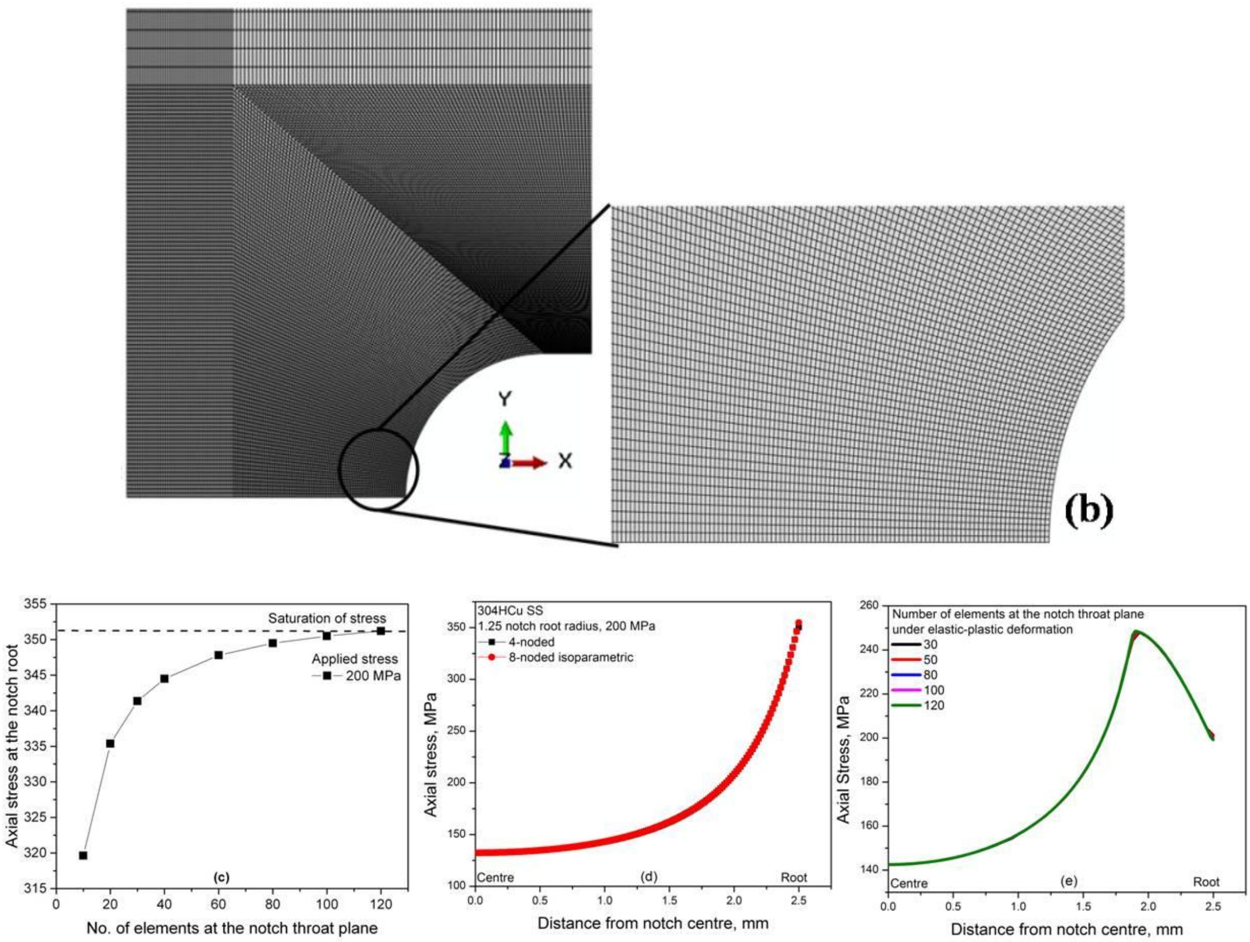

Fig. 2.7 (a) The geometry of the notched specimen along with 1/12th part of the specimen for different root radius and (b) the typical FE mesh used for FE analysis mesh independency analysis, (d) axial stress distribution for 4-noded and 8-nodded isoparametric elements, (e) effect of mesh size on axial stress distribution under elastic-plastic deformation for notch root radius of 1.25mm at 200 MPa.

2.7 Continum damage mechanics

The damage evolution of the material under multiaxial state of stress has been studied by using continuum damage mechanics proposed by Kachanov [35] and has been widely accepted and used for predicting the tertiary creep damage of the material.

Under uniaxial stress conditions, the creep strain and damage rate equation converges to the following expression

$$\dot{\varepsilon}_c = A\left(\frac{\sigma}{1-\omega}\right)^n \qquad (2.1)$$

and

$$\dot{\omega} = \frac{B\sigma^{\chi}}{(1-\omega)^{\varphi}} \qquad (2.2)$$

For virgin material, ω = 0, the creep rate equation (2.1) becomes Norton's creep law

$$\dot{\varepsilon}_s = A\sigma^n \qquad (2.3)$$

At a constant stress, the damage evolution (equation (2.2)) can be integrated as follows

$$\int_0^{\omega_{cr}} (1-\omega)^{\varphi}\, d\omega = \int_0^{t_r} B\sigma^{\chi} dt$$

where t_r is the rupture life and ω_{cr} is the critical damage (=1). The above integration leads to the following expression.

$$t_r = \frac{1}{B(1+\varphi)\sigma^{\chi}} \qquad (2.4)$$

where m is the slope (χ) of the uniaxial creep rupture plot and $M = \frac{1}{B(1+\varphi)}$.

All of the above equations are valid for constant stress condition. The 304HCu SS material is much more to creep cavitation susceptible with limited ductility as compared to ferritic steel. Primary creep deformation was limited for this type of steel.

The slope of the logarithmic of time of rupture (t_r) and logarithimic of applied stress is given by –χ and the intersection is B(1+ φ). The values of B and φ can be obtained by trial and error or by optimization procedure for minimum deviation.

The damage evolution can be calculated by integrating the damage rate equation which gives the following expression

$$\omega = 1 - [1 - B(1+\varphi)\sigma^{\chi} t]^{\frac{1}{(1+\varphi)}} \qquad (2.5)$$

Implementing the above relation (equation (2.5)) in the strain rate equation (equation (2.1)) and further integration leads to the following relation which has been used for the prediction of creep strain based on the continuum damage mechanics from the experimental time of rupture data.

$$\dot{\varepsilon}_c = \frac{A\sigma^{(n-\chi)}}{B(n-\varphi-1)}\left\{[1-B(1+\varphi)\sigma^{\chi}t]^{\frac{\varphi+1-n}{\varphi+1}}-1\right\} \qquad (2.6)$$

2.8 SEM fractograph and Micrograph investigation

Fractographic investigation of the creep ruptured specimens was carried out by employing Scanning Electron Microscopy (SEM). Fractography of fractured surface of creep tested samples was carried out using a Scanning Electron Microscope of Model No: XL 30 ESEM of M/s FEI the, Netherlands. The specimen preparation consists of sectioning and ultransonic cleaning for 15 minutes. SEM was also used to study the creep cavitation and cracking in the unfailed notch. Unfailed notches were sectioned longitudinally and polished up to half of their length of surface finish up to 0.25μm. To study the presence of precipitates and change in size due to creep exposure, the samples were etched electrolytically with 60%HNO_3.

2.9 Electron Backscatter Diffraction (EBSD) Study

Electron Back Scatter Diffraction (EBSD) studies were carried out to understand the deformation behavior of the steel under multiaxial state of stress. For EBSD studies, the unfailed notch of the creep ruptured specimens was extracted and mechanically polished. Finally, the specimens were polished using colloidal suspension of silica to remove the residual stresses and then electro-chemically polished for better indexing of the image. EBSD measurements were conducted using SEM equipped with an EBSD-system operating at an accelerating voltage of 20 kV and camera length of 178 mm having the pre-tilted stage at 70° with respect to horizontal axis. HKL software was used for the data acquisition and analysis.

2.10 Transmission Electron Microscopy Study

Transmission Electron Microscopy (TEM) studies were carried out using CM 200 TEM (M/s FEI, The Netherland) operating at an accelerate voltage of 200 kV. SAED combined with EDS were used for the identification of precipitates. Thin foils of 3mm diameter extracted at two locations viz., close to the failed notch and far away from notch (from the parallel length) of creep tested specimens. For smooth specimen, the samples were extracted far away from the fractured zone. Following mechanical grinding of the slices, they were electrolytic thinned for achieving final TEM specimens. The electrolyte for jet thinning was 10 % Perchloric acid in methanol and the thinning was carried out at -35^{0}c. The foils were examined with a 200 kV TEM to study the dislocation structure after creep failure.

2.11 Hardness measurements

The Vickers hardness measurements were carried out by UHL, VMHT Techishe Mikroscopie, Germany which consisted of a diamond indenter in the form of a pyramid with a square base. The samples were well polished employing standard metallographic procedures. The load used for micro hardness testing was 200 gf for 15 sec. The length of the two diagonals of the indentation made on the surface of the material after removal of the load was measured using a microscope and their average value was calculated. Vickers hardness (HV) was evaluated using the formula as shown below:

$$HV = 1.854\frac{F}{d^2} \qquad (2.7)$$

F= Load in kgf, d= Arithmatic mean of two diagonals after indentation

Chapter: 3

Analysis of Uniaxial Creep Behaviour

3.1 Introduction

Before investigating creep behaviour under multiaxial state of stress of 304HCu SS, it is necessary to study the creep deformation behaviour under uniaxial state of stress. The deformation behaviour of material under multiaxial state of stress requires the uniaxial creep and tensile properties. Further, detailed understanding of different stages of creep behaviour based on analytical work will be useful in designing purpose of AUSC. In this chapter, tensile deformation, creep deformation, damage and rupture behaviour of 304HCu SS have been investigated over wide range of temperature and stress. The transient creep behaviour has been analyzed in the framework of Garofalo equation [77] and steady state creep deformation by invoking the concept of back stress. Further, the creep damage through the Kachanov-Rabotnov (KR) [35, 36] model coupled with finite element analysis (FE) has been studied.

3.2 Microstucture and tensile properties of the steel

The SEM microstructures of the as-received (after solution annealing at 1373 K for 30 minutes) steel is shown in Fig. 3.1(a). Austenitic grains, containing annealing twins, with grain boundaries decorated with particles can be noticed in Fig. 3.1(a). The average grain size was around 25 μm as estimated by intercept method. TEM micrograph of the solution annealed steel is shown in Fig. 3.1(b). A few primary undissolved Nb(C,N) metal-carbonitride particles as identified by selected area diffraction pattern were observed in the solution annealed steel. Some copper particles were also observed along with the metal-carbonitrides and they appeared as bright phase because of the lower atomic weight of copper than the iron matrix. Copper precipitates out as nano-size elemental particles because of its low solubility in the austenitic matrix. Similar observations of the precipitation of Cu-particles in niobium stabilized austenitic stainless steels after thermal and creep exposures have also been reported [13,128]. The hardness of the as-received steel was around 185 HV.

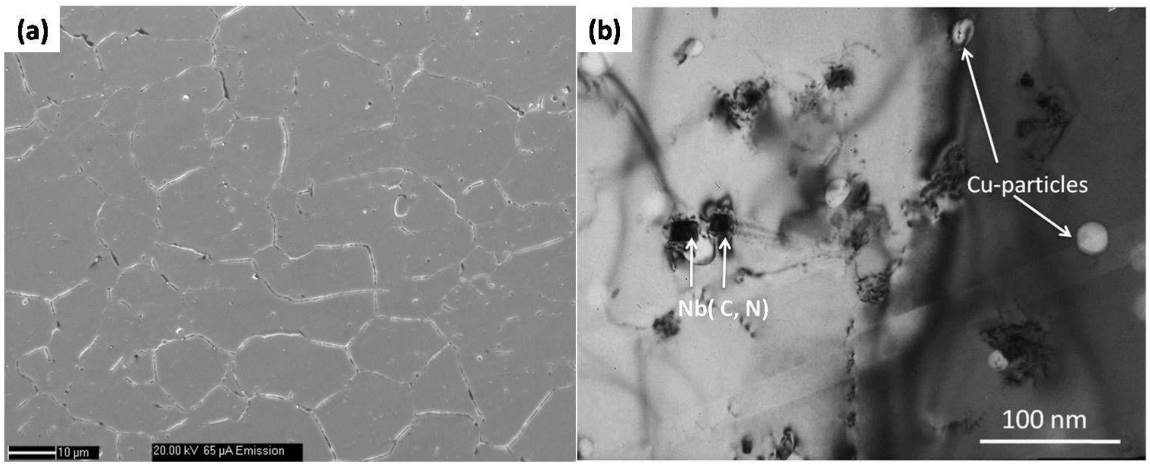

Fig. 3.1 SEM and TEM micrograph of the 304HCu SS in solution annealed condition

The tensile tests were carried out on smooth specimens in air at 923, 973 and 1023 K at a strain rate of $3\times10^{-4}\ s^{-1}$. Tensile curves of the steel at all these temperatures are shown in Fig. 3.2. Both yield stress and ultimate tensile strength decreased with increasing temperature.

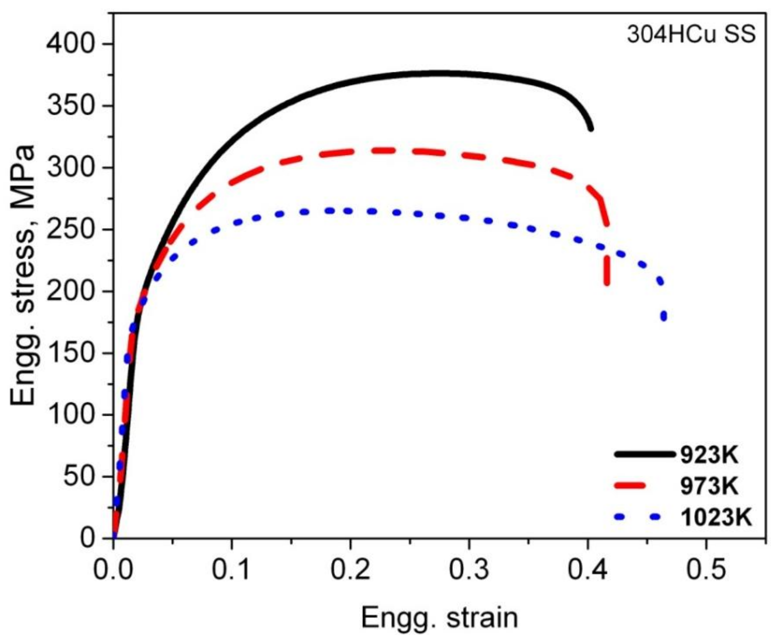

Fig. 3.2 Tensile curves of the steel at 923, 973, 1023 K

True stress-True plastic strain behaviour of the steel at 923, 973 and 1023 K is shown in Fig. 3.3. Holloman relation $\sigma_t = K\varepsilon_p^{n'}$; where σ_t is the true stress, ε_p is the true plastic strain, n' is the strain hardening exponent, K is the strength coefficient has been used to describe the plastic flow behaviour of the steel. The values of n' and K at 923, 973 and 1023 K obtained from this relation are shown in table-3.1

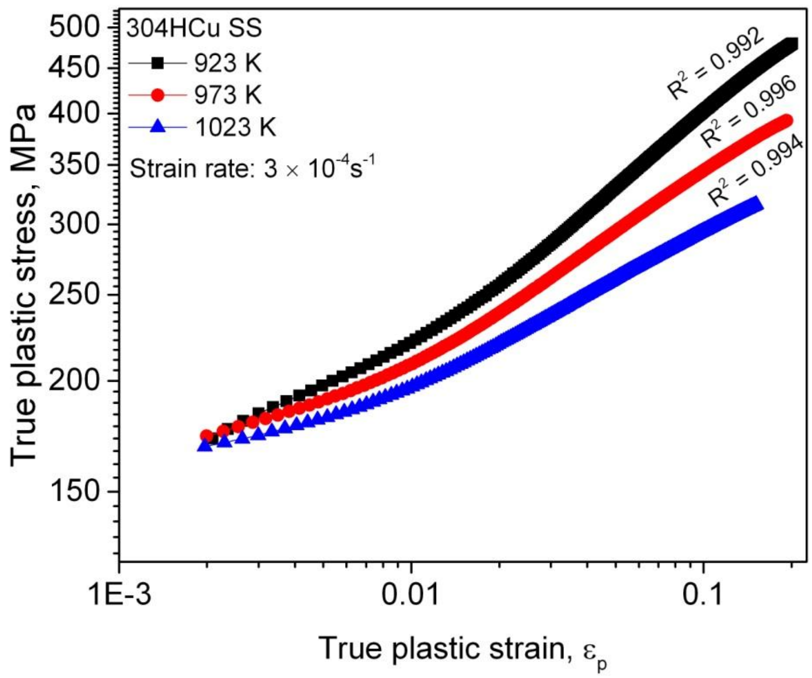

Fig. 3.3 True stress vs True strain of the steel at 923, 973, 1023 K

Table-3.1 Uniaxial tensile properties of 304HCu specimen at a strain rate of $3\times10^{-4}s^{-1}$ at three different temperatures.

Temperature (K)	YS(MPa)	UTS (MPa)	%Elong.	%RA	n'	K
923	177	376.27	30.2	38.2	0.255	720.46
973	170.2	314	36.3	46	0.21	554.1
1023	166	263.86	39	43	0.1686	433.42

3.3 Creep deformation and rupture behaviour

Creep tests were carried out at 923, 973 and 1023 K over a wide stress range (100-240 MPa). The variations of creep strain with creep exposure of the steel at 923, 973 and 1023 K for different applied stresses are shown in Fig. 3.4(a)-(c), that portray all the stages of creep deformation i.e., instantaneous strain on loading, a transient primary stage and a steady state followed by prolonged tertiary stage.

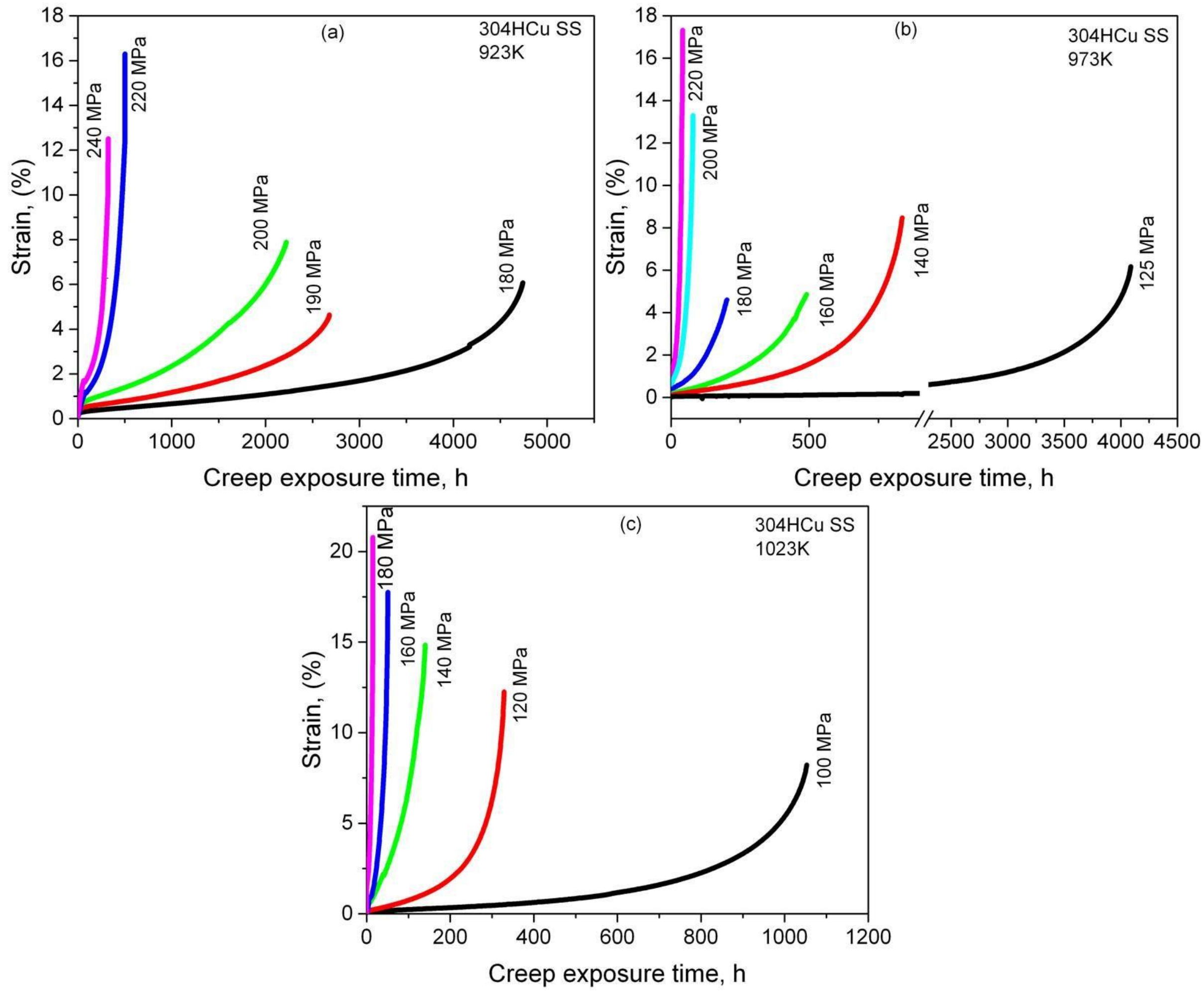

Fig. 3.4 Creep curves of the steel tested at (a) 923 K, (b) 973 K and (c) 1023 K at different stresses.

The variation of creep rate ($\dot{\varepsilon}$) with creep exposure time is shown in Figs. 3.5(a)-(c) for different test temperatures. As apparent, the creep rate decreased with time, attained a steady state creep rate followed by acceleration leading to the final failure of specimen. The duration of primary stage was relatively small compared to the steady state and tertiary stages.

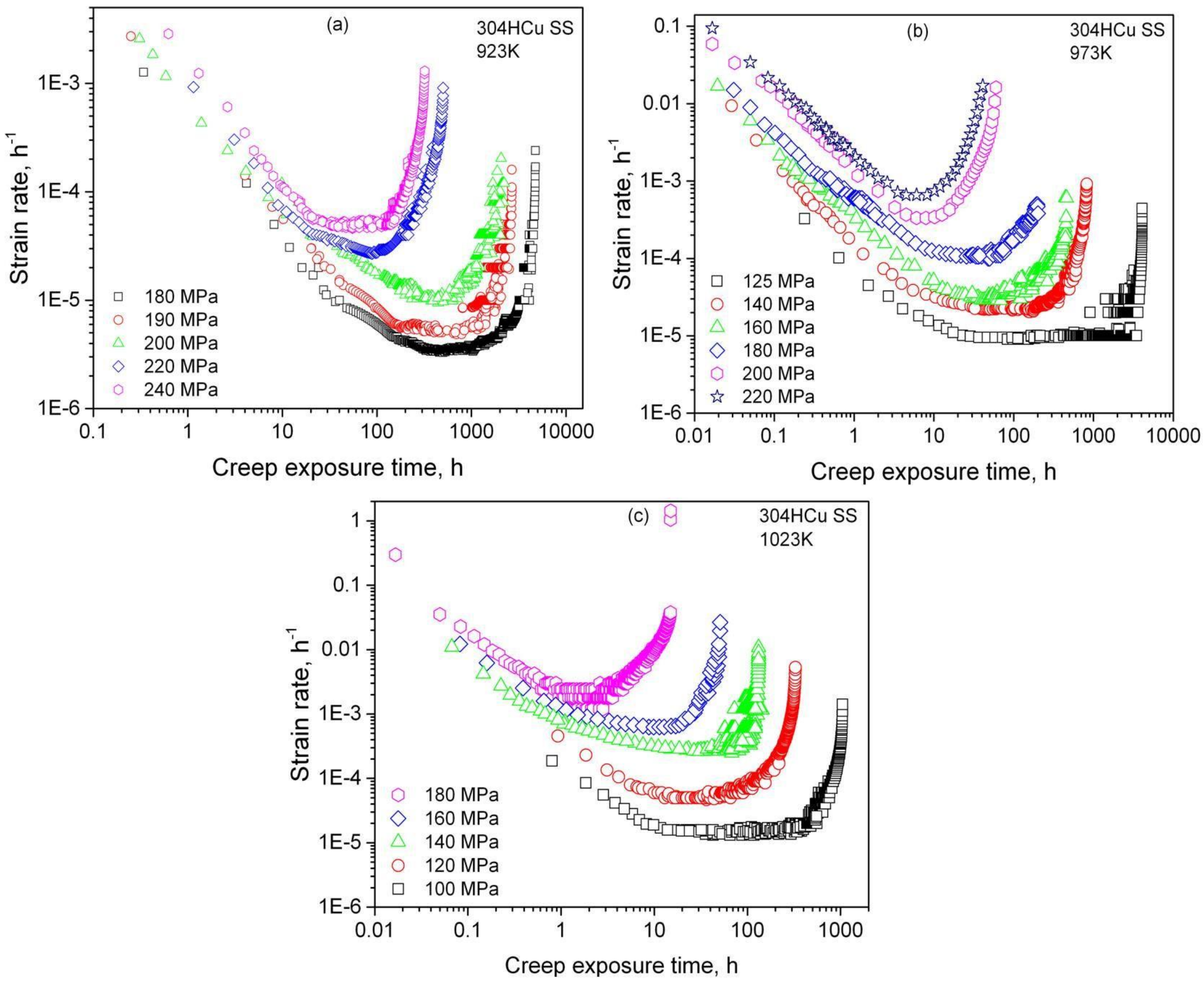

Fig. 3.5 Variation of creep rate with time of the steel at (a) 923 K, (b) 973 K and (c) 1023 K at different stresses

In order to examine the competition between the microstructural hardening and softening, the work hardening behavior of the material is assessed by plotting the work hardening rate of the material as a function of tensile plastic strain, as shown in Fig. 3.6. It is evident from the figure that the strain hardening in the steel gets rapidly exhausted at high homologous creep test temperatures (Fig. 3.6) and hence the microstructure induced creep damage accumulation is expected to govern the tertiary stage of creep deformation appreciably. The coarsening of precipitates [128] along with intergranular creep cavitation could be attributed to the prolonged tertiary stage of creep deformation (Fig.3.4&3.5).

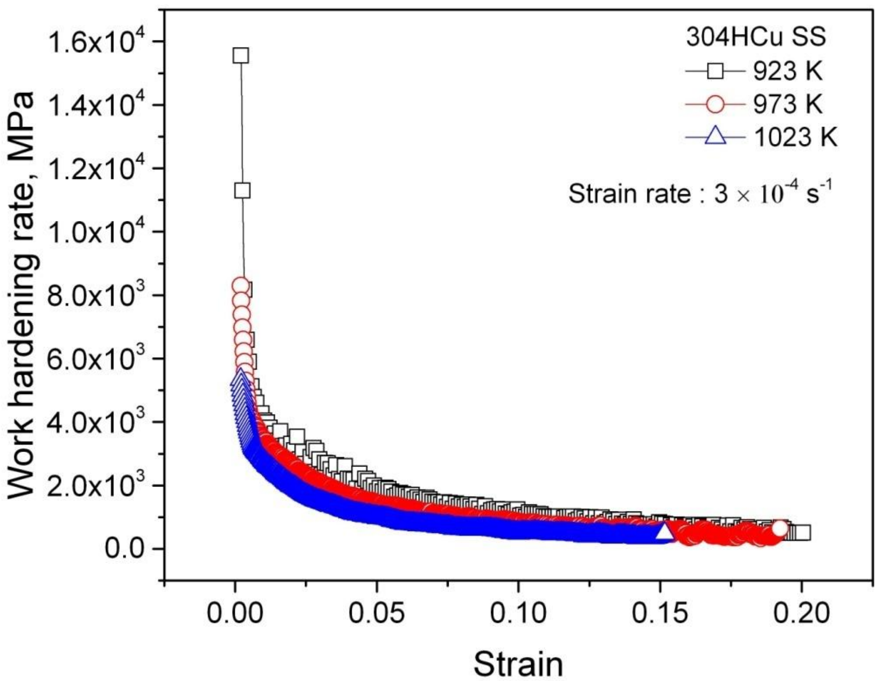

Fig. 3.6 Variation of work-hardening rate with plastic strain of the steel at 923, 973 and 1023 K.

The variations of steady state creep rate ($\dot{\varepsilon_s}$) with applied stress (σ) at all the test temperatures are shown in Fig. 3.7 in log-log scale. The variation obeyed Norton's power law relation ($\dot{\varepsilon_s} = A\sigma^n$), where A is a constant and n is the stress exponent. The stress exponent 'n' was found to decrease with increase in temperature. The variations of rupture life (t_r) of the steel with applied stress at different temperatures in double logarithmic plot are shown in Fig. 3.8. The variation obeyed power law relation ($t_r = A'\sigma^{-m}$), where $A'$and m are stress coefficient and stress exponent, respectively. The absolute values of m (relating rupture life with stress) and n (relating steady state creep rate with stress) at a given temperature are close to each other and opposite in nature. This variation suggests that creep deformation and rupture behaviour are controlled by the same mechanism [129].

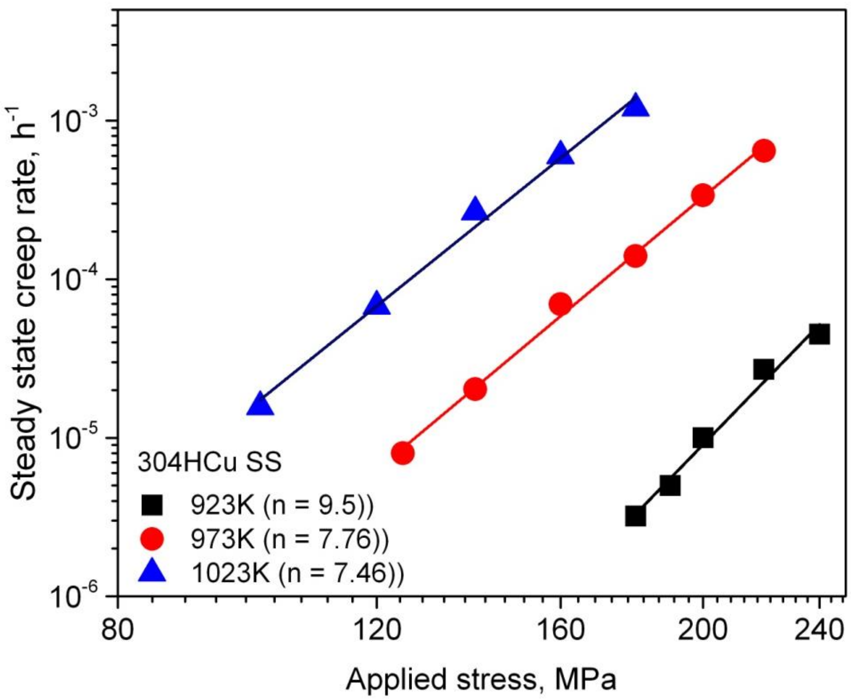

Fig. 3.7 Variation of steady state creep rate with applied stress of the steel at 923, 973 and 1023K

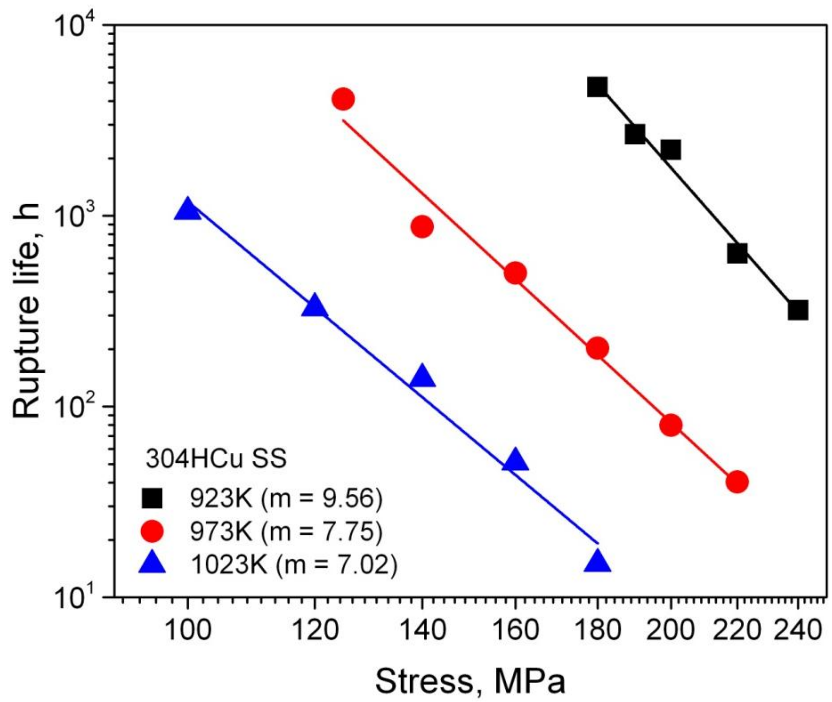

Fig. 3.8 Variation of rupture life with applied stress of the steel at 923, 973 and 1023K

The creep rupture ductility (reduction in area %) is shown in Fig. 3.9. Creep rupture ductility of the steel decreased quite drastically with rupture life. Testing temperature has significant effect on rupture ductility. With increase in test temperature, the ductility of the steel decreased more drastically with rupture life. Reduction in ductility with creep exposure is attributed to the increasing propensity to intergranular creep cavitation with increase in temperature (Fig.3.10) as well as in the increase in hardness of the steel on creep exposure (Fig.3.11).

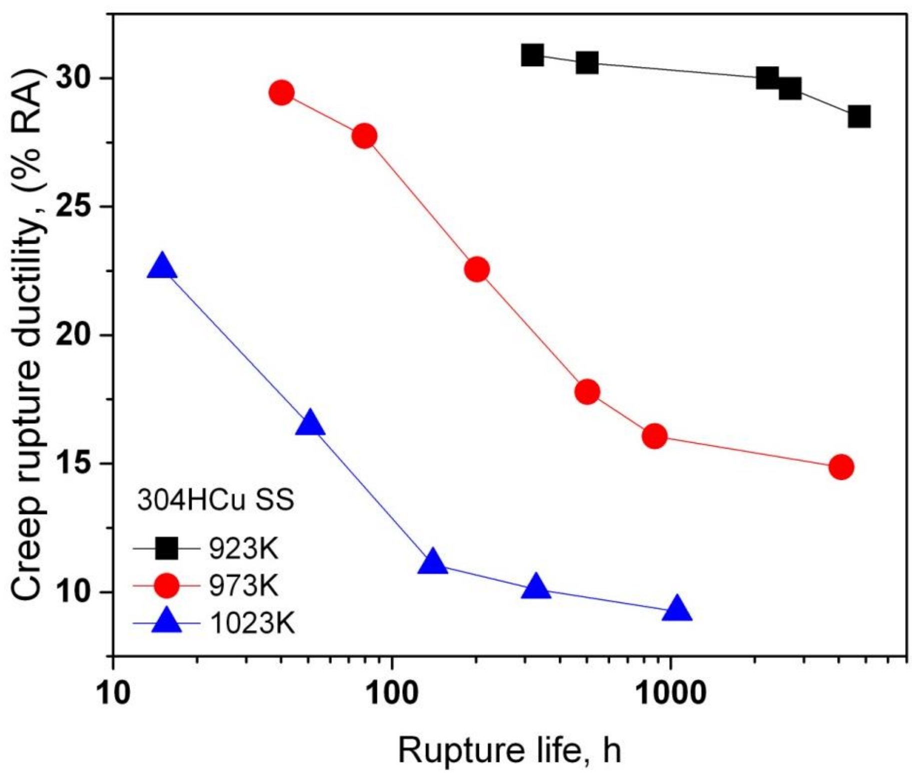

Fig. 3.9 Variation of creep ductility with rupture life of the steel 923, 973 and 1023K.

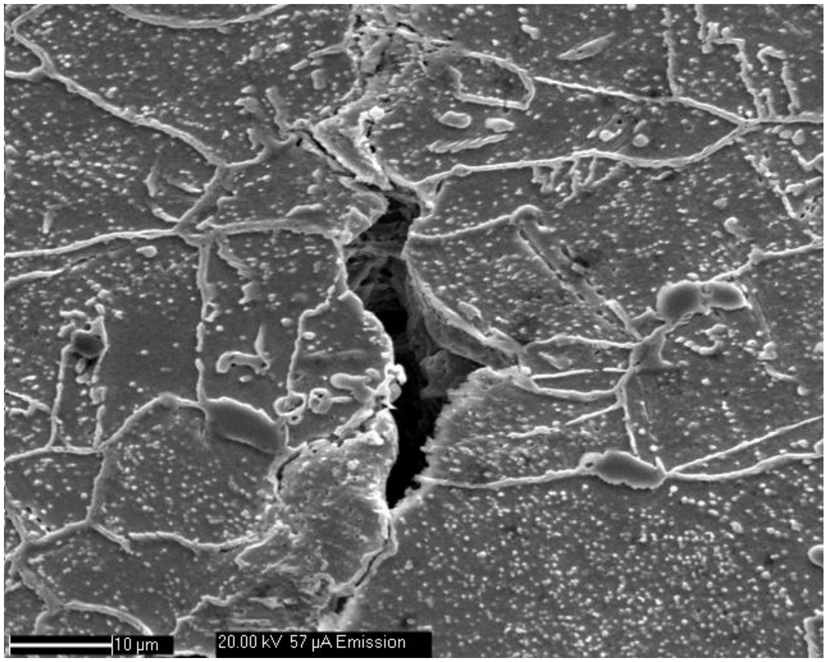

Fig.3.10 Intergranular creep cavitation of the steel creep exposed at 1023 K, 100 MPa.

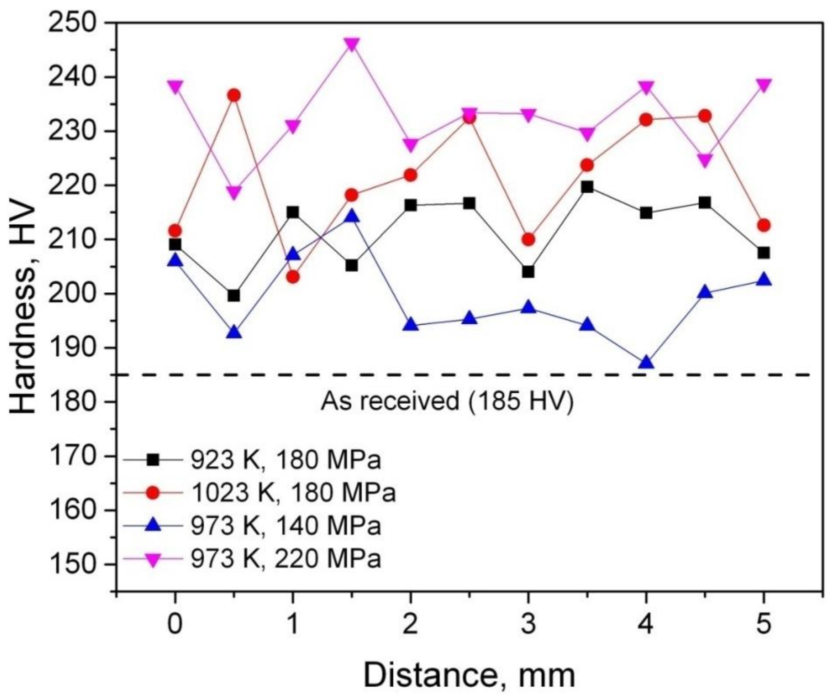

Fig. 3.11 Hardness variation across the gauge length of creep ruptured specimens (much away from fractured zone) tested at different stresses and temperatures.

3.4 Transient creep behaviour

The analysis of transient creep deformation in the framework of the Garofalo relationship, $\varepsilon = \varepsilon_0 + \varepsilon_T[1 - exp(-r'.t)] + \dot{\varepsilon_s}.t$ has been carried out using the procedure illustrated in Section 2.2. The variation of rate of exhaustion of transient creep (r′) with applied stress for different test temperatures is shown in Fig. 3.12 in log-log scale. Power law relationships are observed as in the case of variations of steady state creep rate with stress [Fig. 3.7]. The stress index for the variation of r′ with stress resembles very closely with that of the steady state creep rate with stress [Fig. 3.7] and decreases with increase in test temperature. This indicates the mechanistic resemblance of steady state creep rate and rate of exhaustion of transient creep. In fact, the primary creep leads to the steady state creep deformation with the balance of hardening and recovery [81]. The variation of r' with stress obeying power law relationship has been reported by many investigators [130, 131]. For 70 to 30 α-brass, the stress index for power law variation of r' with stress was 3.5 [130]; whereas for Ni-20%. Cr and Nimonic 80A it was 4.8 and 6.4, respectively [131].

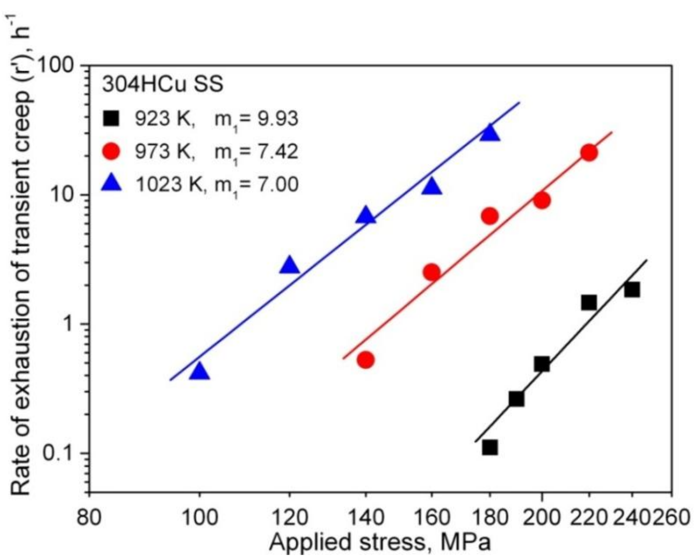

Fig. 3.12 Variations of rate of exhaustion of transient creep r' with the applied stress of the steel at different temperatures.

The variations of rate of exhaustion of transient creep (r′) with time to onset of steady state creep deformation (t_{os}) for different temperatures is shown in Fig. 3.13 in log-log scale. The variation follows a unique power law relationship with exponent close to unity over the temperature range investigated. Vanaja et al. [71] studied the variation of rate of exhaustion with time to reach minimum/steady creep rate for different tungsten containing RAFM steels at 873 K and showed independence of the power law variation on composition of the steels. Similarly, materials such as 70 to 30 α-brass [130], Ni-20%Cr alloy, Nimonic 80A [131] and 304 austenitic stainless steel [132] also show unique variation of r′ with t_{os}. It can be envisaged from the above that for a set of test temperatures as well as for a set of similar kind of materials, if the deformation mechanism does not change appreciably, the parameters (viz. r′ and t_{os}) of transient creep deformation are interrelated.

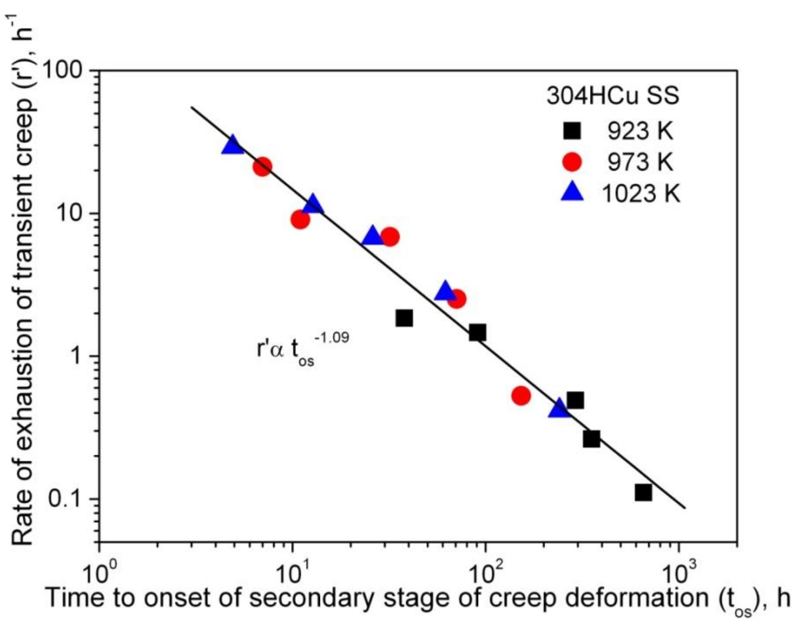

Fig. 3.13 Variations of rate of exhaustion of transient creep r′ with the time to reach steady state creep rate (t_{os}) of the steel at different temperatures.

The variations of rate of exhaustion of transient creep (r′) with steady state creep deformation rate ($\dot{\varepsilon}_s$) for different test temperatures are shown in Fig. 3.14 in log-log scale. A unique power law relationship is found to obey over the investigated temperature range. Similar relationship of independent of temperature has been reported [70] in austenitic stainless steel and Nimonic 80A [131], provided the same deformation mechanisms prevailed. Vanaja et al. [71] has reported a similar unique relation between r′ and $\dot{\varepsilon}_s$ for RAFM steel with different tungsten contents.

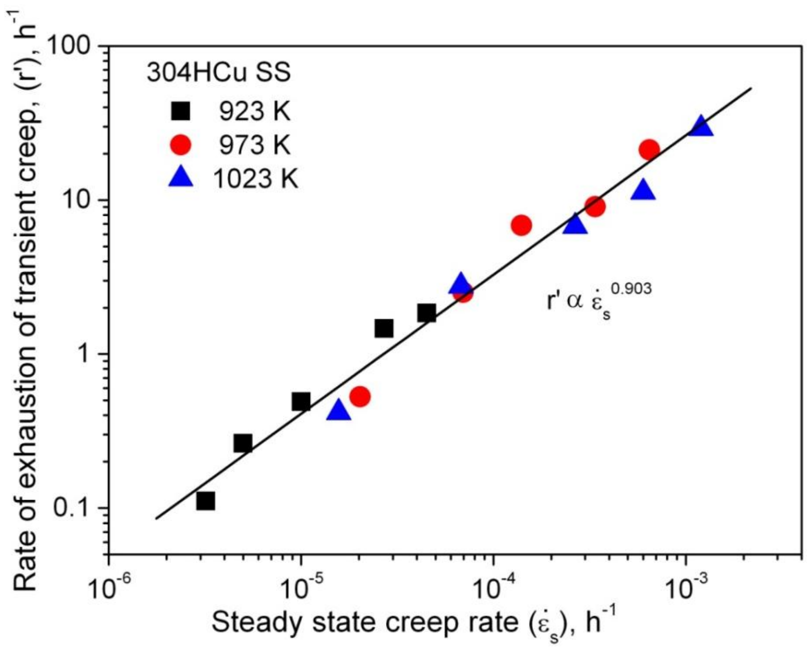

Fig. 3.14 Variations of rate of exhaustion of transient creep r′ with steady state creep rate of the steel at different temperatures.

The relation reveals that creep rate during primary stage of creep deformation (through ($\dot{\varepsilon}_s = {}^{r}/_{h}$), where r is the recovery rate and h is the strain hardening rate [81]) and steady state creep deformation are related to each other as they are controlled by the similar mechanism. This is also confirmed by the relationship of initial creep rate ($\dot{\varepsilon}_i$) with steady state creep rate ($\dot{\varepsilon}_s$). The initial creep rate was calculated from the relation $\dot{\varepsilon}_i$ = r′.ε_T + $\dot{\varepsilon}_s$. The variation of initial creep rate on loading (ε_i) with steady state creep deformation rate ($\dot{\varepsilon}_s$) for different test temperatures is shown in Fig. 3.15 in log-log scale. A unique power law relationship independent of temperature with exponent close to 1.5 is observed.

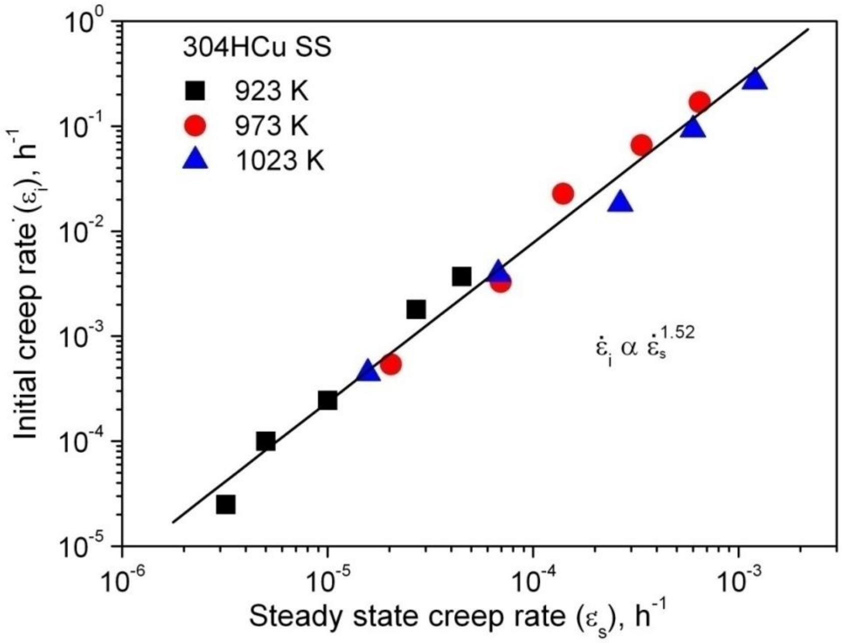

Fig. 3.15 Variation of initial creep rate ($\dot{\varepsilon}_i$) with steady state creep rate ($\dot{\varepsilon}_s$) of the 304HCu SS at different temperatures.

The variation of transient strain (ε_T) with applied stress at different temperatures is shown in Fig.3.16. The transient creep strain increases with stress and attains higher value at higher temperature. The variation of transient creep strain with stress is in consistent with those for 70-30 α-brass [130] and Ni-20% Cr alloy [131]. For RAFM and 9Cr-1Mo steels [71, 129] the transient creep strain decreased with stress; whereas it remains almost constant for many pure metals and simple alloys [81, 133, 134]. The unique relationships of the transient creep parameters with steady state creep rate and the applied stress, facilitates the construction of a master transient creep curve applicable for all the test temperatures and stresses. Figure 3.17 shows such a plot of the variation of $(\varepsilon-\varepsilon_o)/\varepsilon_T$ vs. $(\dot{\varepsilon}_s.t)/\varepsilon_T$, depicting near merger of transient creep portion of the creep curves for all test temperatures and applied stress levels. Such a master curve has been reported for RAFM steels having different percentage of tungsten content [71], for small punch creep of 316LN SS [135] and for 304 SS [132].

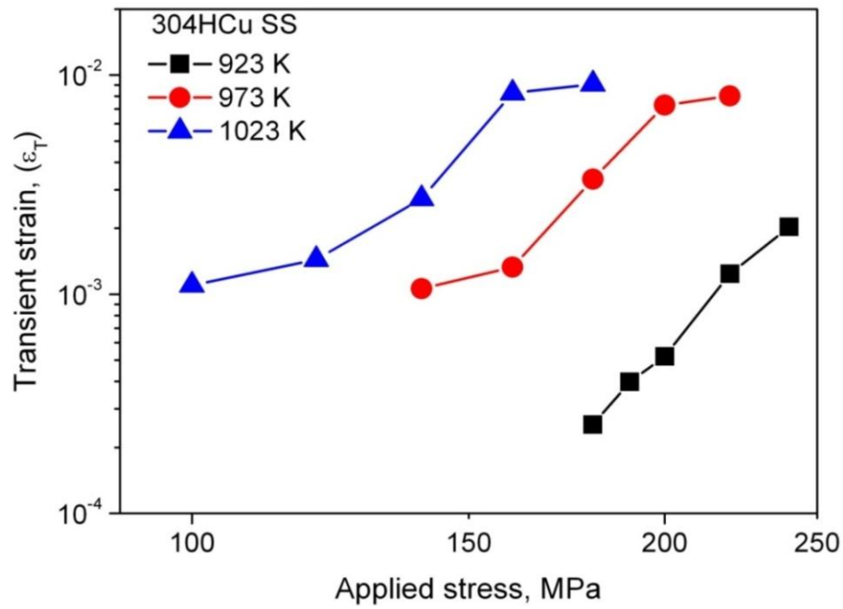

Fig. 3.16 Variation of transient creep strain (ε_T) with applied stress at different temperature of the 304HCu SS

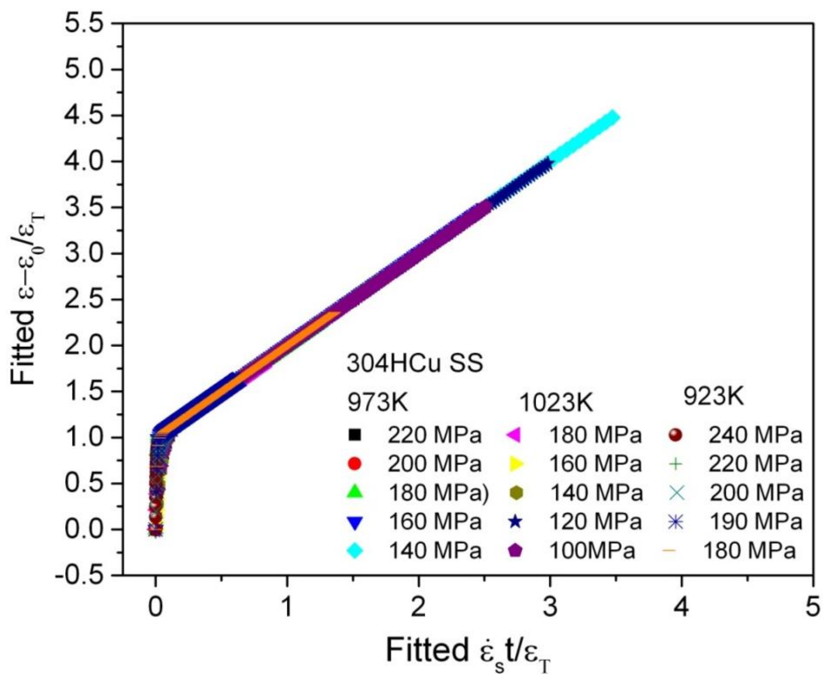

Fig. 3.17 Master transient creep deformation plot of $\frac{\varepsilon-\varepsilon_0}{\varepsilon_T}$ vs $\frac{\dot{\varepsilon}_s t}{\varepsilon_T}$.

The basis of such master curve has been illustrated in detail by Phaniraj et al. [132] wherein it stated that that if transient creep strain (ε_T) is constant over the test temperature and stress range then a plot of (ε-ε_o) with ($\dot{\varepsilon_s}$.t) would lead to a master curve. However, such a plot is shown in Fig. 3.18, indicating failure to have a master curve, probably due to non-constant nature of 'ε_T' with stress (Fig.3.16). It therefore becomes necessary to normalize both the axis with ε_T to develop the master curve [Fig. 3.17] for transient creep behaviour of the 304HCu SS at all temperatures and stresses investigated.

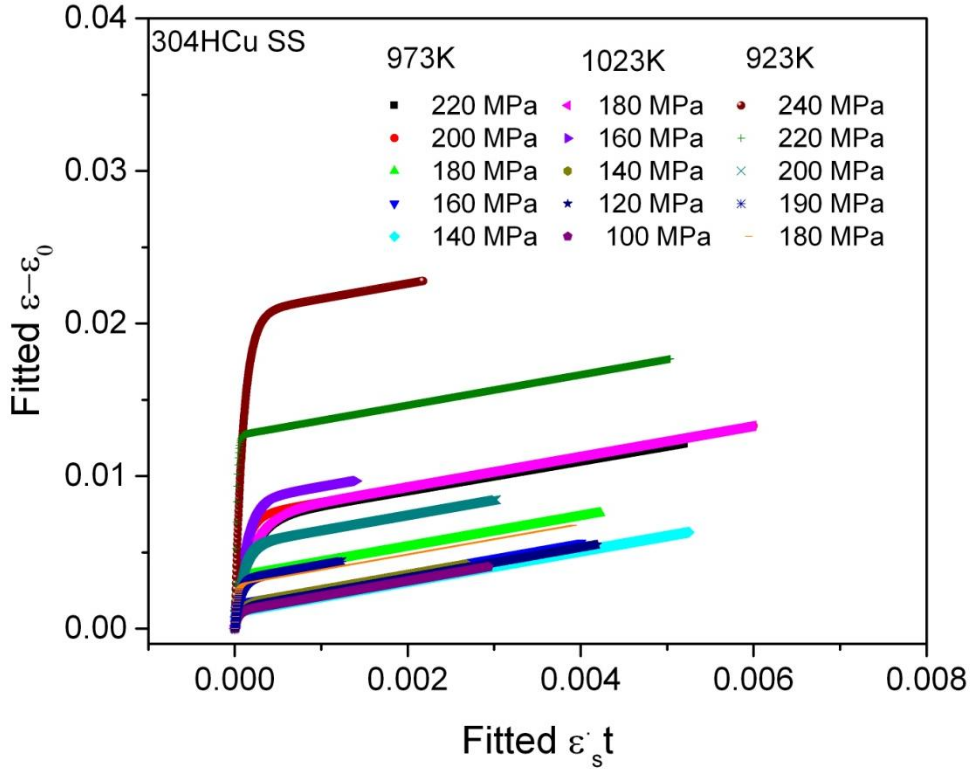

Fig. 3.18 Master transient creep deformation plot of $\varepsilon - \varepsilon_0$ vs $\dot{\varepsilon}_s t$ for the 304HCu SS at different temperatures and stresses.

3.5 Steady state creep deformation

The Norton's power law relation between steady state creep rate ($\dot{\varepsilon}_s$) and applied stress (σ_a) considering the temperature variation is expressed as $\dot{\varepsilon}_s = \frac{AD\mu b}{(kT)\left(\sigma_a/_\mu\right)^n}$, with D =

$D_o\exp(-Q_c/RT)$, where D is the self-diffusion coefficient, D_o is the frequency factor, Q_c is the activation energy for creep deformation, R is gas constant (8.314 J mol^{-1} K^{-1}), T is temperature in Kelvin, $\mu$is the shear modulus, b is the Burgers vector, k is Boltzmann's constant, n is the stress exponent and A is a dimensionless constant. The stress exponent 'n' was found to decrease with increase in temperature [Fig. 3.7]. In general, the decrease in 'n' value with increase in temperature suggests the change in creep deformation mechanism. Classically, dislocation creep results in 'n' value of 4 or 5, whereas 1 for diffusional creep. However, such change in deformation mechanism is not expected under the presently investigated stress and temperature ranges. In dispersion/precipitation hardened engineering alloys, the value of 'n' is reported to be substantially higher than those of pure metals or single phase alloys [70, 136, 137]. Such higher values of 'n' in precipitation-hardened alloys could not be interpreted in terms of conventional creep theories. It has been proposed that the creep deformation of precipitation hardened alloys can be rationalized by conventional dislocation creep theories by expressing creep rate in terms of the effective stress i.e. difference of the applied stress (σ_a) and the resisting stress (σ_R), ($\sigma_a - \sigma_R$) instead of applied stress alone [138]. The resisting stress is associated with the operation of particle by-pass mechanism of dislocation for creep deformation [138]. On this basis, the dependence of creep rate with stress and temperature takes the form $\dot{\varepsilon_s} = (\frac{A_0 D\mu b}{kT})((\sigma_a - \sigma_R)/\mu))^p$, with 'p' having a constant value of around 4 over the entire stress and temperature regime where dislocation creep is the rate controlling creep deformation mechanism. However, in view of the experimental difficulties for evaluation of σ_R values, Lagneborg and Bergman [65] proposed a graphical method to estimate the resisting stress $\sigma_R$by plotting ($\dot{\varepsilon_s}$kT/Dμb) $^{1/4}$ against applied stress σ_a. The resisting stress σ_R was obtained as the stress intercept by extrapolating the straight-line plot to zero-creep rate. Figure 3.19

shows such a plot of $(\dot{\varepsilon_s}kT/D\mu b)^{1/4}$ against σ_a/μ, where reported values of D, μ and b of 304 SS were used [139]. The σ_R values are determined from the plot at the stress intercepts where $\dot{\varepsilon_s}$=0 and found to be 59.7 MPa, 80.1 MPa and 113.2 MPa, respectively at 923, 973 and 1023 K. Figure 3.20 shows the variation of normalized creep rate, $(\dot{\varepsilon_s}kT/D\mu b)$, with normalized effective stress, the unique variation$(\sigma_a - \sigma_R)/\mu$, showing the validation of the concept of back stress in describing the creep deformation in 304HCu steel.

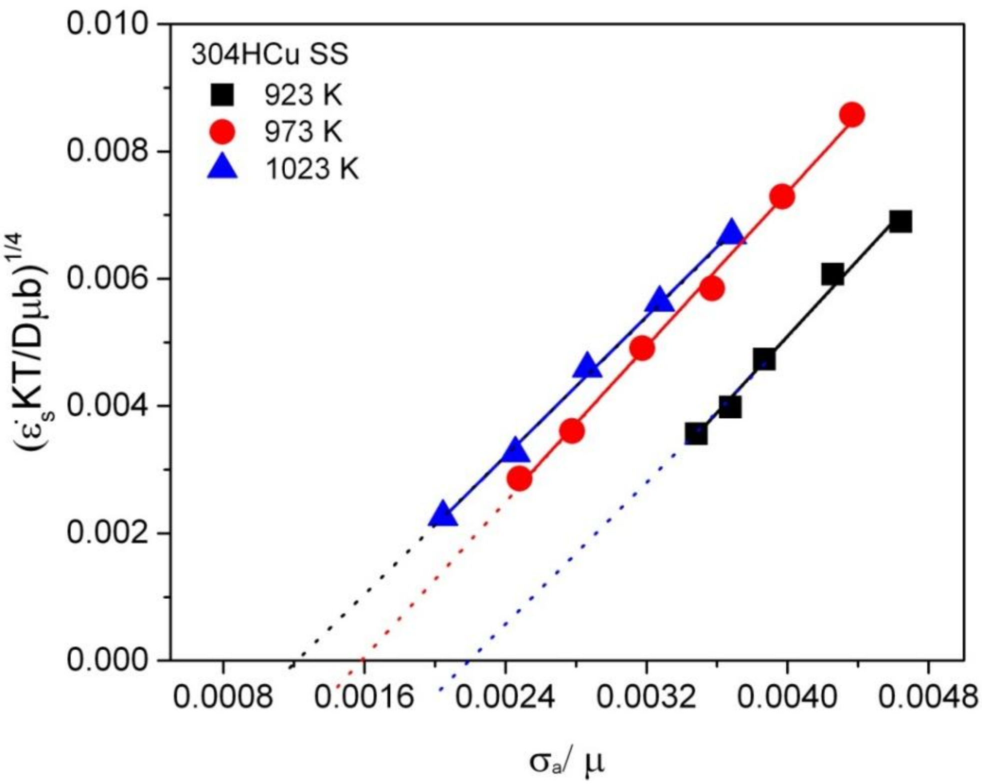

Fig. 3.19 The variation of $(\dot{\varepsilon_s}kT/D\mu b)^{1/4}$ against applied stress (σ_a/μ) of 304HCu SS at different temperature and stresses

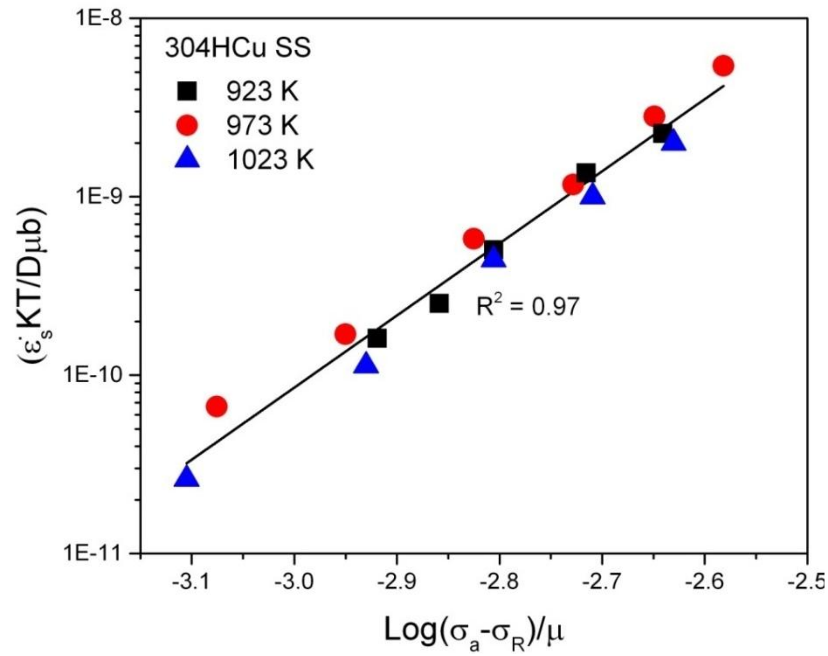

Fig. 3.20 The variation of diffusivity compensated creep rate with normalised effected stress on log-log scale following method suggested by Lagneborg and Bergman [65] of the 304HCu SS at different temperatures

To avoid such complexity, Wilshire and Scharning [140] have proposed an empirical relation between creep rate and stress on normalizing the stress with ultimate tensile strength and expressing creep rate as $\dot{\varepsilon}_s$exp (Q_c/RT), where Q_c is the activation energy for self-diffusion. The method has been successfully used to develop 'master curves' between stress and creep rate for different tempered martensitic steels to predict the creep rate at lower applied stress [70, 132]. The same is also applied for the data in the present study and Figure 3.21 shows the dependence of temperature-compensated minimum creep rate with applied stress normalized by ultimate tensile strength for the steel, illustrating the applicability of the unique relation for 304HCu steel. Fig. 3.21 shows a two slope behaviour i.e. a linear regime between temperature compensated creep rate and normalized stress and a nonlinear regime where sudden increase in temperature compensated creep rate with normalized stress was observed. This is because; at lower stress (applied stress is less than yield stress) temperature assisted diffusion creep predominant over dislocation creep and material is more prone to intergranular creep cavitation failure. Under this stress level, temperature compensated creep rate follows a linear region with normalized stress. At higher stress plasticity induced ductile failure predominates in addition to creep cavitation failure. At higher stress, both temperature and stress increases the creep rate significantly and makes temperature compensated creep rate increase to sudden higher value compared to its lower stress level. This procedure has been reported to produce good life management of power plant components made of ferritic steels with continuously evolving microstructure on service exposure [141].

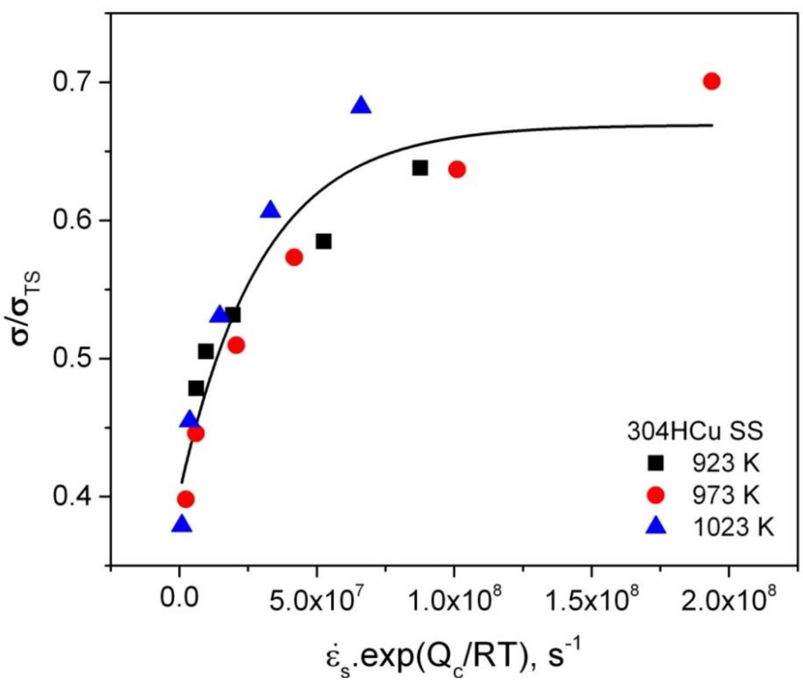

Fig. 3.21 The variation of (σ/σ_{UTS}) with temperature-compensated creep rate of the 304HCu SS at different temperatures.

3.6 Tertiary creep and damage

Following the steady state creep deformation, extended tertiary stage of creep deformation is observed in the present material before the failure (Fig. 3.4). Rupture life possess the signatures of steady state creep rate as well as tertiary stage. It is evident that the processes are inter-related. The variation of rupture life (t_r) with steady state creep rate ($\dot{\varepsilon_s}$) can be correlated through Monkman-Grant relationship ($\dot{\varepsilon}_s^{\alpha} t_r = C$), where α is a constant close to unity and C is the Monkman-Grant constant [142]. The applicability of Monkman-Grant relationship for the present steel is shown in Fig. 3.22. A unique relationship in log-log scale independent of temperature was obtained. The values of α and C were found to be 1.01 and 0.024, respectively. Low value of constant 'C' indicates limited contribution of transient primary creep to the overall creep strain and predominance of creep strain accumulation during the tertiary stage of creep deformation [143].

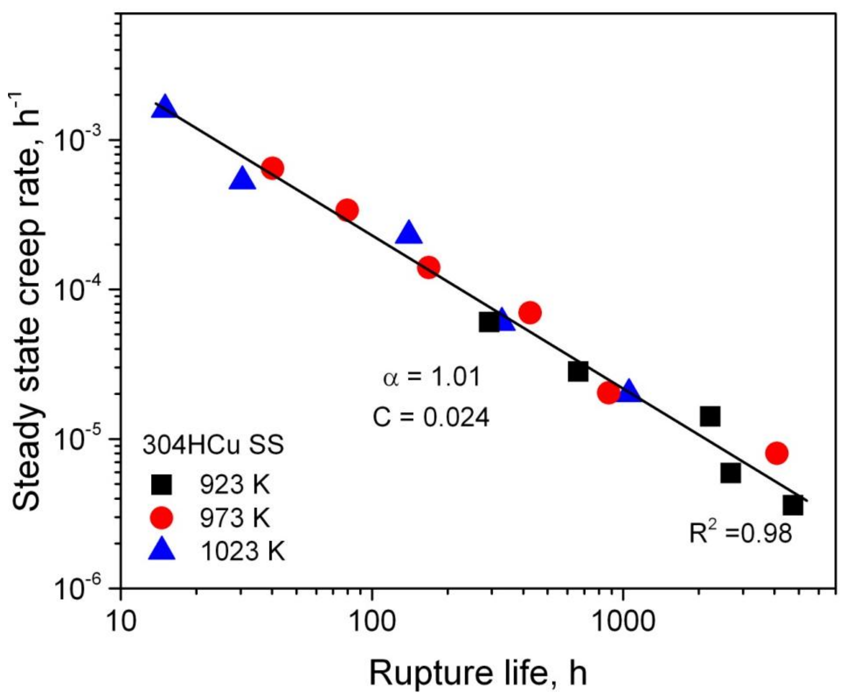

Fig. 3.22 Variation of steady state creep rate with rupture life of 304HCu SS at different temperatures obeying Monkman's grant relationship.

The time to onset of tertiary stage of creep deformation (t_{ot}) was measured as the time at which the creep rate started increasing from secondary stage of creep deformation. It is a useful and important design parameter for creep analysis. The variation of 't_{ot}' with rupture life

't_r' is shown in Fig. 3.23, which follows a unique linear relationship ($t_{ot} = f.t_r$) irrespective of temperature. The value of constant 'f' was around 0.39. This indicates that the tertiary creep of 304HCu SS occupies about 61 percentage of its total life. This type of tertiary creep behaviour in 304HCu SS is quite evident as this material has higher strength with limited ductility than conventional 18Cr-8Ni steel. Early onset of tertiary stage of creep deformation in the precipitation hardened 304HCu steel can be related to the coarsening of the precipitate, intergranular creep cavitation apart from the increase in stress due to decrease in specimen diameter on creep exposure of the 'constant load' creep test and also due to the oxidation.

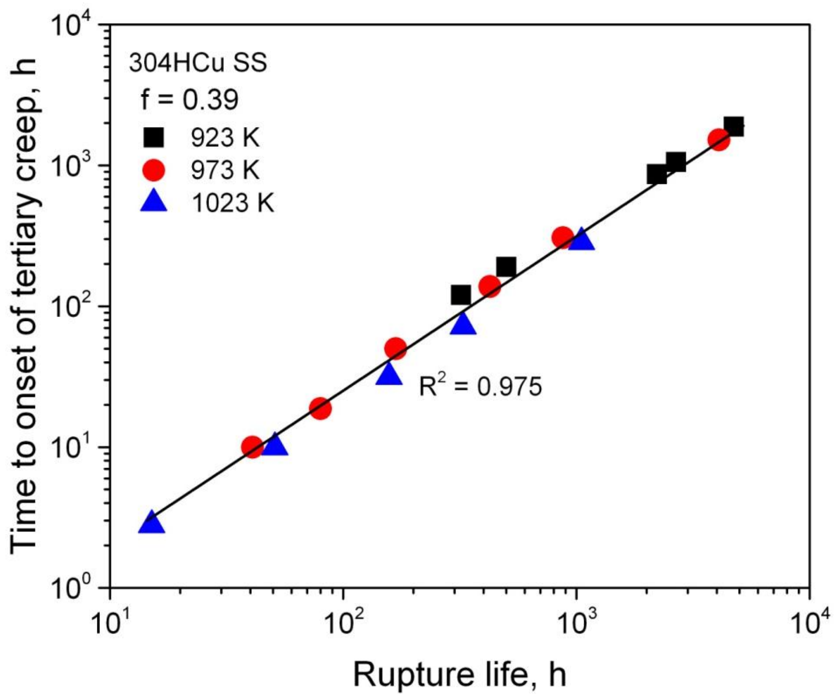

Fig. 3.23 Variation of time to onset of tertiary stage of creep deformation with rupture life of the 304HCu SS at different temperatures.

The creep damage can be assessed by continuum damage mechanics (CDM) approach. An indication of damage process initiating tertiary creep is provided by the creep damage tolerance factor (λ) which is defined as the ratio of strain to failure (ε_f) to the steady state creep rate ($\dot{\varepsilon}_s$) and rupture life (t_r) [144, 145] as given below.

$$\lambda = \frac{\varepsilon_f}{\dot{\varepsilon}_s . t_r} \qquad (3.1)$$

Individual damage mechanism acting alone can result in a characteristics shape of the creep curve and a corresponding value of λ. It has been predicted that for values of λ between 1.5 and 2.5, the tertiary stage of creep deformation is due to nucleation and growth of intergranular creep cavities by diffusive transfer of atoms from cavity surface on to the grain boundary due to the stress gradient between the cavitated and uncavitated grain boundary area.

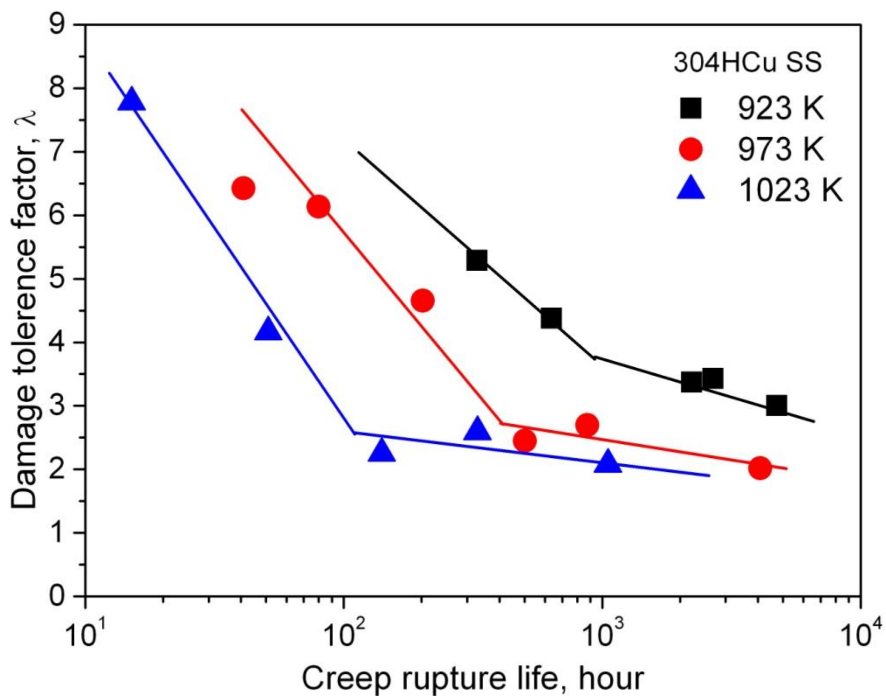

Fig. 3.24 Variation of damage tolerance factor with rupture life of 304HCu SS at different temperatures.

Further, if the value of λ exceeds 4 then it is attributed to the microstructural degradation on creep exposure [145]. In the present steel, the value of λ is found to decrease with increase in rupture life and trends to around 2 on longer creep exposure, which occurs early with increase in test temperature [Fig. 3.24]. The high value of λ indicates coarsening of precipitates and dislocation cell formation [146]. The decrease in value of λ indicates the tendency towards intergranular creep cavitation failure, particularly on long term creep exposure. SEM fractographic investigation clearly reveals the transition from predominantly transgranular dimple ductile failure to intergranular creep failure with the increase in creep rupture life (Fig. 3.25). The transition occurred at all the test temperatures with the early onset of transition at higher temperature as predicted by the damage tolerance factor [Fig. 3.24]. Extensive intergranular creep cavitation [Fig. 3.25(b)] was observed in the steel especially at higher temperature for relatively longer creep exposure. Though, the intergranular fracture is not clearly evident from the SEM fractograph in Fig. 3.25(b) due to severe oxidation, the nucleation of cavities associated with grain boundary particles and their coalescence leading to the formation of intergranular microcracks can be clearly observed from the SEM image in Fig. 3.10. In contrast, large density of intragranular cavities manifested in the form of dimples is noticed in Fig. 3.25(a) corresponding to the creep damage with high $\lambda > 4$. In 347 SS, the details of creep cavitation role of grain boundary sliding and microalloying with boron and cerium in controlling the creep cavitation have been investigated in details by Laha et al. [13, 123] in an effort to develop creep cavity resistance steel for enhancing creep rupture life. In fact, one reason for enhanced creep cavitation with increase in rupture life might be due to the increase in strength of the matrix on enhanced precipitation (reflected in increase in hardness on creep exposure (Fig. 3.11) on creep exposure. This results in inadequate accommodation of stress around the grain boundary irregularities such as grain boundary triple points, precipitates, ledges etc. due to by grain boundary sliding.

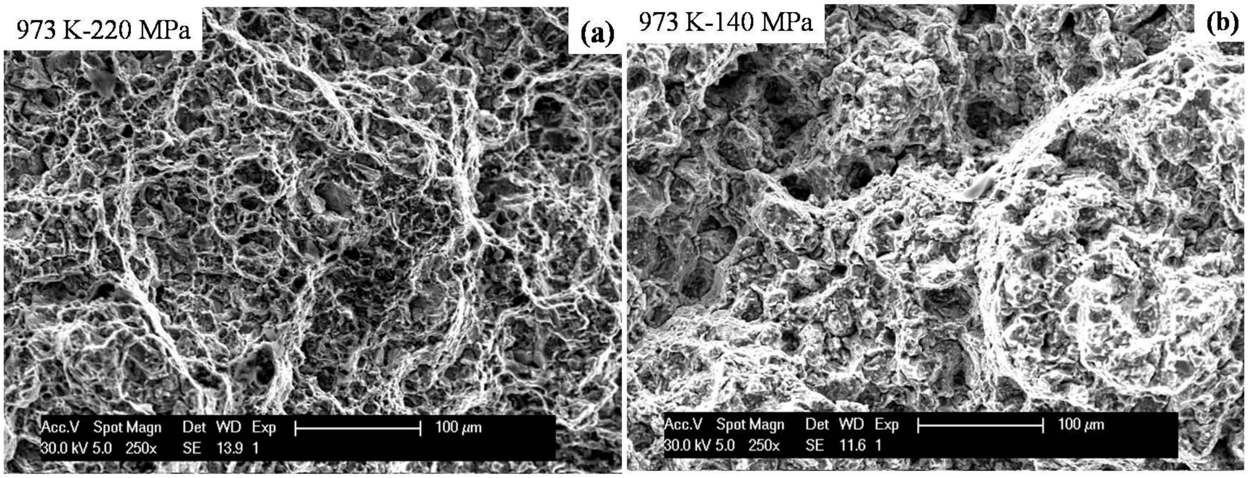

Fig. 3.25 SEM fractography, showing change in fracture mode from (a) ductile fracture with dimple appearance to (b) intergranular creep cavitation with increases in rupture life.

3.7 Microstructural investigation after creep failure

Precipitation in the steel on thermal and creep exposure, which immensely affect the creep deformation and fracture behaviour, has been reported in several studies [13, 123, 124, 147]. Extensive precipitation of intergranular chromium rich $M_{23}C_6$ and transgranular Nb(C,N) and Cu-particle has been reported. Extensive grain boundary precipitation on creep exposure is observed (Fig. 3.26). It shows that grain boundary triple points are extensively decorated with elongated $M_{23}C_6$ carbides where size of precipates have been increased significantly at 1023 K, 140 MPa.

Figure 3.27 shows TEM micrographs of the steel creep tested at 1023 K under stress of 100 MPa (t_r=1053) and 160 MPa (t_r=51 hours) respectively, showing extensive precipitation of Nb(C,N) carbides as well as Cu-rich particles (with white contrast).

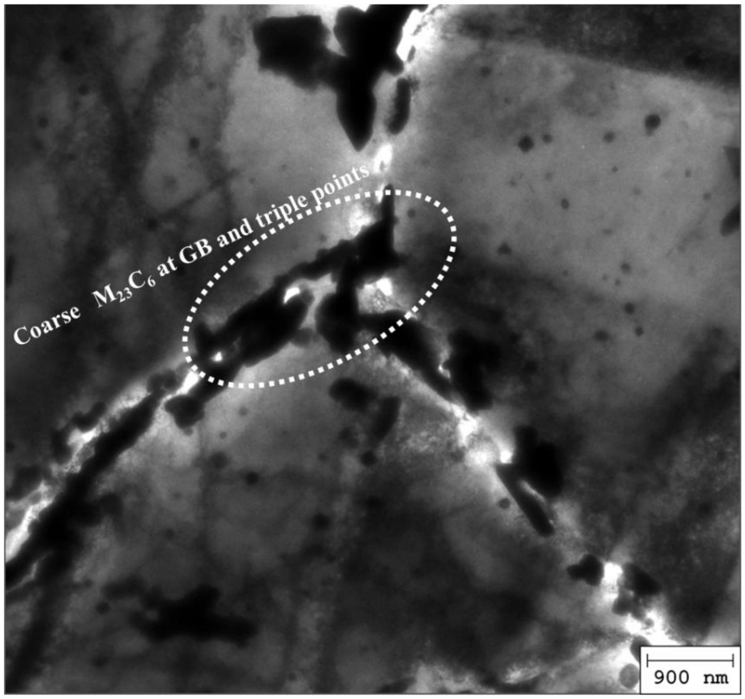

Fig. 3.26 TEM microstructure of 304HCu SS creep tested at 1023 K, 140 MPa showing extensive grain boundary precipitation

It must be noticed that these second phase particles strongly pin the dislocations restricting them from forming dislocation tangles, well defined cell dislocation structures and recovery type of structures (such as dislocation sub-grains) [Fig. 3.27(b)]. These types of structures though enhance the strength but generate strong strength gradients between the grain and grain boundary, thereby increasing the tendency of the latter to intergranular damage, particularly upon prolonged exposures. The average diameter of the Cu-rich particles are only about 23 nm [Fig. 3.27(a)] and 20 nm [Fig. 3.27(b)] for the rupture lives of 1053 and 51 hours tests at 1023 K, respectively, thereby indicating an insignificant increase in size of Cu-particles under these conditions. The $M_{23}C_6$ carbide precipitates at grain boundary which retards the grain boundary sliding and in doing so results in decohesion of particle-matrix at grain boundary interfaces and results in stress concentration build-up that could either cause cavity or crack depending upon the stress level and temperature. The coarse $M_{23}C_6$ carbide acts as a stress raiser at the grain boundary due to its high hardness and less coherent. The dislocation pile up against this hard particle builds up stress concentration at the interface between matrix and precipitate and acts a preferable site for cavity nucleation at higher stresses.

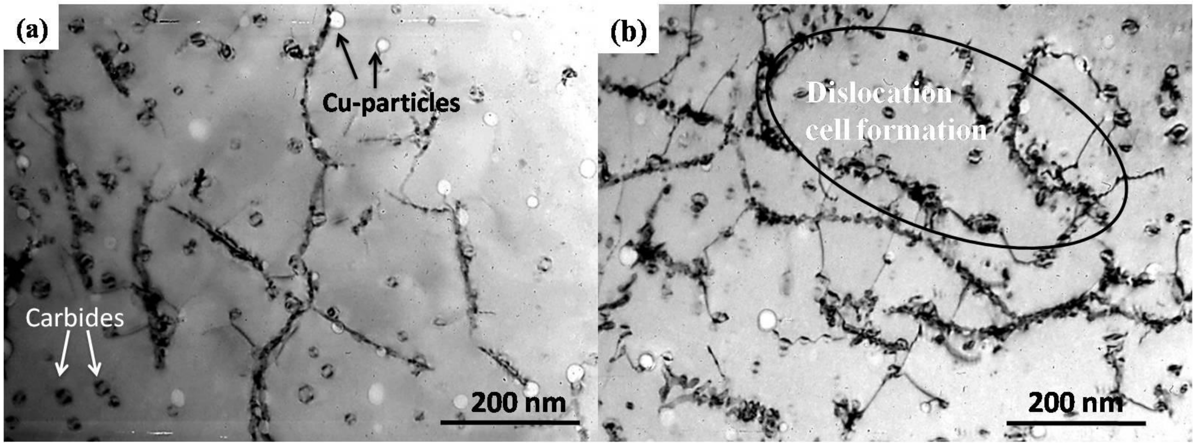

Fig. 3.27 TEM microstructure of 304HCu SS creep tested at (a) 100 MPa (t_r=1053 hours) and (b) 160 MPa (t_r=51 hours), showing Cu-particle, decorating dislocation and enhance precipitation with increase in creep exposure.

Ping Ou et al. [128] reported the average particle diameter of the Copper as 34 nm when aged at 923 K for 5000 h. The rate of growth of Cu-rich particle is thus rather slow signifying the stable microstructure in 304HCu SS at elevated temperatures. Since the Cu-rich particles are coherent with the austenite matrix, the energy of the interface between Cu-rich particles and austenite matrix could be insufficient to cause rapid growth rate of Cu-rich precipitates. Further, Ping Ou et al. predicted the coarsening of Cu-rich particles through LSW theory and reported that the coarsening of Cu-rich particle is mainly due to the volume diffusion of the Cu-atoms in the austenite matrix [148]. These second phase particles in the grain retards the motion of dislocations to reduce the creep deformation rate, thereby leading to the decoration of dislocations with particles, as a fore mentioned. The combined distribution of $M_{23}C_6$ and Nb(C, N) particle number density and its size with creep exposure is shown in Fig. 3.28, revealing the increased precipitation on creep exposure. It is apparent that the coarsening and number of particles (intergranular and intragranular) didn't change significantly under these conditions which show the stability of the material under long term exposure. The observed increase in hardness of the steel (Fig. 3.11) is due to this enhanced precipitation on creep exposure.

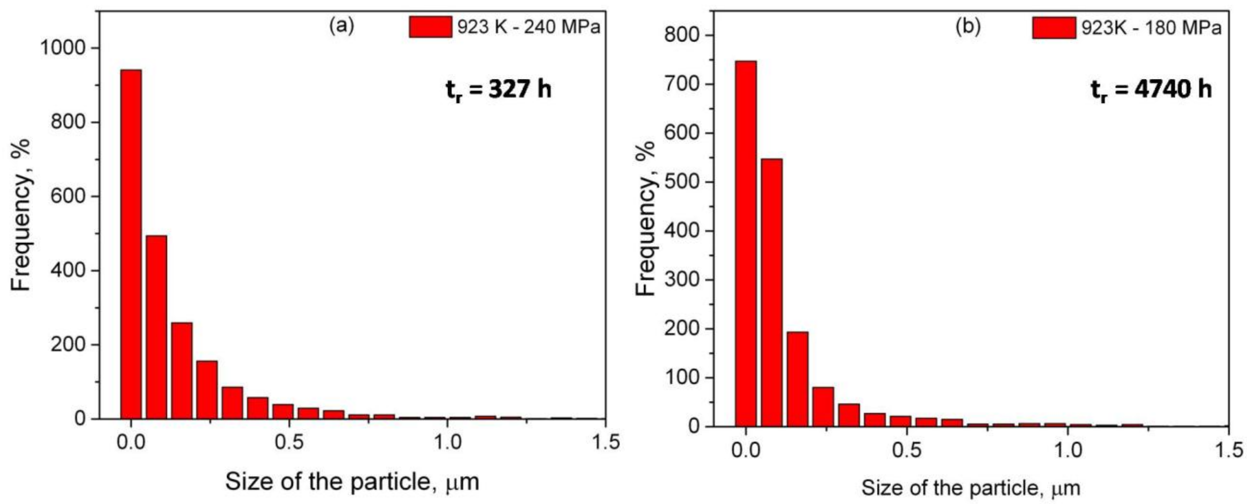

Fig. 3.28 Particle size distribution for precipitates in the steel at different creep exposure at 923 K.

3.8 Creep rupture life prediction based on FE-CDM

FE analysis coupled with continuum damage mechanics (FE-CDM) has been extensively used for the prediction of creep damage and rupture life of the materials. The creep damage can be assessed by continuum damage mechanics (CDM) approach. The CDM model proposed by Kachanov [35] coupled with FE-analysis has been used, in the present study, to predict the deformation and damage behaviour of the 304HCu SS. The governing equation used for calculating creep strain and damage rates from creep data are [149]:

$$\dot{\varepsilon}_s = A\left(\frac{\sigma}{1-\omega}\right)^n \qquad (3.2)$$

and

$$\dot{\omega} = \frac{B\sigma^{\chi}}{(1-\omega)^{\varphi}} \qquad (3.3)$$

where, $\dot{\varepsilon}_s$ is the steady state creep rate, A and n are Norton's law ($\dot{\varepsilon}_s = A\sigma^n$) coefficients, B, φ and χ are coefficients of the stress-rupture life plot, and ω and $\dot{\omega}$ are damage and damage rate respectively. The details of parameter evaluation and their physical significance have been discussed by Goyal et al. [149] and in section 1.8.1.1. The equation used for calculating creep strain based on the CDM model is given below:

$$\varepsilon_c = \frac{A\sigma^{(n-\chi)}}{B(n-\varphi-1)}\left\{[1 - B(1+\varphi)\sigma^{\chi}t]^{\frac{\varphi+1-n}{\varphi+1}} - 1\right\} \quad (3.4)$$

The Eq. (5) has been used to predict the creep deformation at different temperatures. FE analysis coupled with continuum damage mechanics (FE-CDM) has been extensively used for the prediction of creep damage and rupture life of the materials. FE analysis of creep damage was carried out by incorporating the creep rate equation (Eq. 3) creep damage law (Eq. 4). The value of χ was obtained from the slope of log-log plot of rupture life and stress and the intersection with X-axis (rupture life) provided the value of $B(1+\phi)$. The values of B and ϕ were obtained by trial and error for minimum deviation in predicting the creep strain and rupture life as compared to experimental creep data [149]. The calculations were carried out at all the temperatures of investigation. The values of material constants used in the analysis are given in Table 2. The FE analysis is conducted on the creep specimen geometry shown in Fig. 3.29.

Table:3.2 Elastic, creep and damage constants of steel at 923, 973 and 1023K.

304HCu SS	E/G Pa	γ	A	n	χ	φ	B
923K	137.5	0.3	8.71×10^{-28}	9.57	9.55	8.5	2.01×10^{-27}
973K	134.0	0.3	1.32×10^{-21}	7.56	7.05	4.9	2.34×10^{-19}
1023K	130.0	0.3	2.04×10^{-20}	7.46	7.02	3.9	2.82×10^{-19}

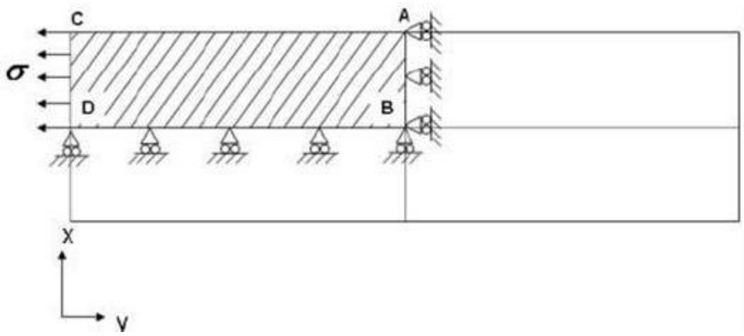

Fig. 3.29 Boundary conditions for finite element analysis of creep deformation.

The nodes along line AB were restrained in Y-direction and nodes along BD were restrained in X–direction. Uniform stress was applied on line CD. The analysis was carried out considering elastic-creep behaviour of the steel. The steel was assumed to deform elastically during initial loading followed by creep deformation. Tensile tests were carried out on the steel and the Table-3 shows the tensile properties of the steel at the selected temperatures of relevance to finite element analysis of creep deformation and damage. The coupled rate equations for creep strain and damage were solved and the increment of creep strain and damage was calculated and at the end of increment these variables were updated. It may be noted that the primary part of creep deformation is ignored in calculating the creep damage evolution with time. The comparison of estimated creep curve from FE-CDM and experimental creep curves for 304HCu SS creep tested at 923, 973 and 1023 K are shown in Fig. 3.30. The predicted creep curves are found to be in good agreement with experimental ones. The comparison between the experimental and predicted creep rupture life are shown in Fig. 3.31. The predicted creep rupture lives were found to be in good agreement with the experimental ones at all the stress levels and follows a narrow scatter band with a factor of 1.4. The damage evolution of the steel at 180 MPa (the only common stress for all the three temperature) for 923, 973 and 1023 K was shown in Fig. 3.32. The creep exposure has been normalized with creep rupture life at 180 MPa. The creep damage was found to be in increasing order with temperature as observed experimentally. The higher extent of damage at 1023 K, 180 MPa is due to the increased precipitation and more propensity of dislocation cell formation [Fig. 3.27(a, b)] and creep cavitations.

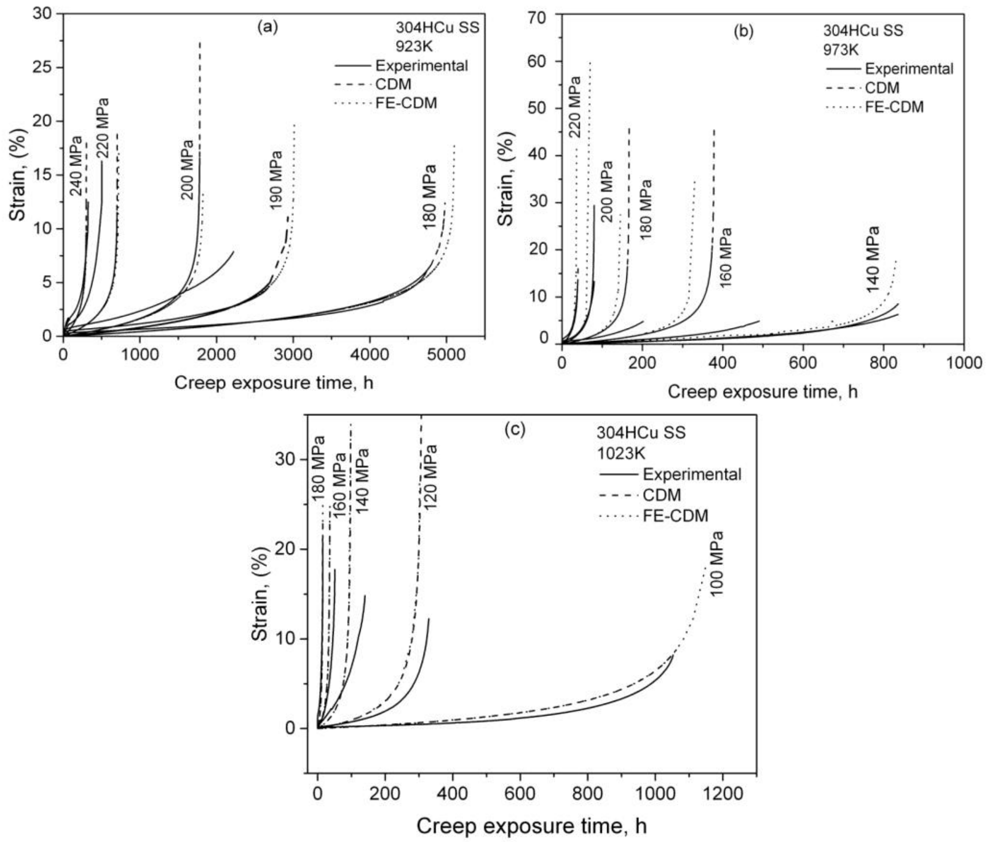

Fig. 3.30 Creep curve prediction with CDM and FE-CDM in comparison to experimental at different stress levels and temperatures (a) 923 K, (b) 973 K and (c) 1023 K.

In the present investigation creep tests were carried out for relatively short duration. However, during long term creep exposure microstructural changes such as coarsening of $M_{23}C_6$, MX and Cu nano-particles along with precipitation of new phases could occur. The formation of M_6C, Z-phase, χ-phase and σ-phase also prevails under long term creep exposure. Long term life prediction from CDM approach could be appropriate if change in dislocation density, phase change, formation of new precipitates and the coarsening are also considered

[150]. Therefore, in order to incorporate the microstructural degradation, the parameters considering decrease in dislocation density, coarsening of precipitates and nucleation and growth of new phases could be included in the CDM for better estimation of creep rupture life for long duration exposure.

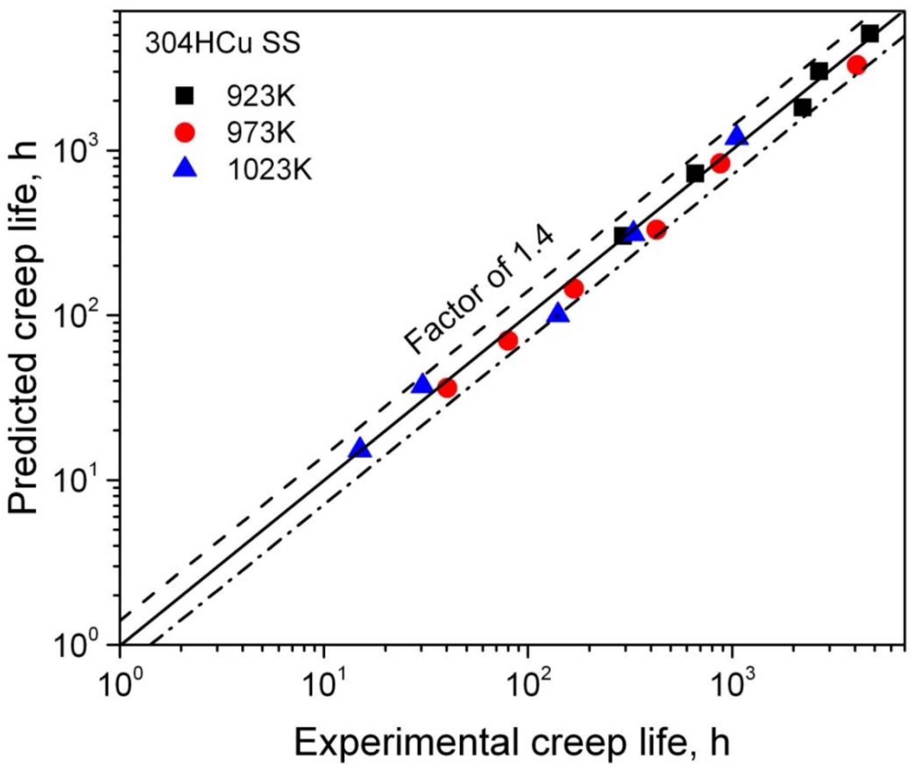

Fig. 3.31CDM-FE prediction of creep rupture life of smooth specimen at various applied stress and temperatures.

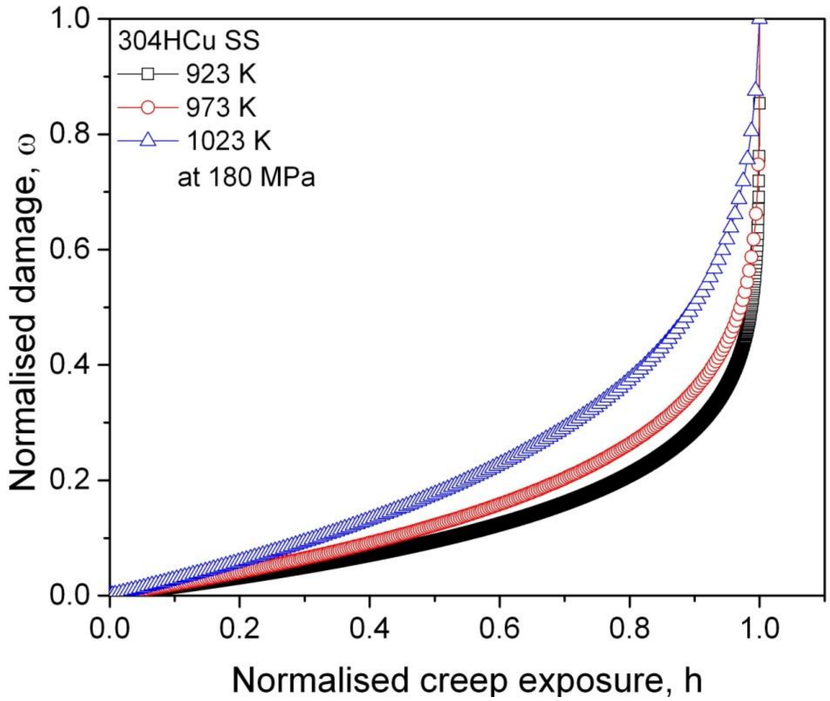

Fig. 3.32 Comparison of damage evolution as a function of creep exposure in steel of 923, 973 and 1023K as estimated by FE-CDM analysis.

3.9 Conclusions

Creep deformationand rupture behavior of 304HCu SS is presented at temperatures 923, 973, 1023 K over the stress range of 100-240 MPa. The transient and steady state creep is analyzed using Garofalo equation and Dorn's equation (with back stress), respectively. The tertiary creep, that occupied about 61% of the creep life, is modelled using Kachanov-Rabotnov CDM model coupled with finite element analysis. The following observations have been drawn from the present study.

1. The creep deformation of 304HCu SS is characterized by short primary stage followed by secondary creep and relatively extensive tertiary stage of creep deformation.

2. Transient creep described in the framework of Garofalo relationship enabled the generation of master transient creep curves obeying the first order reaction rate theory. This is attributed to the power law relationship between i) r'vs $\dot{\varepsilon}_s$, ii) r'vs t_{os} and iii) initial creep rate vs$\dot{\varepsilon}_s$, with exponents close to unity.

3. The stress and temperature dependence of steady state creep rate is successfully rationalized by invoking the concept of back stress. The back stress calculated from the Lagneborg and Bergman graphical method is found to be 59.7 MPa, 80.1 MPa and 113.2 MPa, respectively at 923, 973 and 1023 K.

4. Increase in temperature and decrease in stress level enhanced the tendency of 304HCu SS to intergranular damage accompained by a decrease in creep damage tolerance factor $\left(\lambda = \frac{\varepsilon_f}{\dot{\varepsilon}_s \cdot t_r}\right)$ and is in line with the microstructural observations.

5. The particle size distribution of the both intergranular and intragranular carbides and negligible change in size of the Cu-particles (from TEM observation) in the creep tested samples suggest the stability of the material for relatively long creep exposures.

6. The creep deformation and damage assessment of the steel made using Kachanov-Rabotnov CDM model, coupled with finite element analysis, could predict well the creep deformation behavior. The predicted creep rupture life lies within a factor of 1.4.

Chapter: 4

EFFECT OF NOTCH SHARPNESS ON CREEP DEFORMATION, DAMAGE AND RUPTURE LIFE

4.1 Introduction

In the last chapter, the uniaxial creep deformation behaviour of 304HCu SS along with microstructural characterization and rupture life estimation by FE-CDM analysis has been presented on carrying out creep tests at 923, 973 and 1023 K. In the present chapter, the multiaxial creep rupture behaviour of the material has been studied in the presence of circumferential U-notch in the smooth specimen with root radius varying from 0.25-5 mm at 923, 973and 1023 K over a wide range of stress. Further, FE-analysis has been carried out at the notch throat plane to study the influence of notch on creep rupture strength compared to plain specimen through different components of multiaxial state of stress. Detailed finite element analysis of stress distribution across the notch throat plane on creep exposure has been carried out to assess the creep failure of the material in presence of notch. On the other hand, SEM fractography and micrography study has been carried out to study the creep cavitation induced damage study. EBSD has been used to map strain distribution at the notch throat plane of the unfailed notch through HKL software.

4.2 Effect of notch sharpness on rupture life

Creep tests were carried out on notched specimens at 923, 973, 1023 K over the stress range of 100 – 260 MPa. The temperature was maintained within ±2 K across the specimen during the creep tests. For notched specimens, the net applied stress (σ_{net}) was calculated based on the minimum area of the specimens. The variations of rupture life with applied stress for both the smooth and notched specimens at different temperatures are shown in Fig. 4.1(a, b, c). In the presence of notch, creep rupture life of the steel increased appreciably and the extent of increase was more for relatively sharper notches. The variations of rupture life as a function of notch acuity ratio (d/R) for different applied stresses at different temperatures are shown in Fig. 4.2(a, b, c). The rupture lives increased sharply with notch acuity ratio (notch sharpness) and tend to a saturation value at higher notch acuity ratio at 973 K [Fig. 4.2(a)]. However, the strengthening with notch sharpness showed a decline instead of saturation trend for the sharpest notch of NAR 20 at 923 K [Fig. 4.2(b)]. Hence, it is expected that for very sharp notches, the material may undergo tendency to notch weakening for long-term creep exposure (lower applied stress).Similar observations (tendency to decline for sharper notches) have been identified in the case of 1023 K at relatively lower stresses [Fig. 4.2(c)].The creep rupture ductility (reduction in area %) was found to decrease with increase in notch acuity ratio and decrease in stress [Fig. 4.3 (a, b, c)] and exhibited saturating trend for higher notch acuity ratios at all the temperature investigated. In generally, ductility decreased with decrease in stress (longer creep rupture life). This indicated that the material's susceptibility to brittle intergranular creep failure became more predominant in presence of notch and its sharpness and duration of creep exposure.

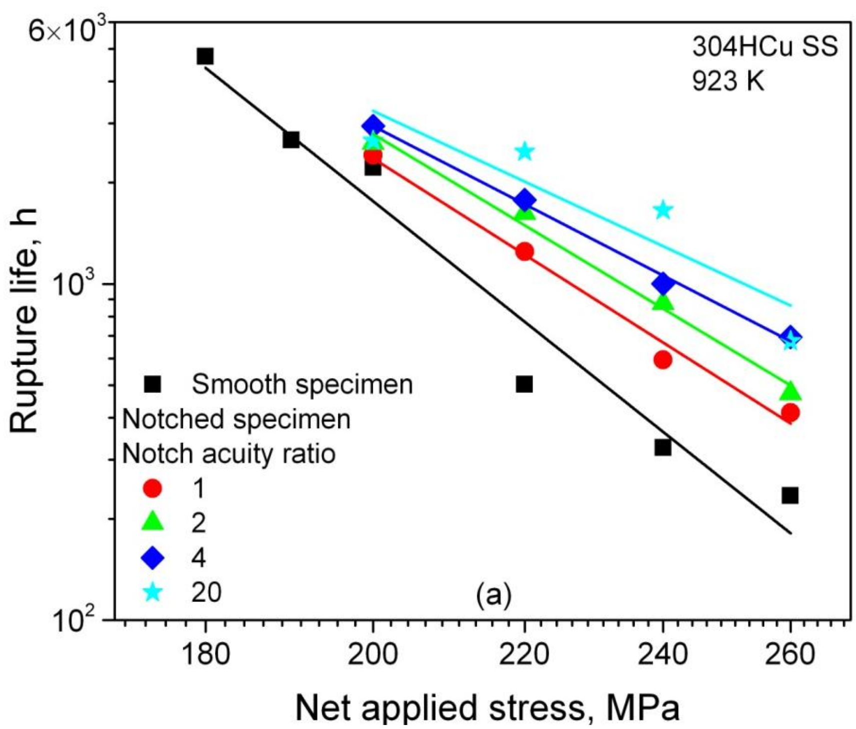

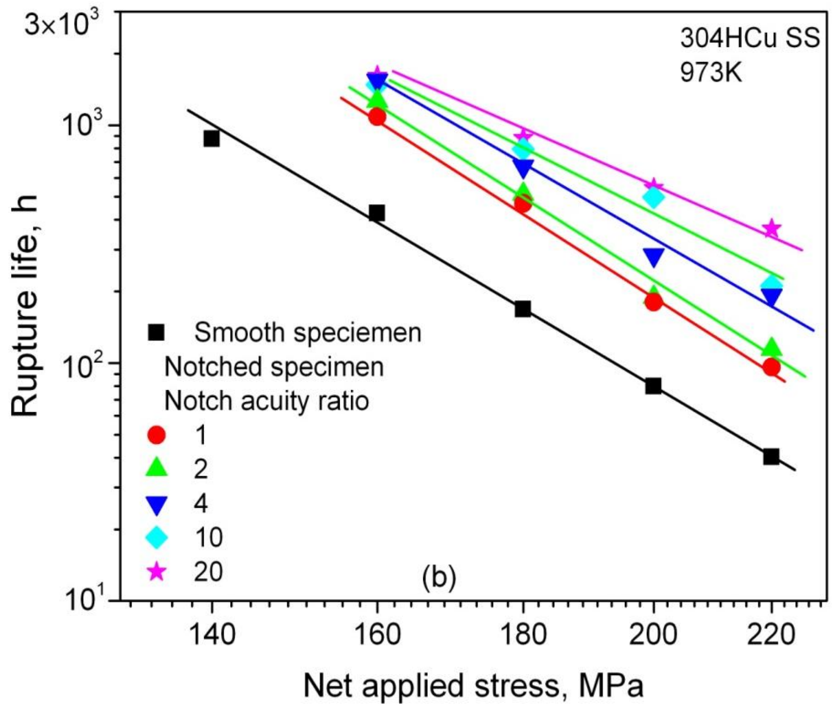

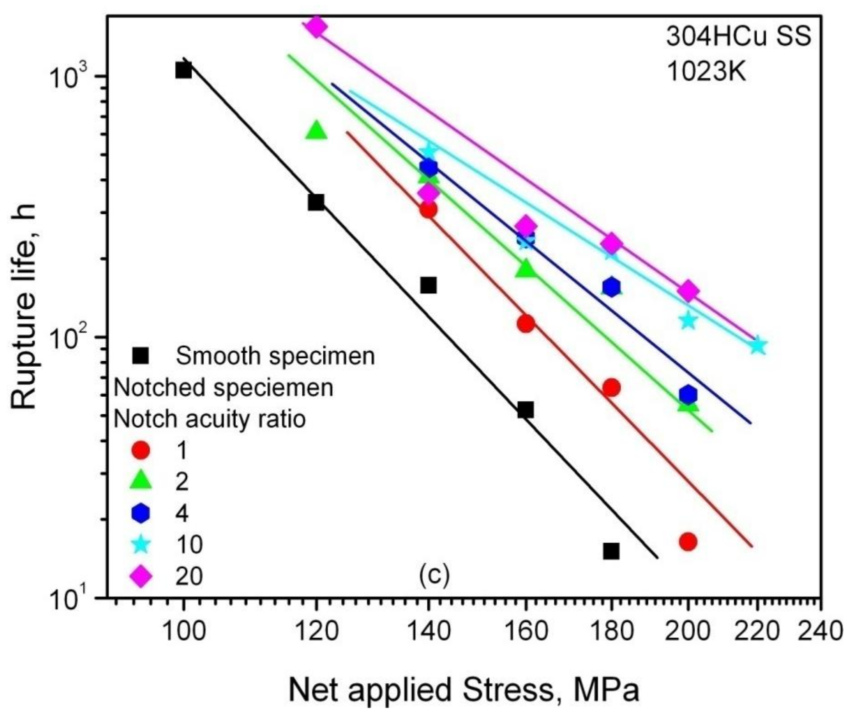

Fig. 4.1 Variations of creep ruptures life of both smooth and notched specimens of the steel with net applied stress at 923, 973 and 1023 K.

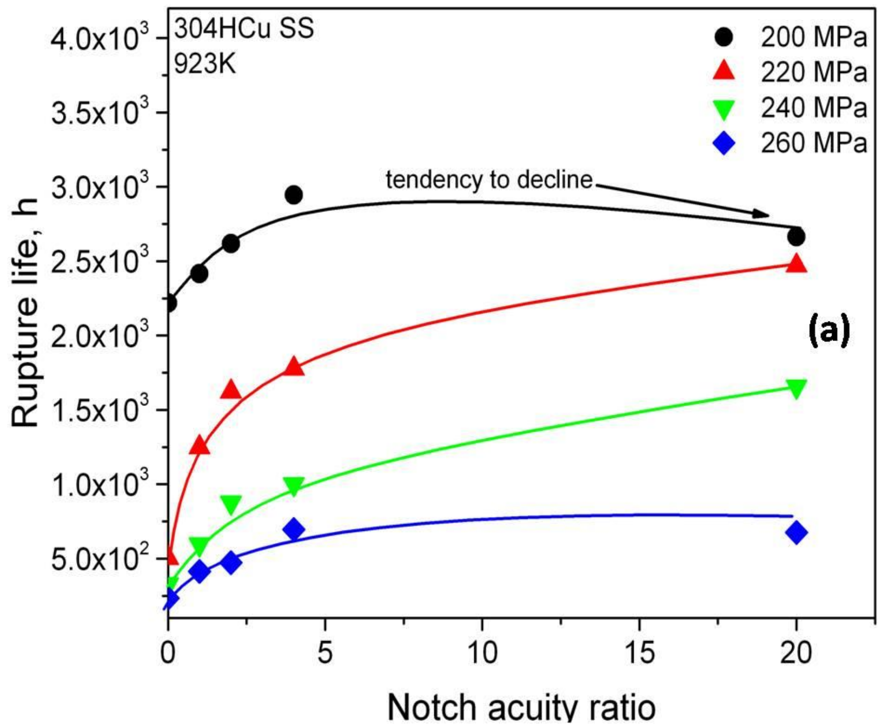
304HCu SS
923K
200 MPa
220 MPa
240 MPa
260 MPa
tendency to decline
(a)
Rupture life, h
Notch acuity ratio

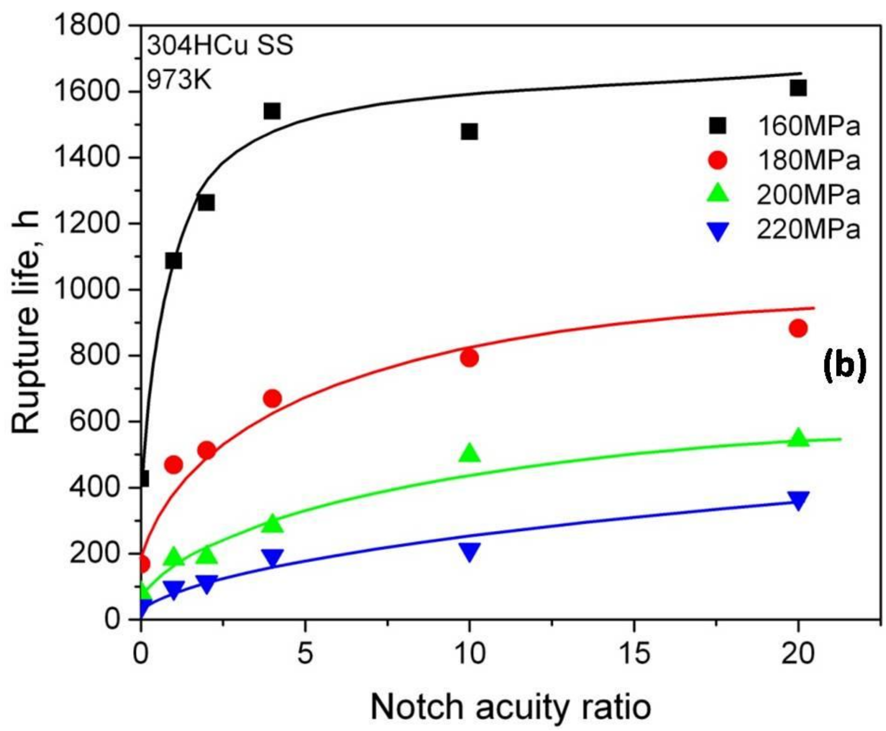
304HCu SS
973K
160MPa
180MPa
200MPa
220MPa
(b)
Rupture life, h
Notch acuity ratio

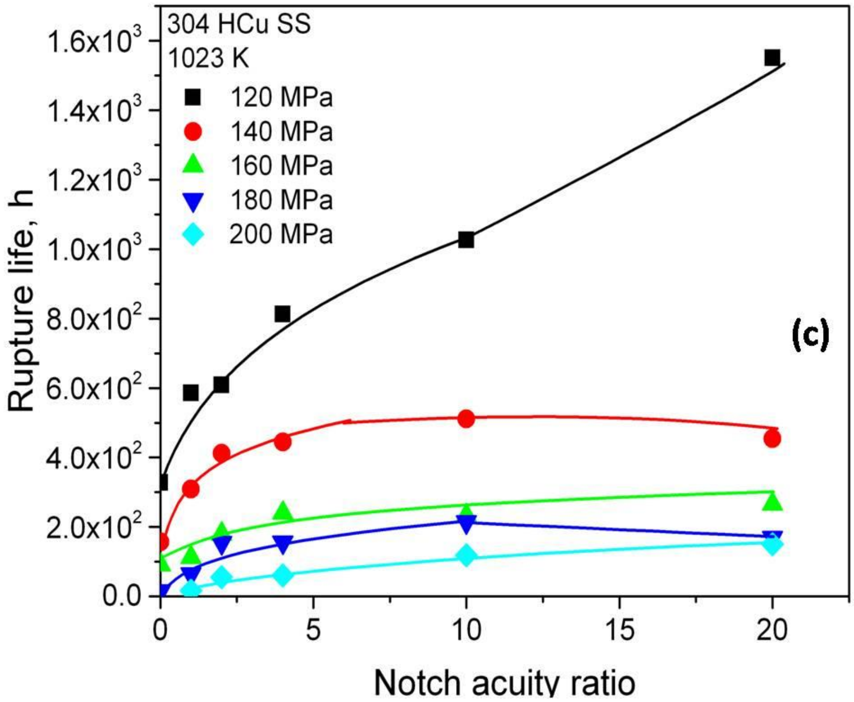

Fig. 4.2 Variations of creep rupture life of both smooth and notched specimens of the steel with notch acuity ratio, creep tested at 973 K and different stresses.

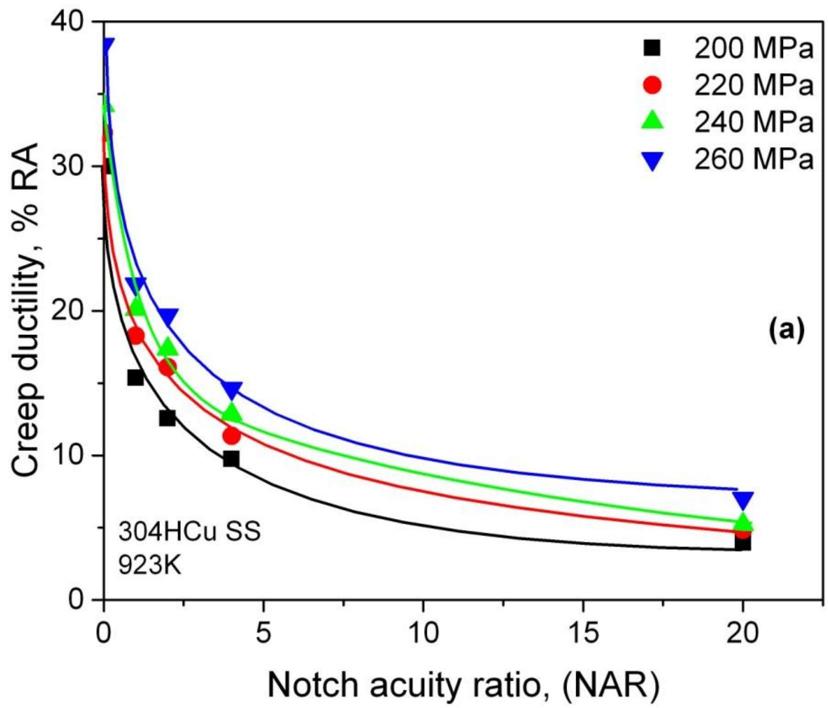

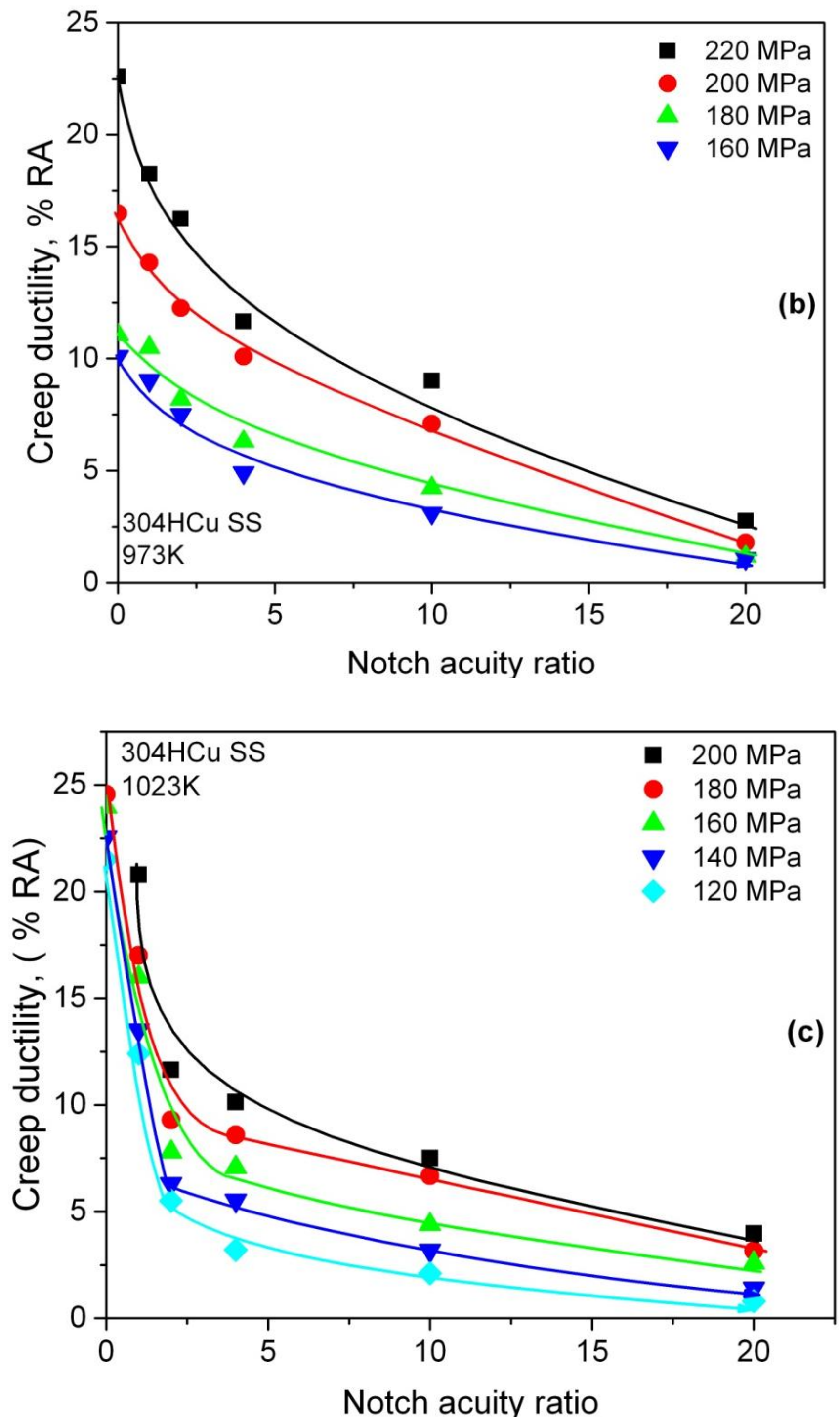

Fig. 4.3 Variations of creep rupture ductility (reduction in area %) of both smooth and notch specimens of the steel with notch acuity ratio, creep tested at 973 K and different stresses.

4.3 Fracture appearance of smooth and notched specimens

The SEM fractographic investigation has been carried out to illustrate the signatures of failure mechanism in the steel under both uniaxial and multiaxial state of stresses. SEM fractograph of the smooth specimen tested at 200 MPa, 973 K is shown in Fig. 4.4. Mixed mode failure consisting of predominantly ductile dimple with some intergranular creep cavitation is evident from the fractograph [Fig. 4.4(a)]. Almost similar features of failure across the cross section were observed, with shear lip formation at the edge at higher applied stresses. More evidence of intergranular creep cavitation brittle failure was found for testing

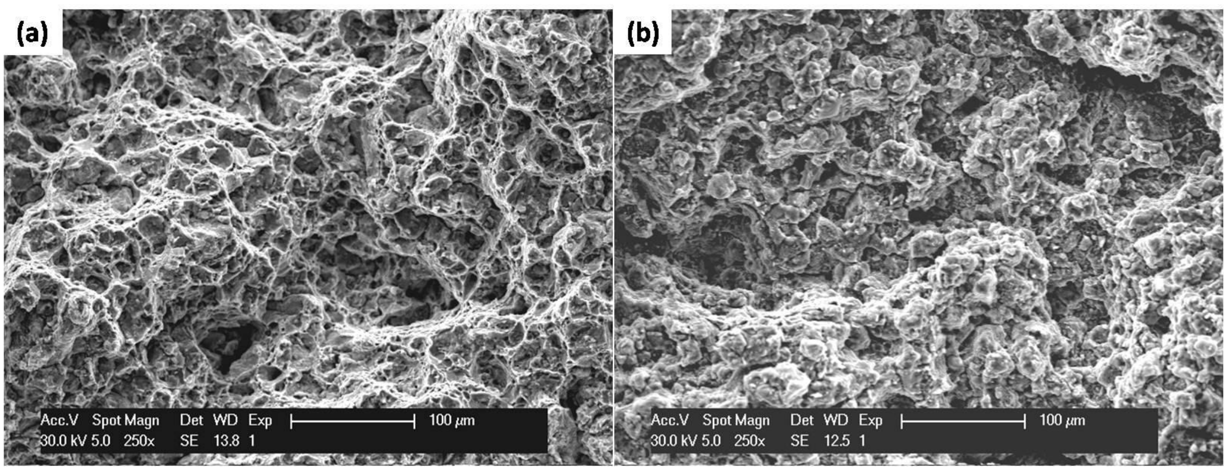

Fig. 4.4 SEM fractograph of the smooth specimen of the steel, creep tested at (a) 200MPa and 973 K, (b) 140 MPa and 973K.

Distinctly different mode of creep failure was observed in notched specimens due to the multiaxial state of stress experienced by the specimen. The fracture appearance was also found to change with the notch root radius. The appearance of fracture surface for notch root radii of 2.5 mm and 0.25 mm creep tested at 200 MPa and 973 K are shown in Figs. 4.5 and 4.6 respectively. For relatively shallow notches the fractograph exhibited mixed mode failure consisting of predominantly ductile dimple at and around the central location and predominantly intergranular creep cavitation at and close to the notch root (Fig. 4.5). With increase in notch sharpness, intergranular creep cavitation was more pronounced and predominant creep cavitation was observed even at the central location of creep specimen (Fig. 4.6). With decrease in applied stress and increase in notch sharpness more intergranular creep cavitation was observed.

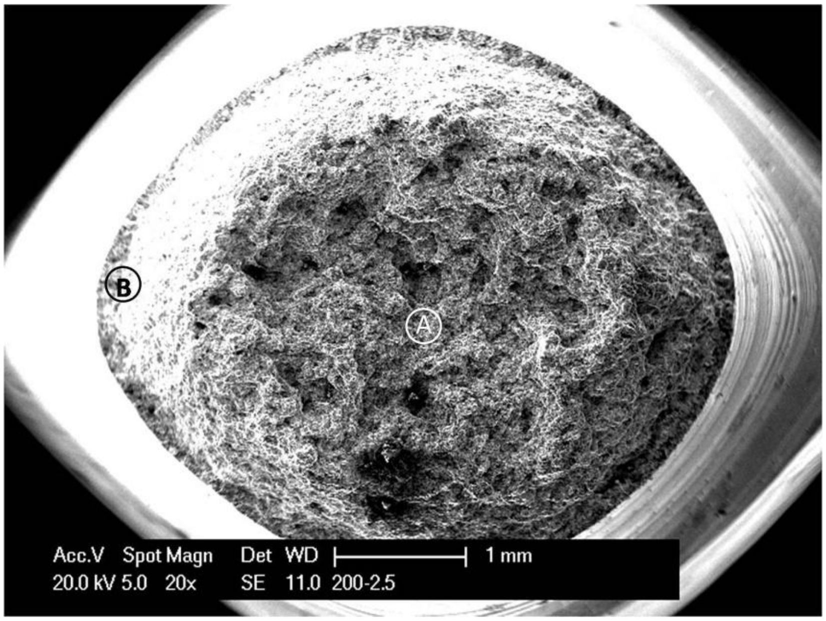

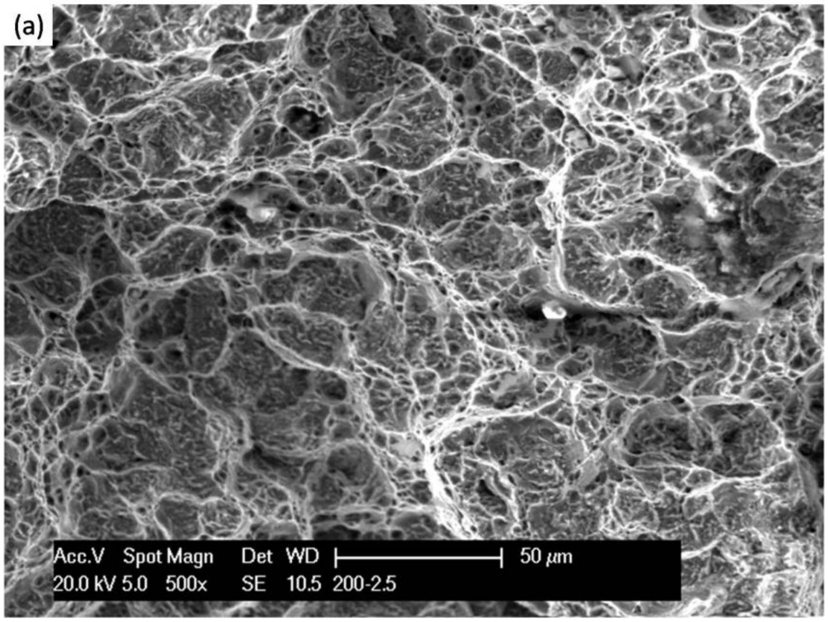

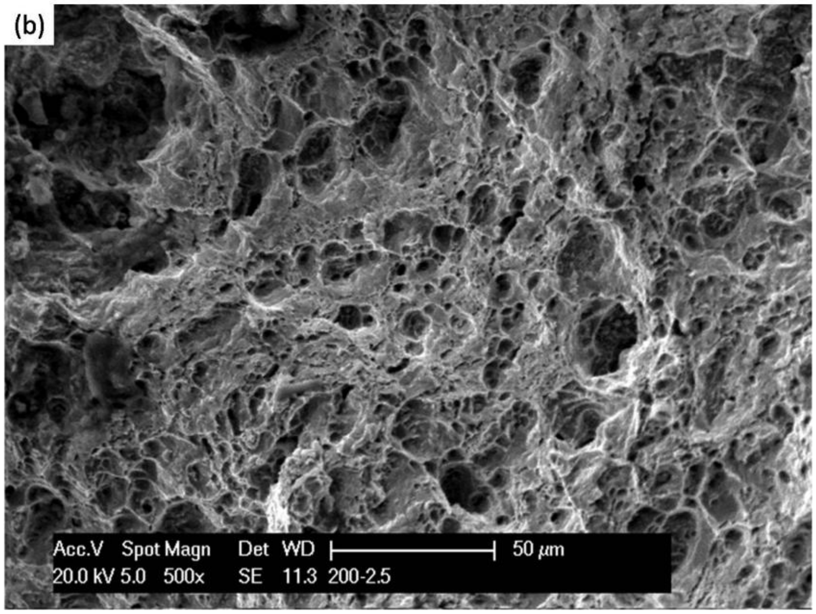

Fig. 4.5 SEM fractograph of shallow notched specimens (notch acuity ratio 2) at (a) centre and (b) root, creep tested at 200 MPa and 973 K.

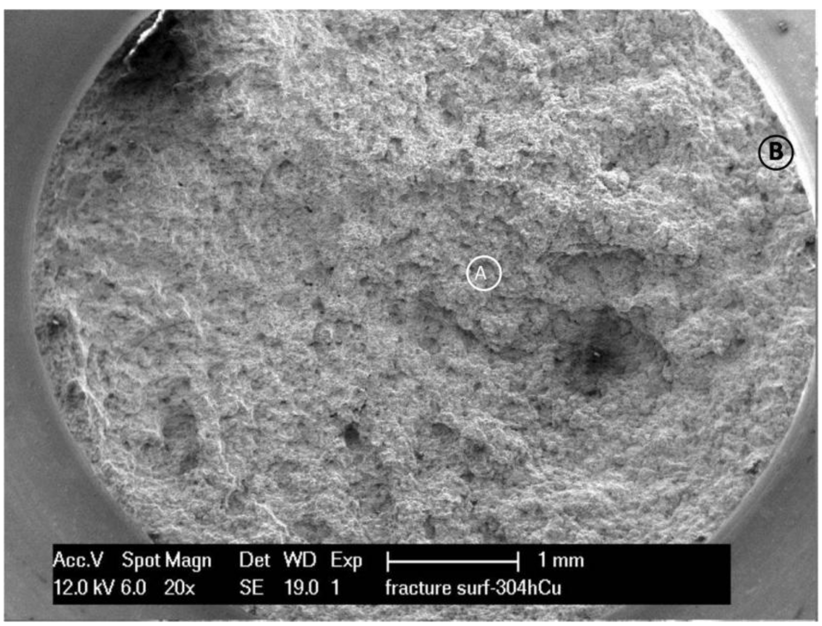

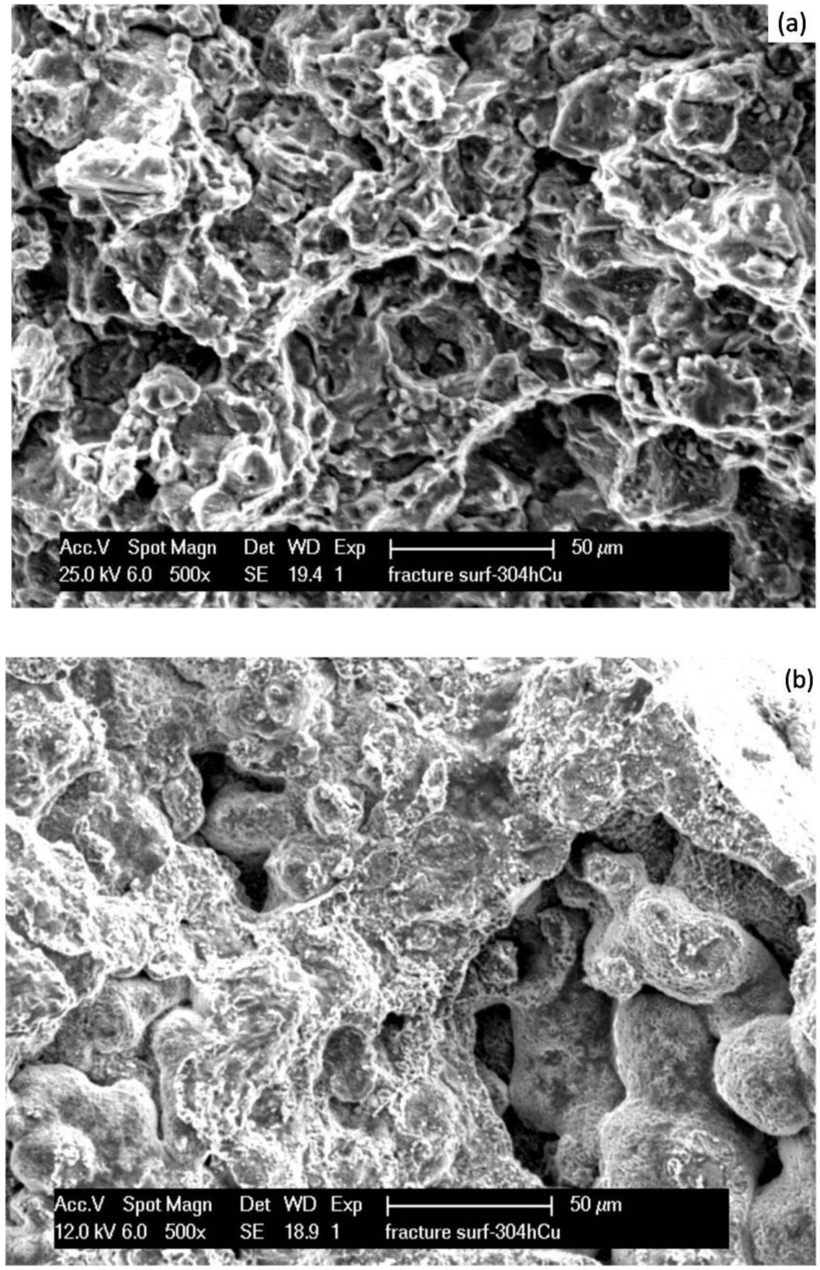

Fig. 4.6 SEM fractograph of sharper notched specimens (notch acuity ratio 20) at (a) centre and (b) root, creep tested at 200 MPa and 973 K.

The SEM metallography was also carried out on the unfailed notch of the creep ruptured specimen to understand the extent of damage caused during creep. Extensive cracking at the notch root has been observed in the case of relatively sharper notches, which is manifested as the intergranular creep cracks at the notch root and their propagation towards the centre of the specimen (Fig. 4.7). At the center of notch throat plane of sharper notches, isolated intergranular creep cavities were observed (Fig. 4.8). On the other hand, in case of shallow notch (Fig. 4.9), small crack at notch root region and random distribution of wedge (w-type) crack and r-type cavities near the notch root were observed. The propensity of cracking decreased away from the notch root (towards the center of the notch).

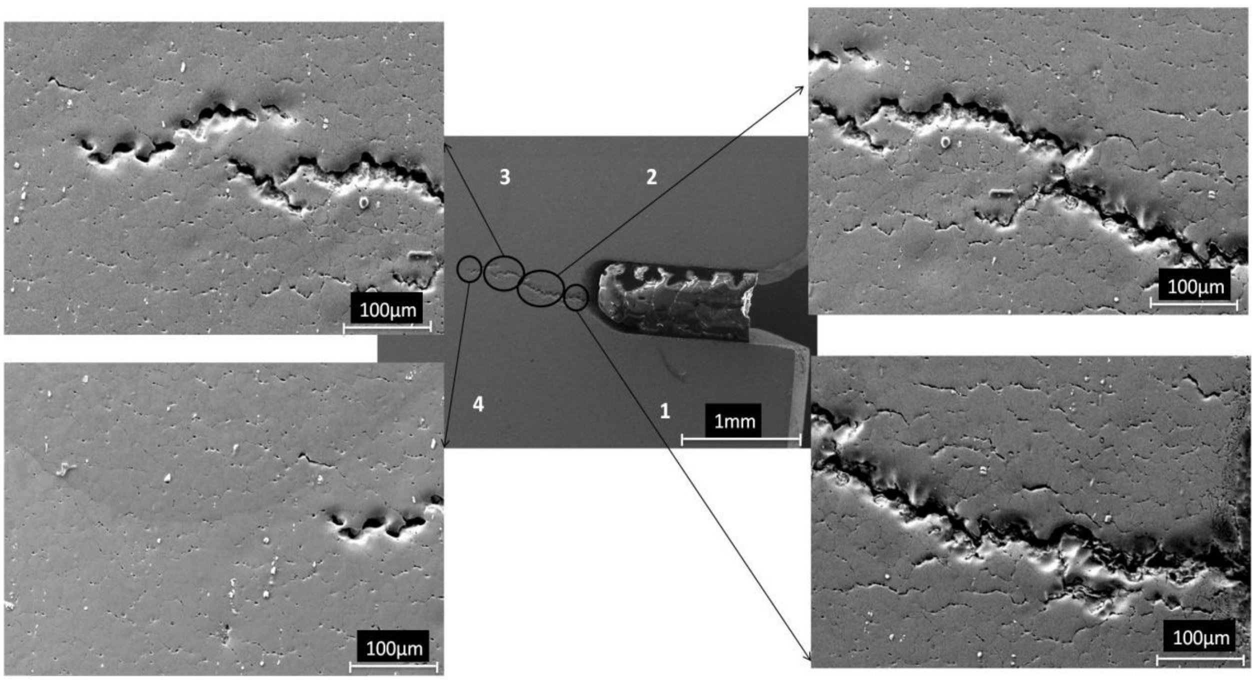

Fig. 4.7 SEM micrograph of unfailed notched creep specimen of notch root radius 0.25 mm, creep tested at 200 MPa and 973 K.

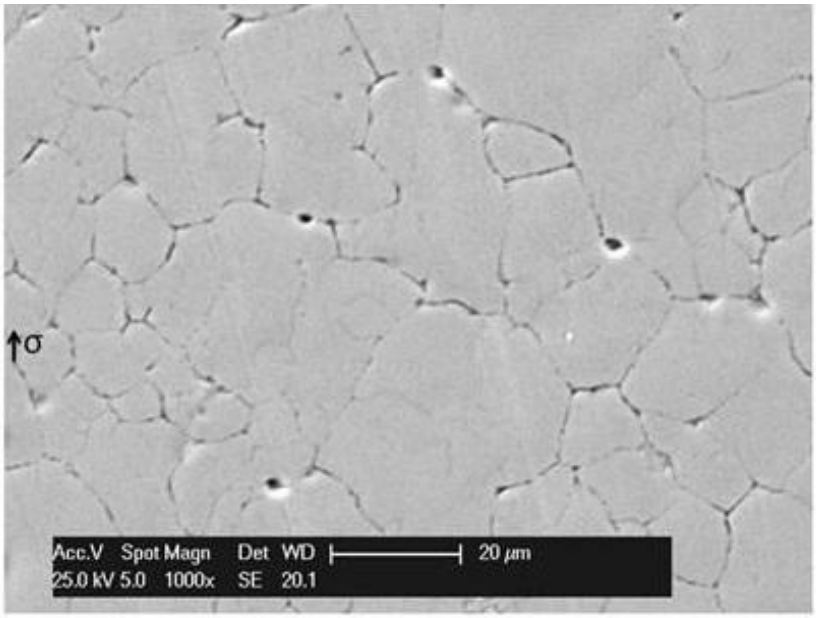

Fig. 4.8 Creep cavitations at the centre of the notch throat plane nucleated at grain boundaries for creep specimen of notch root radius 1.25 mm, creep tested at 200 MPa and 973 K.

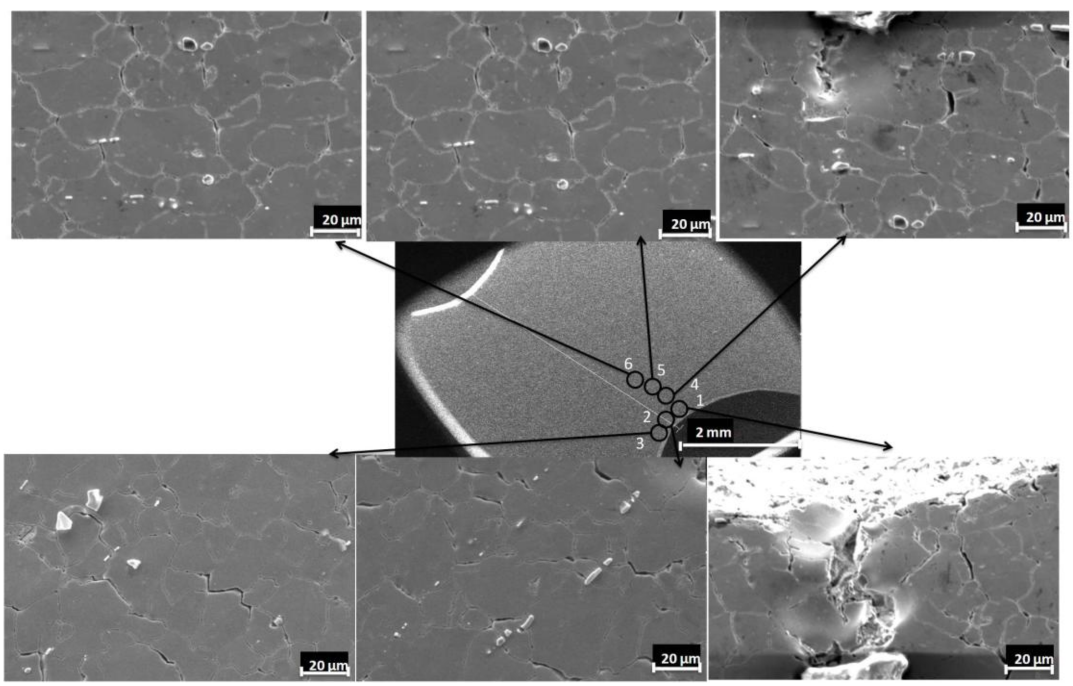

Fig. 4.9 SEM micrograph of unfailed notched creep specimen of notch root radius 2.5 mm, creep tested at 200 MPa and 973 K.

Effect of notch sharpness on creep cavitation behaviour has reported by several investigators [82, 151, 152]. For relatively ductile materials like modified 9Cr-1Mo and 316LN austenitic stainless steel, Goyal et al. [95, 153] have reported that for relatively shallow notches, intragranular cavities (dimples) nucleate at the center of notch and propagate towards the notch root; whereas for relatively sharper notches the intergranular cavities nucleate at the notch root and propagate towards the center of the specimen. A predominantly intergranular creep cavity has been reported in Inconel alloy X-750 superalloy in the presence of notch [97]. In the present investigation, cracking behaviour of the 304HCu SS in presence of notch is found to be closer to that of the behaviour of relatively intergranular creep cavitation prone materials. Details of the creep cavitation for the notched specimen at the notch root are shown in Fig. 4.10. Nucleation of creep cavities at the grain boundary triples points, their growth and their coalescence led to the creep crack.

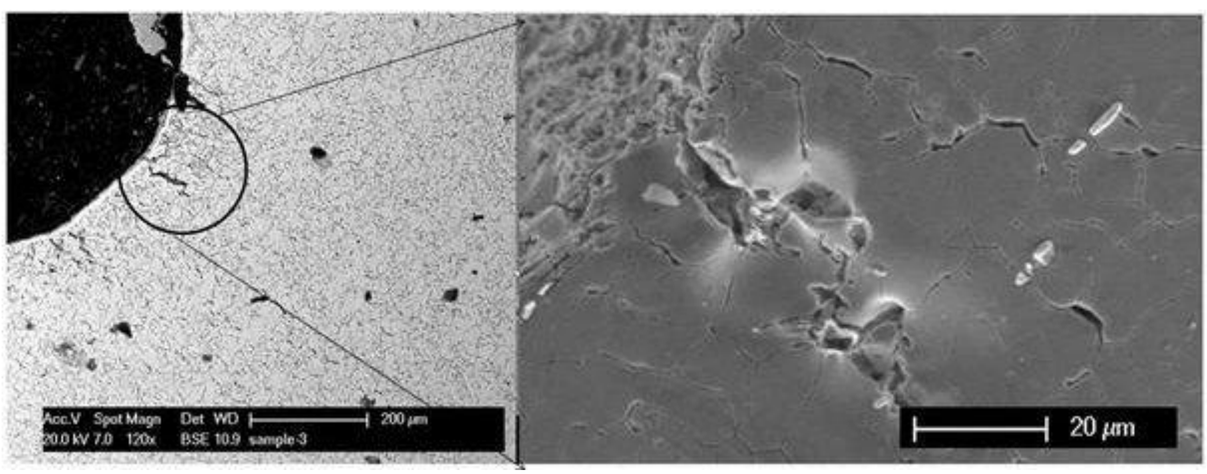

Fig.4.10 Details of creep cavitation at the notch root, notch root radius 2.5 mm, creep tested at 973 K and 200 MPa.

Grain boundary sliding is considered for the nucleation of intergranular creep cavities [154]. If the stress concentration at the grain boundary particles or grain corners etc. produced by grain boundary sliding is not relaxed, then cavities nucleate at the irregularities on the grain boundary by athermal rupturing of atomic bonds [155]. Differential vacancy concentration those at the cavity and its surrounding under stress gradient propel the cavities to grow by diffusive transfer of atoms from the cavity surface to regions far away [21]. Apart from the diffusivities of matter in the cavity surface and grain boundary [156] along which the atoms move, state of stress plays a decisive role in the cavitation of materials during creep [157]. Matrix creep deformation rate and grain boundary sliding rate along with grain size, precipitates on the grain boundary and state of stress play significant role in intergranular creep cavitation of the materials [158, 159]. Figure 3.7 indicates that with the value of stress index n = 7.76 of Norton's law ($\dot{\epsilon_s} = A\sigma^n$), the creep deformation mechanism is power law creep as modified by intragranular precipitates. Role of relative creep deformation rate to grain boundary sliding rate on intergranular creep cavitation in different grade of austenitic stainless steels has been studied by Laha et al. [160]. Even though grain boundary sliding rate is more or less proportional to creep rate, the ratio (sliding rate / creep rate) is more for precipitate hardened material. It has been demonstrated that addition of copper in 347 steel (niobium added austenitic stainless steel) even though decreased the creep rate substantially, the relatively long-term creep rupture strength decreased compared to 347 steel [13, 123] and was accompanied with extensive intergranular creep cavitation. Short-term creep rupture strength (higher applied stress) increased because of higher matrix/grain strength but once the intergranular creep cavitation became predominant (needs time since the cavity growth process is diffusion controlled) long-term creep rupture strength decreased. More pronounced intergranular creep cavitation at lower applied stress(relatively long-term test), as observed in the present investigation, is basically due to that of diffusion controlled intergranular creep cavitation which is a time dependent process. Creep deformation rate under the multiaxial state of stress is controlled by von-Mises stress [8]. Therefore, it is reasonable to say that the intergranular cavity nucleation is mostly controlled by von-Mises stress as the grain boundary sliding rate is proportional to creep rate and its (grain boundary sliding) improper accommodation leads to creep cavitation [103]. Diffusive transfer of atoms is controlled by maximum principal stress as the vacancy concentration depends on the normal stress [161] and hydrostatic stress also plays an important role in cavity growth at relatively higher stress [92]. It is quite expected that multiaxial state of stress influences the creep deformation and cavitation behavior leading to appreciable effect on creep rupture strength in presence of notches of different sharpness. It is essential to estimate the state of stress across the notch throat plane to understand creep deformation and fracture and has been carried by finite element analysis as illustrated in the next section.

4.4 Stress distribution across the notch throat plane

Finite element analysis of stress distribution across the notch throat plane during creep exposure was carried out to understand the difference in notch strengthening of the materials.

4.4.1 Elastic, Elastic-Plastic, Elastic-Creep, Elasto-Plastic-Creep stress distribution

The time dependent creep deformation coupled with elastic and elastic-plastic analysis was carried out to understand the stress distribution across the notch throat plane on creep exposure. The FE analysis was initially carried out for 1.25 mm notch root radius specimen at net applied stress of 200 MPa, 973 K. The variation of flow stress with true plastic strain was fitted using Hollomon equation, $\sigma_t = K\epsilon^{n'}$. The strength coefficient (*K*) and strain hardening exponent (*n'*) were obtained from the log-log plot of flow stress and true plastic strain and incorporated in the analysis(Table 4.1).A comparative variation of von-Mises stress across the notch root throat plane on considering elastic and elasto-plastic deformation (time independent) is shown in

Fig.4.11 along with elastic-creep and elasto-plastic-creep deformation (time dependent) separately for relatively long creep exposure.

Table-4.1 The tensile and creep properties of the smooth specimen at 973 K used in FE analysis

Tensile properties at 973K			**Uniaxial creep properties at 973K**	
Yield Stress (MPa)	K	n′	A($MPa^{-n} h^{-1}$)	n
174	554.1	0.21	1.32×10^{-21}	7.56

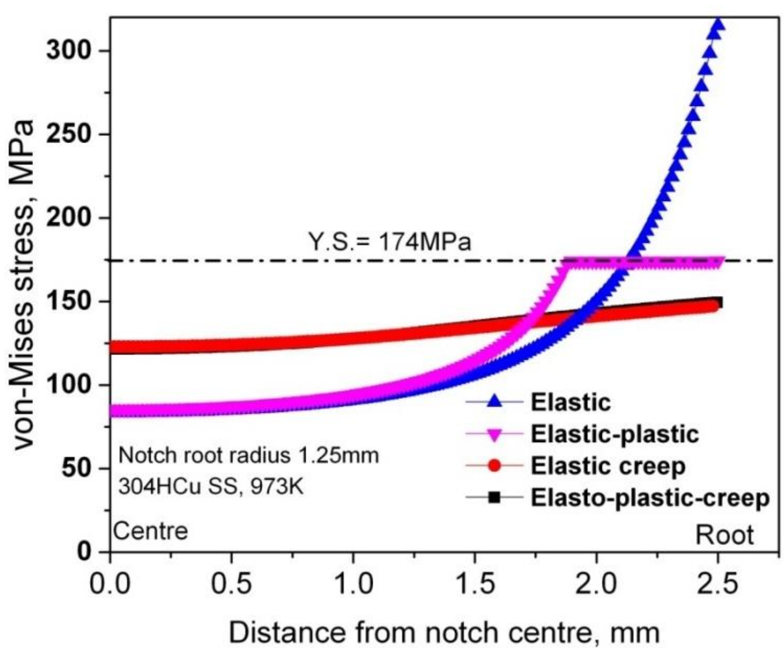

Fig. 4.11 FE analysis of von-Mises stress distribution across the notch throat plane for notched specimen of root radius 1.25 mm, creep tested at 200 MPa, 973 K, considering elastic-creep and elasto-plastic-creep behaviour.

The elastic analysis revealed very high stress concentration at the notch root. The von-Mises stress was found to be significantly higher at the notch root due to stress concentration. In order to maintain the force equilibrium, the stress decreased in the central region of the notch. In the case of elastic-plastic stress analysis, plastic deformation around the notch root limits the stress to yield stress (174 MPa at 973K) with lower stress around the central region, Fig. 4.11. Further analyses were carried out by considering elastic-creep and elasto-plastic-creep conditions. It is interesting to note that the stress distribution in the notch throat plane remained same irrespective of the plastic strain in the notch region. Earlier studies by Goyal et al. [95, 153] for Grade 9 steel revealed that the role of plastic deformation in the stress distribution across the notch throat plane under creep condition was almost negligible, which is also observed in the present case. Hence, further analysis of stress distribution across the notch root throat plane has been carried out considering the elastic-creep behavior of the material.

4.4.2 Elastic-Creep stress distribution across the notch plane

Stress redistribution across the notch throat plane during creep exposure has been reported by several investigators [93,161]. The variations of the von-Mises and maximum principal stresses across notch throat plane as a function of creep exposure at net applied stress of 200 MPa, 973 K are shown in Fig. 4.12 and Fig. 4.13, respectively for relatively shallow notch (notch root radius of 5 mm) and relatively sharper notch (notch root radius of 0.25 mm).

The stress redistribution with creep exposure was found to be dependent on the notch root radius significantly. The stress redistribution across the notch root throat plane evolved with time and attained the stationary state distribution. The time to attain stationary state (τ_{ss}=875 hour) for sharper notch of root radius 0.25 mm (notch acuity ratio of 20) was found significantly higher than its rupture life (t_r = 544 hour) while for shallow notch of root radius 5 mm (notch acuity ratio of 1) the time to attain stationary state (τ_{ss}=10 hour) was significantly lower than the time to rupture (t_r=180.3 hour).

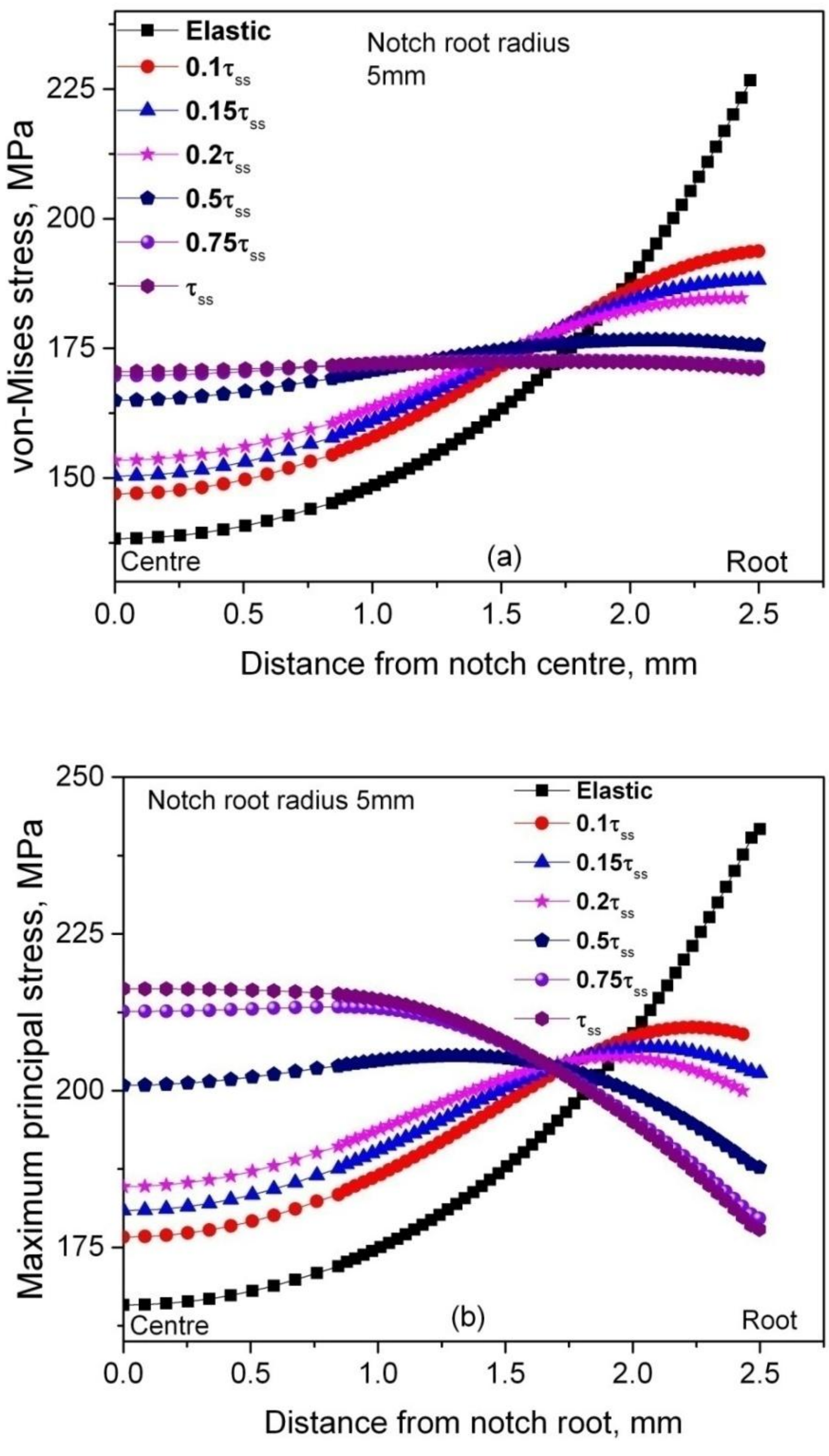

Fig. 4.12 Variations of (a) von-Mises stress and (b) maximum principal stress across the notch throat plane as a function of creep exposure time for shallow notch (notch root radius 5 mm).

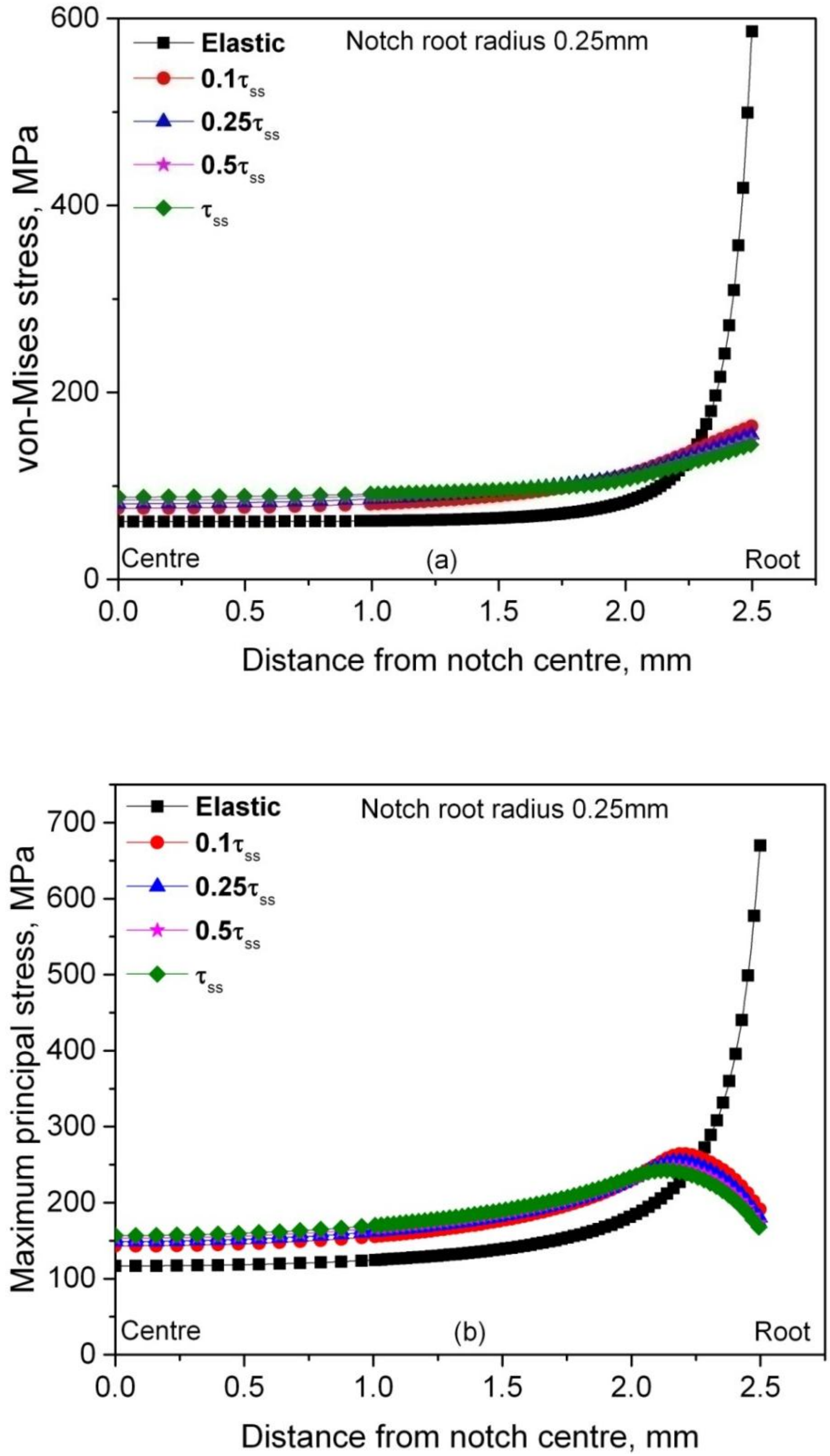

Fig. 4.13 Variations of (a) von-Mises stress and (b) maximum principal stress across the notch throat plane as a function of creep exposure time for sharper notch (notch root radius 0.25).

It suggests that in the presence of sharper notch (notch acuity 20) the material has failed before achieving the stationary state distribution. Hayhurst and Henderson [93] have reported that the time to attain stationary stress distribution is larger for relatively intergranular creep cavitation prone materials than that for the creep ductile materials. In this relatively intergranular creep cavitation prone304HCu SS, very long time to attain stationary state of stress distribution even higher than the rupture life of sharper notch (notch acuity ratio 20) is not very surprising. For shallow notch (Fig. 4.12(a)), the von-Mises stress decreased with creep exposure from high value to close to yield stress (174MPa) around the notch root region and increased from lower value close to yield stress around the notch central region. At stationary stress state, almost uniform stress distribution across the notch throat plane was observed. The principal stress (Fig. 4.12(b)) distribution followed the similar evolution process as the von-Mises stress with stationary state distribution having higher stress at the notch central region and lower value at the notch root region. For relatively sharper notches with creep exposure, the von-Mises stress (Fig. 4.13(a)) increased at the notch central region and decreased at the notch root region leading to stationary state having high stress at the notch root region and lower stress at the notch central region. The maximum principal stress distribution possessed peak at close to notch root with a value higher than the net applied stress (200MPa) for relatively sharper notches (Fig. 4.13(b)). The stationary von-Mises stress was less than the net applied stress for both the shallow and sharper notches (Figs. 4.12(a) and 4.13(a)); whereas the stationary maximum principal stress was more than the net applied stress at central region for relatively shallow notches (Fig. 4.13(b)) and at close to notch root region for relatively sharper notches (Fig. 4.13(b)).

In general, stress redistribution would be faster for brittle materials than that of ductile materials. For shallow notch, in the early stage of stress redistribution high von-Mises stress coupled with high principal stress might have induced creep cavitation at the notch root [Fig. 4.5(b)], which could not proceed further due to complete redistribution to stationary state that causes almost uniform distribution of von-Mises stress at the notch throat plane and decrease in maximum principal stress at the notch root. After complete stress redistribution uniform distribution of von-Mises stress and maximum principal stress at notch centre results predominantly transgranular ductile dimple failure [Fig. 4.5(a)].

In case of sharper notch, both the von-Mises and maximum principal stresses possess peak near the notch root region throughout the stress redistribution with creep exposure. Since the intergranular creep cavity nucleation is enhanced under high von-Mises stress and diffusion-controlled creep cavity growth is enhanced under high principal stress coupled with long creep exposure (due to lower von-Mises stress), the cracking induced by cavity nucleation and growth will propagate toward the central region, resulting in almost intergranular creep failure across the entire notch throat plane [Fig. 4.6(a,b)].

4.4.3 Stress distribution across the notch plane after attaining stationary state

The variations of stationary von-Mises, maximum principal and hydrostatic stresses across the notch throat plane after attaining stationary state for different notch acuity ratios (notch sharpness) are shown in Fig. 4.14, 4.15 and 4.16, respectively. The von-Mises stress across the notch throat plane decreased with notch sharpness and exhibited higher values at notch root for relatively sharper notches but much lower than the net applied stress (200 MPa, for the analysed case) (Fig. 4.14). The maximum principal stress exhibited peak value at intermediate location between the center and notch root, which became pronounced for relatively sharper notches and was higher than the net applied stress (Fig. 4.15). In other words, the value of the peak was higher and the location of the peak became closer to notch root with increase in notch sharpness. The variation of hydrostatic stress with notch sharpness was similar to that of the principal stress (Fig. 4.16). However, the hydrostatic stress remained lower than the net applied stress across the notch throat plane with peak value shifting towards the notch root with increase in notch sharpness.

Triaxial state of stress generated across the notch throat plane imposes constraint to plastic deformation. The extent of triaxiality depends on the notch geometry and material properties [161]. Several factors which are manifested in the constraint to plastic deformation in notched specimen have been discussed by Wu et al. [92]. The most relevant and important factor is the triaxiality which is the ratio of hydrostatic stress to the von-Mises stress as given below:

$$\text{Triaxiality factor (TF)} = \left(\frac{\sigma_1+\sigma_2+\sigma_3}{3}\right)\frac{1}{\sigma_{vm}} \qquad (4.1)$$

The variation of triaxiality factor across the notch plane for notch acuity ratio 1-20 was shown in Fig. 4.17. The triaxiality factor across the notch throat plane was found to increase with increase in notch acuity ratio. The state of stress along with stress triaxiality governs the deformation and fracture behaviour of the material to determine its rupture life and ductility. The maxima in triaxiality was found near the notch root for sharper notch and decreased and shifted towards centre for shallow notches. Higher value of triaxiality near the notch root results extensive intergranular creep cavitations and cracks for sharper notch [Fig. 4.7]. Uniform and lower value of triaxiality for shallow notch compared to sharper notch results trangranular ductile dimple failure with little cavities and wedge cracks at notch root [Fig. 4.9] and predominant transgranular dimple failure with very less intergranular cavities at the notch centre.

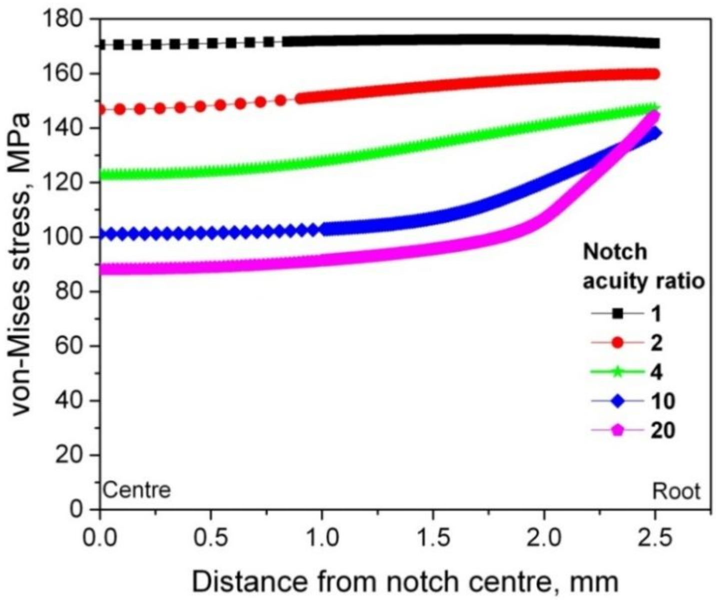

Fig. 4.14 Variations of stationary von-Mises stress at the notch throat plane for different notch acuity creep exposed at 973K, 200MPa.

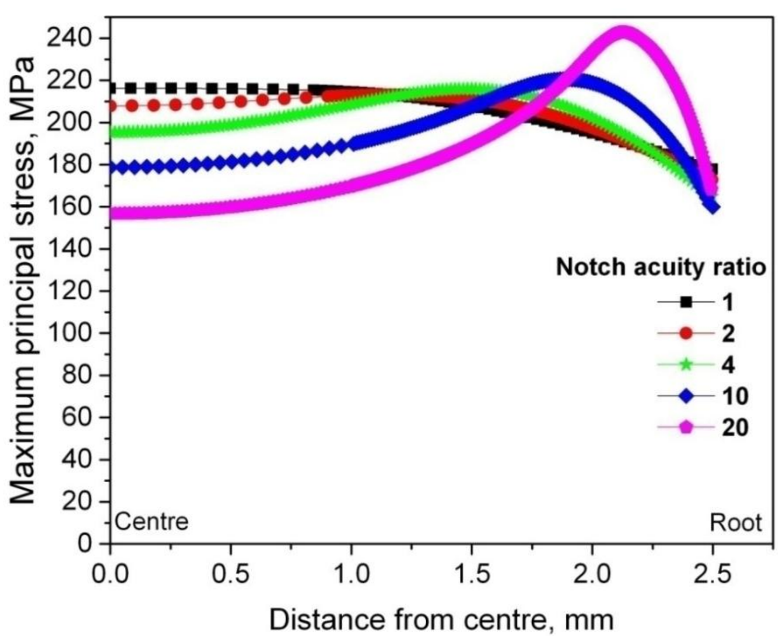

Fig. 4.15 Variation of stationary maximum principal stress at the notch throat plane for different notch acuity creep exposed at 973K, 200MPa.

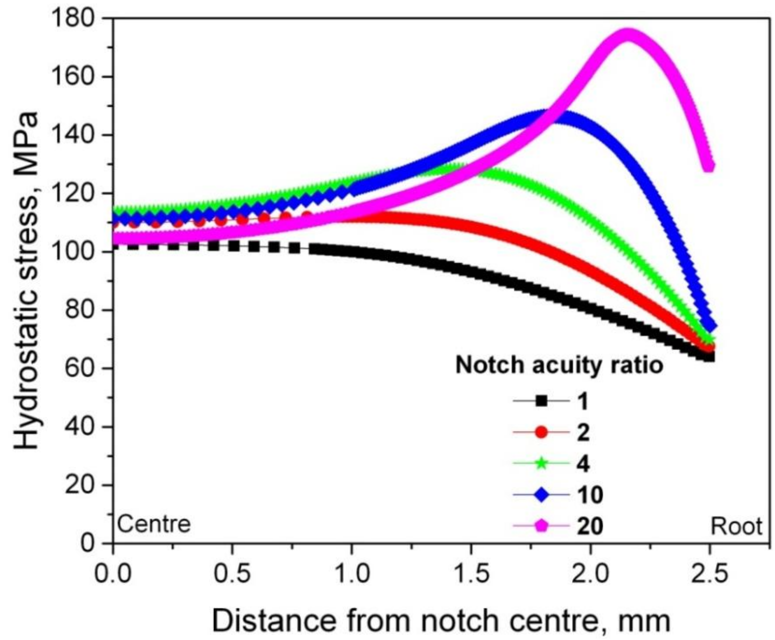

Fig. 4.16 Variations of stationary hydrostatic stress at the notch throat plane for different notch acuity creep exposed at 973K, 200MPa.

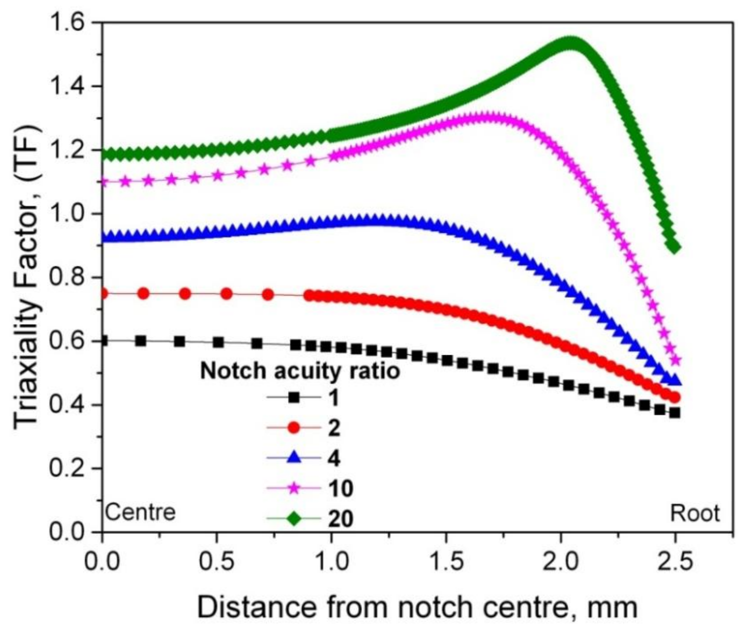

Fig. 4.17 Variations of traixiality state of stress at the notch throat plane for different notch acuity creep exposed at 973K, 200MPa.

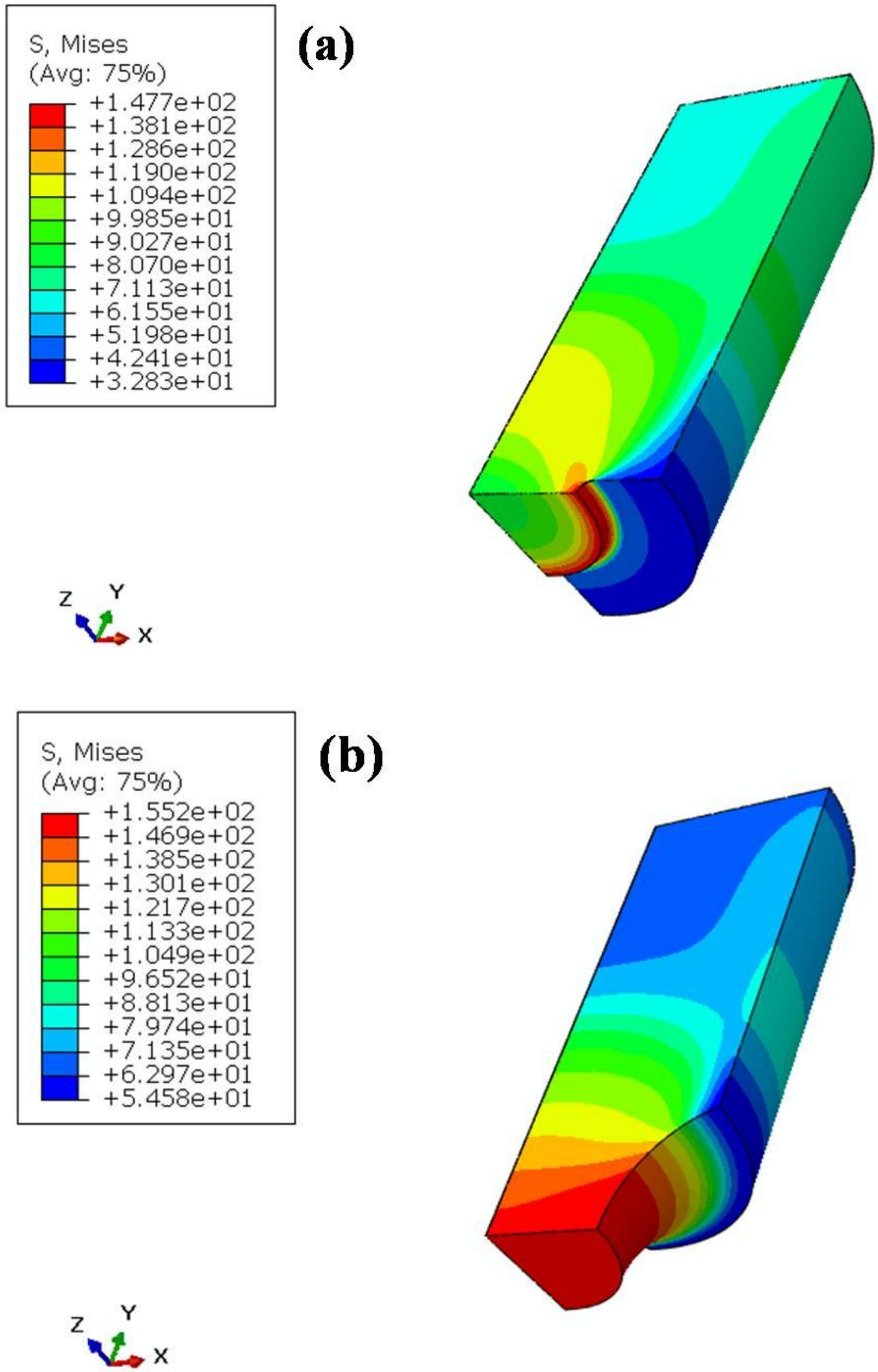

Fig. 4.18 The contour view of von-Mises stress for sharper notch (NAR=20) and shallow notch (NAR=2) after attaining the stationary state creep at 973 K, 200MPa.

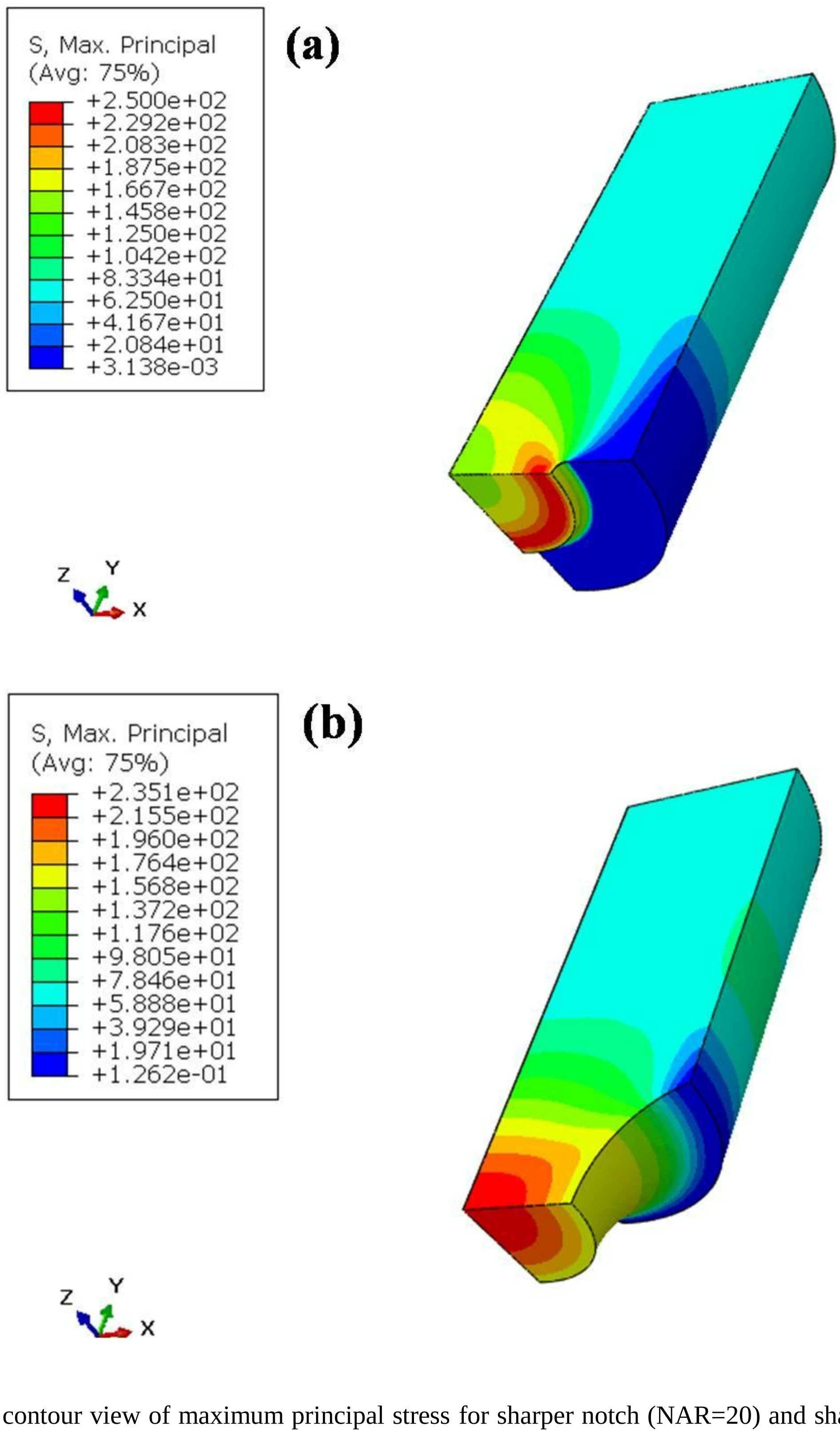

Fig. 4.19 The contour view of maximum principal stress for sharper notch (NAR=20) and shallow notch (NAR=2) after attaining the stationary state creep at 973 K, 200MPa.

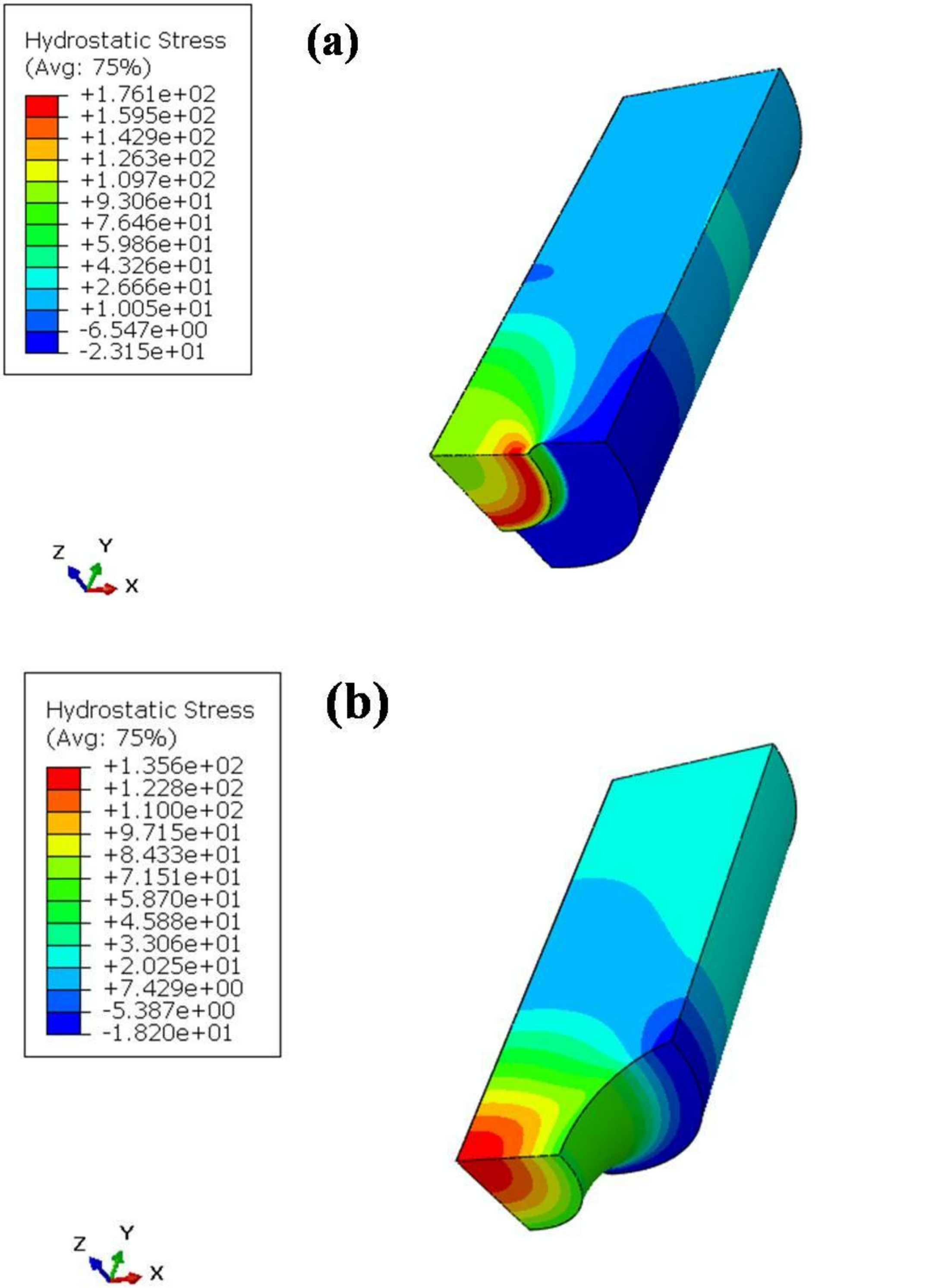

Fig. 4.20 The contour view of hydrostatic stress for sharper notch (NAR=20) and shallow notch (NAR=2) after attaining the stationary state creep at 973 K, 200MPa.

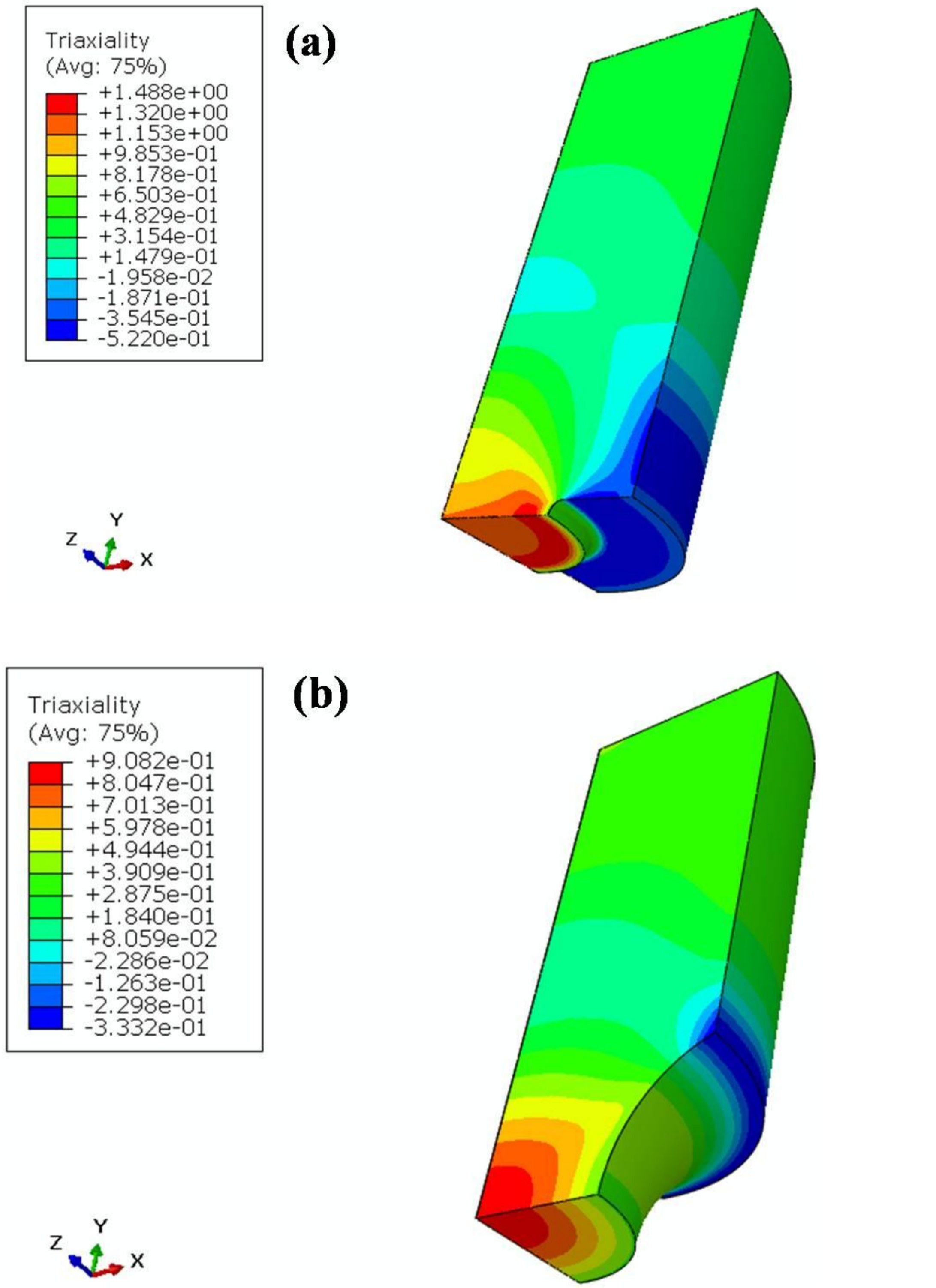

Fig. 4.21 The contour view of triaxiality factor for sharper notch (NAR=20) and shallow notch (NAR=2) after attaining the stationary state creep at 973 K, 200MPa.

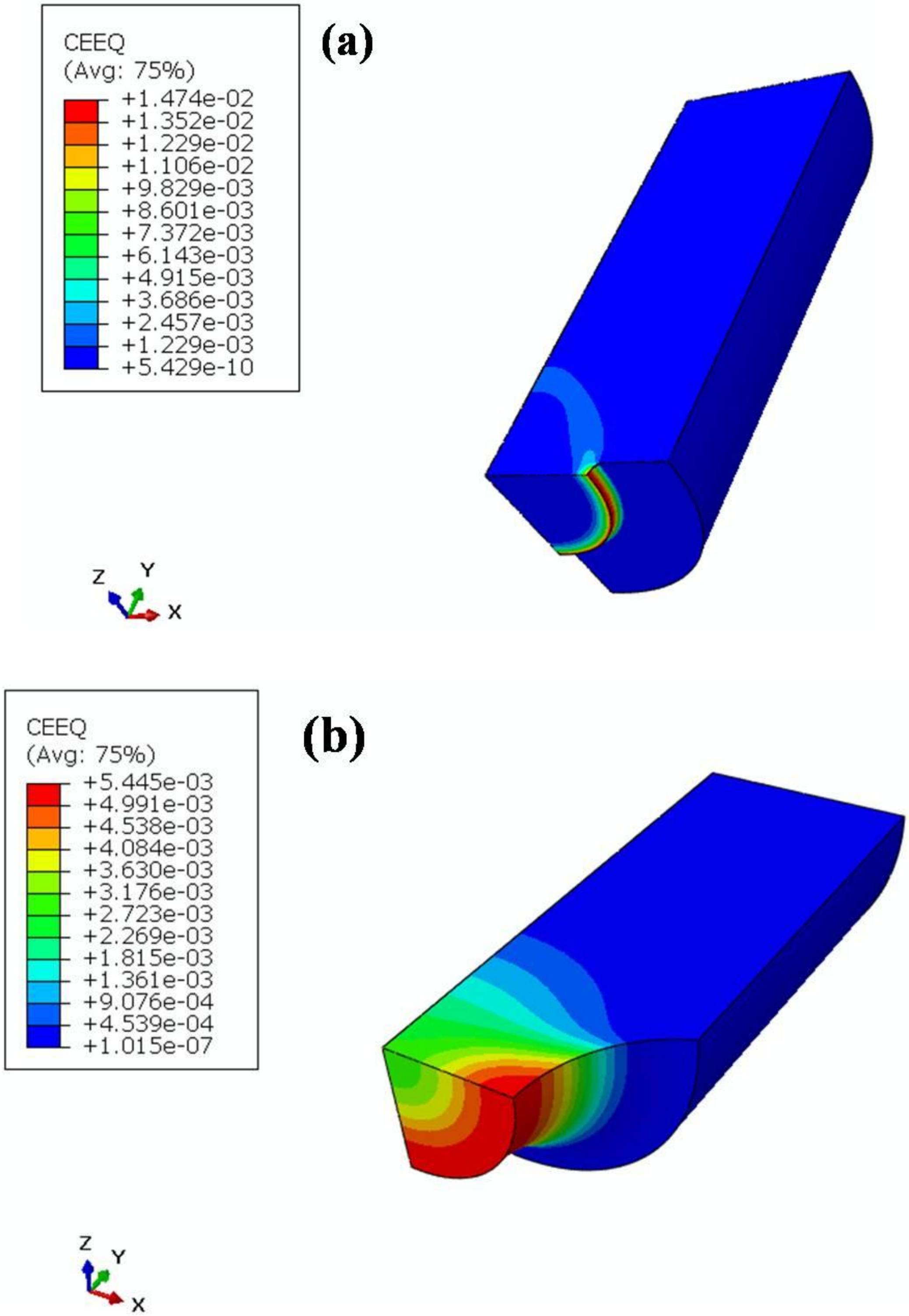

Fig. 4.22 The contour view of CEEQ for sharper notch (NAR=20) and shallow notch (NAR=2) after attaining the stationary state creep at 973 K, 200MPa.

The contour views of the stationary state of von-Mises stress, maximum principal stress and hydrostatic stress, triaxiality factor and CEEQ distributions across the notch for sharper and shallow notch, as estimated by finite element analysis, are shown in Fig. 4.18, Fig. 4.19, Fig. 4.20, Fig. 4.21, Fig. 4.22, respectively. It shows that for sharper notch all these distributions are more concentrated towards the notch root while for shallow notch these distributions are more concentrated towards the centre.

4.5 Effect of notch sharpness on creep deformation through EBSD analysis

For shallow notch broad distribution of the stress across the notch throat was observed whereas for sharper notch, localized concentration of stress at the notch root was observed as estimated through FE-analysis. In order to understand strain evolution, the SEM scans were performed by taking 1100000 points approximately through a cross-section of 1200 × 898µm at a rate of 0.0443sec/pt with a scan step size of 0.5µm. Fig. 4.23(a) and Fig. 4.24(a) respectively, represents the IPF map of shallow (root radius = 2.5 mm) and sharper notch (root radius = 0.25 mm) at the notch root where different colors represent the grain lattice orientation distribution. Fig. 4.23(b) and Fig. 4.24(b) shows various misorientaion values in KAM map analyzed through HKL software.

As expected from the FE analysis [CEEQ value, (Fig. 4.22)], localized strain distribution around at the notch root, which was much more for the sharper notch, was observed than that in the shallow notch specimen. For shallow notch, misorientation values were uniformly distributed at the notch throat plane while for sharper notch misorientation values showed maxima exactly at the notch root [Fig. 4.24(b)] which is having similarity with CEEQ values of sharper notch Fig. 4.22(a).

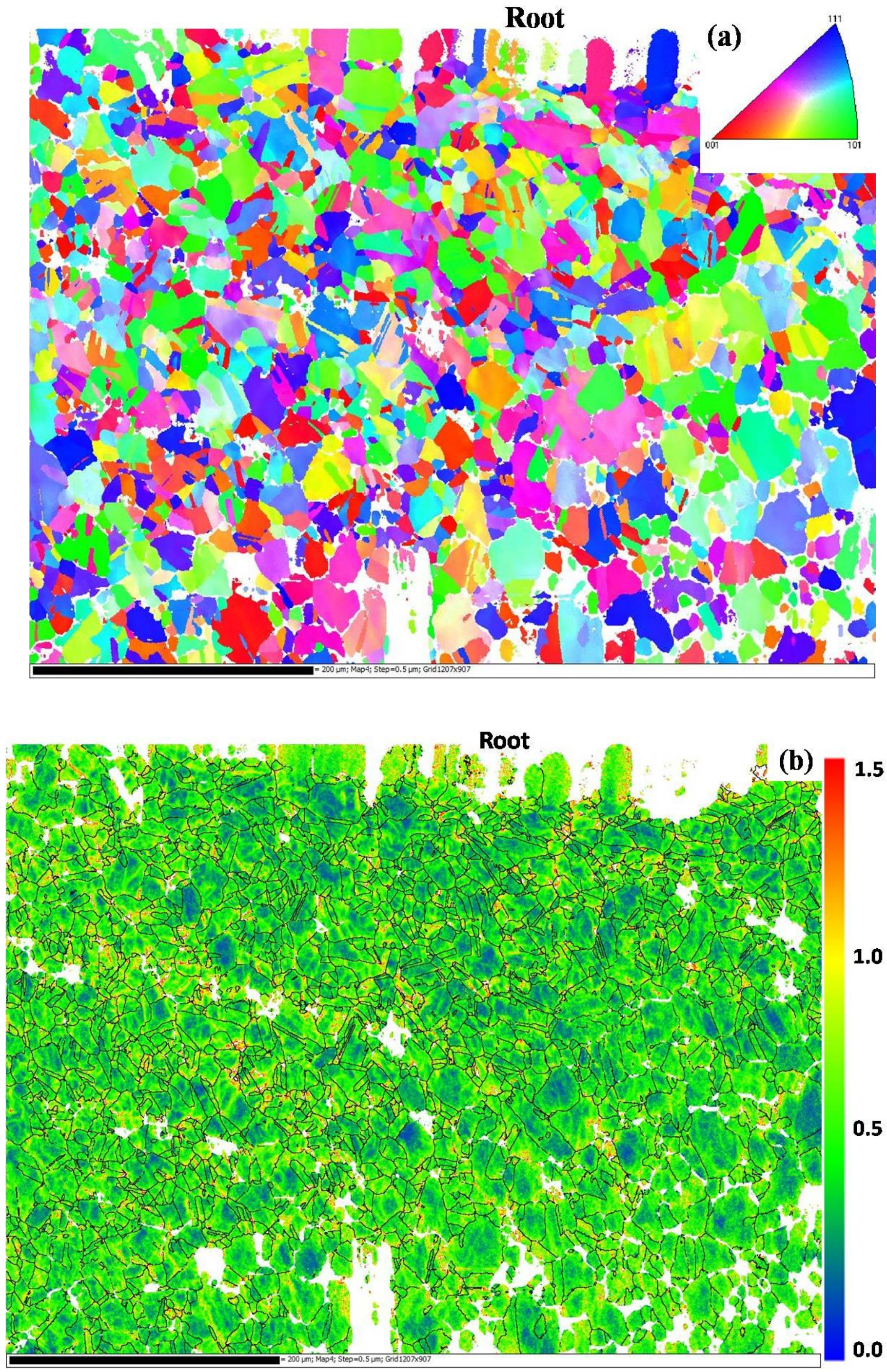

Fig. 4.23 (a) IPF map and (b) KAM map at the notch root for shallow notch (root radius = 2.5mm) creep tested at 973 K, 200 MPa

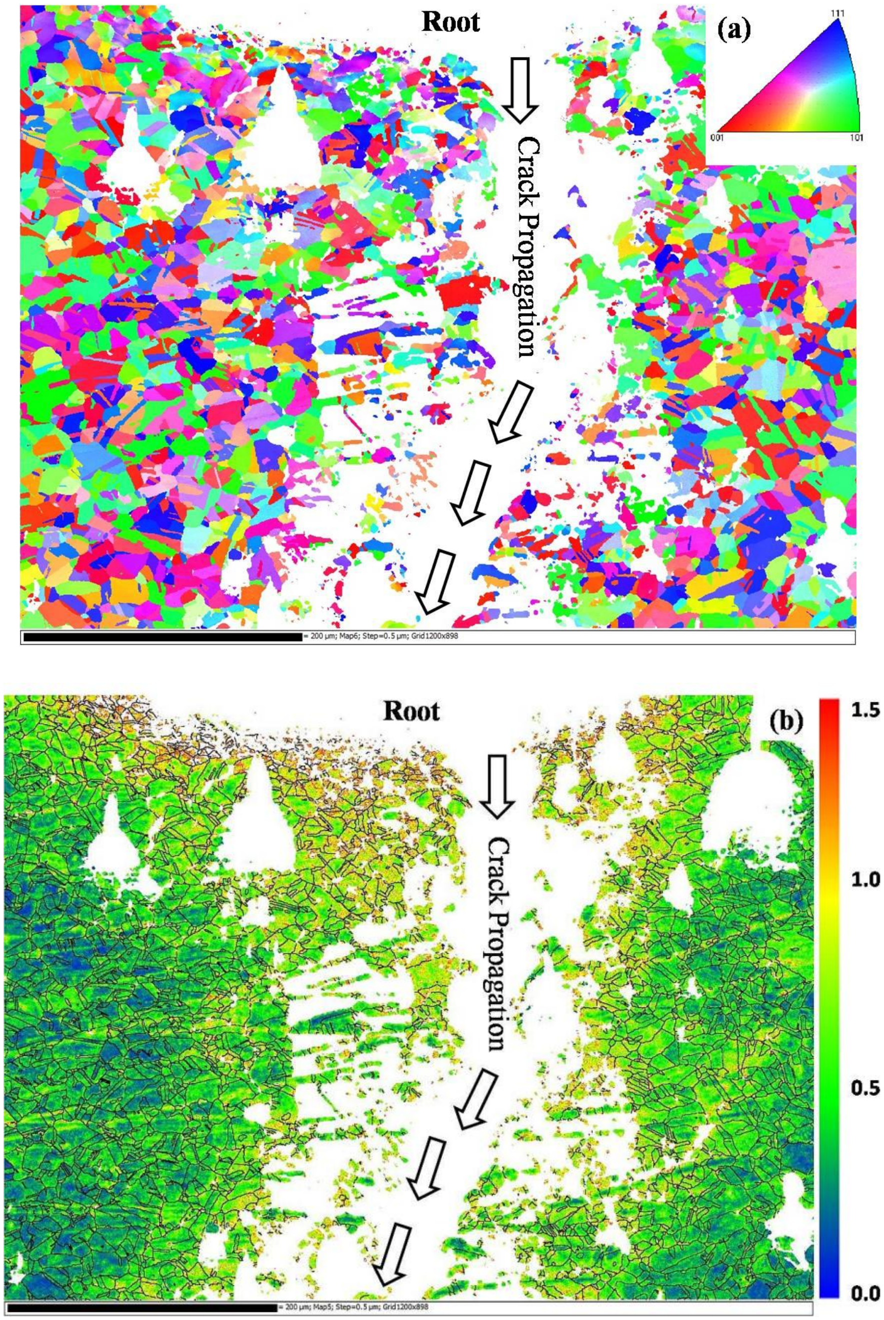

Fig. 4.24 (a) IPF map and (b) KAM map at the notch root for shallow notch (root radius = 0.25mm)creep tested at 973 K, 200 MPa.

4.6 Hardness distribution

The variation of micro-hardness distribution across the notch throat plane of unfailed notch of creep tested specimen at 220 MPa and 973 K for the notches of root radius 0.5 mm and

2.5 mm are shown in Fig. 4.25.The hardness variation showed a dip at the notch root, which was higher for sharper notch than for the shallow notch. Present alloy being hardened steel, interparticle spacing plays an important role in governing strength. The steel is strengthened by Nb(C, N) precipitates and copper particle [13, 123].

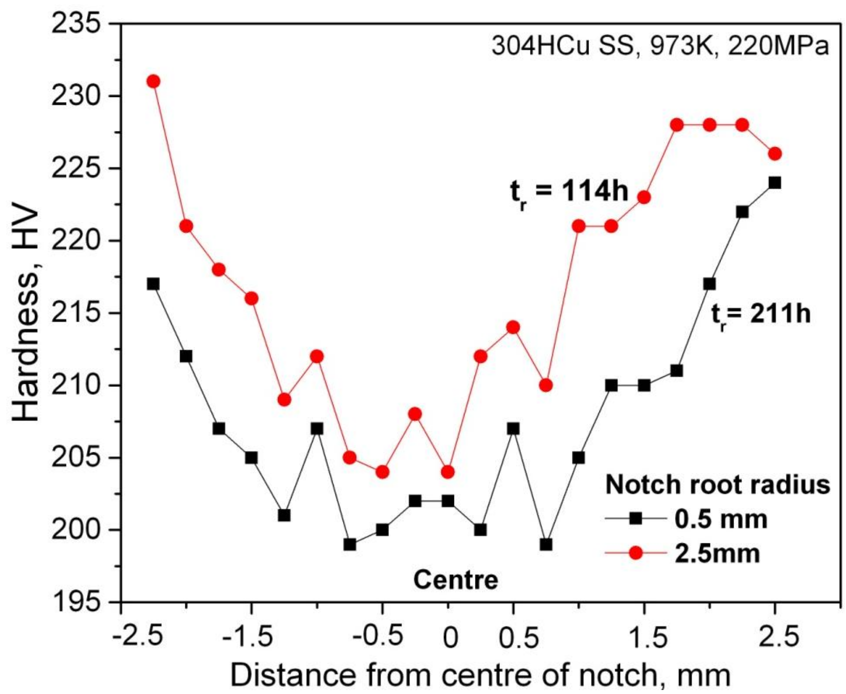

Fig. 4.25 Hardness variation across the centre of notch (un-failed notch) for shallow notch (notch root radius 2.5 mm) and sharp notch (notch root radius 0.5 mm), creep tested at 220 MPa and 973 K.

TEM micrographs of the creep test (200 MPa, 973 K) notch specimen (notch root radius 1.25 mm) are shown in Fig. 4.26. Figure 4.26(a) was from the TEM specimen extracted at the notch centre and Fig. 4.26(b) away from the notch centre but close to notch root. The multiaxial state of stress enhanced carbide particle coarsening along with the tendency towards the dislocation cell formation for relatively sharper notches. In general, low stacking fault energy materials have reduced tendency to form cell structures [164]. However, stress concentration factor associated with notch triaxiality leads to the activation of multiple slip system thereby increases the dislocation interaction [Fig. 4.26(a)] and tendency to cell formation. This also increases generation of point defects and enhanced the diffusion of solute elements responsible for coarsening of carbides.

The deformation band structure away [Fig. 4.26(b)] from the notch root decreases the hardness of the steel as the deformation proceeds More severe localized deformation for relatively longer period (increase in rupture life with notch sharpness) decreased the hardness to a greater extent for sharper notch specimen (Fig. 4.25).

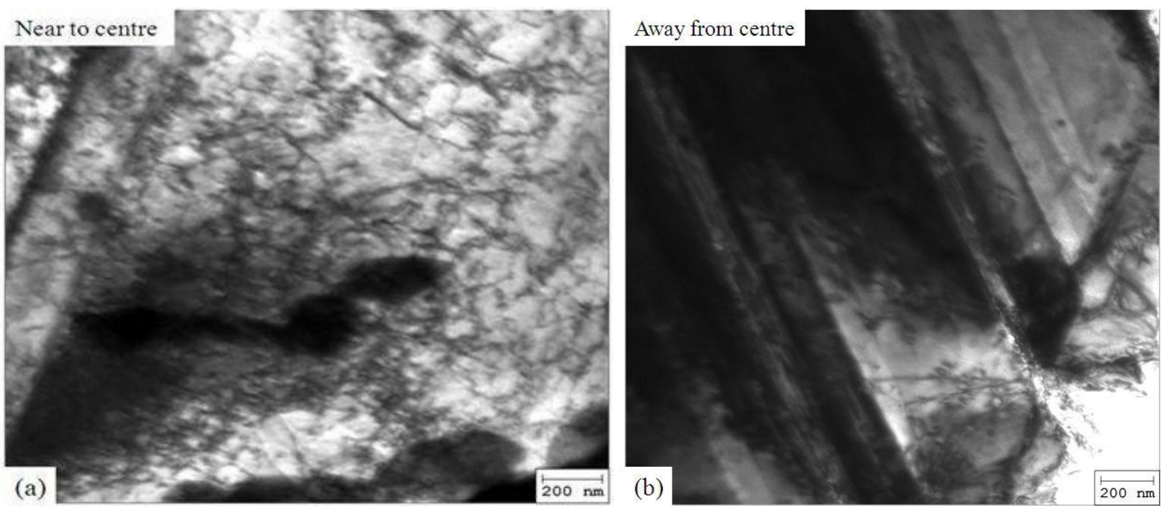

Fig. 4.26 TEM microstructure of the specimens extracted from unfailed notch (1.25 mm root radius) creep tested at 200 MPa and 973 K, (a) near to notch centre and (b) away from the notch centre.

4.7 Conclusions

Based on the studies on creep rupture behaviour of 304HCu steel under multiaxial state of stress incorporated on introducing notch of different notch acuity ratios in smooth specimen along with FE analysis, SEM and EBSD, following conclusions are drawn:

1. Rupture life of the 304HCu austenitic stainless steel increased in presence of notch, indicating notch strengthening. The strengthening increased drastically with notch sharpness and tends to a saturation value. The strengthening was also associated with decrease in rupture ductility.

2. Fracture appearance depends on notch acuity ratio and applied stress. For relatively high stresses and shallow notches, ductile dimple appearance was observed at the central region with intergranular creep cavitation at/near the notch root. For relative lower stresses and sharper notches, extensive intergranular creep cavitation at the notch root regions propagated towards the central region.

3. Localized creep cavitation at the notch root is preceded by localized creep strain around the notch root region as measured through EBSD analysis.

4. Finite element analysis of the stress distributions across the notch throat plane clearly demonstrates that the creep behaviour of the notched specimen is governed by severity of the notch. Reduction of von-Mises stress across the notch throat plane led to the increase in creep rupture strength. Extensive creep cavitation has been correlated with high principal stress.

Chapter: 5

EFFECT OF NOTCH GEOMETRY AND TEST TEMPERATURE ON CREEP DEFORMATION, DAMAGE AND RUPTURE LIFE

5.1 Introduction

In the present chapter creep rupture behaviour of 304HCu SS in the presence of circumferential U-notch (0.25 mm to 5 mm) has been studied with the effect of temperature (at 923, 973 and 1023 K) over wide range of stresses. The selection of test temperatures was based on the possible usage of the steel over 673 - 948 K in AUSC boiler. Also, there is a necessity to understand the influence multiaxial creep deformation on fracture and damage behaviour of the steel. The creep deformation and stress distribution with the influence of temperature has been studied at the notch throat plane through FE-analysis. On the other hand damage distribution at the notch throat plane has been studied with Optical micrography, SEM metallographic and Orientation imaging microscopic (OIM) analysis through EBSD.

5.2 Effect of temperature on creep rupture life and ductility

Presence of notch on smooth specimen resulted in significant variation in creep rupture life and ductility depending on the geometry of the notch, applied stress and temperature. Variations of rupture life of the steel having Notch Acuity Ratio (NAR) of 4 along with smooth specimen with net stress are shown in Fig. 5.1(a) for different temperatures, showing general effect of decrease in creep rupture life and stress sensitivity in rupture life with increase in temperature. In the presence of notch, the effect of stress sensitivity on rupture life decreased and the decrease was more significant at 923K and was least for 1023 K. It can be seen that rupture life of both notched and unnotched specimen are comparable to each other when stress level is around 180 MPa. It may result notch weakening if the applied stress is less than 180 MPa of the given notch at 923 K. Further, it is evident that for all the temperatures under investigated stress range, the slope value was not found to change from higher stress to lower stress level for both smooth and notch specimen for rupture lives less than 7000 hours. In the present study, the intergranular creep fracture in the material is mainly due to stress triaxiality (notch specimen) and high temperature (above the service temperature). It may however be anticipated that, the changes in constant due to change in slope may occur during long term tests upon change in fracture mode (from transgranular to intergranular) due to microstructural changes in the material. The extent of strengthening with varying NAR for different temperatures is shown in Fig. 5.1(b) for an applied stress of 200 MPa. The strengthening increased with notch sharpness (NAR) but the extent of strengthening depended on the testing temperature appreciably. The strengthening tendency with notch sharpness became more with increase in temperature, signifying that the stress distribution in presence of notch impeding the deformation is relatively more at higher temperatures, the detailed aspects of which will be discussed in subsequent section. The creep ductility (reduction in area, %) decreased with notch sharpness and the testing temperature had relatively insignificant effect (Fig. 5.1(c)).

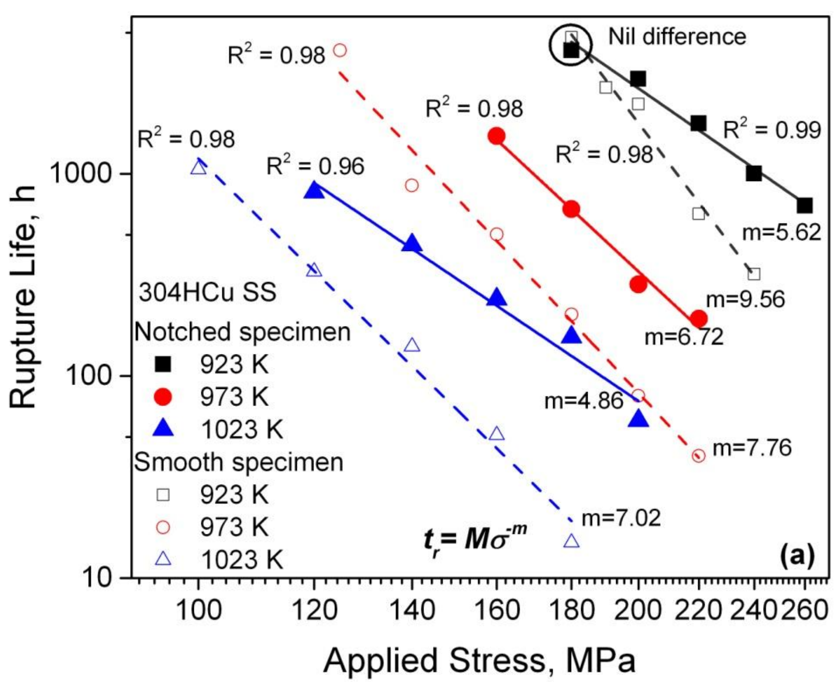

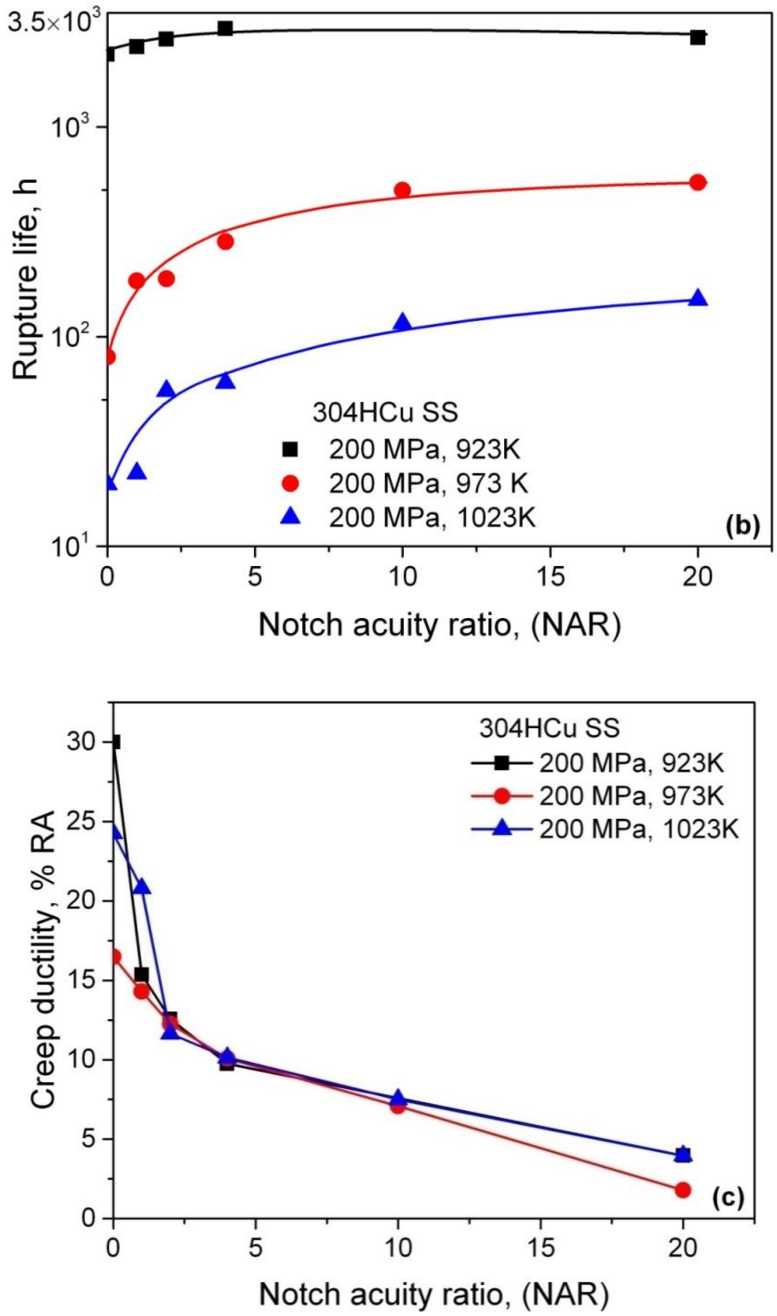

Fig. 5.1 Variations of (a) creep rupture life of notched specimens of the steel with net applied stress, (b) creep rupture life and (c) creep ductility with notch acuity ratio at 923 K, 973 K and 1023 K at 200 MPa.

5.3 Effect of temperature on fracture appearance and damage assessment

To assess the effect of temperature on fracture appearance, SEM fractography at notch root region was carried out on failed specimens creep tested at 923 K, 973 K and 1023 K and at 200

MPa for notch root radius of 1.25 mm (NAR =4) (Fig. 5.2)). The fracture was mostly dimple appearance at 923 K with some isolated creep cavities, Fig. 5.2(a). As the temperature increased, the extent of creep cavitation increased in the notch root region Fig. 5.2(b) and Fig. 5.2(c), depicting that increase in temperature enhanced the creep cavitation propensity [165]. Further investigation of creep cavitation was carried out by polishing the un-failed notch (failed at one notch, other two are left for investigation) for notch root radius of 0.25 mm creep tested at 923 K, 973 K and 1023 K and 200 MPa (Fig. 5.3). The extent of intergranular creep cavitation was significantly less at lower temperature, Fig. 5.3(a). With increase in temperature, the extent of creep cavitation increased as shown in Fig. 5.3(b) and Fig. 5.3(c). At 1023 K, the crack in the un-failed notch reached to the extent of complete fracture, Fig. 5.3(c).

5.3.1 Damage Area fraction calculation for different notch acuities

In order to understand the effect of temperature and notch sharpness on damage, damage area fraction was calculated through Image-J software by capturing several images at different distance from notch root towards the center for three notches of notch root radius of 0.25, 1.25 and 2.5 mm creep tested at 923 K, 973 K and 1023 K and at 200MPa are shown in Fig. 5.4. Relatively extensive damage was observed in the notch root region than at the notch central region. The extent of damage across the notch throat increased with increase in temperature. The damage was found to be least for relatively shallow notch (NAR=2) and low temperature. It clearly indicates that the extent of damage increases with increase in notch sharpness and test temperature.

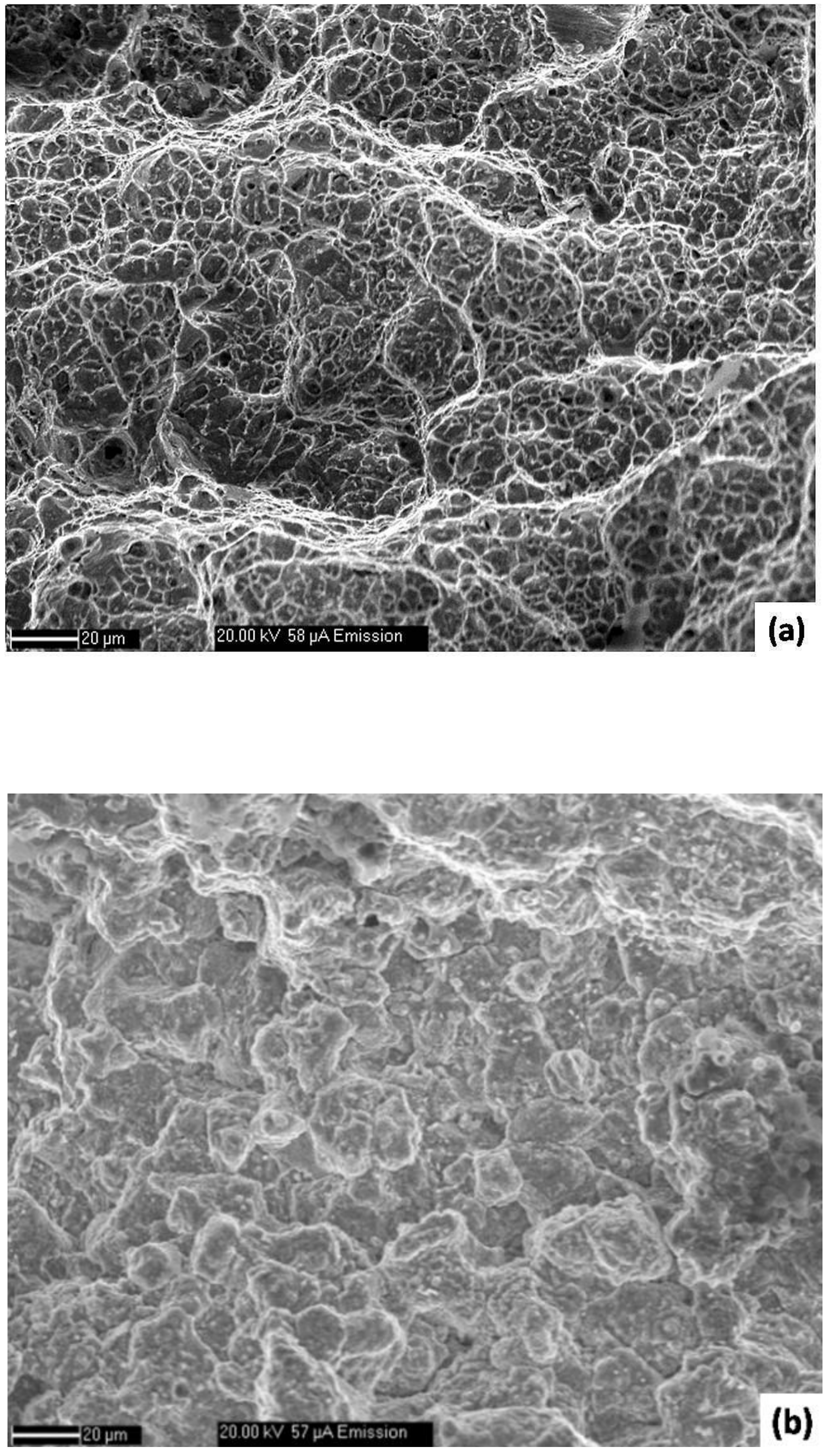
20 µm
20.00 kV 58 µA Emission
(a)
20 µm
20.00 kV 57 µA Emission
(b)

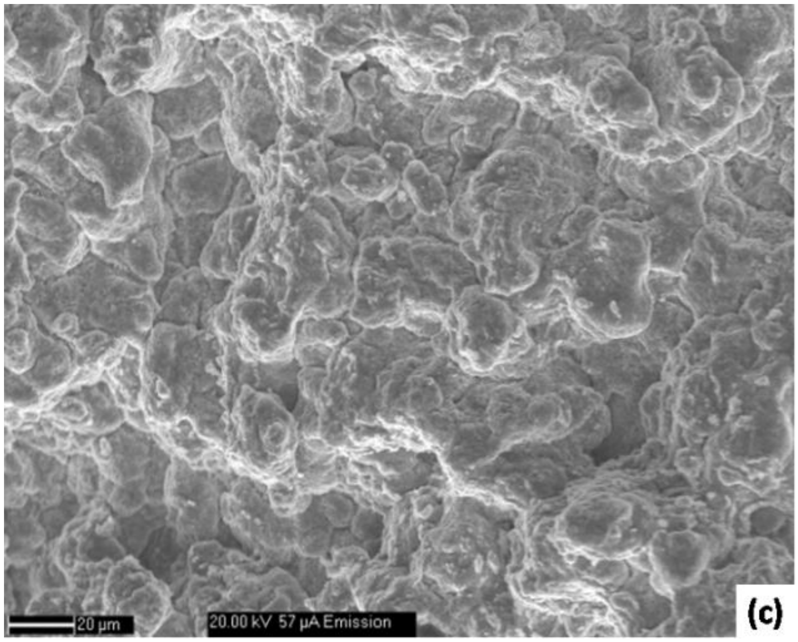

Fig. 5.2 Fracture appearances near notch root in creep tested specimens at (a) 923 K, (b) 973 K and (c) 1023 K and 200 MPa for notch root radius of 1.25 mm NAR=4).

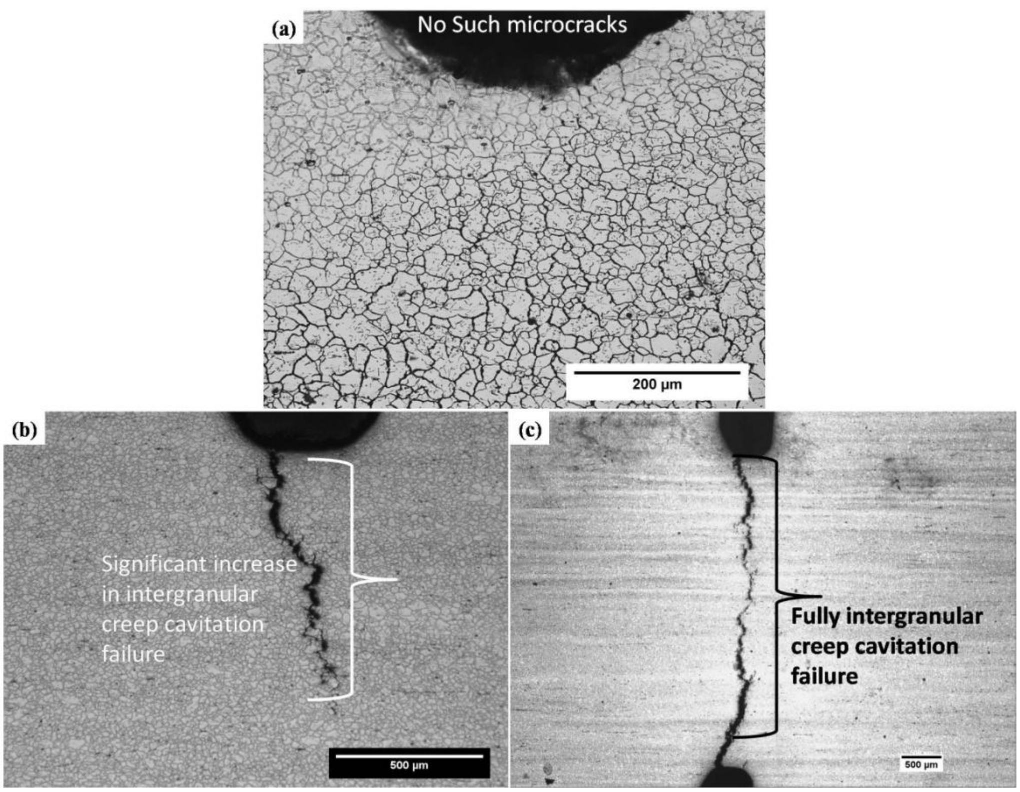

Fig. 5.3 Optical micrographs of the unfailed notch (notch root radius of4.25 mm, NAR=4) creep tested at200 MPa at temperatures of (a) 923 K, (h) 973 K and (c) 1023 K.

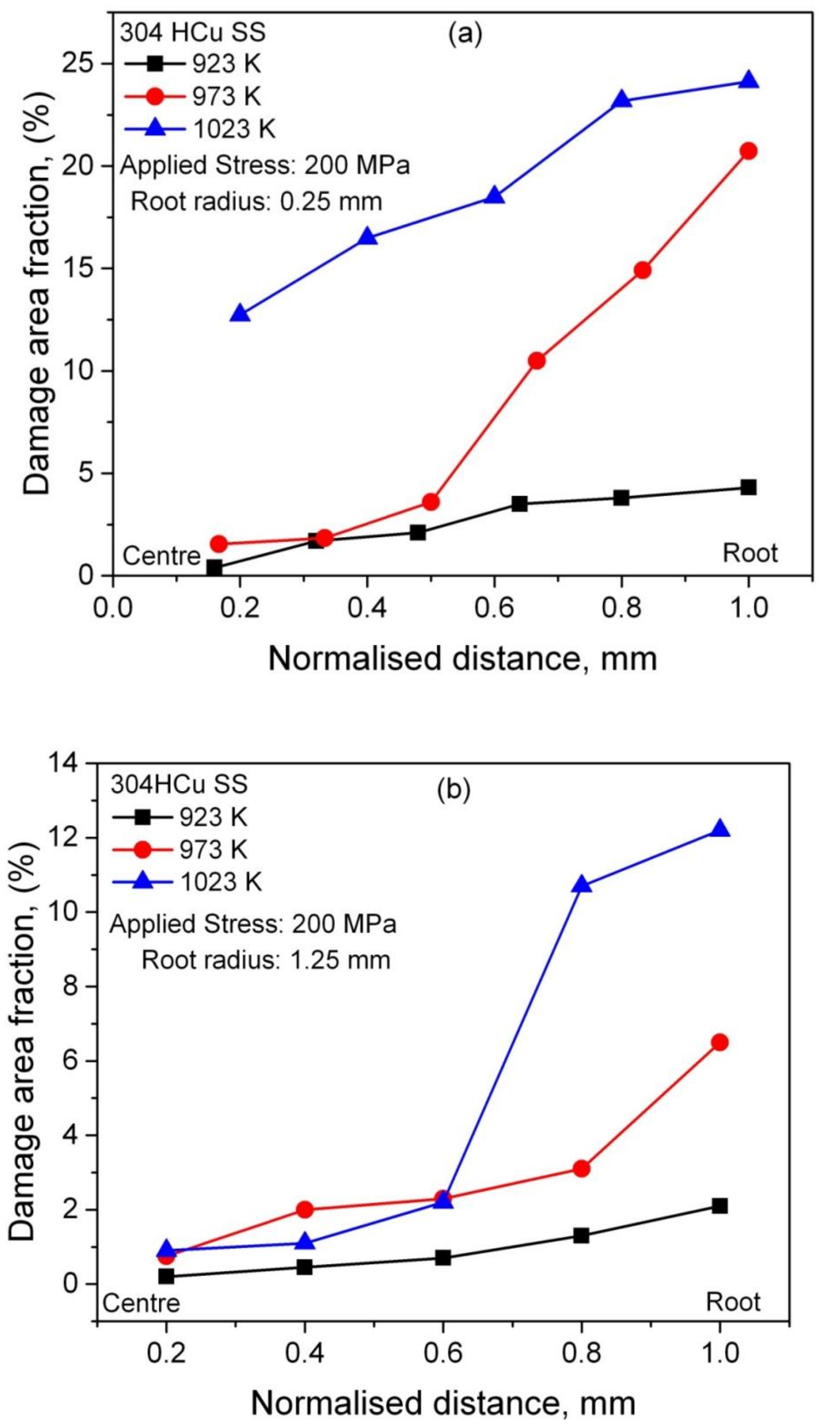
304 HCu SS
(a)
923 K
973 K
1023 K
Applied Stress: 200 MPa
Root radius: 0.25 mm
Damage area fraction, (%)
Centre
Root
Normalised distance, mm
304HCu SS
(b)
923 K
973 K
1023 K
Applied Stress: 200 MPa
Root radius: 1.25 mm
Damage area fraction, (%)
Centre
Root
Normalised distance, mm

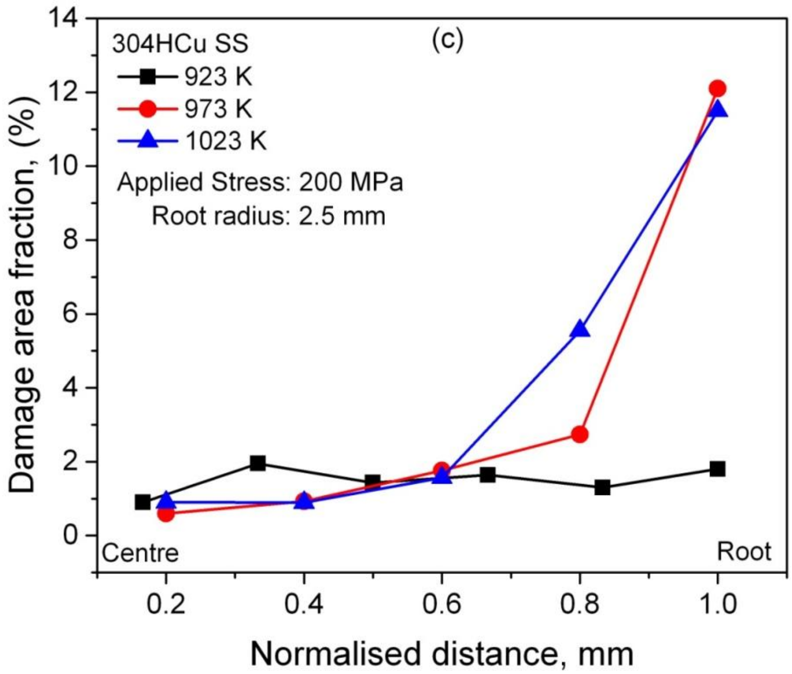

Fig. 5.4 The variations of damage area fraction with normalized distance from notch root to center at 923 K, 973 K, 1023 K and 200 MPa for notches of root radius (a) 0.25 mm (NAR=20) (b) 1.25 mm (NAR= 4) and (c) 2.5 mm (NAR =2).

5.3.2 Hardness variation as damage assessment

Variation in hardness of the steel on creep exposure is also considered as a means for assessing the creep damage. Hardness measurements on creep exposure (notch specimen having NAR = 4, 200 MPa and 923 K, 973 K and 1023 K) were taken in two directions, viz., along the (i) radial direction from notch root to notch center in notch throat plane and (ii) loading direction (perpendicular to notch throat plane) from notch center to notch shoulder (Fig. 5.5), schematics embedded in the figures show hardness measurement plans. The steel in before-creep-test condition (as-received) had hardness of around 186HV. On creep exposure, hardness near the notch root was much higher than the hardness value before creep testing and gradually decreased towards central region (Fig. 5.5(a)).With increase in test temperature, the overall hardness decreased across the notch throat plane and remained above the hardness value before creep testing for the steel tested at 923 K and 973 K. However, at 1023 K the hardness values reduced than the hardness value before creep testing. Hardness change in loading direction from center on notch throat plane towards the notch shoulder showed hardness increased unto around notch shoulder then decreased to values close to the before-creep-test value or even below (Fig. 5.5(b)). The overall hardness variation from notch throat plane center towards the notch shoulder decreased on increase in creep test temperature (Fig. 5.5(b)). The hardness variations across the notch both across notch throat plane as well as perpendicular to it indicated a complex interaction of multiaxial state of stress due to the presence of the notch which generated localized creep deformation, strain induced precipitation [166] and structural recovery upon creep exposure [167]. Figure 5.6 (a) and (b) represents the TEM micrographs taken near to the notch throat plane and far away from the notch throat plane respectively of the unfailed notch at 1023 K for an applied stress of 120 MPa of notch acuity 4. Extensive dislocation cell formation as well as precipitation of Cu-particles pinning the dislocation movement were observed near to the notch root [Fig. 5.6 (a)]. This is due to higher degree of triaxiality (relatively sharper notch) which results increase in strain induced precipitation and their complex interaction with dislocations results well defined dislocation structures/cells and tangles and increases hardness at the notch root. On the other hand, homogeneous precipitations of Cu-particles with Nb(C, N) were observed far away from the notch location with no such dislocation cell formation resulting decrease in hardness compared to earlier one [Figure 5.6 (b)]. A systematic study invoking finite element analysis for multiaxial state of stress and strain, and stress/strain induced precipitation and recovery of the present steel may help to assess performance of the steel under complex tri-axial stress environment generated due to the presence of the notch.

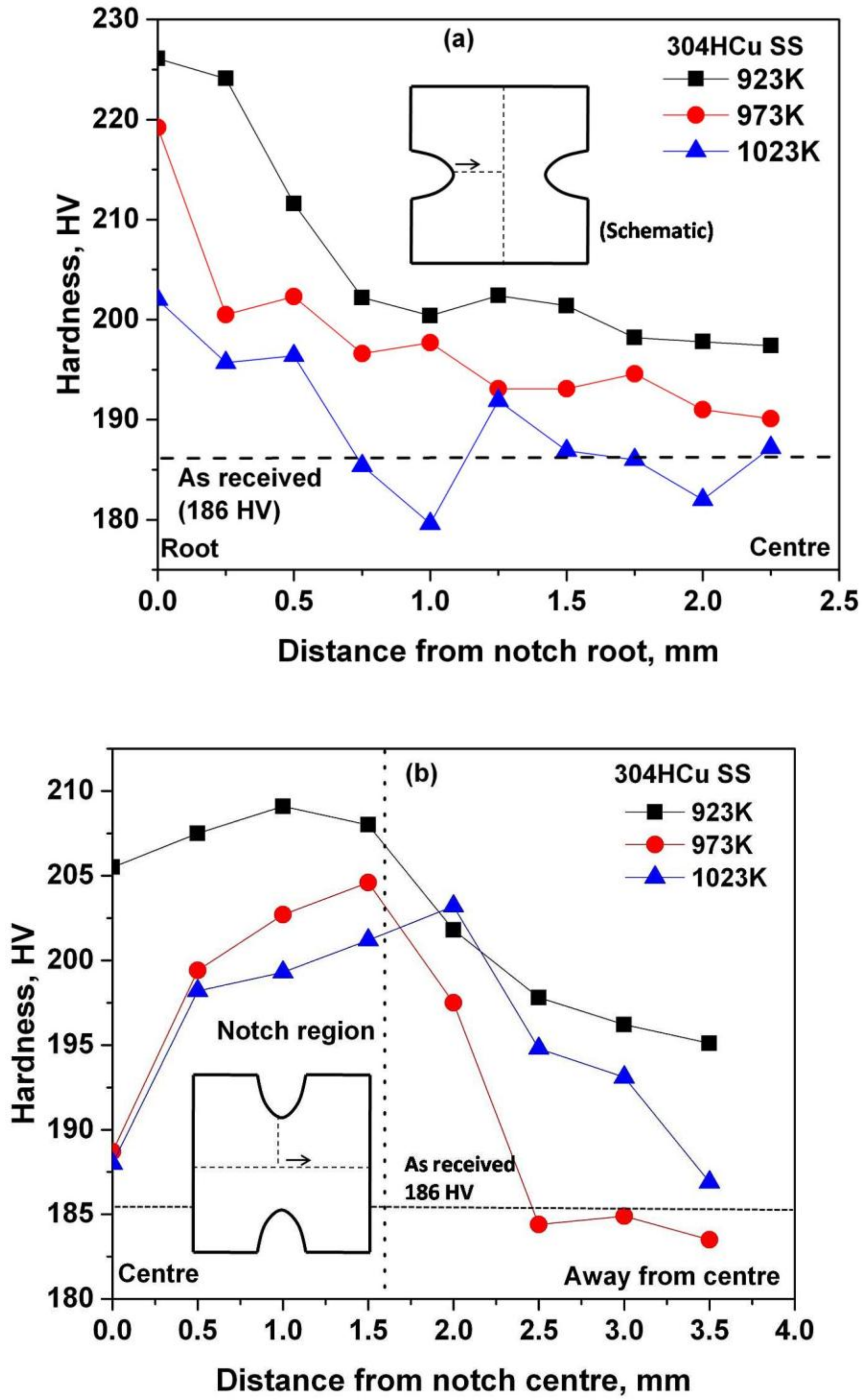

Fig. 5.5 Hardness variation across (a) root to center of (un-failed notch) and (b) center to away from the centerfor 1.25 notch (Notch acuity 4) creep tested at 200 MPa and 973 K (testing planes are inserted in the figure).

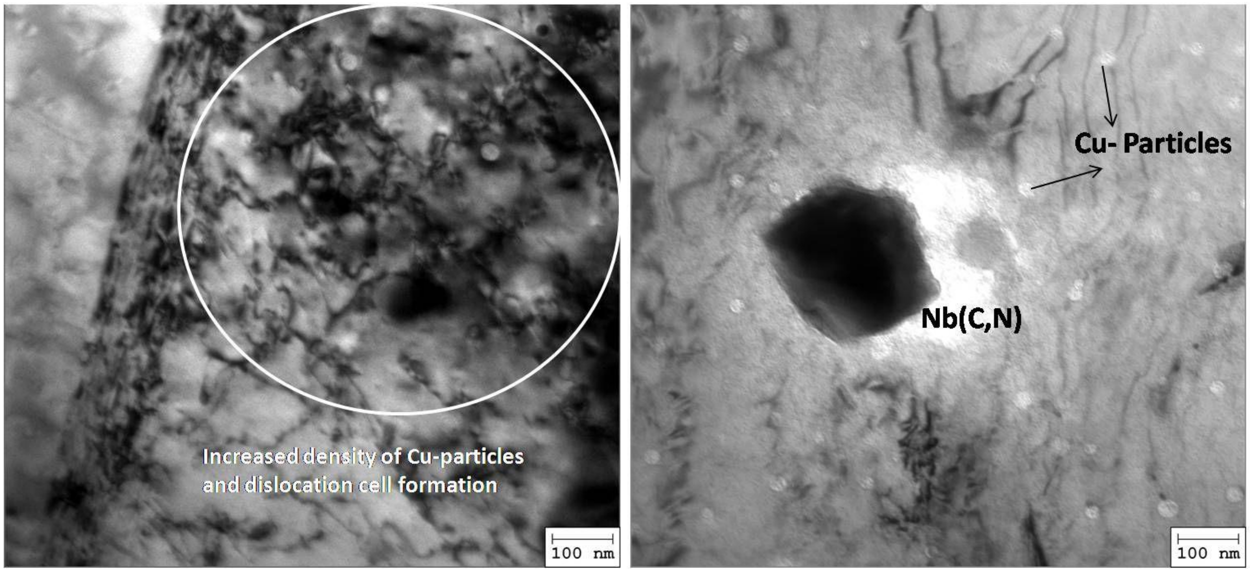

Fig. 5.6 TEM microstructure of 304HCu SS creep tested at 1023 K, 120 MPa for notch acuity ‘4’ (a) near to the notch root and (b) far away from the notch root.

5.3.3 Damage Assessment using OIM analysis (EBSD)

To understand the underlying causes resulting in variation in creep damage with respect to change in temperature and normalized stress, Orientation Imaging Microscopy (OIM) was carried out. The KAM and the twin density were mapped using OIM analyzed adjacent to the notch root regions. The KAM map has been widely used to estimate the localized strain evolution resulting from slip [168]. The damage evolution observed from optical micrographs was correlated with the KAM and twin density mapping.

In order to compare the effect of temperature, normalizing was done to iron out the differences in applied stress and yield stress values. The stress values are reported as Normalized Stress Ratio (NSR) which is the ratio of applied stress to the yield stress at the corresponding temperature. Though the tests at 923 and 1023 K were conducted at varying stress levels, the normalizing resulted in only two distinct NSR values (i.e, 1.1 and 1.2) for each temperature. Hence a straightforward comparison could be made on the effect of temperature on the steel tested at 923 K/ 200 MPa and 1023 K/ 180 MPa as both these tests had a similar NSR value of 1.1. Similar normalizing for the steel tested at 923 K/ 220 MPa and 1023 K/ 200 MPa resulted in NSR value of 1.2. Figure 5.7shows the optical micrographs taken at the notch root at 923 K (NSR-1.1), 1023 K (NSR-1.1), 923 K (NSR-1.2) and 1023 K (NSR-1.2) for notch of notch root radius 1.25 mm (NAR 4) showing creep cavitation tendency. It could be seen that for the steel tested at 923 K, the type of isolated inter-granular cavities uniformly distributed at the notch root irrespective of the change in NSR; whereas in case of the steel tested at 1023 K, creep cavities coalesced and formed inter-granular cracks at both the NSRs.

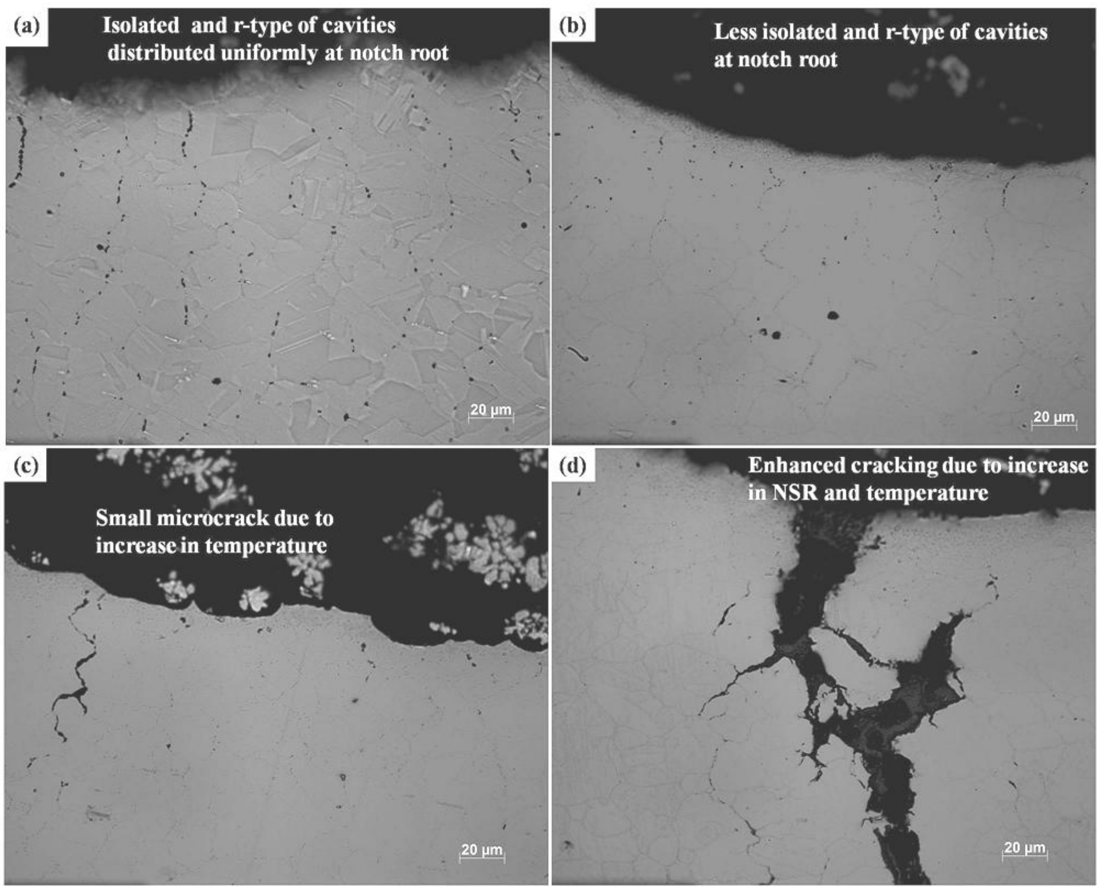

Fig. 5.7 Optical micrographs taken near to notch root at (a) 923 K (NSR-1.1), (b) 923 K (NSR-1.2) (c) 1023 K (NSR-1.1), (d) 1023 K (NSR-1.2) for notch of notch root radius 1.25 mm (NAR 4).

Through FE-analysis it could be seen that the equivalent stress i.e. von-Mises stress is same at the notch root for 923 K and 1023 K at 1.1 and 1.2 NSR, the damage evolution was quite different under each of these testing conditions [Fig. 5.8]. It is therefore necessary to compare the strain accumulation at the notch root for different NSRs to comment on the damage evolution.

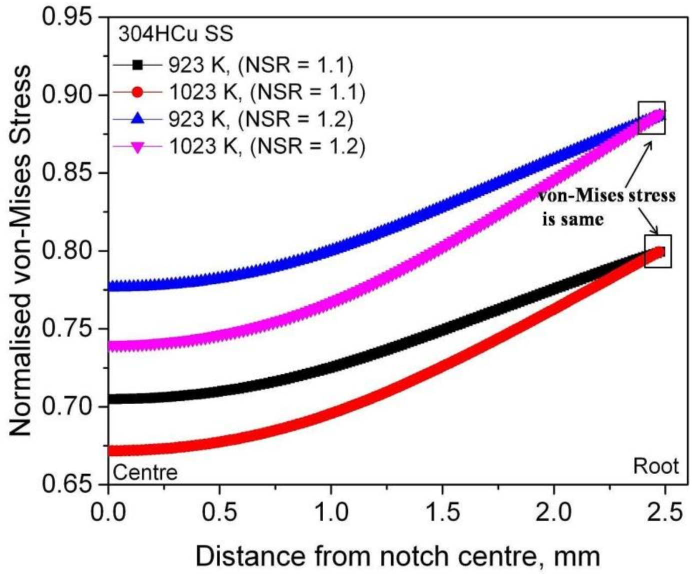

Fig. 5.8 shows the distribution of normalized von-Mises stress (NSR=1.1& 1.2) with distance from notch centre at 923, 1023 K.

The KAM maps taken at the notch root are shown in Fig. 5.9 (a-d). It shows that the local misorientation values are more at the grain boundaries than inside the grains. This suggests that the ability of the material to fail in intergranular manner. The misorientation spread which is an estimate of the localized strain accumulation is plotted in Fig. 5.10.For the steel tested at 923 K and NSR value of 1.2, the misorientation values were lower than the steel tested at all other conditions, indicating lower strain accumulation due to slip (Fig. 5.10).

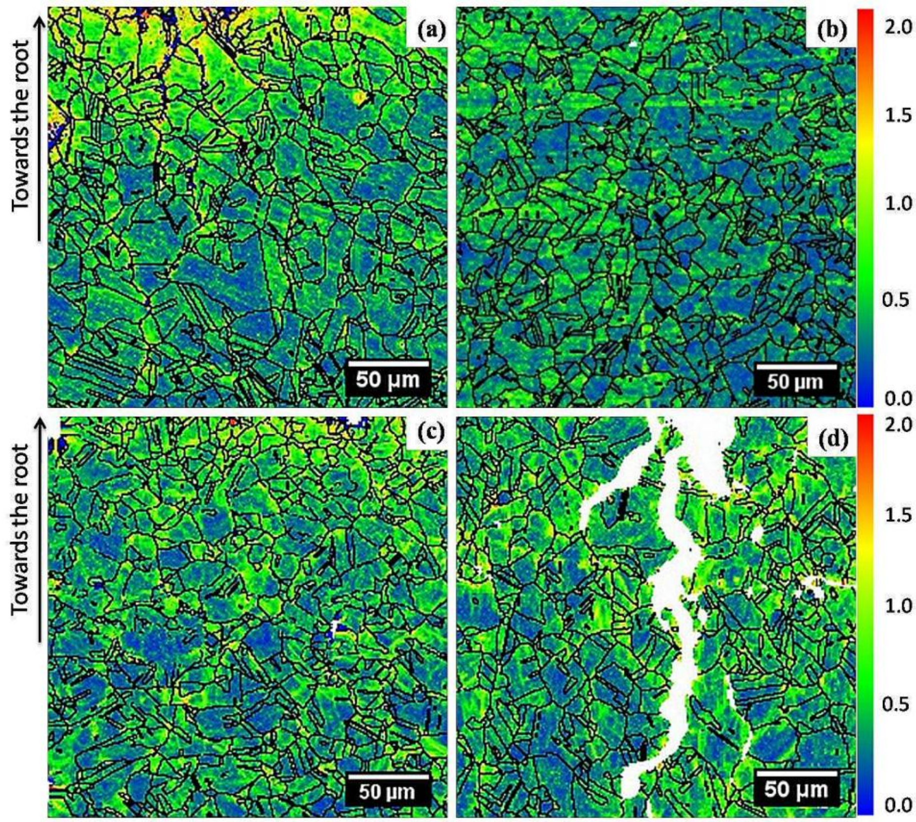

Fig. 5.9 OIM-KAM map at (a) 923 K, 200MPa (NSR=1.1), (b) 923 K, 220MPa (NSR=1.2), (c) 1023 K, 180MPa (NSR=1.1), (d) 1023 K, 200MPa (NSR=1.2).

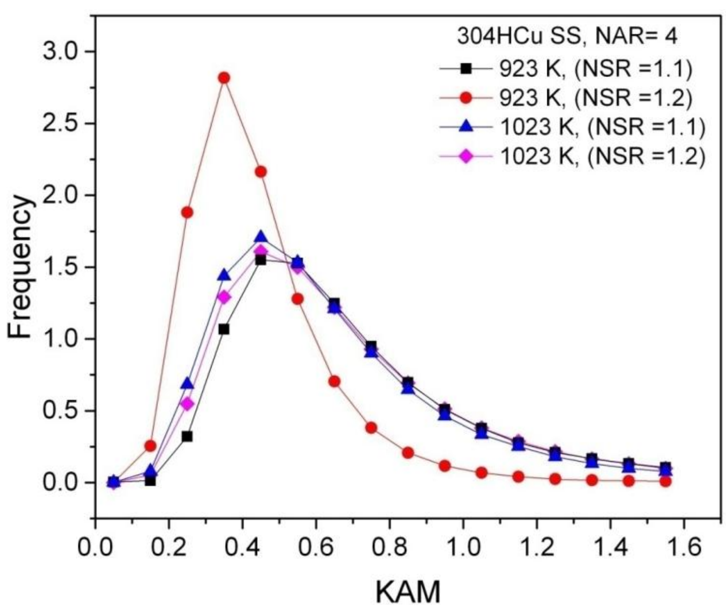

Fig. 5.10 Shows the frequency vs KAM plot at different conditions of NSR and temperature.

The twin density map obtained at the same regions is shown in Figures 5.11 (a-d). The values of twin density are quantified in Table 5.1. For the steel tested at 923 K and NSR value of 1.2 the twin density was substantially higher than all the other conditions. The increase in temperature results in softening of the microstructure which results in lowering the constraint induced by the notch. It has been reported that the strengthening caused by the copper rich precipitates is higher at 923 K when compared to 1023 K [128]. The constraint generated due to the presence of the notch restricts plastic deformation due to slip which results in onset of twining or creep cavitation.

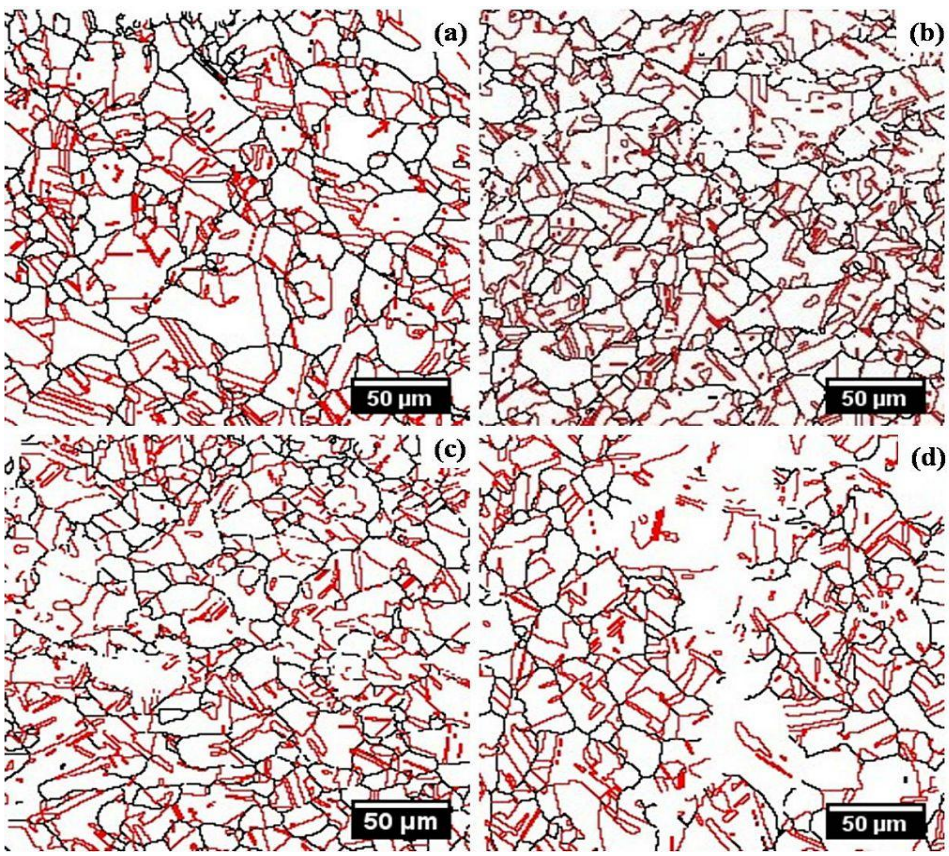

Fig. 5.11 Twin density map through EBSD (a) 923 K, 200MPa (NSR=1.1), (b) 1023 K, 180MPa (NSR=1.1), a) 923 K, 220MPa (NSR=1.2), a) 1023 K, 200MPa (NSR=1.2).

Table- 5.1 Shows the percentage of twin density at different normalized stress ratio and temperature

Temperature	Twin Density	
	1.1 (NSR)	1.2 (NSR)
923 K	32.2 %	46.4%
1023 K	39.3%	38%

Though isolated creep cavities were observed under both the NSR values at 923 K they were more prominent at NSR 1.1. Isolated cavities nucleate at this condition due to the localized strain accumulation generated by the constraint developed due to the presence of the notch and prolonged exposure at elevated temperature. It has been shown that cavity nucleation can occur due to localized strain accumulation (due to the presence of notch) which results in formation of vacancies and condensation of these vacancies which is a time dependent phenomena [9]. However at this temperature, for the steel subjected to higher NSR of 1.2, relatively lower density of the isolated cavities were observed. At this testing condition the twin density was significantly higher. The enhanced constraint generated due to higher applied NSR resulted in activation of twinning. It has been reported that the critical stress required for activating twin systems is relatively higher when compared to activating slip systems [169]. As a consequence of increase in twin density, the localized strain accumulation reduced which precluded nucleation and condensation of vacancies. The KAM map of the steel subjected at 923 K and NSR value of 1.2 clearly shows lower localized strain accumulation when compared to the steel tested at all other test condition [Fig.5.9(b)]. In summary, increase in temperature and stress results increase in twin density; however stress has significant effect compared to temperature.

At 1023 K, the kinetics of cavity nucleation is lower as the steel becomes relatively weaker due to the coarsening of the copper rich precipitates. At this temperature, though the numbers of isolated cavities are lower, its growth resulting in the formation of micro-cracks which occurs with little hindrance due to the ease of plastic flow [24]. The increased plastic flow at this temperature resulted in higher values of misorienation spread in the KAM maps (Fig.5.9). This result in generation of more number of micro-cracks when compared to the steel tested at 923 K. The application of higher normalized stress of 1.2 resulted in considerable increase in von-Mises stress resulting in extensive growth of the micro-cracks.

5.4 Finite element analysis of stationary state of stress across the notch:

Incorporation of notches of different sharpness on smooth specimen redistribute the stress across the notch during creep resulting in multiaxial state of stress [93] influencing the creep rupture life of the steel (Figs. 4.1 and 5.1). Creep deformation leads to failure of the material and the failure is accompanied with intergranular creep cavitation consisting of nucleation of creep cavities at a grain boundary and their growth and linkage into discrete cracks leading to final fracture [8, 96]. Different components of multiaxial state of stress in causing cavity nucleation and growth have been discussed by many investigators [82, 151, 152]. Nucleation of creep cavity is dependent on von-Mises stress [104]. Creep cavity nucleation is generally associated with stress and strain concentrations at the discontinuities on the grain boundary, such as precipitates, ledges, grain boundary triple points, etc. If the stress concentrations, produced when grain boundary sliding is held up by a finite amount of material around a discontinuity like a precipitate on a grain boundary are not relaxed, then cavities nucleate at the precipitate/matrix interface by athermal decohesion of atomic bonds between the precipitate and matrix [11]. Since grain boundary sliding is controlled by matrix deformation, von-Mises stress is important in creep cavity nucleation [104]. However, maximum principal stress decides the stability of the nucleated creep cavity by the following expression

$$r_c = 2\gamma_c/\sigma_1 \tag{5.1}$$

where r_c= critical cavity size, γ_c is the cavity surface energy and σ_1 is the maximum principal stress. Forthe growth of the nucleated creep cavity, it has to attain the critical size (r_c) otherwise it will sinter.

Two mechanisms of creep cavity growth have been primarily put forward: (i) inelasticity controlled growth and (ii) stress-directed flow of atoms (diffusive growth). Cavity growth by inelasticity occurs as a result of creep deformation of the matrix surrounding the grain boundary cavities in the absence of vacancy flux [6]. This mechanism of cavity growth during creep is closely related to the cavity growth during low-temperature/high-stress/short-term ductile failure, making von-Mises stress as the governing stress component aiding its growth. The diffusion-controlled cavity growth mechanism is described as time dependent stress directed flow of atoms from cavity surface to grain boundary through cavity surface and grain boundary diffusions, making normal stresses like principle and hydrostatic stresses as the controlling stress components [14]. However, the diffusion of atoms to grain boundary from cavity surface needs room as provided by deformation of the surrounding matrix and once again the von-Mises will be important stress component under constraint creep cavity growth situation [104].

FE-analysis has been extensively used for obtaining the stress distribution in the notched specimens under creep deformation [96, 135, 170]. The analysis has been carried out by considering the elastic deformation followed by time-dependent creep deformation. The FE analysis was performed on the notch root radius of 1.25mm (NAR 4) at 200 MPa and at 923 K, 973 K and 1023 K.The analysis was continued till the stationary state was achieved [171].The variations of normalized (with respect to yield stress) von-Mises, maximum principal and hydrostatic stresses across the notch throat plane for notch root radius of 1.25 mm at 200 MPa and at 923 K, 973 K and 1023 K are shown in Fig. 5.12. The normalization was carried out to compare the result at different temperatures. The normalized von-Mises stress distribution was found to be significantly lower at notch throat plane for 923 K resulting in significantly higher creep rupture strength than that for 1023 K (Fig. 5.1). With increase in test temperature, higher normalized von-Mises, principle and hydrostatic stresses, facilitated more creep cavity nucleation (von-Mises stress) and growth (normal stresses) which resulted in more pronounced creep cavitation at higher temperature under multiaxial state of stress (Figs. 5.2 and 5.3).

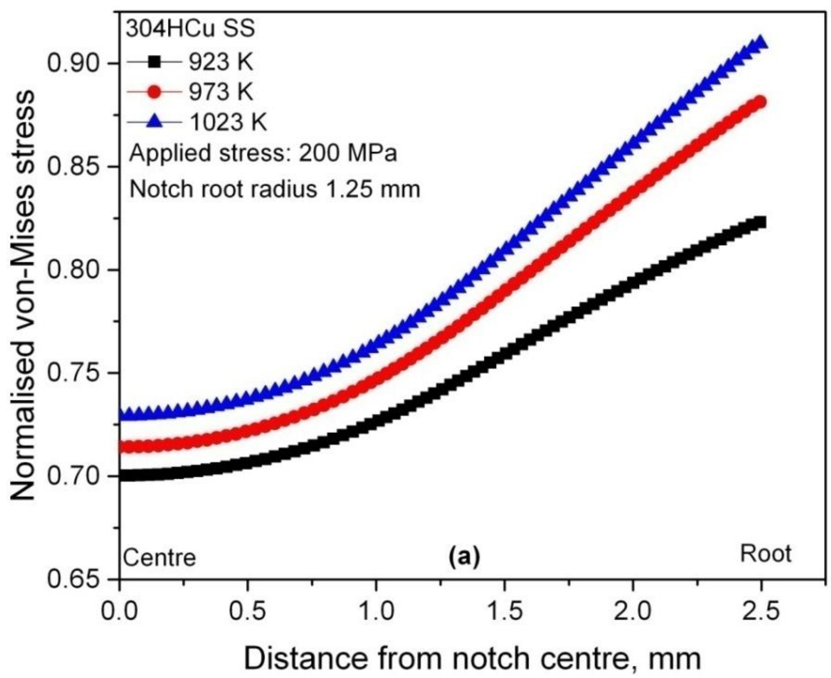

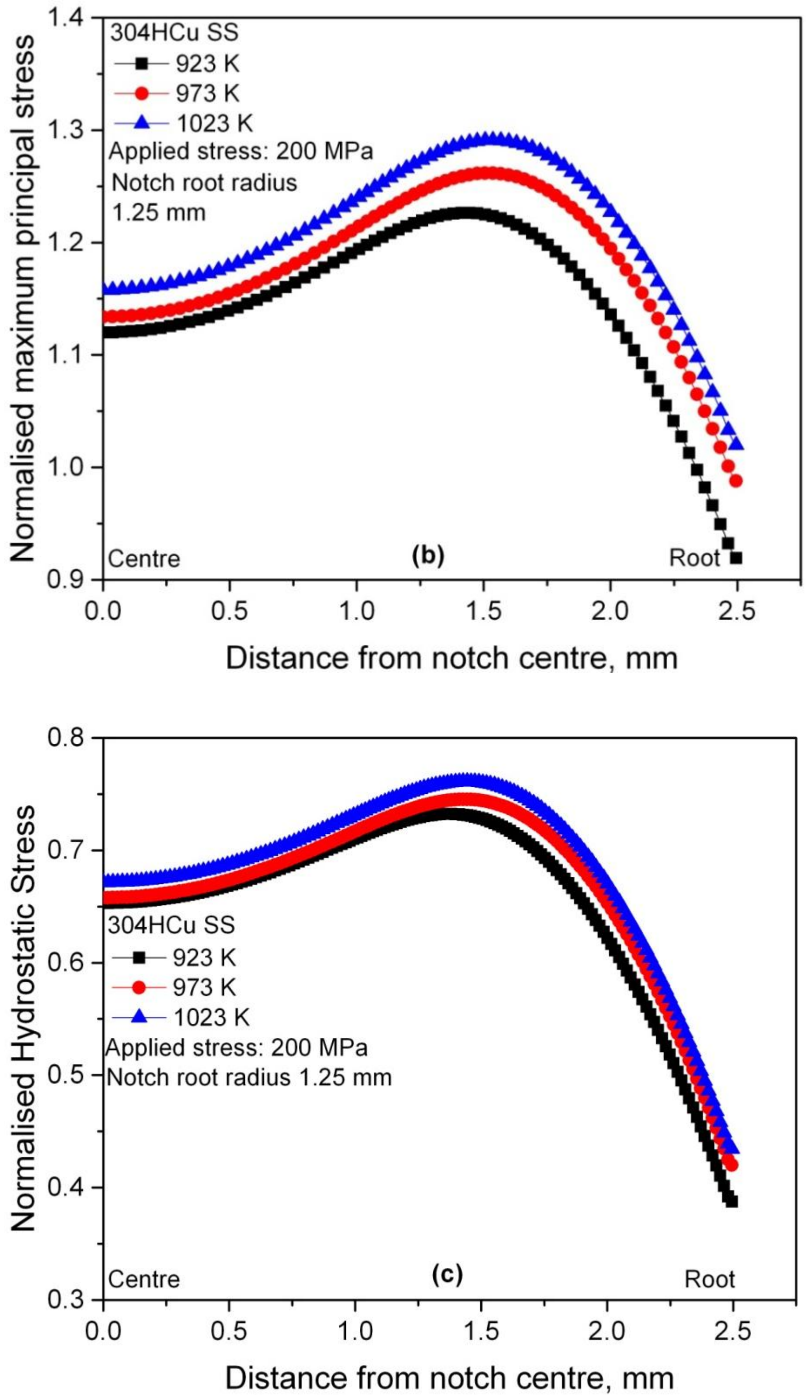

Fig. 5.12 Distributions of normalized (a) von-Mises, (b) maximum principal, and (c) hydrostatic stresses across the notch throat plane after attaining the stationary state for notch acuity 4 creep tested at (a) 923 K (b) 973 K (c) 1023 K, 200 MPa.

The influence of triaxial state of stress on creep deformation and fracture behaviour has already described by Wu et al. [92]. The triaxial factor depends on the notch geometry and material properties. The triaxilaity was found to increase with increase in temperature. More extent of triaxial state of stress at higher test temperature (Fig.5.13) also aids extensive creep cavitation under multiaxial state of stress.The higher degree of triaxiality resulted in enhanced creep cavitation inducing brittle failure (sharper notch) while lower degree of triaxiality results transgranular dimple failure (shallow notch) which has been reported in section 4.5. Similarly, lower creep tested temperature results transgranular dimple failure with little cavitations and higher creep tested temperature results intergranular creep cavitation brittle failure [Fig. 5.2].

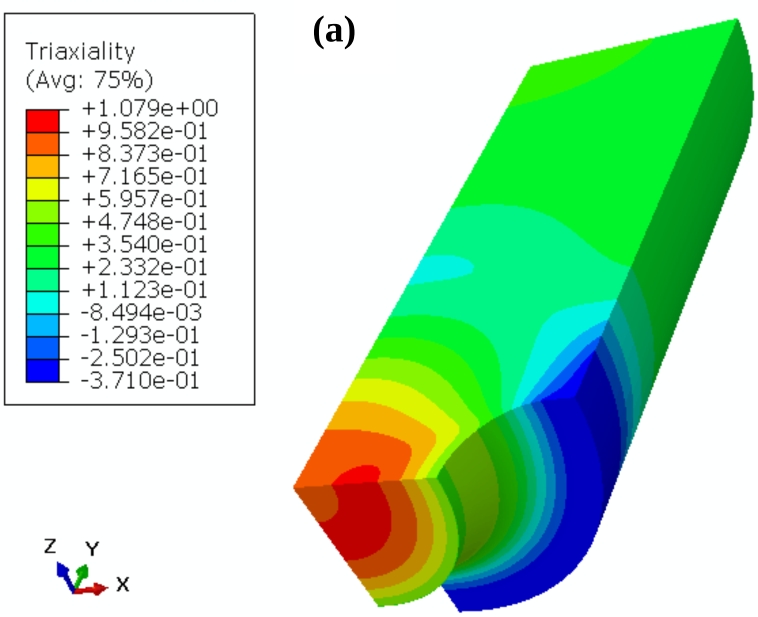

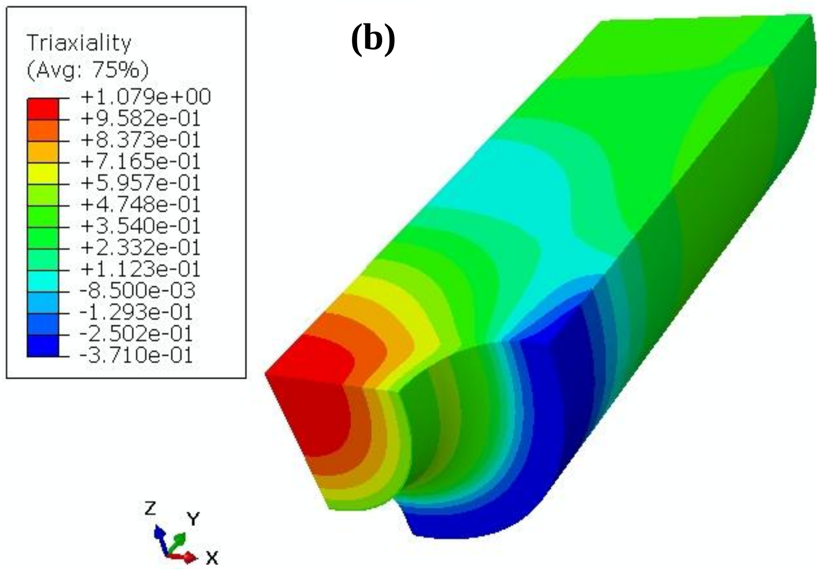

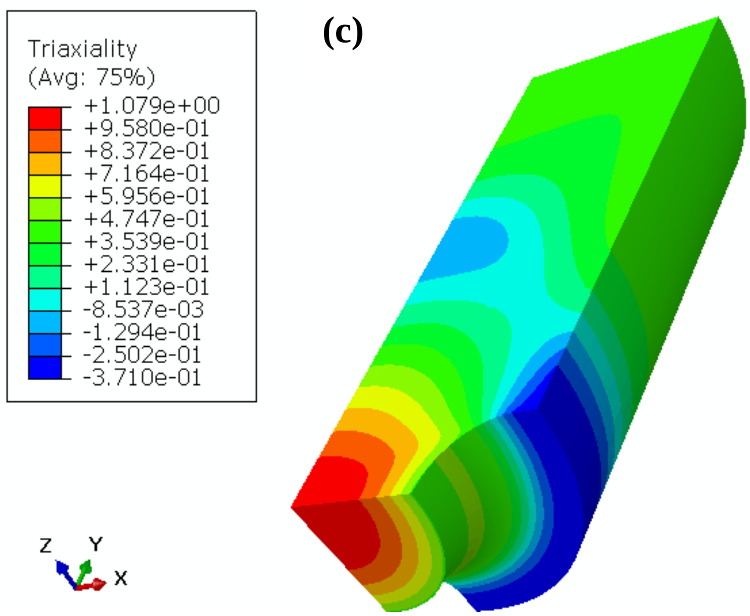

Fig. 5.13 Pictorial variation of triaxiality at the notch root for (a) 923, (b) 973 and (c) 1023 K at an applied stress of 200 MPa.

5.5. Conclusions: Based on detailed studies on the creep rupture behaviour of 304HCu steel at different temperatures under multiaxial state of stress incorporated on introducing notches of different root radius, following conclusions are made:

1. Creep rupture life of the steel increased under multiaxial state of stress over uniaxial stress, showing tendency towards saturation or slight deep with increase in notch sharpness. The increase in stress, notch sharpness and test temperature increased the rupture strengthening tendency. Creep rupture ductility of the material decreases significantly with increase in notch sharpness while effect of temperature on multiaxial ductility shows negligible difference.

2. Similar to increase in rupture life with notch sharpness, decrease in rupture life with testing temperature was associated with negligibledecrease in rupture ductility with change in fracture appearance from transgranular dimple to intergranular creep cavitation. Further, material exhibits higher damage for sharper notch (root radius=0.25 mm) creep exposed at 1023 K and least for shallow notch at 923 K.

3. OIM investigation showed that increase in KAM value which is a signature of enhanced localized strain accumulation resulted in considerable nucleation of cavities and micro-cracks. However, in case of the steel tested at 923 K and NSR 1.2 the activation of twinning resulted in lowering the localized strain accumulation which resulted in lower incidence of isolated cavities.

4. Finite element analysis demonstrated significantly higher normalized von-Mises, maximum principle and hydrostatic stresses for higher test temperature resulting in enhance creep cavitation and decreases strengthening ability of the material.

Chapter: 6

CREEEP LIFE PREDICTION UNDER MULTIAXIAL STATE OF STRESS AND CONSTRUCTION OF MASTER PLOT

6.1 Introduction

Mainly structural components operating at high temperature are subjected to creep damage, which is due to the growth and coalescence of creep cavities and particle coarsening and dislocation cell or subgrain formation [8]. Evaluation of creep strength of materials is generally carried out under uniaxial state of stress. However, the boiler tube is subject to multiaxial state of stress due to internal pressure, bends, change in section thickness and presence of weld joint having inhomogeneous structures etc. The deformation and fracture behaviour of material generally depend on state of stress [172]. Therefore, It is necessary to predict the life of such components under multiaxial state of stress and also the multiaxial ductility in the presence of notch. In chapter 4, the influence of notch sharpness on creep deformation and rupture behaviour, their systematic characterization by different techniques with FE-analysis to assess the stress distribution across the notch throat plane have been discussed. Chapter 5, explained about the influence of temperature for a given notch on creep deformation and fracture and results have been corroborated with FE-analysis. In the present chapter, the multiaxial creep rupture life prediction has been carried out at different temperatures based on the dependency of representative stress on different components of stresses at the skeletal point, proposed by Hayhurst [102], Cane [103], and Nix et al. [104]. A unique master plot between representative stress and rupture life has been proposed which is independence of notch geometry (including smooth specimen data) and temperature. In addition to that, multiaxial ductility of the material has been predicted by using the models proposed by Rice and Tracey [116], Cocks and Ashby [117] and Manjoine [118]. On the other hand creep rupture of the 304HCu SS tube under internal pressure has been predicted using Cane's model through FE-analysis.

6.2 Creep life prediction under multiaxial state of stress

The dependency of rupture life on applied stress under uniaxial loading is expressed as:

$$t_r = M\sigma^{-m} \qquad (6.1),$$

where 'm' is the slope of uniaxial creep plot.

Creep rupture life under multiaxial state of stress can also be described in a similar way, replacing the applied stress by a representative stress.

$$t_r = M\sigma_{rep}^{-m} \qquad (6.2)$$

The 'σ_{rep}' is the representative stress when applied to the uniaxial specimen which will result the same rupture life as that of uniaxial specimen. If $\sigma_{rep}>\sigma_{net}$ (net stress applied to the notched specimen), then presence of notch weaken the material i.e. notch weakening". If $\sigma_{rep}<\sigma_{net}$ then presence of notch strengthen the material i.e. material will exhibit "notch strengthening". The representative stress can be expressed in terms of von-Mises, maximum principal and hydrostatic stresses to obtain the rupture life under multiaxial stresses. The stress distribution across the notch throat plane during creep exposure is found to attain steady state condition (Fig. 4.12 and Fig. 4.13) which is not uniform across it. Under these circumstances, it is difficult to find a location where the stress could be considered as representative stress for creep rupture life prediction. It is imperative to indentify a unique location at which components of stress are invariable and the representative stress can be calculated.

6.2.1 Skeletal point concept :

Webster et al. [94] and Hayhurst and Webster [91] have introduced the concept of skeletal point through FE analysis of stress distribution across the notch throat plane. The skeletal point is the location in the notch throat plane where stationary state stresses remains same irrespective of values of the coefficient ‘n’ in Norton’s creep law. The skeletal point of stresses were obtained by carrying out FE analysis of stress distribution across the notch throat plane for different values of stress exponent ‘n’ in the Norton’s law of creep from 1 to 12 for a net applied stress of 200 MPa. The coefficient value ‘A’ was obtained at a creep strain rate of 10^{-5} h. The variations of von-Mises, maximum principal and hydrostatic stress for different values of stress exponent ‘n’ for notch acuity ratio ‘10’ are shown in Fig. 6.1(a), (b) and (c) respectively. Similar observation was for other notch acuities. It was observed that except for ‘n’ between 1 and 3 (‘n’ values are more than 3 in this investigation), there exists a skeletal point at which stress variation for different stress exponent intersects. Stress exponent of 1 and 3 are not significant in this investigation since the creep deformation in the steels under investigation is controlled by dislocation creep mechanism having ‘*n*’ value more than 4.

The variation of normalized stress components at the skeletal point with notch acuity ratio are shown in Fig. 6.2. At the skeletal point, the value of maximum principal stress was more than the net applied stress while value of von-Mises and hydrostatic stress was less than the net applied stress. Further, the value of von-Mises skeletal point stresses decreases with increase in notch sharpness while maximum principal and hydrostatic stress increases with increase in notch sharpness. The stresses at the skeletal point for a given notch at different applied stresses are obtained by multiplying normalized stress with applied stress. The stresses estimated at this point have been used to characterize the deformation, damage and life prediction of the material. Similar approach has been adopted by Goyal et al. [95] for predicting life of steel under multiaxial state of stress considering the stresses at the skeletal point.

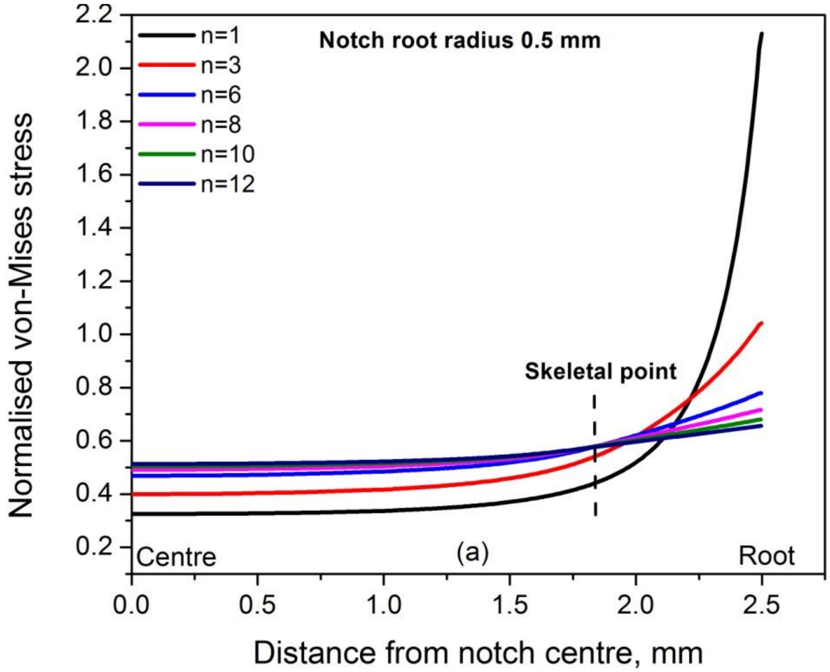

n=1
n=3
n=6
n=8
n=10
n=12
Notch root radius 0.5 mm
Skeletal point
Centre
(a)
Root
Normalised von-Mises stress
Distance from notch centre, mm

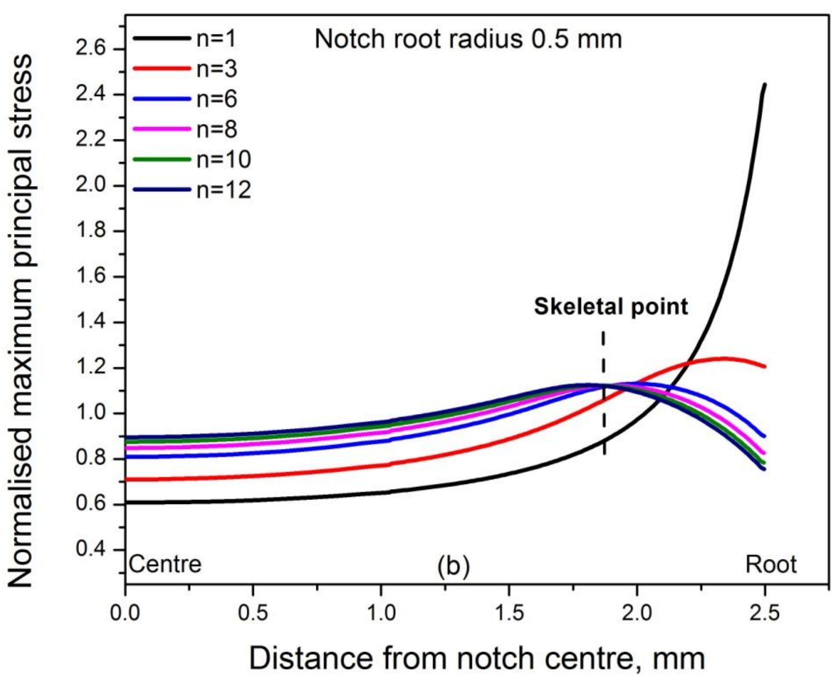

n=1
n=3
n=6
n=8
n=10
n=12
Notch root radius 0.5 mm
Skeletal point
Centre
(b)
Root
Normalised maximum principal stress
Distance from notch centre, mm

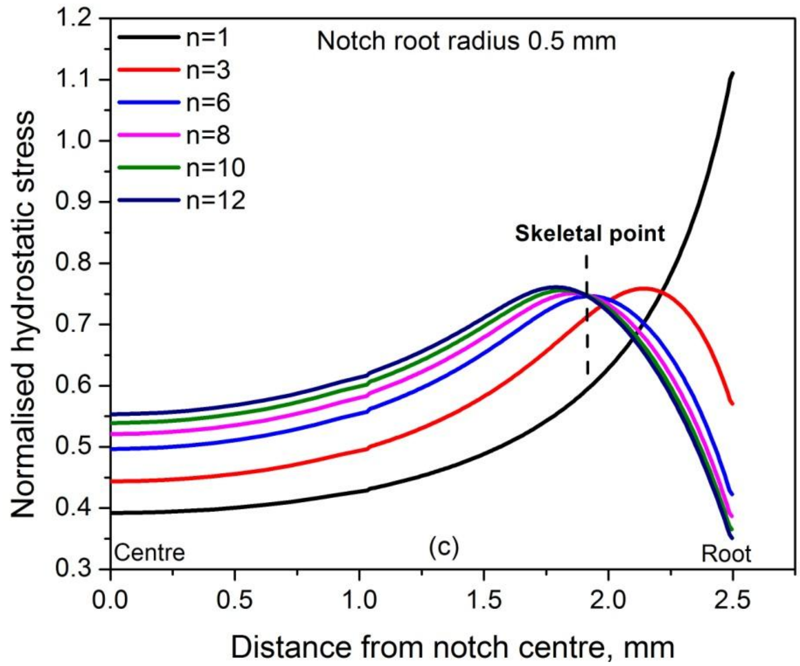

Fig. 6.1 Variations of normalized (a) von-Mises stress, (b) maximum principal stress and (c) hydrostatic stress across the notch throat plane for different stress exponent for notch of root radius 0.5 mm (Notch acuity ratio = 10).

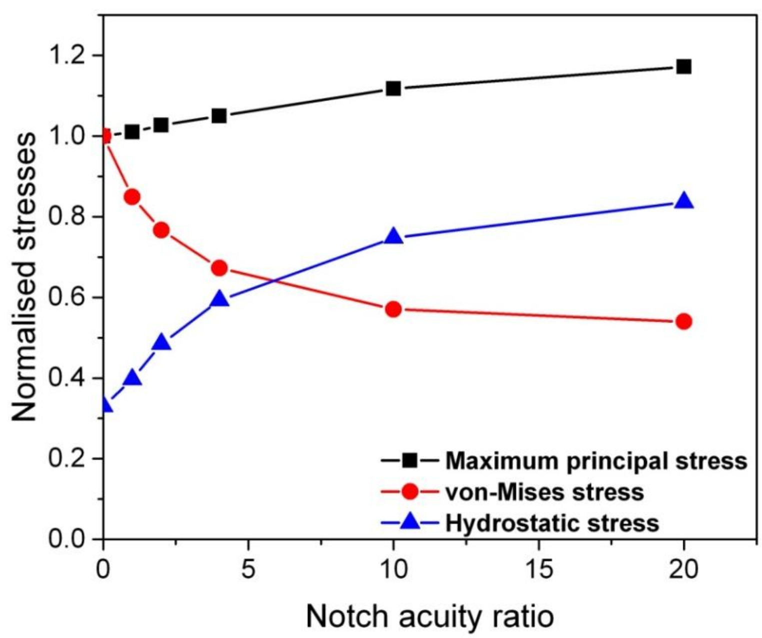

Fig. 6.2 Variation of skeletal point stresses as a function of notch acuity ratio for creep test at 200 MPa and 973 K.

6.2.2 Creep life prediction at different temperatures

In this investigation, creep life prediction at different temperatures has been carried out based on the dependency of representative stress on different components of stresses at the skeletal point, proposed by Hayhurst et al. [102], Cane [103] and Nix et al. [104]. The relationships are given below:

Hayhurst's model $\sigma_{rep} = \alpha\sigma_1 + (1-\alpha)\sigma_{vm}$ (6.3)

Cane's model $\sigma_{rep} = \sigma_1^{\gamma/m}\, \sigma_{vm}^{(m-\gamma)/m}$ (6.4)

Nix model $\sigma_{rep} = 2.24\, \sigma_1 - 0.62(\sigma_2 + \sigma_3)$ (1.43)

where m, γ, and α are material constants and 'σ_1' is the maximum principal stress and 'σ_{vm}' is the von-misses stress, σ_2 is the intermediate principal stress and 'σ_3' is the minimum principal stress respectively. For α=0 and γ=0, $\sigma_{rep} = \sigma_{vm}$ i.e. representative stress completely depends on the von-misses stress. For α=1 and γ=m, $\sigma_{rep}=\sigma_1$ i.e. representative stress completely depends on the maximum principal stress.

For the calculation of 'α' for Hayhurst model (Eq. 6.3), the regression analysis was carried out for the representative stress based at the skeletal point stress for different notch geometries. The best fit value of 'α' was found to be 0.5, 0.34, 0.32 (Fig. 6.3), and with correlation coefficient of 0.92, 0.951 and 0.92 (Fig. 6.4) for this steel at 923, 973 and 1023 K. It indicates that the contribution of von-Mises stress and maximum principal stress in creep deformation and rupture for this steel is 50% each for 923 K, 66% and 34% for 973 K, 68% and 32% for 1023 K respectively. The value of 'γ' for Cane's model (Eq. 6.4) was calculated using the similar procedure as in the case of Hayhurst model and the value of γ was found to be 5.9, 3.9 and 2.9

with correlation coefficient of 0.92, 0.95 and 0.913 for 923, 973 and 1023 K [Fig. 6.5 and 6.6]. Relatively high value of 'α' and 'γ' in the austenitic steel (as compared to ferritic steel [96, 127] signifies that the maximum principal stress plays a dominant role in the failure of notched specimens of the steel. Again, the value of 'α' and 'γ' decreased with increase in temperature, signifying with increase in temperature importance of principal stress decreases and von-Mises stress increases. The observation that the creep cavitation tendency increases with increase in temperature (Fig. 5.3) clearly brought out that in this significant precipitation hardened steel, creep cavity nucleation assisted by von-Mises stress [Fig. 5.13(a)] and this is the controlling factor for cavitation. Once the cavity is nucleated, its growth and coalescence are quite rapid due to increase in von-Mises stress that causes subsequent failure (Fig. 5.3).

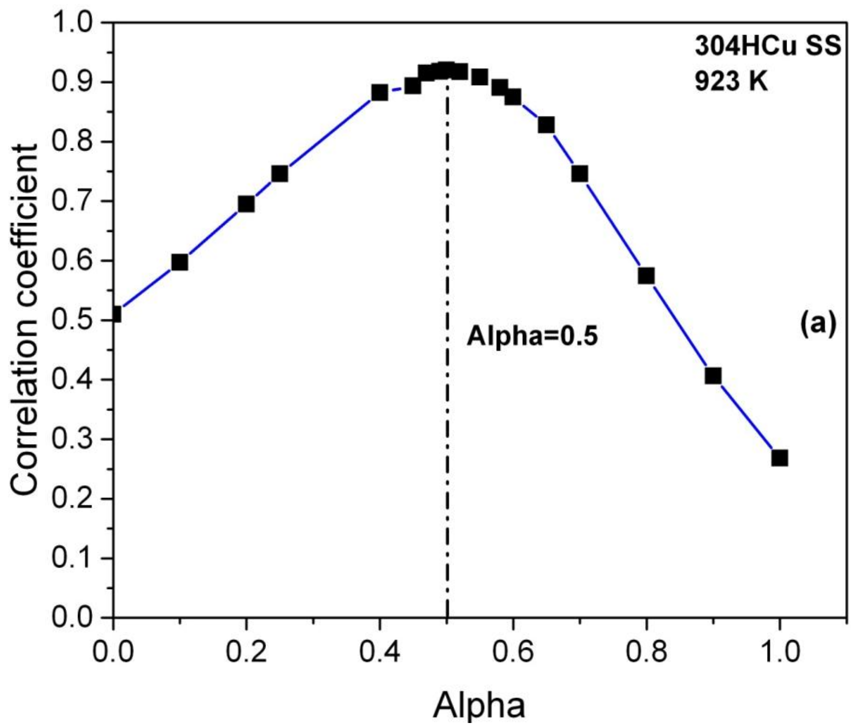

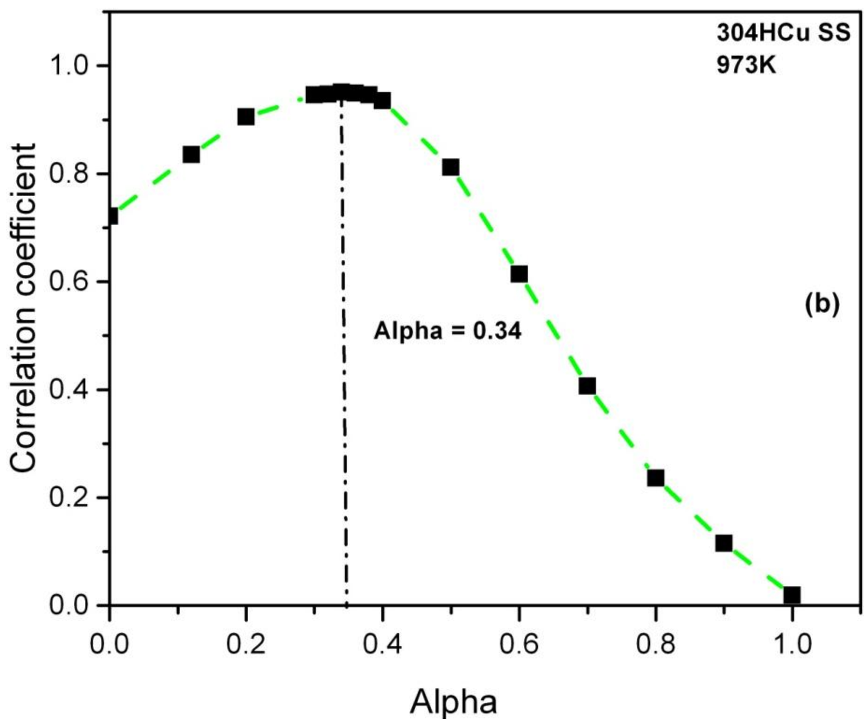

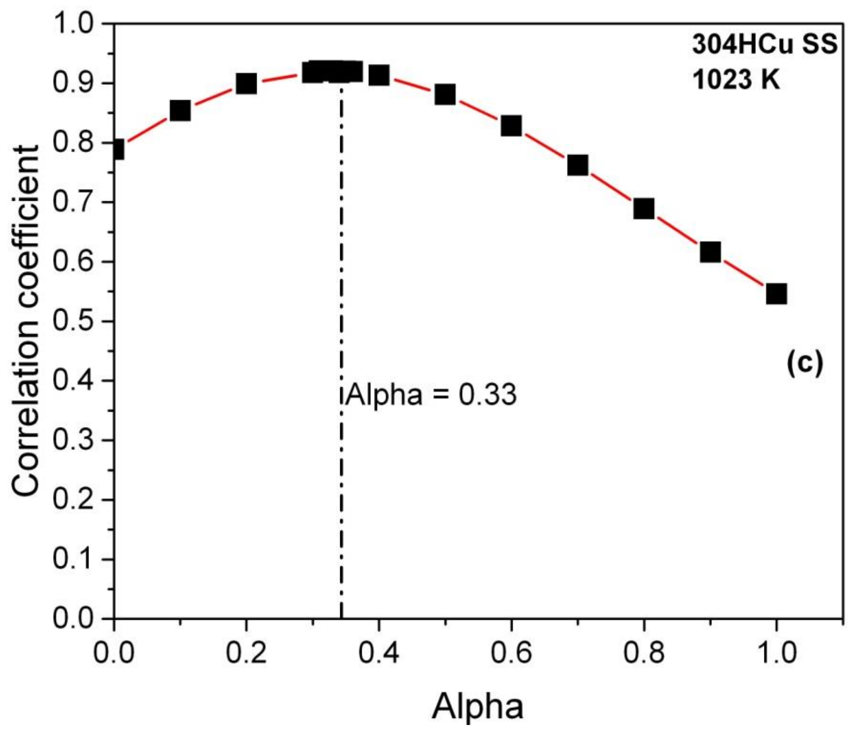

Fig. 6.3 Optimization of the value of α in the σ_{rep} for Hayhurst model at 923, 973, 1023 K.

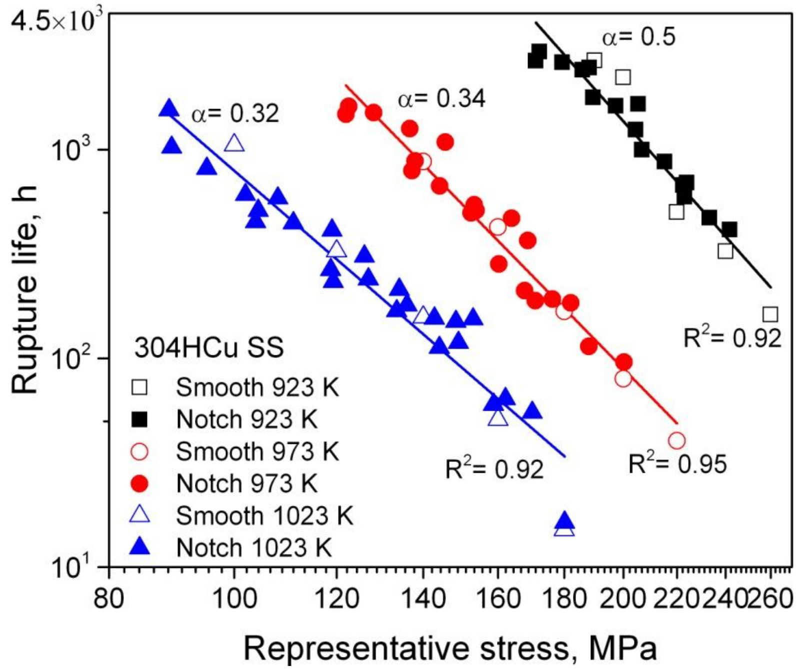

Fig. 6.4 Presentation of multiaxial creep rupture life based on the σ_{rep} calculated through skeletal point method based on the model proposed by Hayhurst.

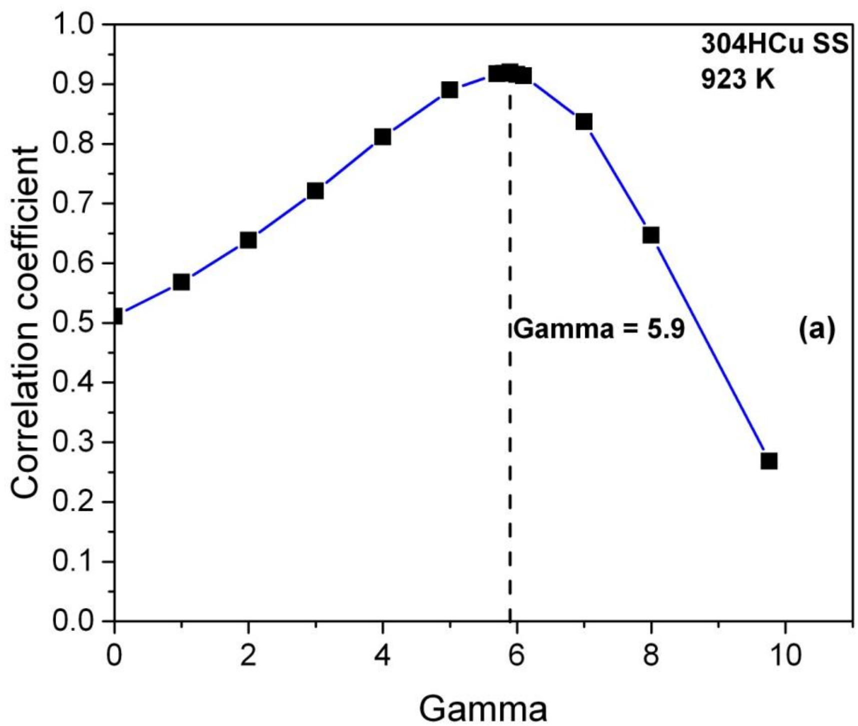

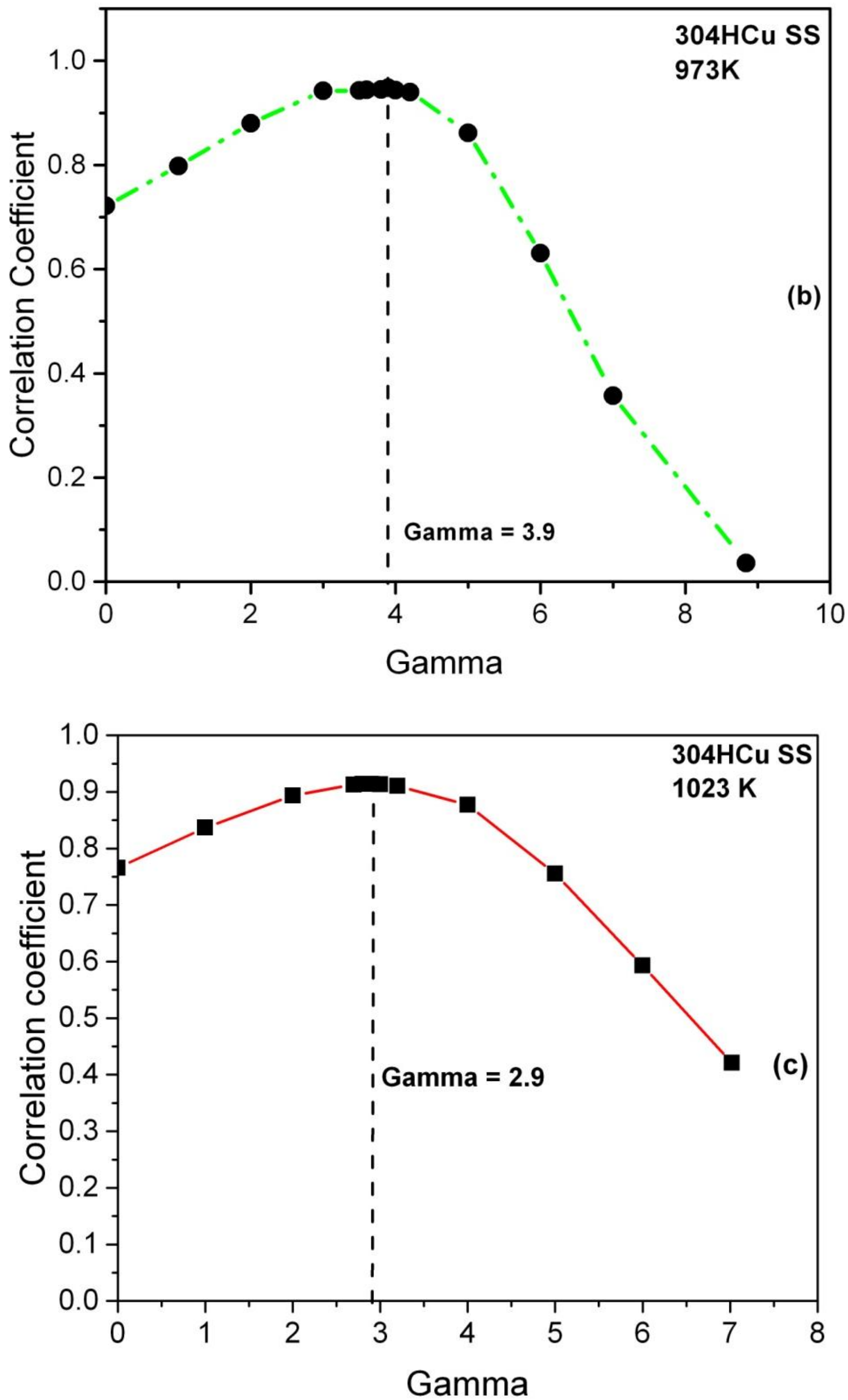

Fig. 6.5 Optimization of the value of γ in the σ_{rep} for Cane's model at 923, 973, 1023 K.

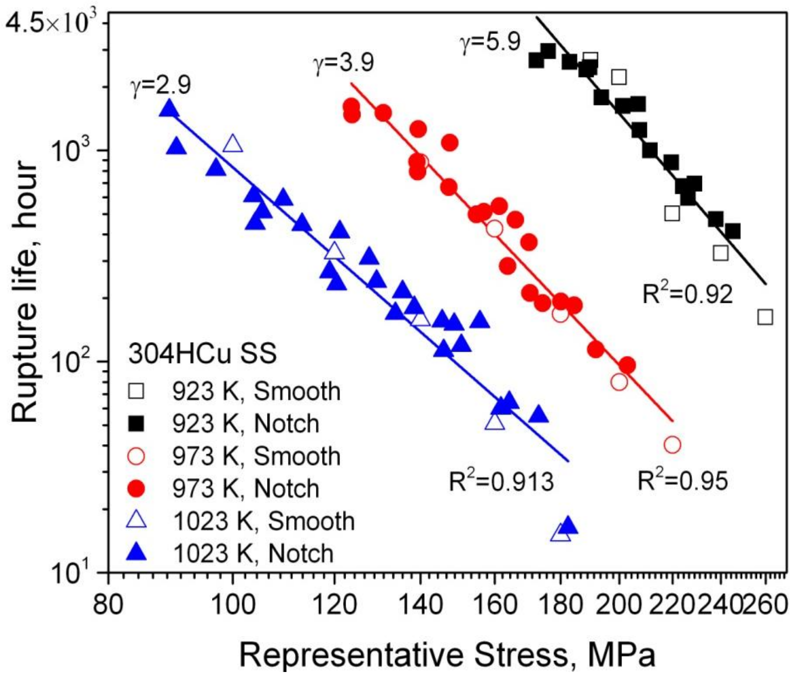

Fig. 6.6 Presentation of multiaxial creep rupture life based on the σ_{rep} based on the model proposed by Cane.

Nix model defines the representative stress as a principal facet stress which is a function of maximum principal stress and hydrostatic stress. The variation of representative stress with rupture life was found with correlation coefficient of 0.86, 0.95 and 0.78 for 923, 973 and 1023 K respectively as shown in Fig. 6.7. Multiaxial life prediction through Nix model was not found suitable for 923 and 1023 K. This may be due to the inconsistency in creep rupture life results i. e ability of the material to show tendency towards notch weakening for relatively sharper notches at lower stresses. However, at 973 K, Nix model was found suitable in predicting multiaxial creep rupture life. Nix model is particularly suitable for creep cavity prone materials.

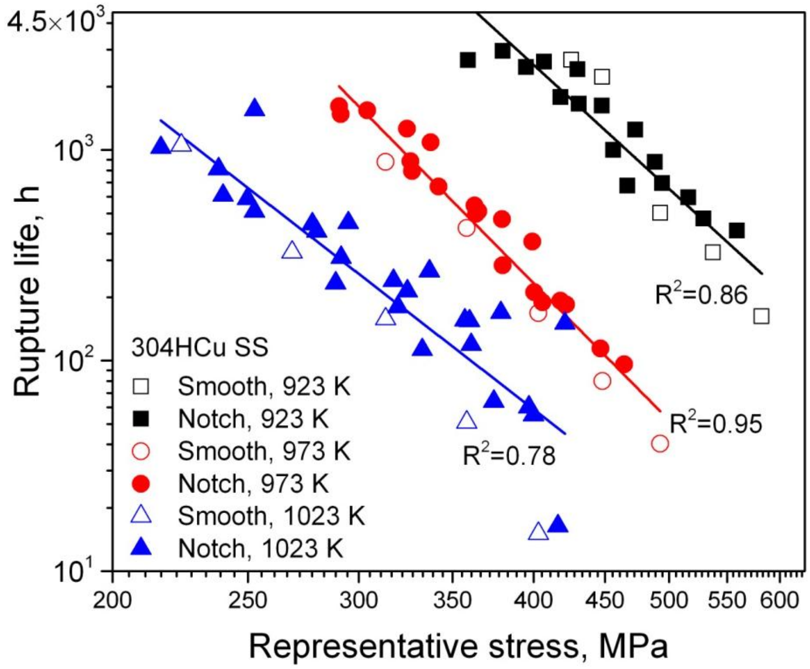

Fig. 6.7 Presentation of multiaxial creep rupture life based on the σ_{rep} as principal facet stress (Nix model) for 304HCu SS at 923, 973 and 1023 K.

As observed experimentally, the 304HCu SS is more prone to intergranular creep cavitations with limited ductility. Nix model could predicted the multiaxial creep life prediction reasonably well at 973K for this material compared to ferritic steels which are less prone to creep cavitation [170]. However, Browne et al. [174] and Aplin et al. [175] commented that the creep rupture life prediction under multiaxial state of stress cannot be represented as algebraic sum of different components of multiaxial state as the deformation and damage occurring in different components of stresses is not independent to each other. However based on good correlation of Hayhurst model with experimental rupture life, along with Cane's model, Hayhurst model [102] was found suitable for creep life prediction of 304HCu SS at different temperatures.

6. 2. 3 Master plot constructions (independence of test temperature)

In an attempt to normalise the effect of temperature on the variation of rupture life with representative stress, the representative stress is normalised with yield stress and temperature compensated rupture life (t_r) is expresses as t_r.exp (-Q/R'T), where Q is the activation energy for creep deformation (inverse of rupture life) and R' is the gas constant. The value of Q was 464.77 KJ/mole which has been calculated at a particular stress (180 MPa) at two different temperatures (923 K and 1023 K). The temperature compensated creep rupture life (t_r) is plotted with normalized representative stress in semi log-scale. It can be stated as,

$$\log\left[t_r.\,exp\left(-\frac{Q}{R'T}\right)\right]\ \alpha\ \frac{1}{\left(\frac{\sigma_{rep}}{\sigma_{YS}}\right)}$$

$$i.e. \qquad \log\left[t_r.\,exp\left(-\frac{Q}{R'T}\right)\right] = A\cdot\frac{1}{\left(\frac{\sigma_{rep}}{\sigma_{YS}}\right)} + B \qquad (6.6)$$

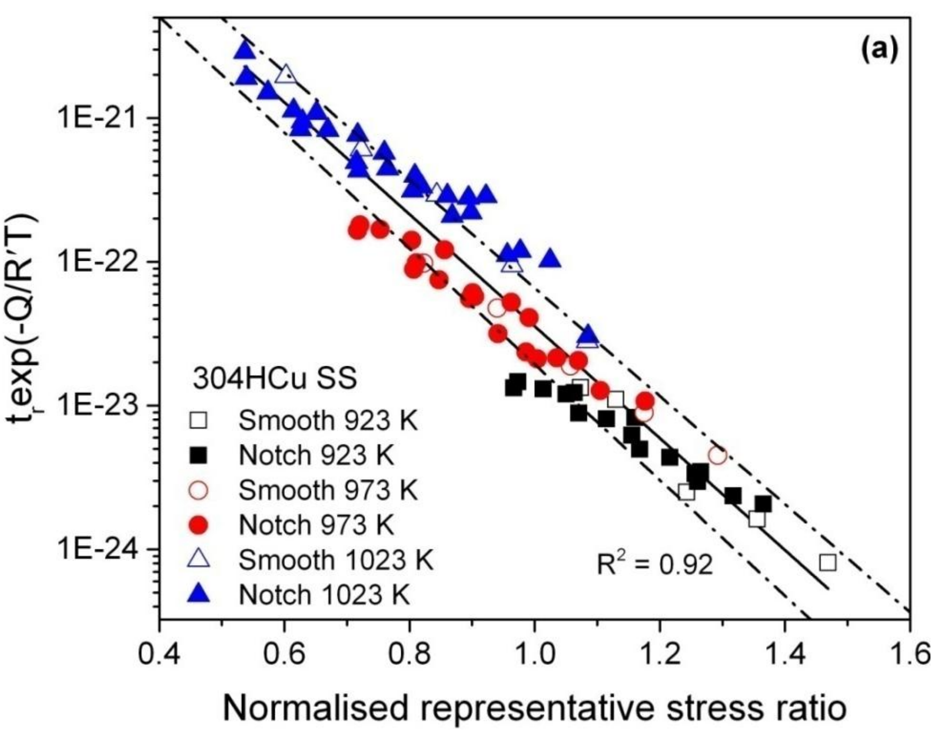

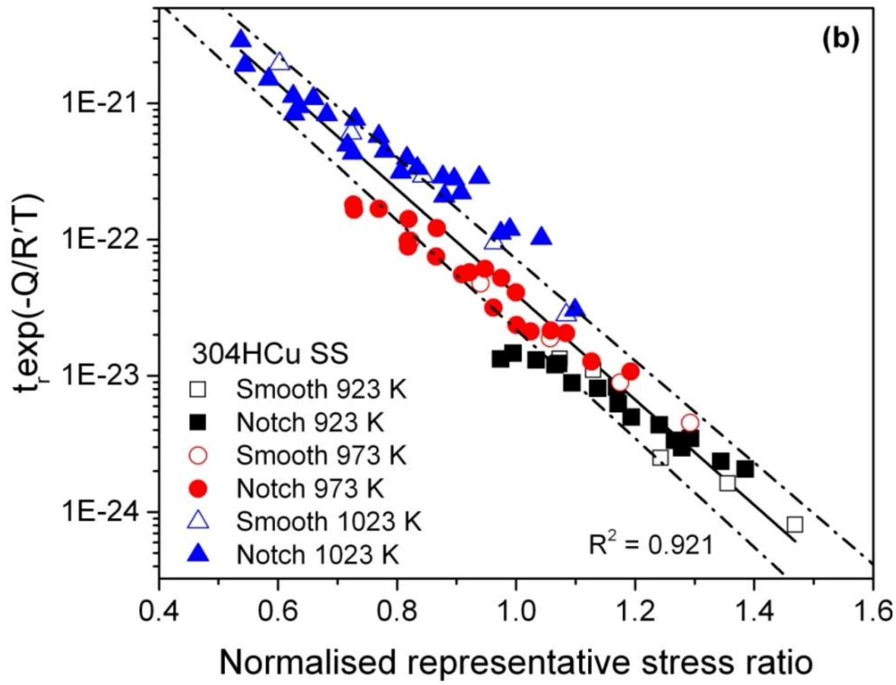

Fig. 6.8 Master plot showing independence of temperature for both smooth and notch carried out by temperature compensation of creep rupture life with normalized representative stress ratio (σ_{rep}/σ_{YS}) calculated through (a) Hayhurst and (b) Cane model.

Where 'A' is proportionality constant and 'B' is the intercept between temperature compensated creep rupture life and inverse of normalized representative stress. Both 'A' and 'B' are material dependent parameter, independent of state of stress (i. e. notch and smooth) and temperature. The value of 'A' and 'B' are -3.8639 and -18.53721 within 12% of standard error. Figure 6.8 (a, b) shows such a unified plot paving way to generalized creep rupture life plot applicable for multiaxial state of stress based on Hayhurst and Cane's model over a wide temperature range for application of the steel in power plant. It follows a master plot which is unique and irrespective of state of stress and tested temperature and predicts the rupture life within a 12% error. The scatter in the result is due to the non-consistency in the creep rupture life of some notched specimen with increase in notch sharpness (tendency to decline with increase in notch sharpness at lower stresses). Therefore, the accurate prediction of the deformation behaviour and rupture life is possible if change in dislocation density, phase change, grain boundary sliding, precipitation coarsening etc. are considered in the model.

In this investigation over the stress and temperature ranges, predominantly notch strengthening was observed for relatively short term rupture life of less than 5000 hours. It would be interesting to study the relatively long-term creep tests to assess the response of the material to multiaxial state of stress.

6.3 Multiaxial Creep rupture ductility prediction

Multiaxial creep failure of the material is related to the nucleation of creep cavity and their growth, which is related to the distribution of stress across the notch throat plane. Creep ductility of the material is strongly dependent on the state of stress which in turn depends upon the different components of multiaxial state of stress. Different models have been proposed to account the dependence of multiaxial ductility with the growth of the void i.e. indirectly depends upon the von-Mises stress and hydrostatic stress. Generally, the increase in Hydrostatic stress results decrease in multiaxial ductility. McClintock [25], Rice and Tracey [116] indicated the exponential amplification of the growth rate of micro-voids with stress triaxiality in elastic-perfectly-plastic material.

6.3.1 Cocks and Ashby model

Cocks and Ashby [117] carried out approximate calculations with the effect of temperature of the grain boundary cavity growth rates of creeping material under multiaxial state of stress and its consequence on ductility based on the physical based continuum damage mechanics. The mathematical expression which relates ratio of multiaxial ductility to uniaxial ductility with skeletal point triaxiality is given by.

$$\frac{\varepsilon_f^*}{\varepsilon_f} = \sinh\left[\frac{2}{3}\left(\frac{n-\frac{1}{2}}{n+\frac{1}{2}}\right)\right] \Bigg/ \sinh\left[2\left(\frac{\mathrm{n}-\frac{1}{2}}{\mathrm{n}+\frac{1}{2}}\right)\frac{\sigma_{\mathrm{m}}}{\sigma_{\mathrm{vm}}}\right] \qquad (1.46)$$

where $\frac{\varepsilon_f^*}{\varepsilon_f}$ is the ratio of multiaxial to uniaxial creep ductility (Normalised ductility), $\frac{\sigma_{\mathrm{m}}}{\sigma_{\mathrm{vm}}}$ is the ratio of hydrostatic state of stress to von-Mises stress at the skeletal point and 'n' is the creep stress exponent in the variation of steady state creep rate with applied stress.

6.3.2 Rice and Tracey model: Rice and Tracey [116] model is based on the concept of hole growth by rigid plastic deformation of the surrounding matrix without considering the effect of temperature. They have established a relation between void growth and stress triaxiality for a material subjected to uniform stress and strain rate in the domain of continuum plasticity for relatively ductile material where large growth and coalescence of voids occurs.

$$\frac{\varepsilon_f^*}{\varepsilon_f} = exp\left(\frac{1}{2} - \frac{3\sigma_m}{2\sigma_{vm}}\right) \qquad (1.47)$$

Same expression has been used by different authors [153, 176, 177] to see the closeness of the variation of multiaxial ductility with their experimental data.

6.3.3 Manjoine model: Manjoine [118] proposed empirical relationship based on creep tests on different materials and expressed normalized ductility with power function of skeletal point triaxility. The expression is given by,

$$\frac{\varepsilon_f^*}{\varepsilon_f} = 2^{(1-3(\sigma_m/\sigma_{vm}))} \qquad (1.48)$$

The estimated multiaxial ductility as a function of triaxiality based on various models is shown in Fig. 6.9. At 923K Cocks and Ashby model was found relatively good in predicting the multiaxial ductility of the notch specimen [Fig. 6.9 (a)]. At 973K Rice and Tracey model was found relatively good compared to other two models [Fig. 6.9(b)]. At 1023 K, Manjoine model was found relatively good and Cocks and Ashby was found good for relatively sharper notches in predicting the multiaxial ductility of the notch specimen [Fig. 6.9(c)].

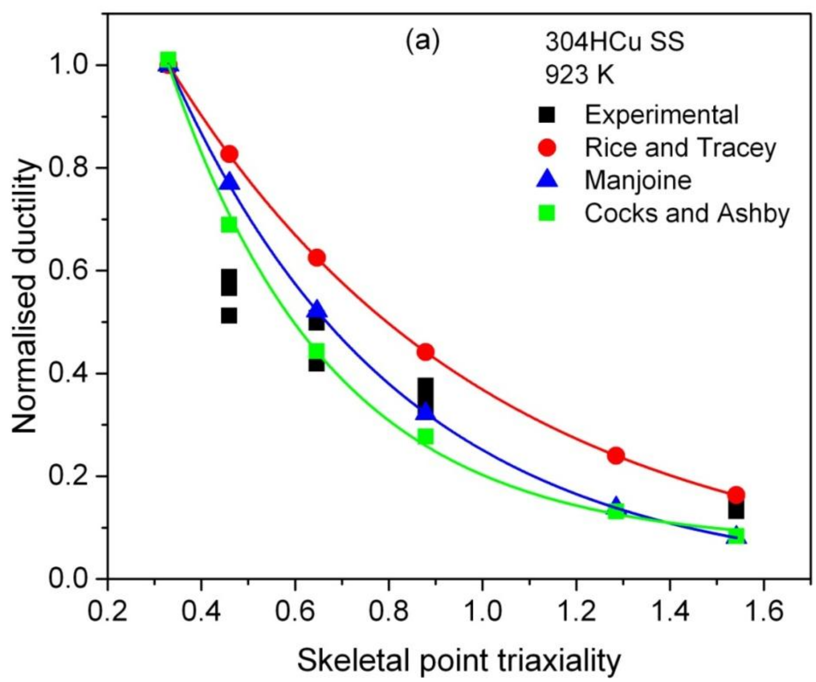

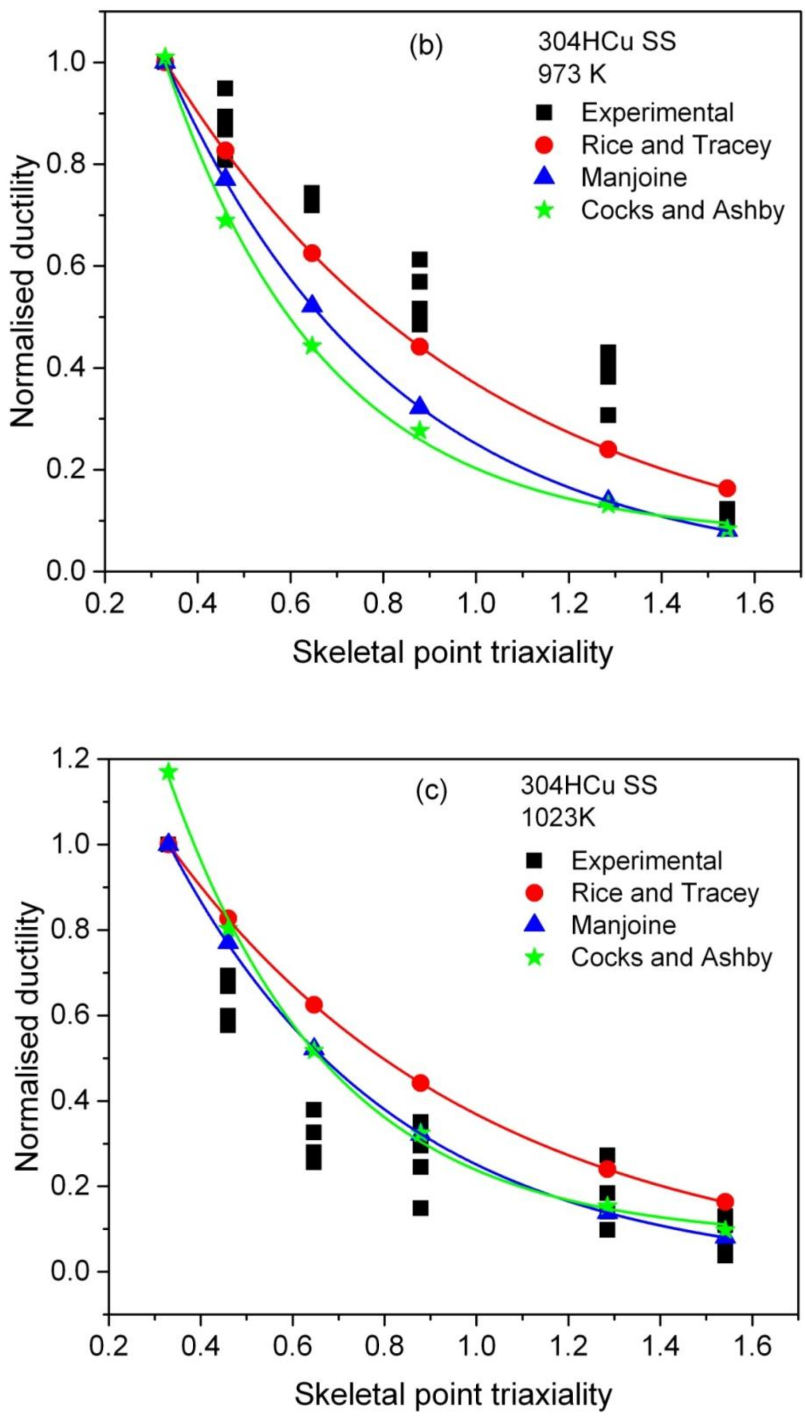

Fig. 6.9 Variation of normalized ductility (both experimental and predicted based on different models) with skeleton point triaxility factor for different stresses at (a) 923 K, (b) 973 K and (c) 1023 K.

Cocks and Ashby model [117] depends upon the temperature through the factor ‘n’ while other two models are independent of temperature. Further, it was reported that Cocks and Ashby model reasonably fits well for the material having large σ_m/σ_{vm} value which is consistent with ductile fracture at low temperature [117]. This shows that the failure of the material is mainly due to the uniform growth of creep cavities and subsequent linkage to final failure. This is the reason for showing good prediction of multiaxial ductility at 923 K. Rice and Tracey model [116] correlated between the growths of the void with the stress triaxiality in the domain of continuum plasticity. This type of behaviour was commonly seen in ductile solids where uniform expansion of cavities predominantly occurs. At 973 K material exhibits relatively more ductile than 923 K and 1023 K at different state of stress and hence this model suits at 973 K. Manjoine model [118] predicts the multiaxial ductility of the material at elevated temperature where time and rate dependent factors must be considered. At elevated temperature for a long time service the damage of the material is due to the initiation and propagation of the crack by maximum principal stress and strain accumulation due to shear stress. It is well known that intergranular creep cavitation and their rate of linkage to final failure increases with increase in temperature. Since, at 1023 K, most of the possible type of damage mechanics operates, multiaxial ductility can be well predicted with Manjoine model

6.3.4 Proposed model: In the above section, different models have been found good at different temperatures for the multiaxial creep rupture ductility prediction. Hence, it is necessary to propose a unique model which can fit at all the test temperature. The different behaviour is mainly due to the variation of creep exponent (n) and not choosing appropriate fitting functions. For this reason, a cumulative model which considers the common factor of Rice and Tracey and Manjoine model and temperature dependence factor of Cocks and Ashby model has been combined into another new equation for multiaxiality ductility prediction. The common factor is

$1 - 3(\sigma_m/\sigma_{vm})$ and the temperature dependence factor is $\frac{2}{3}\left(\frac{n-\frac{1}{2}}{n+\frac{1}{2}}\right)$. After trying with several functions such as sine, exponential, power etc., we found that exponential function of product of above those two terms was reasonably good compared to the above mentioned models. Therefore, we have proposed a unique model which is the cumulative model of all the above three model and can be used for the multiaxial creep ductility prediction at any temperatures for this material and may be for other ferrous material also. It is given by,

$$\frac{\varepsilon_f^*}{\varepsilon_f} = exp\left\{\left[\frac{2}{3}\left(\frac{n-\frac{1}{2}}{n+\frac{1}{2}}\right)\right]\left(1 - 3\frac{\sigma_m}{\sigma_{vm}}\right)\right\} \qquad (6.10)$$

n = creep exponent at different temperatures, $\frac{\sigma_m}{\sigma_{vm}}$ is the ratio of hydrostatic stress to von-Mises stress at the skeletal point.

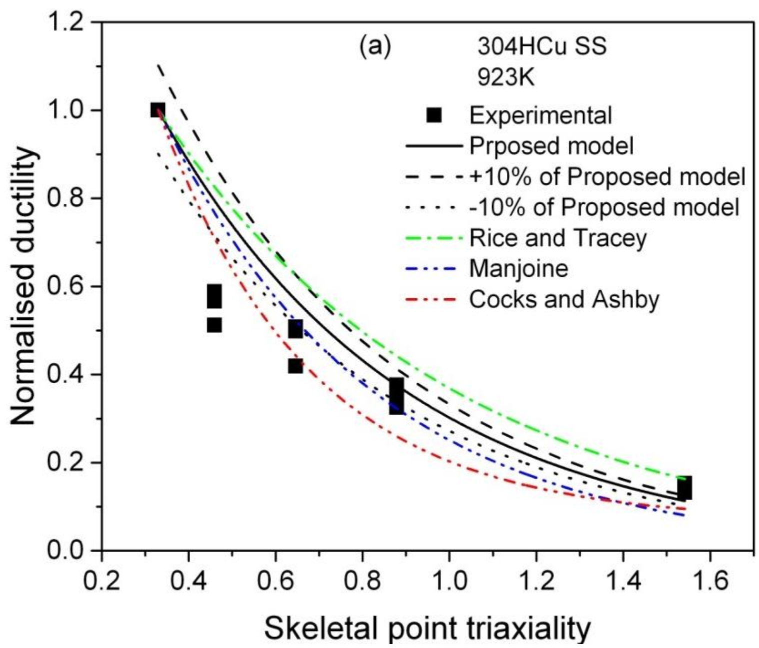

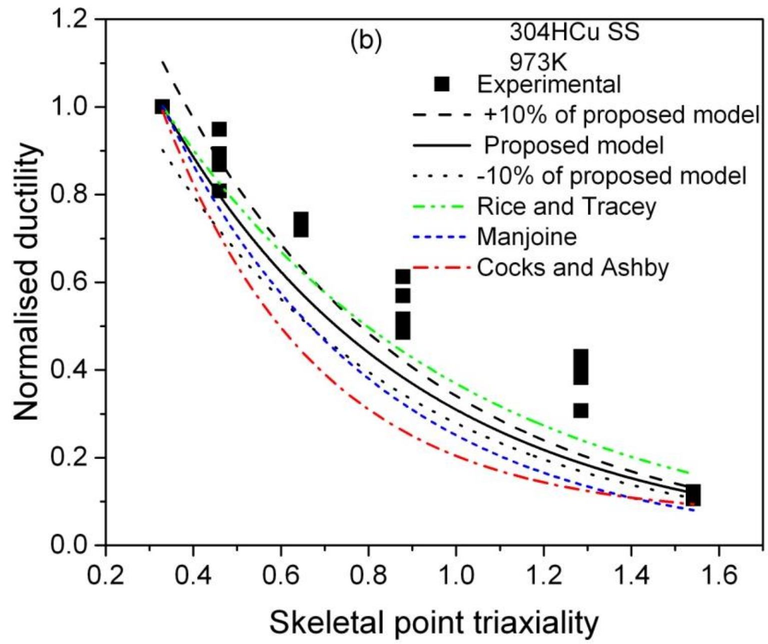

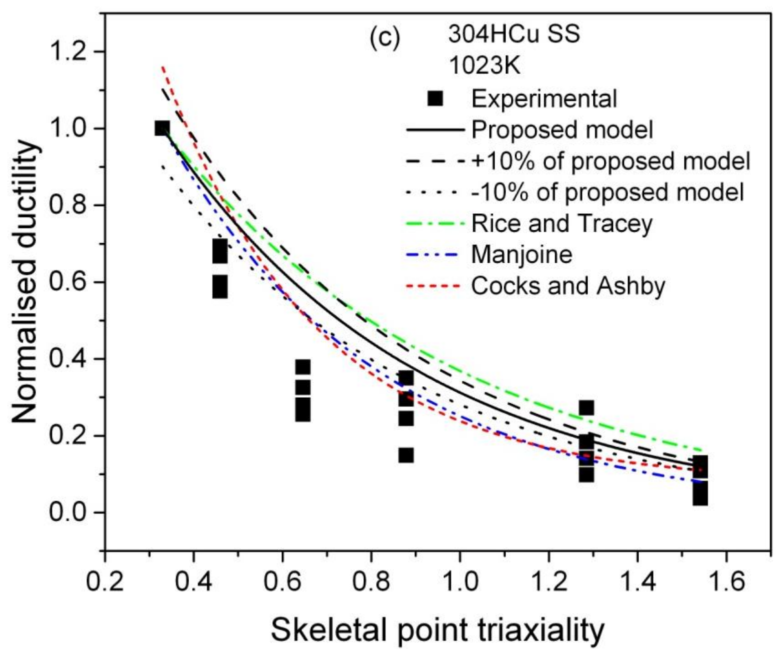

Fig. 6.10 shows the prediction of multiaxial ductility at (a) 923 K (b) 973 K and (c) 1023 K through proposed model within 10% scatter band.

The suitability of the proposed model [Fig. 6.10] for multiaxial creep rupture ductility prediction was checked based on closeness of the experimental points within ±10 % scatter band of the proposed model. In addition to that, this model was checked for 316LN SS at 873K. Goyal et.

al. [153] used Spindler model [176] for 316LN SS at 873 K with different coefficient values of 'p' and 'q' and found that good correlation of fitting values of multiaxial creep rupture ductility with experimental observations occurs when p=0 and q=1. In design prospect, the multiaxial creep ductility may vary at other temperatures and for this reason, trying with different values of coefficients (p and q) leads to time consuming analysis. Hence, the above proposed model has been used for 316 LN SS and found that good fitted values of multiaxial creep ductility with experimental observations [Fig. 6.11].

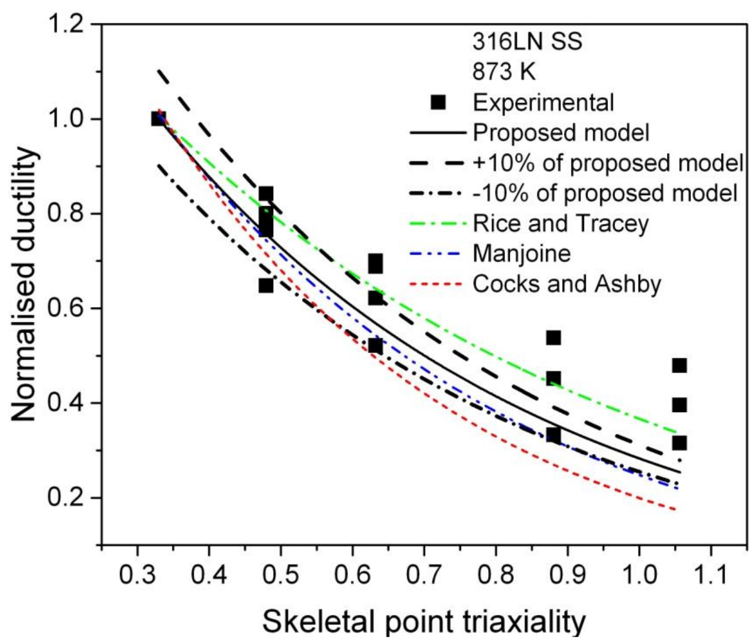

Fig. 6.11 shows the prediction of prediction of multiaxial ductility for 316LN SS at 873 K through proposed model within 10% scatter band.

Although multiaxial ductility under creep condition is not well understood however in the present study a basic research with existing models has been used and a new model has been proposed to predict the multiaxial creep ductility of 304HCu SS at different temperatures. Further research includes different aspects of creep cavity nucleation, growth and coalescence under multiaxial state of stress along with multiaxial deformation characteristics of the material under different creep condition.

6.5 Conclusions

Based on the studies on creep rupture behaviour of 304HCu steel under multiaxial state of stress incorporated on introducing notches of different notch acuity ratios in smooth specimen, along with FE analysis following conclusions have been drawn.

1. Creep rupture lives of the steel under multiaxial state of stress have been predicted based on the represented stress concept at the skeletal point. The model proposed by Cane was found suitable in predicting the multiaxial creep data for 304HCu SS at different temperatures.
2. A unique master plot of multiaxial rupture life with stress, independent of smooth, notch and test temperature has been established and a new equation has been proposed which considers interdependence of notch, smooth and test temperature rupture life and can be used for application of the steel in power plant.
3. Multiaxial creep ductility of the material has been predicted by using the models proposed by Cocks and Ashby, Rice and Tracey and Manjoine. However, different models have been found good at different temperatures. Hence, a unique model which is the cumulative model of all the above three model have been proposed and can be used for the multiaxial creep ductility prediction at any temperatures for this material within 10% scatter band and this model may be fit for other ferrous material also.

Chapter: 7

EFFECT OF U-NOTCH DEPTH ON CREEP BEHAVIOR AND RUPTURE LIFE

7.1 Introduction

Multiaxial creep deformation can occur due to the variation in depth of the notch rather than radius. Very few literatures were available where the creep studies have been carried out on the notch specimen with varying depth. However, Hitham M. Tlilan etal. [178] carried out FEM on varying notch depth where they studied the Strain concentration factor (SNCF) under static tension. They reported that for elastic-plastic deformation the SNCF of the shallow notch (d/D = 0.95) sharply increases with plastic deformation at the notch root, while the SNCF of sharper notch (d/D = 0.2) increases only slightly. Further, they reported that in case of deep notch (d/D = 0.6) the SNCF also increases with plastic deformation and reaches a peak value.

In the present investigation, an attempt has been made to understand creep deformation behaviour on 304HCu SS specimen by varying the notch depth. The notch depth was varied viz. 1.675, 2, 2.5 and 3mm in the specimen periphery which make the inner diameter (d) of 5, 4.35, 3.35 and 2.35 at the notch plane [Fig. 7.1]. Creep stress distribution was calculated on

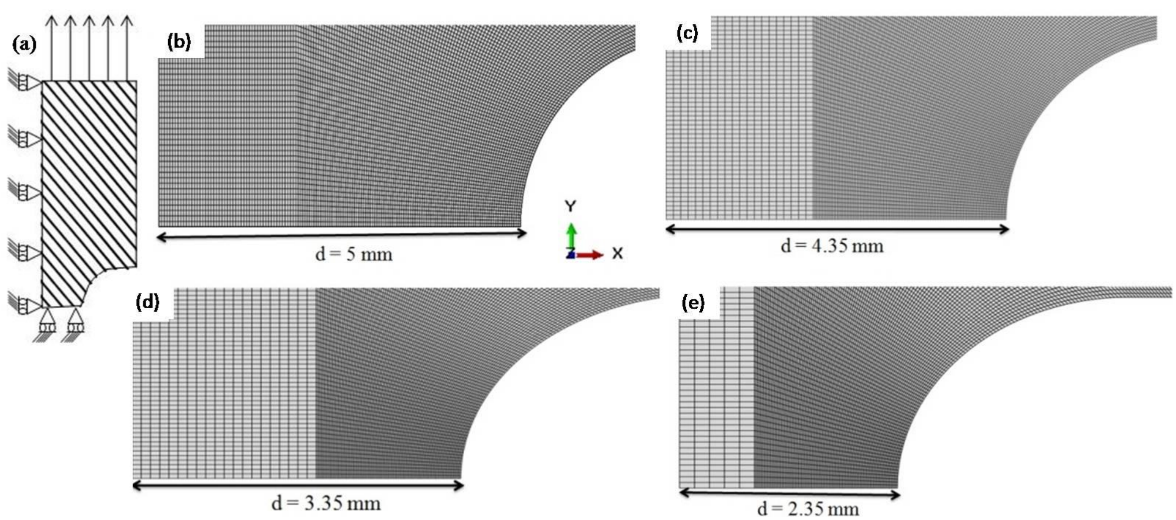

Fig. 7.1 shows (a) Schematic of the boundary condition and loading direction and typical FE-mesh used for (b) 1.675, (c) 2, (d) 2.5 and (e) 3 mm notch depth specimen.

notch plane through FE-simulation by using Norton's power law creep through Elastic-Creep data. The values of E = 134 GPa and Poisson's ratio = 0.3 were chosen for the elastic deformation of the material [179]. The Norton's power law constants (*A* and *n*) 1.32×10^{-21} and 7.56 respectively were used in the analysis [180]. Further, the fracture behaviour and EBSD analysis of different notch depth specimen has been correlated with experimental observations.

7.2 Effect of notch depth on K_t, rupture life and ductility

Creep tests were carried out for both smooth and notched specimen of fixed notch root radius (R) which is equal to 1.25 mm by varying notch depth ratio at a net applied stress (200 MPa) and temperature (973 K). The resulting variation in stress concentration factor (K_t) with R/d ratio is shown in Fig. 7.2(a). The elastic stress concentration factor increased with notch depth. The variation of stress concentration factor with notch root radius is also included for comparison [8 notch depth]. It can be seen that the notch geometry (radius) has more influence on the peak stress at the notch root as compared to notch depth. The two lines in Fig. 7.2(a) are comparable to each other. The variation of creep rupture life of both smooth and notched specimen with different notch depths is shown in Fig. 7.2(b). The dependency of rupture life on notch depth showed three distinct regimes. In the regime I, the rupture life increased at slow pace with notch depth and in the regime II, the rupture life increased drastically with further increase in notch depth and showed a peak for the notch depth of 2.5 mm. It is interesting to note that the material showed notch weakening for further deep notch (regime III). The ductility was found to decrease with increase in notch depth [Fig. 7.2(c)]. However, the rate of reduction in % RA decreased significantly with increase in notch depth.

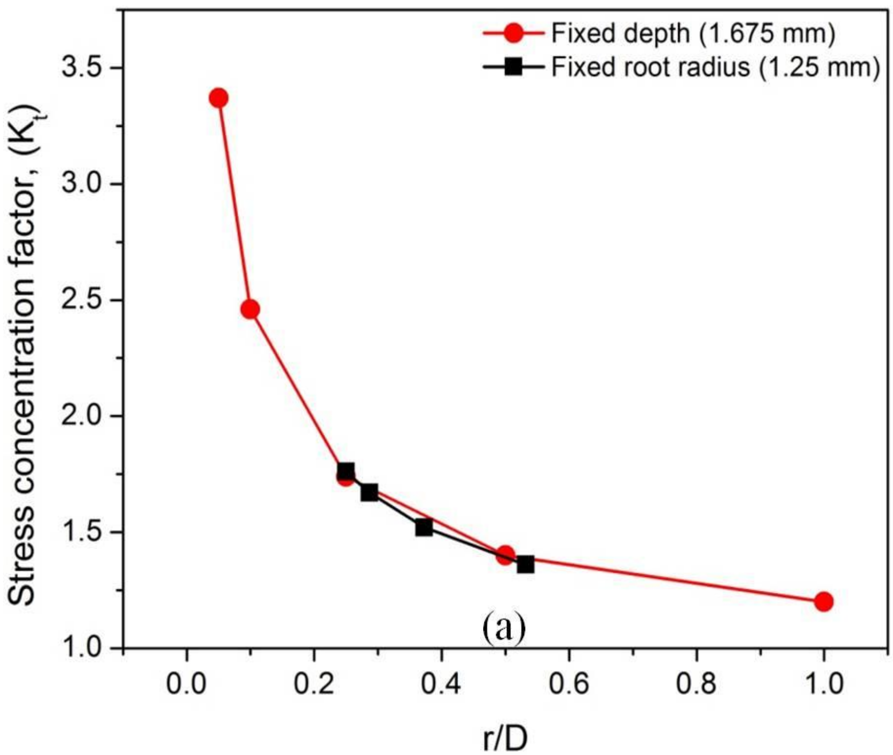
Fixed depth (1.675 mm)
Fixed root radius (1.25 mm)
Stress concentration factor, (K_t)
3.5
3.0
2.5
2.0
1.5
1.0
0.0
0.2
0.4
0.6
0.8
1.0
r/D
(a)

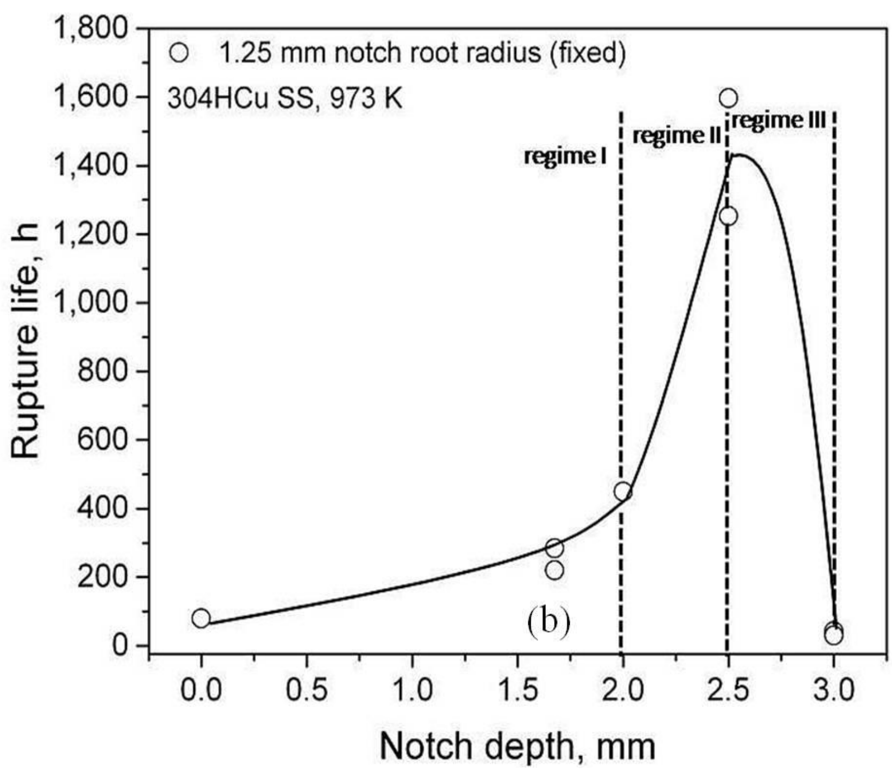
1.25 mm notch root radius (fixed)
304HCu SS, 973 K
regime I
regime II
regime III
Rupture life, h
1,800
1,600
1,400
1,200
1,000
800
600
400
200
0
0.0
0.5
1.0
1.5
2.0
2.5
3.0
Notch depth, mm
(b)

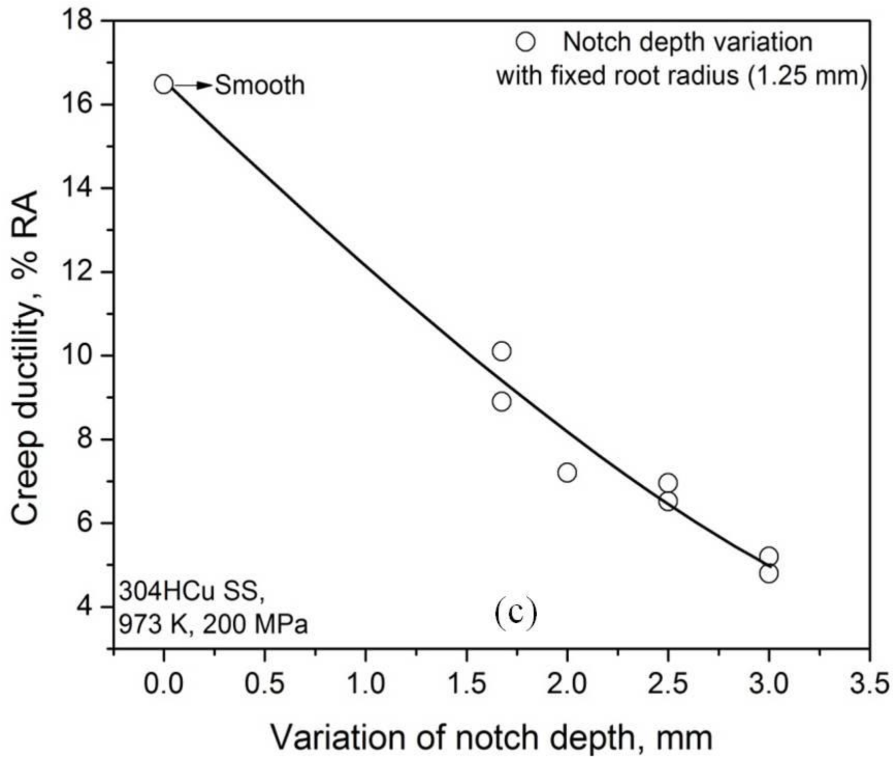

Fig. 7.2 shows the variation of (a) stress concentration factor with R/d ratio, (b) creep rupture life and (c) creep ductility with notch depth.

It has been widely established that increase in notch sharpness (decrease in root radius) for a fixed depth results increase in K_t value and creep rupture life of the material [95, 96, 170]. However, here it is interesting to see that decrease in K_t value results increase in creep rupture life followed by a peak and then decrease in creep rupture life.

7.3 Effect of notch depth on fracture appearance:

The SEM fractographic investigation was carried out to understand the failure mechanisms under multiaxial state of stress. The overall fracture surface for notch depth 1.675, 2.5 and 3 mm are shown in **Fig. 7.3 (a)**, **7.3 (b)** and **7.3 (c)** respectively. In the case of 1.675 mm notch depth, the fracture appearance near to the notch root predominantly consisted of intergranular creep cavities and cracks, **Fig. 7.3 (a-1)**. The fracture appearance in between the notch root and the centre was of mixed mode with little appearance of transgranular ductile dimples with intergranular creep cavities cavities, **Fig. 7.3 (a-2)**. The fracture appearance in the central region of notch throat plane was predominantly transgranular ductile dimples, **Fig. 7.3 (a-3)**. The fracture surface appearance for the notch depth of 2.5 mm (where maximum strengthening was observed) significantly changed across the notch throat plane. Predominantly transgranular dimples with quite less extent of creep cavities were observed at the notch root, **Fig. 7.3 (b-1)**. The transgranular dimples became finer towards the centre of notch, **Fig. 7.3 (b-2)** and mixed mode fracture was observed in the central region (**Fig. 7.3 (b-3)**). It is interesting to note that for the notch depth of 3 mm (where notch weakening was observed), the creep cavitation was predominant in the interior of notch throat plane, **Fig. 7.3 (c-2 and c-3)**, especially in the central region of notch throat plane (**Fig. 7.3 (c-3)**). However, little transgranular ductile dimples were observed in the notch root region, (**Fig. 7.3 (c-1)**).

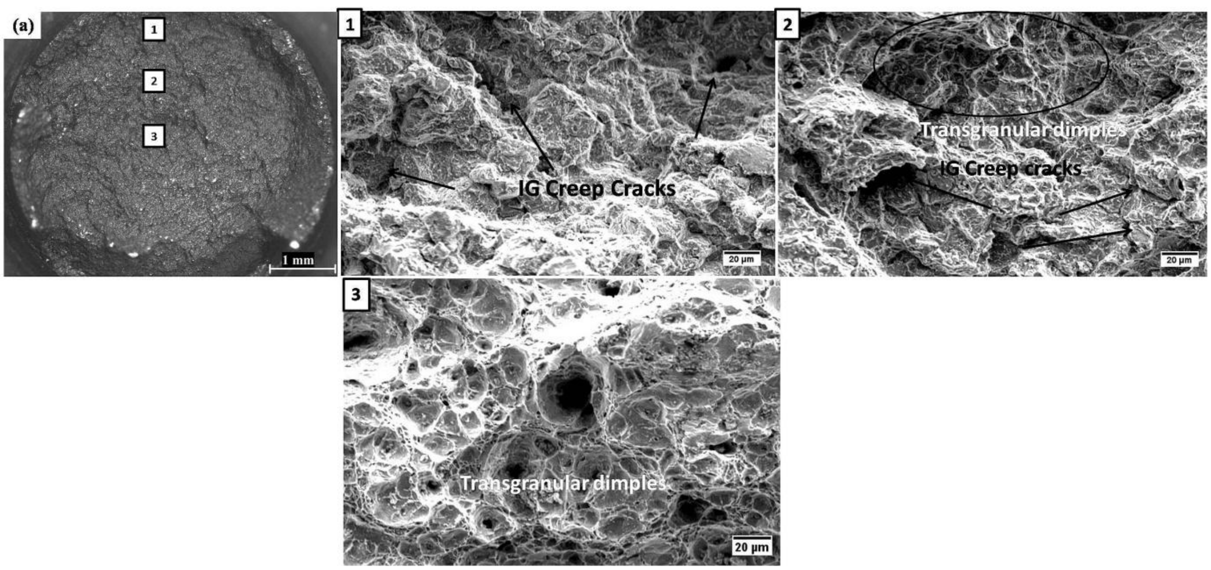

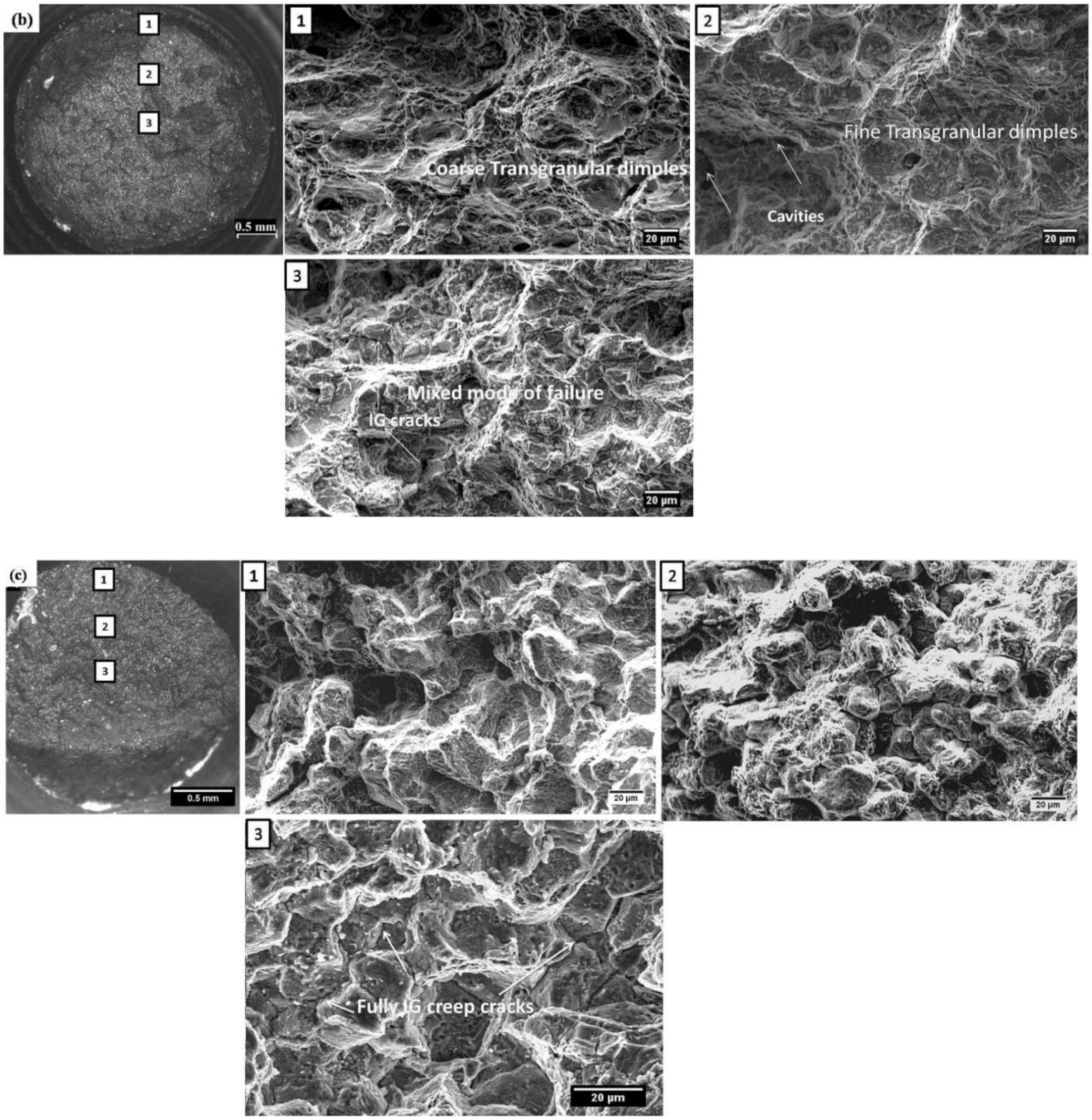

Fig. 7.3 SEM fractograph of the notched specimens with depth of (a) 1.675 (c) 2.5 (d) 3 mm at 973 K and 200 MPa.

Table-7.1 Shows the overall variation in fracture surface with increase in notch depth at 973 K, 200 MPa.

Notch depth	**Overall fracture morphology**
1.675 mm	Predominance ductile dimples with isolated cavities (Coarser in size near to root and fine cavities at and around the centre)
2.5 mm	Coarse transgranular dimples at the notch root and mixed mode of failure with very less ductile dimples at and around centre.
3 mm	Predominance intergranular creep cracks with no such dimples at and around the notch plane.

The SEM metallographic investigation was carried out on the unfailed notch of relatively shallow (1.675 mm) and deep notch (2.5 mm) to observe the distribution of creep cavitation and damage at the notch throat plane **[Fig. 7.4]**. Localized creep cavitation with macro-cracks was found at the notch root and propensity for creep cavitations were found less at the centre for relatively shallow notch **[Fig. 7.4(a)]**. However, for deep notch uniform distribution of creep cavitations with fine micro- cracks were seen from notch root to centre **[Fig. 7.4(b)]**. It shows that creep cavitation was concentrated to root of the notch for relatively shallow notch while for deeper notch nucleation of creep cavitation was almost uniform at the notch throat plane.

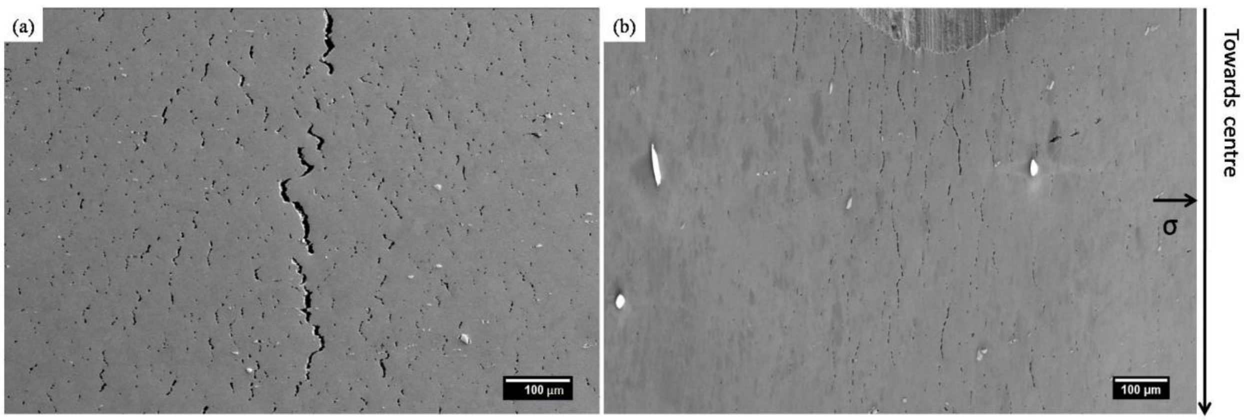

Fig. 7.4 SEM metallography of unfailed notched creep specimen of notch depth (a) 1.675, (b) 2.5 mm creep tested at 200 MPa and 973 K.

7.4 Stationary state of stress distribution across the notch throat plane:

The state of stress in the notched specimens is quite complex and varies from the notch root to centre of notch. In order to understand the variation in appearance of fracture depending on the notch depth, FE analysis has been carried out considering elastic-creep material model. The time dependent creep deformation coupled with elastic analysis has been used to study the stationary state variation in across the notch throat plane during creep exposure. The variation of axial stress after elastic deformation as a function of normalized distance from centre of notch is shown in **Fig. 7.5**. The axial stress was found to lower at the central region of notch than root of the notch for shallow depth. As the notch depth is increased, the stress becomes higher at the central region as compared to notch root. Earlier studies by Goyal et al. [95, 96] for Grade 9 and 316 LN steel revealed that the role of plastic deformation in the stress distribution across the notch throat plane under creep condition was almost negligible [153]. Similar results have also been reported for 304HCu SS material [170, 181].

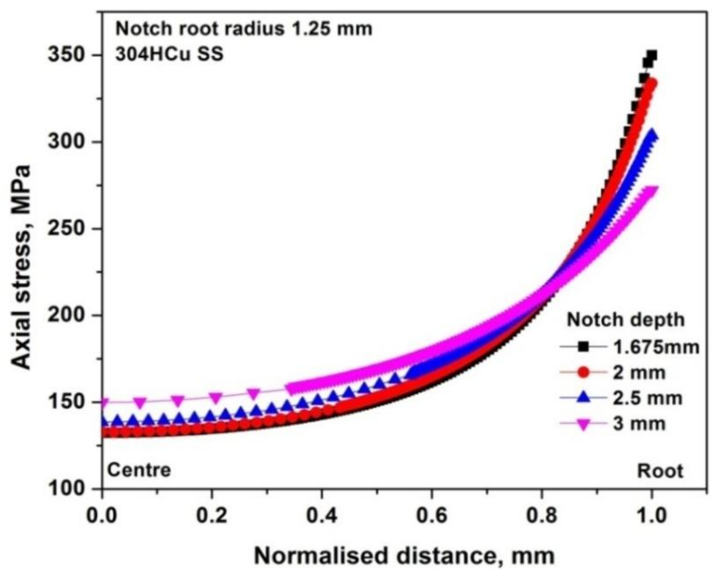

Fig. 7.5 The distribution of Elastic-axial stress for different notch depth specimen.

During time dependent creep deformation, the redistribution of stresses across the notch throat plane takes place **[**91-93, 96, 100, 120**]**. The stresses redistribute with time and attain the stationary state. The extent of stress redistribution depends on the notch geometry and material's deformation characteristics. The variation of von-Mises and maximum principal stress for notch depth 2 and 3 mm at different time of creep exposure before attaining the stationary state were shown in **Fig. 7.6** and **Fig. 7.7** respectively. Peak in von-Mises and maximum principal stress at and nearby root redistributes with creep exposure at different time to attain stationary state.

Significant variation of stress redistributions were observed during creep exposure for 3 mm notch depth in comparison to 2mm notch depth. It shows that the variation in redistribution stress increases with increase in notch depth. Similar type of observation was seen in notch root radius variation study [170]. However, the variation in redistribution stresses with creep exposure were much significant in shallow notches compared to sharper notches where marginal difference were seen with creep exposure in notch depth study. Further, the time to attain stationary state with increase notch depth is consistent. The time taken for attaining the stationary state for notch depth of 1.675, 2, 2.5 and 3 mm were 150, 76, 45 and 23 hours respectively. Moreover, there is no such deviation to attain stationary state with increase in notch depth. Hence, the ability of the material to strengthen or weaken for a given condition cannot be decided based on this. However, the unnotched ductility of the 304HCu material at the same stress is around 15%, the effect on notch may cause strengthening or weakening depends upon the notch geometry [182]. The variation of von-Mises stress, maximum principal stress, hydrostatic stress and triaxiality factor in the notch throat plane depending on the notch depth are shown in **Fig. 7.8**.

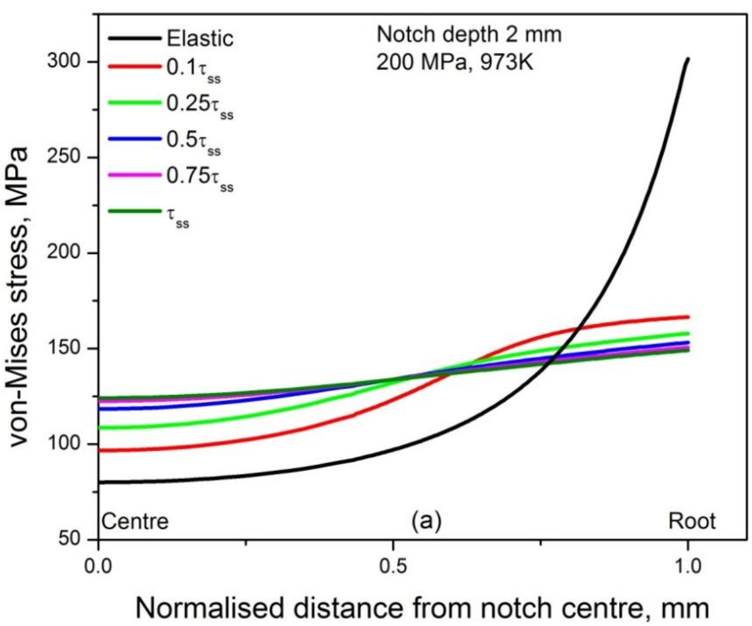

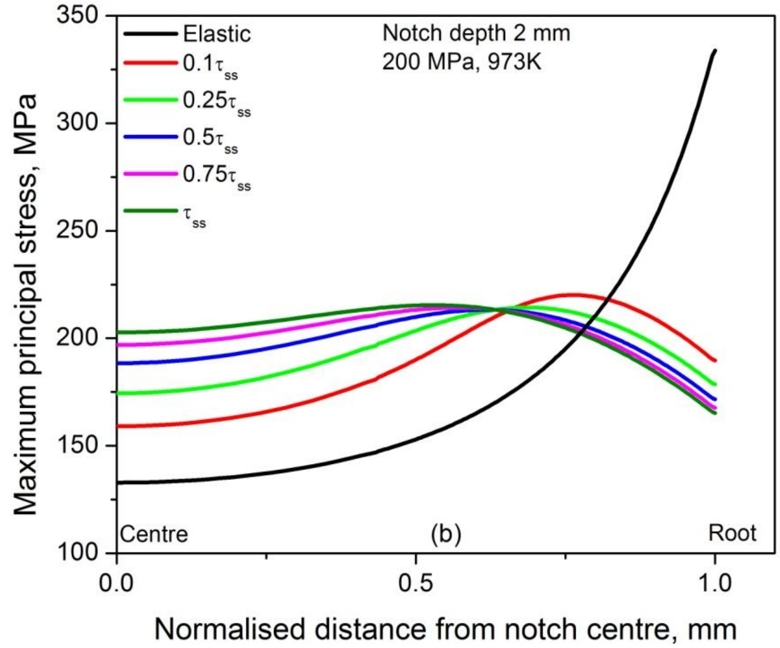

Fig. 7.6 Variation of (a) von-Mises and (b) maximum principal stress across the notch throat plane as a function of creep exposure time for notch depth 2 mm.

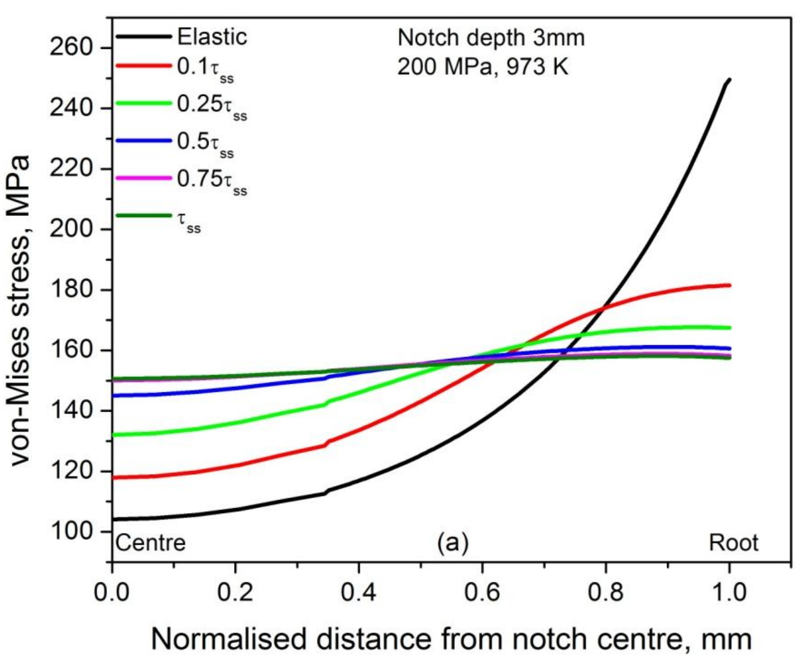

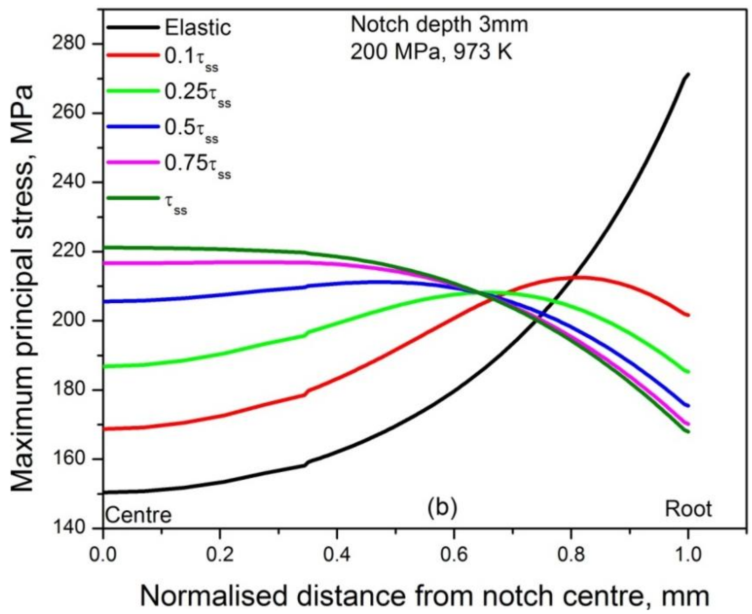

Fig. 7.7 Variation of (a) von-Mises and (b) maximum principal stress across the notch throat plane as a function of creep exposure time for 3mm notch depth.

The von-Mises stress was found to increase across the notch throat plane with increase in notch depth, **Fig. 7.8(a)**. The maximum principal stress showed maxima between centre and root of the notch for shallow depth of notch, **Fig. 7.8(b)**. The maxima shifted towards centre of notch with increase in notch depth. The value of maximum principal stress was more or less similar at the notch root. However, it exhibited a peak between the centre and root and increased towards the centre with increase in notch depth. Trend similar to maximum principal stress was observed for hydrostatic stress also, **Fig. 7.8(c)**. The triaxiality factor (TF) is defined as the ratio of von-Mises to hydrostatic stress. Its variation across the notch throat plane with notch depth is shown in **Fig. 7.8(d)**. The TF showed maxima in the central region of notch throat plane for deeper depth specimens. However, it shifted towards notch root for relatively shallow depth notches. The significant amount of cavitation for 1.675 mm notch close to the notch root (**Fig. 7.4(a**)) and in the central region for 2.5 mm notch depth (**Fig. 7.4(b**)) could be attributed to the difference in distribution of triaxiality factor across the notch throat plane.

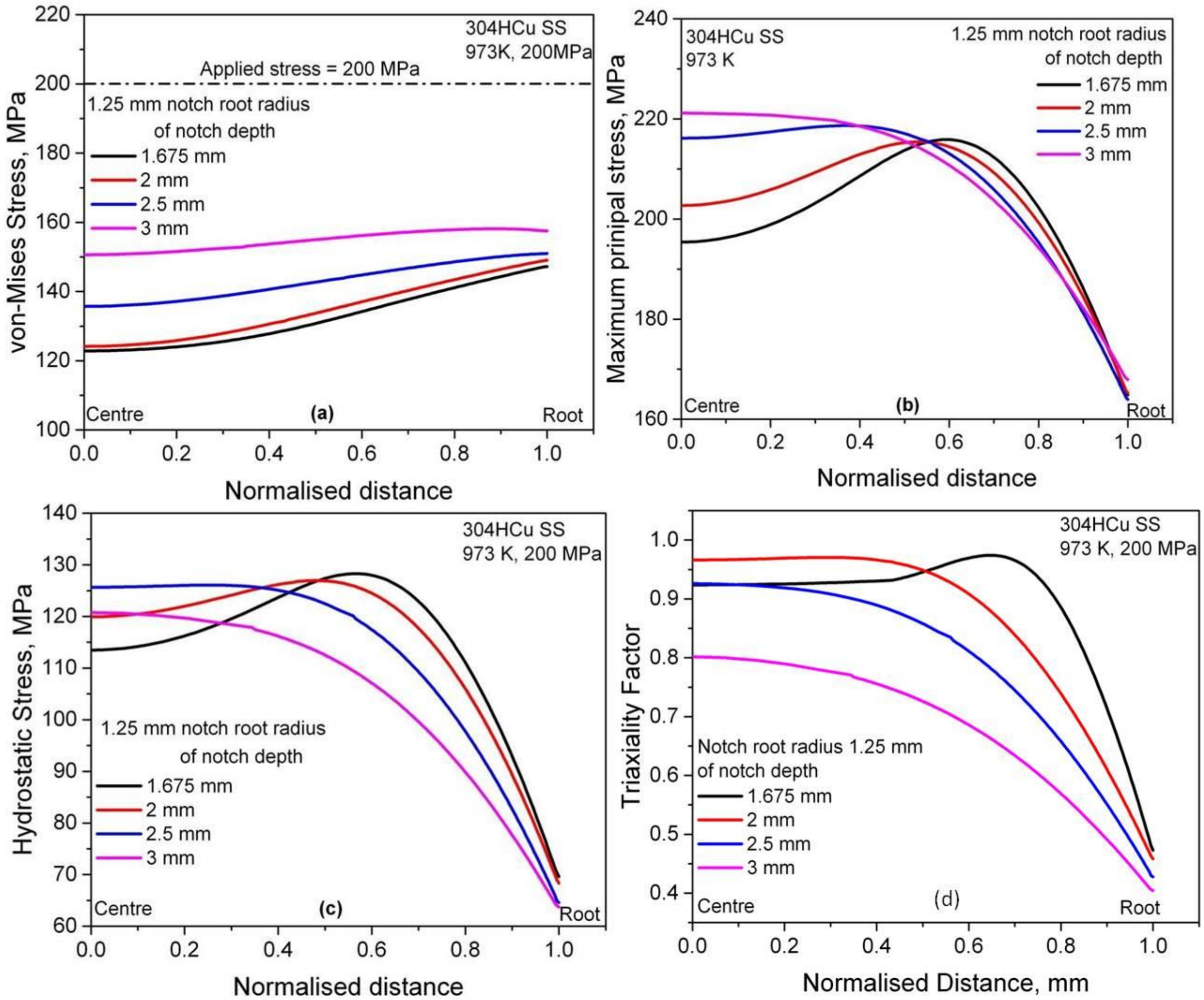

Fig. 7.8 The distribution of (a) von-Mises, (b) maximum principal and (c) hydrostatic state of stress across the notch throat plane after attaining the steady state for different notch depth creep tested at (973K, 200MPa).

The creep cavitation is associated with the creep cavity nucleation, their growth, coalescence and final failure. The von-Mises stress plays a significant role in the cavity nucleation. Whereas, the creep cavity growth is predominantly controlled by maximum principal and hydrostatic stresses [104]. For the shallow depths, the von-Mises stress was found to be higher close to the notch root as compared to centre of notch. Relatively higher von-Mises stress would lead to nucleation of more cavities close to notch root than that of centre. Since the maximum principal stress was higher away from centre, the cavity growth is expected to be higher there resulting in fracture appearance as shown in **Fig. 7.3(a)**. However, for deeper notches such as notch depth of 3.0 mm, the von-Mises stress was uniform across the notch throat plane. Uniform von-Mises stress would result in uniform cavity nucleation across the notch. However, the maximum principal stress was higher at the centre of notch, which will allow the growth of cavities there as shown in **Fig. 7.3(c)**. The increase in rupture life in presence of notch is generally attributed to the decrease in von-Mises stress below the net applied stress across the notch throat plane. It is interesting to note that the rupture life increased initially with increase in depth followed by a decrease in rupture life. The decrease in creep rupture life for deeper notches could be attributed to the extensive creep cavitation observed in the material. The variation of equivalent creep strain distribution in the notches of different depths after attaining the stationary state is shown in next section in **Fig. 7.12**. The accumulated creep strain was found to decrease with increase in notch depth. Further, the time for attaining the stationary state decreased with increase in notch depth. Significant increase in strain accumulation (1.675 mm) could result in lower rupture life as compared to deeper notch depth specimens. The contour view of von-Mises stress, maximum principal stress and hydrostatic stress for 2, 2.5, 3 mm notch depth were shown in Fig. **7.9, 7.10, 7.11** respectively. Further, the time for attaining the stationary state decreased with increase in notch depth. Significant increase in strain accumulation (1.675 mm) could result in lower rupture life as compared to deeper notch depth specimens. In the next section, the distribution of creep equivalent strain after stationary state for different notch depth has been correlated with strain mapping obtained through EBSD-KAM map.

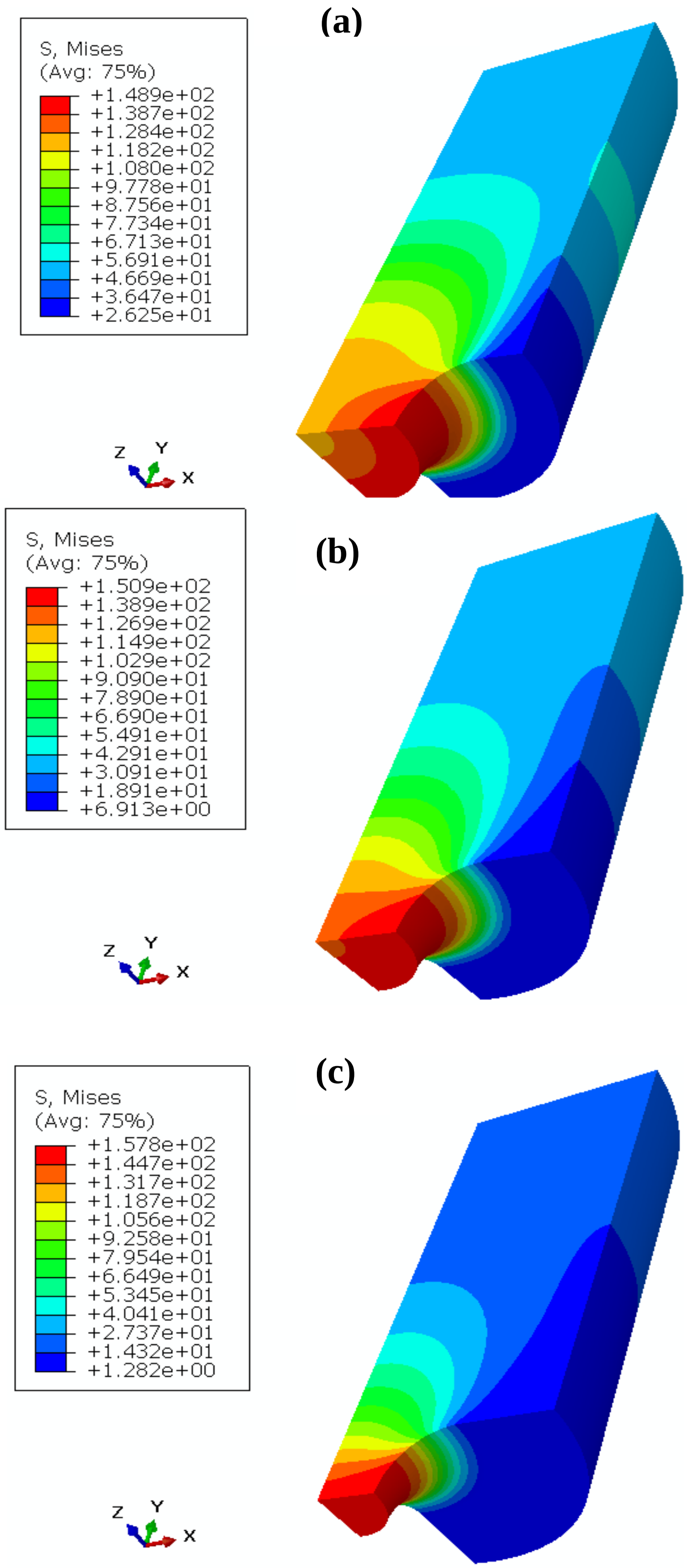

Fig. 7.9 Contour view of von-Mises stress for (a) 2 mm, (b) 2.5 mm, (c) 3 mm notch depth.

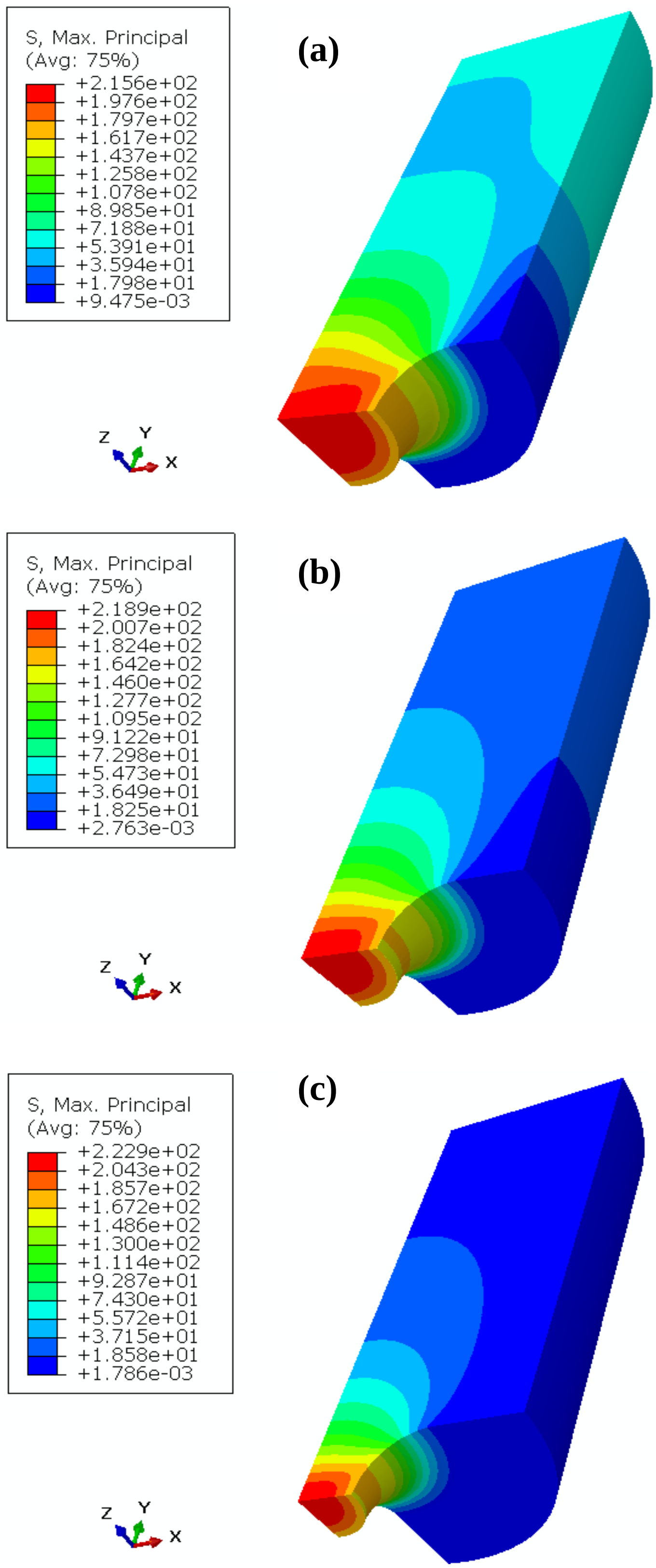

Fig. 7.10 Contour view of maximum principal stress for (a) 2 mm, (b) 2.5 mm, (c) 3mm notch depth.

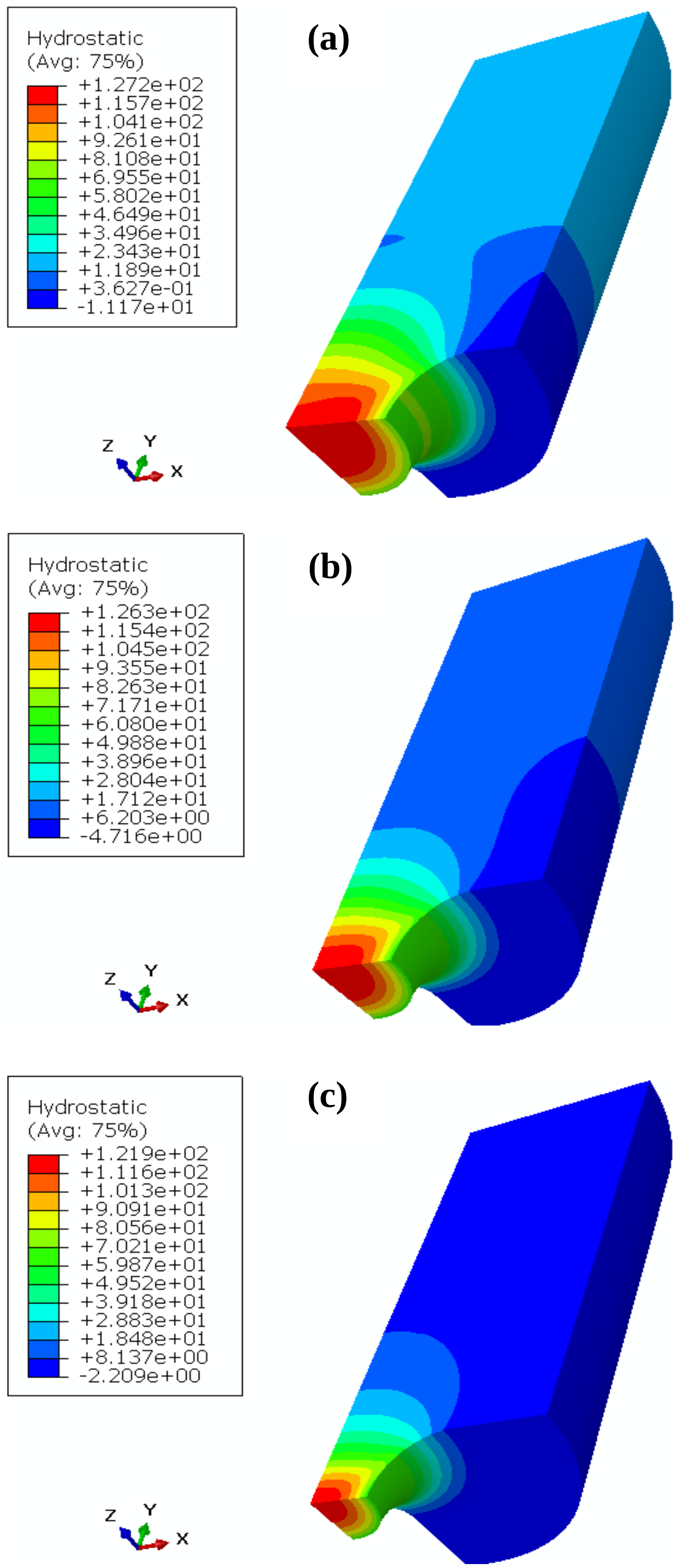

Fig. 7.11 Contour view of hydrostatic stress for (a) 2 mm, (b) 2.5 mm, (c) 3mm notch depth.

7.5 Stationary state of strain distribution across the notch throat plane

The increase in von-Mises stress with increase in notch depth suggests that rupture life of 304HCu SS should decrease subsequently with increase in notch depth which contradicts experimental observation. Hence, same elastic-creep model has been used to study the creep equivalent strain distribution of different notch depth specimen at the same state of stress under constant tensile load.

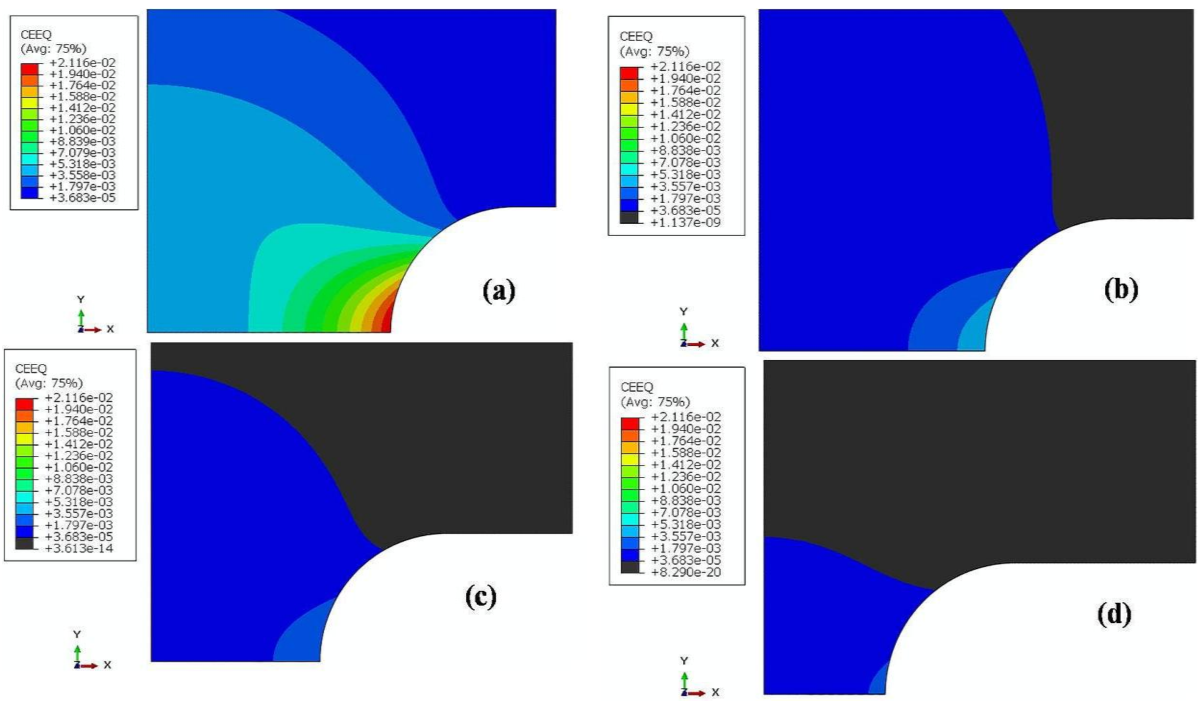

Fig. 7.12 Contour view of CEEQ throughout the specimen for (a) 1.675, (b) 2, (c) 2.5 and(d) 3 mm notch depth specimen at 973 K, 200 MPa.

Creep equivalent (CEEQ) strain distribution [**Fig. 7.12**] under stationary state reveals drastic decrease in creep strain with increase in notch depth. Significant increase in strain accumulation (1.675 mm) could result in lower rupture life as compared to deeper notch depth specimens. The creep strain distribution at the notch throat plane for 2, 2.5 and 3 mm shows no difference at and near to notch centre and marginal decrease in CEEQ at the notch root with increase in notch depth [**Fig. 7.13**].The increase in notch depth also results decrease in creep ductility due to the transition from transgranular ductile dimple with isolated cavities to intergranular crack induced failure with increase in notch depth. The observation of fracture surface and strain distribution with increase in notch depth clearly matches with each other. This revel that the variation in notch depth is mainly controlled by strain induced damage process. The influence of constraint on creep strain distribution for different notch depth specimen has been already carried out by Wu et.al [92]. The constrained factor, which is proportional to the ratio of notch radius to the net radius of the cross section decreases with increase in notch depth. The increase in degree of constraint increases the creep strain and can lead to failure due to plasticity instability with the increase of creep exposure which will be seen in the EBSD-KAM map.

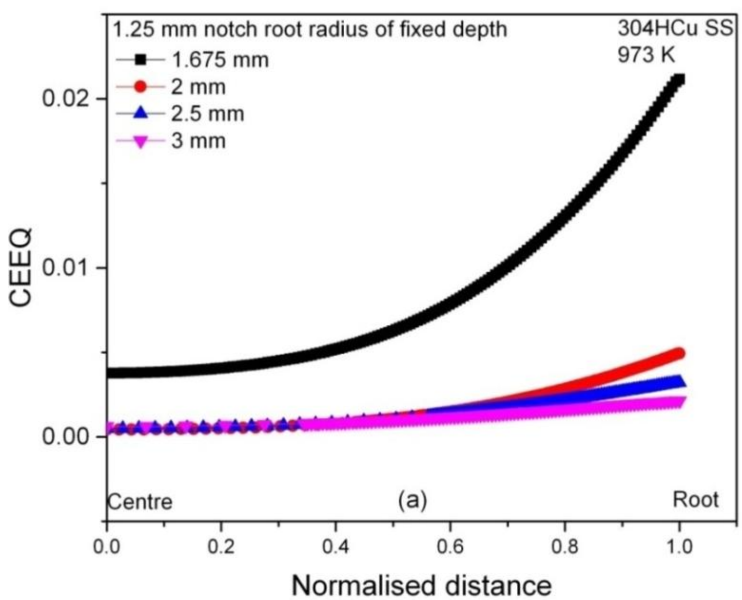

Fig. 7.13 Variation of CEEQ, at the notch throat plane for 1.675, 2, 2.5, 3 mm notch depth specimen at 973 K, 200 MPa.

7.6 Strain mapping using OIM analysis (EBSD studies)

The analysis was further validated by carrying out the EBSD in the notch root region of unfailed notched specimens. The distribution of Kernel Average Misorientation (KAM) map across the notch root is shown in **Fig. 7.14**. The localised strain obtained through KAM map shows higher

KAM value from centre to root for 1.675 mm notch depth specimen than 2.5 and 3 mm which shows good matching with CEEQ value [**Fig. 7.12**]. On the other hand the KAM value of 1.675 mm notch depth was almost uniform at the notch root and higher misorientation value results in enhanced creep cavitation cracking. The creep cavity nucleation is expected to be more in high KAM region due to large local deformation. It is quite evident that creep cavities nucleate along high angle grain boundaries like triple points. Deformation and rotation of the matrix enhances the nucleation of cavities through higher mismatch with neighbouring grains. Hence, higher misorientation angle with relatively higher frequencies increases the tendency for intergranular creep cavitation. Similar observation was seen in 304HCu SS at 923 K and 1023 K at NSR 1.1 and 1023K at NSR 1.2 where NSR represents the ratio of applied stress to the yield stress of the specimen [181]. Higher average value of KAM results enhanced creep cavities at 923 K and 1023 K at lower and high stress region. Further, Wang et al. observed cavities in FGHAZ reflected by high KAM during strain mapping of creep tested P91 steel weldments [183]. Similar observation was seen in IN738LC at 1033 K in the final stage of creep life where sharp rise in misorientation spread was observed near to the crack initiation site [184]. However, there is a significant gradient of KAM value across the notch root for 2.5 and 3 mm notch depth. The frequency distribution of KAM value was shown in **Fig. 7.15**. Clearly, it can be observed that KAM value of 1.675 mm notch depth was significantly higher (around 5) than 2.5 and 3 mm notch depth. On the other hand, the frequency distribution of KAM value for 3 mm notch depth was more than 2.5 mm, the maximum distribution of KAM value was around 1.5^0 for 3 mm notch depth and 1^0 for 2.5 mm notch depth. This observation shows more propensities to intergranular creep cavitation failure for 3 mm notch depth compared to 2.5 mm. Thus increase in KAM value (1.675 mm) results increase in deformation zone which makes the material to cavitate more compared to other and due to heavy strain at the same state of stress material get failed due to plastic instability. In this investigation the clear correlation between rupture lives of different notch depth studies with FE- analysis has not yet done. The present dissertation is limited to short duration. However, as per the literature studies, definitely notch weakening are expected to occur for this type of material with increase in notch depth at lower net applied stresses [185-187]. Hence, further research has to be carried out to take into account the effect of strain induced damage or electron microscopy studies to study the effect of strain induced precipitates, dislocation and precipitation interaction strengthening effect on the rupture life.

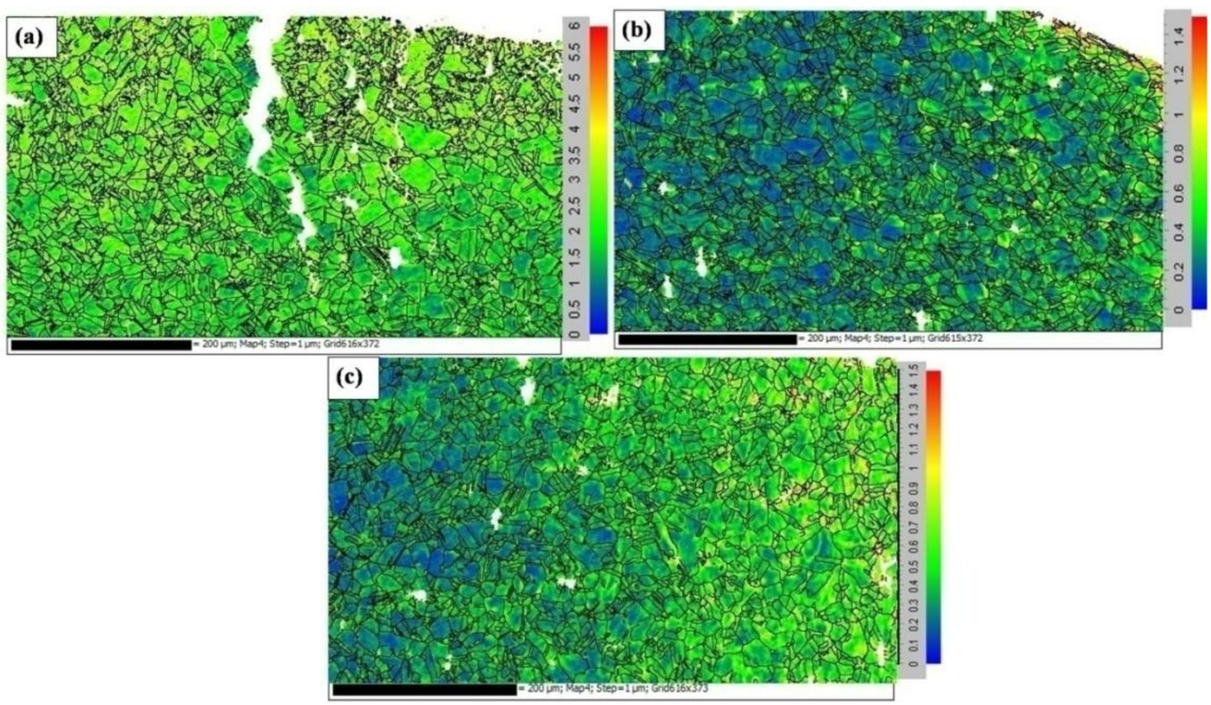

Fig. 7.14 Shows the EBSD-KAM map of (a) 1.675 mm, (b) 2 mm and (c) 3 mm notch depth at 973 K, 200 MPa

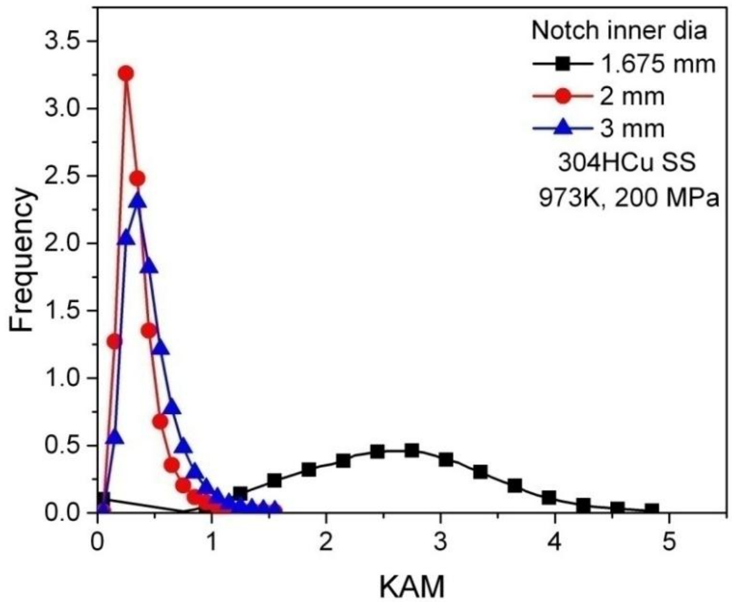

Fig. 7.15 shows the frequency vs KAM plot for 1.675, 2, 3 mm unfailed notch depth, creep tested at 973 K, 200 MPa.

7.6 Conclusions

- 304HCu SS material exhibited notch strengthening for shallow depth notches, whereas, notch weakening for deeper notches.
- The ductility of the material was found to decrease with increase in notch depth and would follow a trend of saturation for deeper notches.
- The fracture surface was found to change from mixed mode fracture for shallow deep notches to intergranular creep cavitation dominant brittle failure for relatively deeper notch.
- The reduction in creep rupture life (notch weakening) is attributed to the extensive creep cavitation for relatively deeper notch.
- The multiaxial creep rupture life of the material under notch depth variation was found to control by both equivalent stress and strain distribution.

- The equivalent strain distribution was found to follow good matching with the local misorientation spread obtained through EBSD-KAM map. Higher degree of misorientation angle (KAM) resulted in enhanced cavitation at the notch root for 1.675 mm notch depth as compared to other notch depth specimens.

REFERENCES

1. Report: 'Why the UK's CO2 emissions have fallen 38% since 1990', Carbon brief analysis, 2017.
2. A. K. Bhaduri, K. Laha, S. K. Albert, T. Jayakumar, S. C. Chetal, Development of High Temperature Boiler Tube Materials for the Indian Advanced ultra Super Critical Thermal power plant , 41st MPA seminar-october 5th and 6th , 2015.
3. D. J. Gooch and I. M. How, Elsevier Applied Science, Amsterdam, 1986, pp. 137- 175.
4. B. Neubauer and U. Wedel, Rest life estimation of creeping components by means of replicas, in Advances in life prediction methods, D.A, Woodford and J.R. Whitehead Eds. ASME, New York, 1983, 307- 314.
5. H. J. Frost and M. F. Ashby, Deformation mechanism maps, Pergamon Press, 1982
6. M. F. Ashby, C. Gandhi and D. M. R. Taplin, Fracture mechanism maps and their construction for FCC metals and alloys, Acta Met., 27 (1979) 699- 729.
7. S. H. Goods and L. M. Brown, The nucleation of cavities by plastic deformation, Acta Met., 27 (1979) 1- 15.
8. W. D. Nix, Mechanisms and controlling factors in creep fracture, Mater. Sci. Engg. A., 103 (1988) 103- 110.
9. R. Raj and M. F. Ashby, Intergranular fracture at elevated temperature, Acta Met., 23 (1975) 653- 666.
10. H. E Evans, Mechanisms of Creep Fracture, Elsevier Applied Science, Essex, UK, 1984.
11. E. Smith and J. T. Barnby, Nucleation of grain boundary cavities during high temperature creep, Metal Sci., 1 (1967) 1- 4.

12. A. S. Argon, Intergranular cavitation in creeping alloys, Scripta Metall., 17 (1) (1983) 5–12.
13. K. Laha, J. Kyono, N. Shinya, Copper, Boron, and Cerium Additions in Type 347 Austenitic Steel to Improve Creep Rupture Strength, Metall. Mater. Trans. A., 43 (2012) 1187-1197.
14. D. Hull and D. E. Rimmer, The growth of grain boundary voids under stress, Phil. Mag., 4 (1959) 673- 687.
15. B. F. Dyson, Constraints on diffusional cavity growth rates, Metal Sci., 18 (1976) 349-353.
16. J. R. Rice, Constraints on the diffusive cavitation of isolated grain boundary facets in creeping polycrystals, Acta Metall., 29 (4) (1981) 675–681.
17. H. Riedel, Cavity nucleation at particles on sliding grain boundaries. A shear crack model for grain boundary sliding in creeping polycrystals, Acta. Metall., 32 (3) (1984) 313–321.
18. W. D. Nix, D. K. Matlock, R. J. Dimelfi, A model for creep fracture based on the plastic growth of cavities at the tips of grain boundary wedge cracks, Acta Metall. 25 (5) (1977) 495–503.
19. I.-W Chen, A. S. Argon, Creep cavitation in 304 stainless steel, Acta Metall. 29 (7) (1981) 1321–1333.
20. I-W Chen, A. S. Argon, Diffusive growth of grain-boundary cavities, Acta Metall. 29 (10) (1981) 1759–1768.
21. W. Beere, M.V. Speight, Creep cavitation by vacancy diffusion in plastically deforming solid, Metal. Sci. 12 (4) (1978) 172–176.
22. J. W. Hancock, Creep cavitation without a vacancy flux, Metal Sci., 10 (1976) 319- 325.

23. Y. Ishida and D. McLean, The formation and growth of cavities in creep, Metal Sci., 1 (1967) 171- 172.

24. Needleman and J.R. Rice, Plastic creep flow effects in the diffusive cavitation of grain boundaries, Acta metall., 28 (1980) 1315- 1332.

25. F. A. McClintock, A criterion for ductile fracture by the growth of holes, J. Appl. Mech., 35 (1968) 363- 371.

26. P. F. Thomason, A theory of ductile fracture by internal necking of cavities, J. of Inst. Metals, 96 (1968) 360- 365.

27. P. F. Thomason, A theoretical relation between fracture toughness and basic material properties, Int. J. Frac. Mech., 7 (1971) 409- 419.

28. L. M. Brown, J. D. Embury, The initiation and growth of voids at second phase particles. Proc 3rd Int Conf on the Strength of Metals and Alloys, Inst of Metals, London, 1973, pp. 164- 169.

29. A. C. F Cocks, M. F. Ashby, Creep fracture by coupled power-law creep and diffusion under multiaxial stress. Metal. Sci., 16 (10) (1982) 465–474.

30. W. D. Nix, Introduction to the viewpoint set on creep cavitation. Scripta Metall., 17 (1) (1988) 1–4.

31. J. Cadek, On the cavity-growth-model-based prediction of the stress dependence of time to creep fracture. Mater. Sci. Eng. A., 117 (1989) L5–L9.

32. H.-M. Lu, T. J. Delph, Models for coupled diffusive/strain controlled growth of creep cavities. Scripta Metall. 29 (3) (1993) 281–285.

33. G. H. Edward, M. F. Ashby, Intergranular fracture during power-law creep. Acta Metall., 27 (9) (1979) 1505–1518.

34. Y. S. Lee, T. A. Kozlosky, T. J. Batt, Effects of grain boundary diffusion and power law creep on cylindrical cavity deformation. Acta Metall. Mater. 41 (6) (1993) 1841–1854.
35. L. M. Kachanov, The theory of Creep (Ed. A.J. Kennedy), National Lending Library, Boston Spa, UK, 1967.
36. Y. N. Robotnov, Creep problems in structural members, North-Holland, 1969.
37. J. Lemaitre and J. L. Chaboche, Mechanics of solid materials, Cambridge University Press, Cambridge, 1990
38. P. J. Bouchard, P. J. Withers, S. A. McDonald, R. K. Heenan, Quantification of creep cavitation damage around a crack in a stainless steel pressure vessel, Acta Mater., 52 (2004) 23–34.
39. M. F. Ashby and B. F. Dyson, Creep damage mechanics and micro mechanisms, Eds. R. S. Valluri, Advances in Fracture Research, vol. 1, Pergamon Press, Oxford, 1984, pp. 3-30.
40. B. F. Dyson, Use of CDM in materials modeling and component creep life prediction, Trans ASME, J. Press. Vess. Tech., 122 (2000) 281- 296.
41. B. F. Dyson and M. McLean, Microstructural evolution and its effects on the creep performance of high temperature alloys, Microstructural stability of creep resistant alloys for high temperature plant applications, Eds. A. Strang, J. Cawley and G.W. Greenwood, The Institute of materials, London, UK, 1998, 371- 394.
42. MTDATA, National Physical Laboratory, Teddington, Middlesex, UK, 1989.
43. F. R. Beckitt and B. R. Clarck, The shape and mechanism of formation of $M_{23}C_6$ carbide in austenite, Acta Metall., 15 (1967) 113-129.

44. D. H. Jack, K. H. Jack, Structure of Z-phase, NbCrN, J. Iron Steel Inst., 210 (1972) 790-792.

45. P.W. Robinson, D. H. Jack, New development in stainless steel technology, (ed R.Lula), , Metals park, OH, American Society for Metals, (1985) 71-76

46. Y. Minami, H. Kimura, Y. Ihara, Microstructural changes in austenitic stainless steels during long-term aging, Mater. Sci. and tech., 2 (1986) 795-806.

47. B. Weiss, R. Stickler, Phase instabilities during high temperature exposure of 316 austenitic stainless steel, Metall. Mater. Trans. B, 3 (1972) 851–866.

48. R. C. Ecob, R. C. Lobb, V. L. Kohler, The formation of G-phase in 20/25 Nb stainless steel AGR fuel cladding alloy and its effect on creep properties, J. Mater. Sci., 22 (1987) 2667-2680.

49. S. Degalaix and J. Foct, Mem. Etud. Sci. Rev. Metall., 84 (1987) 945-653

50. R. F. A. Jargelius-Pettersson, Precipitation trends in highly alloyed austenitic stainless steels, Z. Metallkd, 79 (1998) 177-183.

51. A. Tohyama and Y. Minami, Advanced heat resistant steel for power generation', (ed. R. Viswanathan and J. Nutting), London, IoM communications Ltd. (1999) 494-506.

52. J. K. L. Lai, Precipitate phases in type 321 steel, Materials Science and Technology, 1(2) (1985) 97-100,

53. R. Lagneborg and K. Norrgard: Internal Report AB Atomenergi (MF 22), September 1969.

54. B. Bergman and R. Lagneborg, Jernkontorets Ann., 155 (1971) 368.

55. B. Bergman, Creep Deformation of Gamma Prime-Hardened 80 per cent Ni-20 per cent Cr Alloys, Scand. J. Metallurgy, 4 (1975) 97.

56. P. L. Threadgill, B. Wilshire, The Effect of Particle Size and Spacing on Creep of Two-Phase Copper–Cobalt Alloys, Metal Sci., 8 (1974) 117.

57. B. Bergman, A note on the Strain Transient Dip Technique, Scand. J. Metallurgy, 4 (1975) 177.

58. P. L. Threadgill, B. Wilshire: Proc. Meeting 'Creep Strength in Steels and High-Temperature Alloys', Sheffield 1972, pp; 8-14 (Metals Society)

59. B. Russell, R. K. Ham, J. M. Silcock, and G. Willoughby Metal Sci. J., 2 (1968) 201.

60. A. Oden, Doctoral Dissertation, Royal Institute of Technology, May 1975.

61. C. L. Meyers, J. C. Shyne, and O. D. Sherby, Relation of Structure to Properties in Sintered Aluminum Powder. J. Australian Inst. Met., 8 (1963) 171

62. B. A. Wilcox and A. H. Clauer, Creep of Thoriated Nickel Above and Below 0. 5T_m, Trans. Met. Soc. AIME, 236 (1966) 570.

63. R. A. Stevens and P. E. J. Flewitt The dependence of creep rate on microstructure in a γ' strengthened superalloy, Acta metal.,29 (1981) 867-882

64. B. Reppich, H. Bugler, R. Leistner and M. Schutze. In proceedings int.conf. on creep and Fracture of Engineering Materials and Structures, Swansea, Eds. B. Wilshire and D.R.J. Owens, Piperidge press, U. K., Pages 279, 1984.

65. R. Lagneborg and B. Bergman, The stress/creep rate behaviour of precipitation-hardened alloys**,** Met. Sci. J., 10 (1976) 20–28.

66. H. E. Evans and Knowles, Threshold stress for creep in dispersion- strengthened alloys, Metal Sci., 14 (1982) 262-266.

67. M. Mc. Lean, On threshold stress for dislocation creep in particle strengthened alloy, Acta metal., 33 (1985) 545-556.

68. J. C. Gibbeling and W. D. Nix, The existence of a friction stress for high temperature creep. Metal Sci., 11 (1977) 453-457.

69. H. Burt, J. P. Dennison and B. Wilshire, Friction stress measurements during creep of Nimonic 105, Metal Sci., 13 (1979) 295-300.

70. B. K. Choudhary, C. Phaniraj, K. Bhanu Sankara Rao and S. L. Mannan, Creep deformation behaviour and kinetic aspects of 9Cr-1Mo ferritic steel, ISIJ Int., 41 (2001) S73–S80.

71. J. Vanaja, K. Laha, and M.D. Mathew, Effect of Tungsten on Primary Creep Deformation and Minimum Creep Rate of Reduced Activation Ferritic-Martensitic Steel, Metall. Mater. Trans. A, 45 (2014) 5076-5084.

72. R. C. Ecob and H. E. Evans, Creep of TiN dispersion hardened 20%Cr-25% Ni stainless steel below the transition stress. Acta Metall., 35 (1987) 805-821.

73. R. Singh and S. Banerjee, Resisting stress of a low alloy ferritic steel after creep exposure in service, Acta metal. Mater., 40 (1992) 2607-2616.

74. V. M. Radhakrishnan, P. J. Ennis and H. Schuster, An analysis of creep Deformation and Rupture by β-envelope method, Technical Report No.2535IRW-KFA, Julich, Germany (1991).

75. V. M. Radhakrishnan, Creep fracture of Cr-Mo steel, Fatigue Fract. Engng. Matr. Struct. 15 (1992) 617.
76. V. M. Radhakrishnan, The relationship between minimum creep rate and rupture time in Cr-Mo steels, J. Mater. Engng. performances 1 (1992) 123.
77. F. Garofalo, Fundamentals of Creep and Creep Rupture in Metals, MacMillan, New York, 1965.
78. E. N. Andrade, Proc. Royal Soc., London, A84, 1(1910) and cited in Ahmadieh and A.K. Mukherjee Mater. Sci. Eng. 21 (1975) 115–124.
79. P. G. McVetty, Working stresses for high temperature service, Mech. Eng., 56 (1934) 149-54.
80. R. W. Evans and B. WilShire, Creep of metals and alloys, the inst. of Metals, London (1985).
81. G. A. Webster, A. P. D. Cox, and J. E. Dorn, A Relationship between Transient and Steady-State Creep at Elevated Temperatures, Metal. Sci. J., 3 (1969) 221–225.
82. S. Goyal, K. Laha, K. S. Chandravathi, P. Parameswaran and M. D. Mathew, Finite element analysis of Type IV cracking in 2.25Cr-1Mo steel weld joint based on micro-mechanistic approach, Phil. Mag., 91 (2011) 3128- 3154.
83. J. T. Boyle and J. Spence, Stress analysis for stress, Camelot press, London, 1983.
84. W. Trampczynski and Z. Kowalewski, A Tension-torsion testing technique,Techniques for multiaxial creep testing. Eds. D.J. Gooch and I.M. How, Elsevier Applied Science, Amsterdam, 1986, pp. 79- 92.

85. C. J. Morrison, Biaxial testing using cruciform specimens, Techniques for multiaxial creep testing. Eds. D.J. Gooch and I.M. How, Elsevier Applied Science, Amsterdam, 1986, pp. 111- 126.

86. P. S. Webster and A. C. Pickard, The prediction of stress rupture life of notched specimens in the beta-processed Titanium alloy Ti5331s, J. Strain Analysis, 22 (1987) 145- 153.

87. S. E. Ng, G. A. Webster and B.F. Dyson: in Advances in Fracture Research, ICF-5, D. Francois et al., eds., Pergamon Press, Oxford, 1980, pp. 1275–83.

88. O. Kwon, C.W. Thomas and D. Knowles, Multiaxial stress rupture behavior and stress-state sensitivity of creep damage distribution in Durehete 1055 and 2.25Cr-1Mo steel, Int. J. Press. Vess. Piping, 81 (2004) 535- 542.

89. P. Luka´sˇ, P. Preclı´k, J. Cadek, Notch effects on creep behaviour of CMSX-4 superalloy single crystals, Mat. Sci. Eng. A., 298 (2001) 84–89.

90. Y. Z. Ni, X. Lan, H. Xu & X. P. Mao, Study on creep mechanical behaviour of P92 steel under multiaxial stress state, Mater. High Temp., 32 (2015) 551-556.

91. D. R. Hayhurst and G. A. Webster: in Techniques for Multiaxial Creep Testing. D.J. Gooch and I.M. How, eds., Elsevier Applied Science, Amsterdam, 1986, pp. 137–75.

92. D. Wu, E.M. Christian and E.G. Ellison, Influence of constraint on creep stress distribution in notched bars, J. Strain Anal., 19 (1984) 209–220.

93. D. R. Hayhurst and J. T. Henderson, Creep stress redistribution in notched bars, Int. J. Mech. Sci., 19 (1977)133-146.

94. G. A. Webster, K. M. Nikbin and F. Biglari, Finite element analysis of notched bar skeletal point stresses and dimension changes due to creep, Fat. Frac. Engg. Mater. Struct. 27 (2004) 297- 303.

95. Sunil Goyal, K. Laha, C.R. Das, S. Panneer Selvi, M.D. Mathew, Finite element analysis of uniaxial and multiaxial state of stress on creep rupture behaviour of 2.25Cr–1Mo steel Mats. Sci. Eng. A., 563 (2013)68-77.

96. Sunil Goyal, K. Laha, C. R. Das and M. D. Mathew, Analysis of Creep Rupture Behavior of Cr-Mo Ferritic Steels in the Presence of Notch, Metall. and Mat. Trans. A, 46 (2015) 205-217.

97. M. C. Pandey, A. K. Mukherjee and D. M. R. Taplin, Effect of triaxial stressstate on creep fracture in Inconel alloy- 750, J. Mater. Sci., 20 (1985) 1201-1206.

98. A. E. Johnson, J. Henderson and V. D. Mathur, Complex stress creep fracture of an aluminum alloy: An investigation conducted at an elevated temperature, Aircraft Engg. Aerospace Tech., 32 (1960) 161- 170.

99. A. E. Johnson, J. Henderson and V. D. Mathur, Combined stress creep fracture of commercial copper at 250^0C, The Engineer, 2.2 (1956) 261- 265.

100. D. R. Hayhurst, Creep rupture under multi-axial states of stress, J. Mech. Phy. Solids, 20 (1972) 381- 390.

101. D. R. Hayhurst, P. R. Dimmer and C. J. Morrison, Development of continuum damage in the creep rupture of notched bars, Phil. Trans. Royal Soc. London, 311 (1984) 103- 129.

102. D. R. Hayhurst, On the role of creep continuum damage in structural mechanics, Engineering Approaches to High Temperature Design, Chapter-4, Pineridge Press, Swansea, 1983.

103. B. J. Cane, Creep cavitation and rupture in 2.25Cr-1Mo steel under uniaxial and multiaxial stresses. In: Proceedings of the Int. Conf. on Mechanical behavior of Materials, Eds. K.J.Miller and R.F. Smith, Pergamon Press, Oxford, 1979, 173- 182.

104. W. D. Nix, J. C. Earthman, G. Eggeler and B. Ilschner, The principal facet stress as a parameter for predicting creep rupture under multiaxial stresses, Acta Metall., 37 (1989) 1067-1077.

105. M. Yatomi, A. D. Bettinson, N. P. O'Dowd and K. M. Nikbin, Modeling of damage development and failure in notched bar multiaxial creep tests, Fat. Frac. Engg. Mater. Struct., 27 (2004) 283- 295.

106. T. H. Hyde, A. A. Becker, W. Sun and J. A. Williams, Finite element creep damage analysis of P91 pipes, Int. J. Press. Vess. Piping, 83 (2006) 853- 863

107. A. M. Othman, D. R. Hayhurst and B. F. Dyson, Skeletal point stresses in circumferentially notched tension bars undergoing tertiary creep modeled with physically based constitutive equations, Proc. Royal Soc. Lond. A, 441(1993) 343- 358.

108. G. A. Webster, S. R. Holdsworth, M. S. Loveday, K. Nikbin, I. J. Perrin, H. Purper, R.P. Skelton and M.W. Spindler, A code of practice for conducting notched bar creep tests and for interpreting the data, Fat. Frac. Engg. Mater. Struct., 27 (2004) 319-342.

109. S. Dhar, R. Sethuraman, PM. Dixit, A continuum damage mechanics model for void growth and micro crack initiation, Engng. Fract. Mech., 53 (1996) 917-928.

110. J. Lemaitre, A continuous damage mechanics model for ductile fracture. ASME J. Engng. Mater. Technol. 107 (1985) 83-89.

111. P. F. Thomason, Ductile fracture of metals. Oxford, UK: Pergamon Press, 1990.

112. T. H. Hyde, L. Xia and A. A. Becker, Prediction of creep failure in aeroengine materials under multiaxial stress states, Int. J. mech. Sci., 38 (1996) 385- 403.

113. A. M. Othman, J. Lin, D. R. Hayhurst and B. F. Dyson, Comparison of creep rupture lifetimes of single and double notched tensile bars, Acta Met., 41 (1993) 1215-1222.

114. F. R. Hall and D. R. Hayhurst, Continuum damage mechanics modeling of high temperature deformation and failure in a pipe weldment, Proc. Royal Soc. Lond. A, 433 (1991) 383- 403.

115. Y. P. Jiang, W. L. Guo, Z. F. Yue , J. Wang,On the study of the effects of notch shape on creep damage development under constant loading, Mats. Sci. Eng. A., 437 (2006) 340–347.

116. J. R. Rice and D.M. Tracey, On ductile-enlargement of voids in triaxial stress fields, J. Mech. Phy. Solids, 17 (1969) 201- 217.

117. A. C. F. Cocks and M. F. Ashby, Intergranular fracture during power-law creep under multiaxial stresses, Metal. Sci., 14 (1980) 395- 402.

118. M. J. Manjoine, Ductility Indices at Elevated Temperature, ASME J, Eng. Mater. Technol, 97 (1975) 156–161.

119. P. S. Weitzel, Babcock and Wilcox Power Generation Group: Paper presented at ASME 2011 Power Conf., Denver, CO, July 12–14, 2011.

120. Fujio Abe, Research and Development of Heat-Resistant Materials for Advanced USC Power Plants with Steam Temperatures of 700 °C and Above, Engineering, 1 (2015) 211–224.

121. F. Masuyama, History of power plants and progress in heat resistant steels, ISIJ Int., 41 (2001) 612–25.

122. A. Mathur, O. P. Bhutani, T. Jayakumar, D. K. Dubey, S. C Chetal: Proc. the 7th Int. Conf. on Advances in Materials Technology for Fossil Power Plants, ASM International, Waikoloa, Hawaii, USA,2013, pp. 53-9.

123. K. Laha, J. Kyono, and N. Shinya: An advanced creep cavitation resistance Cu-containing 18Cr–12Ni–Nb austenitic stainless steel, Scr. Mater., 56 (2007) 915–918.

124. N. Shinya, J. Kyono, and K. Laha, Self-Healing Effect of B Segregation on Creep Cavitation in Type 347 Austenitic Stainless Steel, J. Soc. Mater. Sci. Jap, 55 (2006) 317-322.

125. G. Eggeler and A. Dlouhy, Boron segregation and creep in ultra-fine grained tempered martensite ferritic steels, Z. Metallkd., 96 (7) (2005) 743–748.

126. D. R. Hayhurst, F.A. Leckie and J.T. Henderson, Design of notched bars for creep-rupture testing under tri-axial stresses, Int. J. Mech. Sci., 19 (1977) 147-159.

127. Sunil Goyal, K. Laha, C.R. Das, S. Panneer Selvi and M.D. Mathew, Finite element analysis of state of triaxial state of stress on creep cavitation and rupture behaviour of 2.25Cr-1Mo steel, Int. J. Mech. Sci., 75 (2013) 233-243.

128. P. Ou, H. Xing, X. Wang, J. Sun, Z. Cui, and C. Yang, Coarsening and Hardening Behaviors of Cu-Rich Precipitates in Super304H Austenitic Steel, Metall. Mater. Trans. A 46 (2015) 3909–3916.

129. B. K. Choudhary, S. Saroja, K. Bhanu Sankara Rao and S. L. Mannan, Creep-rupture behavior of forged, thick section 9Cr-1Mo ferritic steel, Metall. Trans. A, 30 (1999) 2825–2834.

130. W. J. Evans and B. Wilshire, The high temperature creep and fracture behaviour of 70-30 Alpha-Brass, Metall. Trans.1 (1970) 2133–2139.

131. D. Sidey and B. Wilshire, Mechanisms of Creep and Recovery in Nimonic 80A Met. Sci. J. 3 (1969) 56–60.

132. C. Phaniraj, M. Nandagopal, S. L. Mannan, and P. Rodriguez, The relationship between transient and steady state creep in AISI 304 stainless steel, Acta Metall., 39 (1991) 1651–1656.

133. Ahmadieh and A.K. Mukherjee, Stress-temperature-time correlation for high temperature creep curves, Mater. Sci. Eng., 21 (1975) 115–124.

134. K. E. Amin, A. K. Mukherjee, and J. E. Dorn, A universal law for high-temperature diffusion controlled transient creep, J. Mech. Phys. Solids, 18 (1970) 413–426.

135. J. Ganesh Kumar, K. Laha, V. Ganesan, G. V. Prasad Reddy, Analyses of Small Punch Creep Deformation Behavior of 316LN Stainless Steel Having Different Nitrogen Contents, J. Mater. Eng. Perform., 27(5) (2018) 3341-3347.

136. A. B. Pandey, R. S. Mishra, A. G. Paradkar, Y. R. Mahajan, Steady state creep behaviour of an Al-Al_2O_3 alloy, Acta Metall. Mater., 45 (1997) 1297–1306.

137. D.V.V. Satyanarayana, G. Malakondaiah, D. S. Sarma, Steady state creep behaviour of NiAl hardened austenitic steel, Mater. Sci. Eng. A, 323 (2002) 119–128.

138. J. Cadek, Creep in Metallic Materials, Elsevier, 1988.

139. H. J. Frost and M. F. Ashby: Deformation-Mechanism Maps—The Plasticity and Creep of Metals and Ceramics, 1st ed., Pergamon Press, New York, 1982, p. 62

140. B. Wilshire, P. J. Scharning, Long-term creep life prediction for a high chromium steel, Scripta Mater., 56 (2007) 701–704.

141. B. Wilshire, P. J. Scharning, A new methodology for analysis of creep and creep fracture data for 9–12% chromium steels, Int. Mater. Rev. 53 (2008) 91–104.

142. F. C. Monkman, N. J. Grant, An empirical relationship between rupture life and minimum creep rate in creep rupture tests, Proc. Am. Soc. Test. Mater. 56 (1956) 593.

143. J. Vanaja, K. Laha, R. Mythili, K. S. Chandravathi, S. Saroja and M. D. Mathew, Creep deformation and rupture behaviour of 9Cr–1W–0.2V–0.06Ta Reduced Activation Ferritic–Martensitic steel, Mater. Sci. Eng. A, 533 (2012) 17–25.

144. F. A. Leckie, D. R. Hayhurst, Constitutive equations for creep rupture, Acta Metall., 25 (1977) 1059–1070.

145. B. F. Dyson, T. B. Gibbons, Tertiary creep in nickel-base superalloys: analysis of experimental data and theoretical synthesis, Acta Metall. 35 (1987) 2355–2369.

146. S. Chaudhuri and R. N. Ghosh, Some Aspects of Mechanisms and Modelling of Creep Behaviour of 2.25Cr–1Mo Steel, ISIJ Int.,38 (1998) 881–887.

147. M. Fujiwara, H. Uchida, and S. Ohta, Effect of boron and carbon on creep strength of cold-worked type 316 stainless steel, J. Mater. Sci. Lett. 3 (1994) 557–559.

148. R. Monzen and K. Kita, Ostwald ripening of spherical Fe particles in Cu-Fe alloys, Philos. Mag. Lett., 82 (2002) 373–382.

149. S. Goyal, K. Laha, S. Panneer Selvi, M. D. Mathew: Mechanistic approach for prediction of creep deformation, damage and rupture life of different Cr–Mo ferritic steels, Mater. High Temp. 31 (2014) 211-220.

150. P. W. Davies, W. J. Evans, K. R. Williams, B. Wilshire, 3D creep cavitation characteristics and residual life assessment in high temperature steels a critical review Scr. Mater. 3 (1969) 671–674.

151. B. J. Cane, Creep damage accumulation and fracture under multiaxial stresses Advances in Fracture Research., Proc. 5th Int. Conf. Fract. Cannes, 3 (1981) 1285–1293.

152. I. J. Perrin and D. R. Hayhurst, Creep constitutive equations for 0.5Cr-0.5Mo-0.25V ferritic steel in the temperature range 600- 675° C, Int. J. Press. Vessel. Pip., 76 (1999) 599–617.

153. Sunil Goyal, K. Laha, and A. K. Bhaduri, Response of triaxial state of stress to creep rupture life and ductility of 316LN austenitic stainless steel, J. Mats. Eng. Performance., 26(2) (2017) 752-763.

154. J. He and R. Sandström, Modelling grain boundary sliding during creep of austenitic stainless steels J. Mats. Sci, 51(6) (2016) 2926-2934.

155. J. He and R. Sandström, Formation of creep cavities in austenitic stainless steels J. Mats. Sci, 51(14) (2016) 6674-6685.

156. J. Chuang, K. I. Kagawa, J. R. Rice and L.B. Sills, Overview no.2 : Non-equilibrium models for diffusive cavitation of grain interfaces, Acta Metall., 2 (1979) 265-284.

157. R. Hales, The role of cavity growth mechanisms in determining creep-rupture under multiaxial stresses, Fat. Frac. Engg. Mater. Struct., 17 (1994) 579-591.

158. F. Ghahremani, Effect of grain boundary sliding on steady creep of polycrystals, Int. J. of Solids and Struct., 16 (1980) 847-862.

159. Junjing He: High temperature performance of materials for future power plants, PhD Thesis, KTH Royal Institute of Technology, School of Industrial Engineering and Management, Stockholm, Sweden (2016).

160. K. Laha, J. Kyono and N. Shinya, Suppression of creep cavitation in precipitation-hardened austenitic stainless steel to enhance creep rupture strength Trans. Indian Inst. of Metals, 63 (2009) 437- 441.

161. G. Eggeler and C. Wiesner, A numerical study of parameters controlling stress redistribution in circular notched specimens during creep J. Strain Anal., 28 (1993) 13–22.

162. McLean, B. F. Dyson and D. M. R. Taplin, The prediction of creep fracture in engineering alloys, The Fourth International Conference on Fracture, Vol. 1, Ed. D. M. R. Taplin, University of Waterloo Press, Waterloo, Canada, 1977, pp. 325- 362.

163. E. A. Davis and M. J. Manjoine, Effect of notch geometry on rupture strength at elevated temperatures, ASTM STP 128, pp. 67- 87.

164. A. Aritra Sarkar, A. Nagesha, P. Parameswaran, R. Sandhya, K. Laha, M. Okazak Materials Science & Engineering A. 702 (2017) 360–370D. S. Wilkinson, V.Vitek, The propagation of cracks by cavitation: A general theory, Acta Metall., 30 (1982) 1723-1732.

165. D. S. Wilkinson, V.Vitek, The propagation of cracks by cavitation: A general theory, Acta Metall., 30 (1982) 1723-1732.

166. E. V. Pereloma, B. R. Crawford, P. D. Hodgson, Strain-induced precipitation behaviour in hot rolled strip steel, Mater. Sci. Eng A., 299 (2001) 27–37.

167. S. Bagui, K. Laha, R. Mitra and S. Tarafder, Accelerated creep behavior of Nb and Cu added 18Cr-8Ni austenitic stainless steel. Mater. Res. Expr. 5 (2018) 116515.

168. V. D. Vijayanand, S. D. Yadav, P. Parameswaran, K. Laha , P. K. Parida and G. V. P. Reddy. On Characterizing a Composite Microstructure in 316LN Stainless Steel Weld Metal and a New Damage Micromechanism During Creep. Metall. Mater. Trans. A, 49 (2018) 4409-4412.

169. M. S. Szczerba, T. Bajor and T. Tokarski, Is there a critical resolved shear stress for twinning in face-centred cubic crystals? Phil Mag. 84 (2004) 481–502.

170. K. C. Sahoo , S. Goyal, P. Parameswaran, S. Ravi and K. Laha, Assessment of Creep Deformation, Damage, and Rupture Life of 304HCu Austenitic Stainless Steel Under Multiaxial State of Stress. Metall. Mater. Trans. A., 49 (2018) 881-898.

171. C. R. Calladine, Time-scales for redistribution of stress in creep of structures. Proc. Royal Soc. Lond A., 309 (1969) 363- 375.

172. B. F. Dyson, M. S. Loveday, In: Proceedings of Creep in Structures, TUTAM Symposium. Oxford: Pergamon Press; 1981. pp. 406–421.

173. D. R. Hayhurst, Creep rupture under multi-axial states of stress J. Mech. Phys. Solids., 20 (1972) 381–390.

174. R. J. Browne, P. E. J. Flewitt, D. Lonsdale, M. S. Shammas, J. N. Sao, Multiaxial creep of fine grained 0·5Cr–0·5Mo–0·25V and coarse grained 1Cr–0·5Mo steels, Mater. Sci. Tech., 7 (1991) 707-717.

175. P. F. Aplin and G. F. Eggeler, Multiaxial stress rupture criteria for ferritic steels. Proceedings of the Int. Conf. on Mechanics of Creep brittle materials. Eds. A.C. F. Cocks and A.R.S. Ponter, Elsevier Applied Science 1988; pp. 245-261.

176. M.W. Spindler, The Multiaxial Creep Ductility of Austenitic Stainless Steels, Fatigue Fract. Eng. Mater. Struct., 2004, 27, p 273–281.

177. S. Chandrakanth and P. C. Pandey, An Isotropic damage model for ductile material, Engineering Fracture Mechanic's Vol. 50, No. 4, pp. 457-465, 1995.

178. H. M. Tlilan et al, Effect of notch depth on strain-concentration factor of notched Cylindrical bars under static tension European Journal of Mechanics A/Solids., 24 (2005) 406.

179. Report-SMST-Tubes, DMV 304HCu 04/2008, Salzgitter Mannesmann Stainless Tubes Gmbh, Germany, 2017, print.

180. K. C. Sahoo, S. Goyal, V. Ganesan, J. Vanaja, G.V. Reddy, P. Padmanabhan & K Laha, Analysis of creep deformation and damage behaviour of 304HCuaustenitic stainless steel. Mater. High Temp. 2019;39:388-403.

181. K. C. Sahoo, V. D. Vijayanand, S. Goyal, P. Parameswaran P, K. Laha, Influence of temperature on multiaxial creep behaviour of 304HCu austenitic stainless steel. Mater. Sci. and Tech. 2019;35:2181-2199.

182. E. A. Davis, M. J. Manjoine, Effect of notch geometry on rupture strength at elevated temperatures. Symp. on Strength and Ductility of Metals at Elevated Temperatures: With Particular Reference to Effects of Notches and Metallurgical Changes. STP128, 1953:67-68

183. Y. Wang, R. Kannan, L. Li, Insights into Type-IV cracking in grade 91 steel weldments. Mater. Des. 2020;190:108570.

184. D. Kobayashi, M. Miyabe, Y. Kagiya, R. Sugiura, T. Matsuzaki and A. Toshimitsu Yokobori, Jr. An assessment and estimation of the damage progression behavior of IN738LC under various applied stress conditions based on EBSD analysis. Metall. Mater. Trans. A. 2013;44:3123- 3135.

185. C. GANDHI, R. RAJ, Micromechanisms of creep crack growth in nickel based superalloys. Micro and Macro Mechanics of Crack Growth, Conference Proceedings, 1981, (Edited by K. Sadananda, B. B. Rath, and D. J. Michel) (The Metallurgical Society of AIME, USA).

186. S. E. Ng, G. A. Webster, B. F. Dyson, Notch weakening and strengthening in creep of 0.5Cr-0.5Mo-0.25V steel. Advances in fracture research, ICF-5, Eds. D. Francois et al., 1980, Pergamon Press, Oxford, UK, 1275- 1283.

187. G. Eggeler G, W. Tato, P. Jemmely, B. deMestral, Creep rupture of circular notched P91 specimens: influence of heat treatment and notch geometry, Scr. Mater. 1992;27:1091-1096.

Thesis Highlight

Name of the Student: Kanhu Charan Sahoo

Name of the CI/OCC: IGCAR, Kalpakkam **Enrolment No.: ENGG02201405008**

Thesis Title: Prediction of creep deformation and rupture behavior of 304HCu austenitic stainless steel under uniaxial and multiaxial state of stress at different temperatures

Discipline: **Engineering Sciences** **Sub-Area of Discipline:** **Multiaxial creep life prediction**

Date of viva voce: 12.02.2021

The boiler tubes made of 304HCu austenitic stainless steel (304HCu SS) are subjected to multiaxial state of stress due to internal pressure, bends, changes in section thickness, presence of weld joints and having inhomogeneous structures. In order to study the influence of multiaxial state of stress on 304HCu SS, creep tests have been carried out on both smooth and notched specimens of the given steel at 923 K, 973 K and 1023 K over a wide range of stresses.

Fig. 1 shows the schematic view of obtaining creep results for both smooth and notched specimens with the subsequent analysis using some mathematical equations, finite element method, characterization and multiaxial life and ductility prediction using suitable model. In uniaxial creep deformation, material exhibited very short primary creep regime followed by limited secondary stage and significant tertiary stage. The transient creep is analyzed using Garofalo equation and from steady-state creep regime, back stress was calculated using Lagneborg and Bergman graphical method. In the tertiary stage 304HCu SS has spent about 60, 64 and 72% of their creep rupture life of creep deformation. Creep strain and rupture life of the 304HCu SS were well predicted using the FE-analysis coupled with continum damage mechnics. In the presence of notch, creep rupture strength was found to increase with increase in notch sharpness with associated decrease in ductility. However, at relatively lower stress and high temperatures material exhibited tendency towards notch weakening for relatively sharper notches. The reduction in von-Mises stress below the applied stress at the notch throat plane results in notch strengthening while progressive saturation at the notch root results in saturation in creep rupture life. The cavity distribution, their growth and fracture behavior for shallow and sharp notches have been correlated through SEM and Finite element analysis of different component of stress distribution. Increase in temperature results in increase in normalized von-Mises stress, leading to increase in creep cavitation with decrease in creep rupture life of the material. The multiaxial creep rupture life has been predicted at different temperatures using skeletal point method of representative stress using different models. A temperature-independent unique master plot for multiaxial rupture life as a function of stress has been established and a modified model has been proposed for the prediction of multiaxial ductility at any temperature and other materials. 304HCu SS material showed increase in rupture life followed by a peak and then sudden decrease in rupture life with increase in notch depth which has been correlated with SEM, EBSD and FE-analysis of stress and strain distribution.

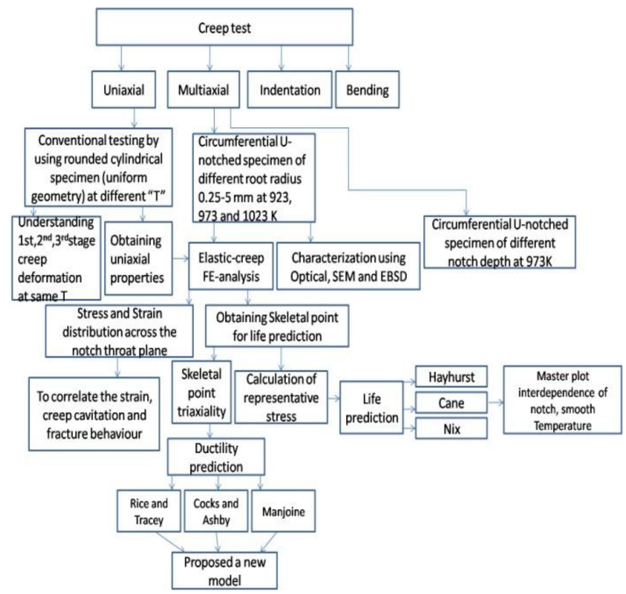

Figure 1. Schematic view of obtaining creep results and their systematic use for further finite element analysis and multiaxial life and ductility prediction of 304HCu SS